Simulations of Shock-Induced Phase Transitions in Silicon



Gabriele Mogni

Trinity College

University of Oxford

A thesis submitted for the degree of

Doctor of Philosophy

Michaelmas Term, 2013

I would like to dedicate this thesis to my loving parents.

Acknowledgements

There are many people who have contributed to the accomplishment of the work presented in this thesis and to whom I would like to express my gratitude. First and foremost, I would like to thank my supervisor Prof. Justin Wark for offering me the truly life-changing opportunity to pursue a DPhil degree at Oxford University, and for guiding and assisting me during the course of its progress. I would also like to thank all the members of the Wark research group in the Clarendon Laboratory with whom I had the opportunity to collaborate and socialise. In particular, I owe my thanks to Andy Higginbotham for helping me and encouraging me during the last four years, and patiently devoting some of his time to take part in countless conversations that have progressively shaped the structure of this thesis (the word "Exergy" in particular comes to mind as a recurring theme!). I would also like to thank the recently appointed new postdoc in our group, Matt Suggit, for assisting me in particular during the initial stages of my DPhil, and for taking me along to my first experiment at LLNL. In this last respect, I want to thank Jim Hawreliak and Robert Cauble for hosting me at LLNL during the course of these experiments. My regards also go to Nigel Park and AWE for providing the funding for my research. The accomplishments of the last four years have also been made possible by collaborations with visiting researchers from abroad, and in particular Katalin Gaál-Nagy from Germany and Eduardo Bringa from Argentina. Last but not least, I thank all my family and friends for providing me with crucial moral support.

Abstract

An understanding of the fundamental mechanism behind the relief of shear stress in single-crystal silicon subject to loading by shock-waves has to this day remained elusive. What is known is that this material undergoes a first-order pressure-induced polymorphic phase transition from its ambient pressure cubic-diamond (*cd*) crystal structure to its first stable high-pressure phase, known as β-Sn, at a pressure of about 120 kbar under hydrostatic compression. By investigating the evolution of the transition parameters for this phase transition as a function of increasing uniaxial shear stress representative of the effects of shock-compression via ab-initio Density Functional Theory computational techniques, we predict a significant lowering of the stress at which the phase transition occurs. This raises the question as to whether the onset of plastic response at the material's Hugoniot Elastic Limit (HEL) reported in experiments corresponds in fact to the phase transition itself, a very plausible possibility which has never been considered before. Furthermore, we present molecular dynamics simulations using a Tersoff-like potential of shock-compressed single crystals of silicon. We find an elastic response up to a critical stress, above which the shear stress is relieved by an inelastic response associated with a partial transformation to a new high-pressure phase, where both the new phase (*Imma*) and the original cubic diamond phase are under close to hydrostatic conditions. We note that these simulations are also consistent with shear stress relief provided directly by the shock-induced phase transition itself, without an intermediate state of plastic deformation of the cubic diamond phase.

Contents

Contents iv

Nomenclature vi

1 Introduction 1

1.1 Shock-waves in solids: an evolutionary perspective 1

1.2 Computational techniques in solid-state shock-wave physics 16

1.3 Role of the Author 19

2 Theoretical Background 22

2.1 Fundamentals of Crystallography 22

2.1.1 Bravais Lattices 22

2.1.2 Unit Cells 25

2.1.3 Miller index labelling system for crystal planes 26

2.1.4 Lattice with a basis: crystal structures 28

2.1.5 Point groups and space groups 30

2.1.6 The reciprocal lattice 33

2.2 The physics of shock-waves in one-dimensional planar geometries . 36

2.2.1 Rankine-Hugoniot jump conditions 37

2.2.2 Conditions for shock-wave formation 42

2.2.3 The Hugoniot curve 44

2.2.4 Real shock-wave profiles and the Hugoniot Elastic Limit . 45

2.3 Classical Molecular Dynamics 51

2.3.1 Elements of Molecular Dynamics simulations 51

2.3.2 Integrators 54

2.3.3 The Tersoff Potential 55
2.4 Density Functional Theory 61
2.4.1 The Kohn-Sham formulation of Density Functional Theory 61
2.4.2 The Local Density and Generalized Gradient approximations for the exchange-correlation energy functional 69
2.4.3 Computational self-consistent solution of the Kohn-Sham equations: the plane-wave pseudopotential method 72

3 Ab-initio investigation of the cubic-diamond → β-tin phase transition in Si and Ge 78
3.1 Motivation 78
3.2 The mechanical response properties of silicon and germanium under shock-compression: the current state of research 82
3.3 The cubic diamond to β-tin phase transition 93
3.3.1 Crystallographic properties of the two phases 93
3.3.2 Thermodynamics of first-order pressure-induced phase transitions 95
3.3.3 Mechanics of non-hydrostatic lattice deformations 96
3.4 Density Functional Theory calculation 100
3.5 Numerical Analysis 103
3.5.1 Transition pressure and enthalpy barrier at hydrostatic conditions 103
3.5.2 Extension to non-hydrostatic conditions 108
3.5.3 Applications to shock-wave loading 111
3.6 Discussion of the results 116
3.7 Conclusions 121

4 The role of the Gibbs free energy in pressure-induced phase transitions under non-hydrostatic stress 122
4.1 Theory of first-order phase transitions 122
4.2 The problem of how to formulate the Gibbs free energy under non-hydrostatic stress 129
4.3 Work under non-hydrostatic stress conditions 136

4.4 The concept of Availability in the theory of phase-transitions . . . 142
4.5 Some illustrative examples of the principle of minimisation of Availability . . . 146
4.5.1 Hydrostatic compression of the system . . . 146
4.5.2 Uniaxial compression of the system . . . 149
4.5.3 System held at constant volume . . . 152
4.6 Availability under general non-hydrostatic stress conditions . . . 156
4.7 Evidence in support of the Availability formulation: pressure-induced phonon softening in silicon . . . 164
4.8 Conclusions . . . 169

5 Molecular Dynamics simulations of the cubic diamond to *Imma* shock-induced phase transition in silicon 171
5.1 Introduction . . . 171
5.2 Molecular Dynamics simulations . . . 174
5.3 Morphology of the mixed-phase region . . . 186
5.4 Thermodynamics of the mixed-phase region . . . 205
5.5 Conclusions . . . 219

6 Conclusions and Future Work 221
6.1 Summary . . . 221
6.2 Future Work . . . 224

References 227

Chapter 1

Introduction

1.1 Shock-waves in solids: an evolutionary perspective

The study of matter under extreme conditions [36, 46, 60, 208] is a interdisciplinary subject with a broad range of applications in the fields of science and mechanics of materials, geophysics, planetary- and astro-physics, high-energy density physics, high-pressure physics and inertial confinement fusion. The application of high pressure is the simplest way to change the lattice spacing and has led to the discovery of new phenomena, new phases and new forms of electronic and ionic order, thus providing new insights into material behaviour under extreme conditions [19, 97, 151]. The properties of materials under high-pressure are normally studied in the laboratory using static and dynamic compression techniques. The two techniques differ drastically in the methods of generating and measuring pressure and in the nature of the final compressed state. In static experiments,

the sample is squeezed between a set of opposing pistons or anvils. Temperatures rarely exceed a few thousand degrees Celsius. The maximum pressures obtained are currently of order 6 Mbar [48], inherently limited by the strengths of the available construction materials. Dynamic shock-compression studies on the other hand obtain high pressures and temperatures by introducing a rapid impulse into a substance through the detonation of a high explosive, the impact of a high-speed projectile or the absorption of an intense pulse of radiation. In shock-wave experiments, the passage time of the shock is short compared to the time that it takes for the sample to disassemble. As a result, the attainable pressures for a given material are limited only by the energy density supplied by the driver. Furthermore, what distinguishes dynamic from static compression are the high strain rates and shear forces in the former. Chemical explosives have been used to obtain pressures up to 1 Mbar in liquids and up to 13 Mbar in metals, with accompanying temperatures of tens of thousands of degrees Kelvin. Final pressures ranging from 20 to 158 Mbar have been measured in underground nuclear explosion experiments. In inertial confinement studies, pellets of deuterium and tritium are subjected briefly to laser-driven dynamic pressures of about 1000 Mbar and temperatures in excess of 10^7 K. The centre of the Earth has a gravitationally-generated pressure of about 3.5 Mbar and temperatures of 6000 K. The conditions in Jupiter's centre are believed to be about 100 Mbar and 24,000 K. The centres of stars and white dwarfs have pressures in excess of thousands of Mbar and with temperatures of tens of millions of K. In neutron stars pressures of millions of Mbar are believed to exist.

Systematic investigations of high-pressure properties date back to the 18th century. By the latter part of the 19th century, the French physicist Emile Am-

agat had extended the pressure measurements on gases to about 3 kbar. P.W. Bridgman, of Harvard, is widely regarded as the founder of modern high-pressure technology and research. Bridgman was actively engaged in high-pressure research from 1903 to his death in 1961 and received the Nobel Prize for Physics in 1946. Near the end of his career he was consistently making measurements above 100 kbar [20]. Most of the early research into high-pressure physics was conducted employing static methods of compression. The most important advance in static high-pressure research has been the development of the diamond anvil cell (DAC) [109]. A small (sub-millimetre sized) sample may be compressed by megabar pressures when the opposing flat parallel faces of two diamond anvils are pressed together. The nature of this compression is always close to hydrostatic. The uniaxial pressure supplied by the DAC may be transformed into uniform hydrostatic pressure using a pressure transmitting medium, such as argon, xenon, hydrogen, helium, paraffin oil or a mixture of methanol and ethanol. The pressure-transmitting medium is enclosed by a gasket and the two diamond anvils, as shown in Fig. 1.1. The important features of this cell come not only from the hardness of the diamond but also to its transparency to both X-ray and visible light, which permits a variety of diagnostic measurements on the sample being compressed. Optical absorption, reflectivity measurements, Raman and Brillouin scattering, and X-ray diffraction studies have hence become possible at extreme pressures [55, 98]. Pressure may be determined by measuring the density of a secondary reference material whose behaviour under pressure is known, and this standard is ultimately linked to shock compression measurements. Common pressure standards include ruby fluorescence, and various structurally simple metals, such as copper or platinum. The pressures achieved in DACs can now

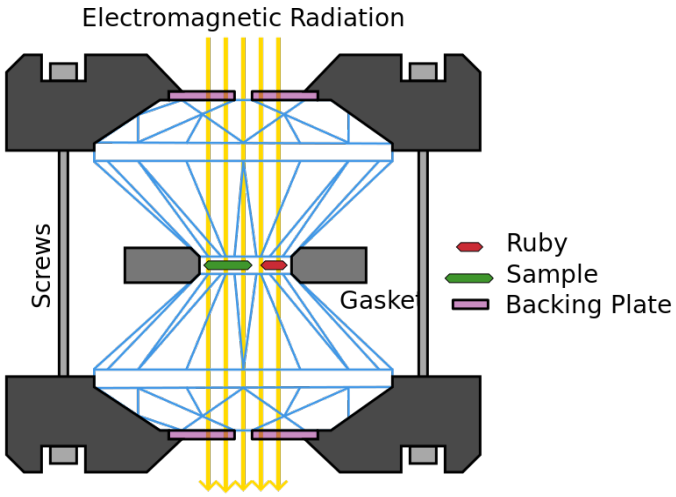


Figure 1.1: Schematics of the core of a diamond anvil cell. The diamond size is a few millimeters at most. (Figure reproduced from Ref. [1].)

exceed 6 Mbar [48], and can therefore be used to recreate the pressure existing deep inside planets such as the Earth, creating materials and phases not observed under normal conditions.

Shock waves are defined as propagating mechanical disturbance waves of finite amplitudes and arise when matter is subjected to strong and rapid dynamic compression. Compared to acoustic waves, which are waves of very small, almost infinitesimal amplitudes, shock waves can be described by four unusual properties: firstly, a pressure-dependent, supersonic velocity of propagation; secondly, the formation of a steep wave front with abrupt and discontinuous [1] change in all thermodynamic quantities describing the state of matter such as pressure, density and temperature; thirdly, for nonplanar shock-waves, a strong decrease of the propagation velocity with increasing distance from the centre of origin; and finally

[1] The width of the discontinuity is generally a few molecular mean-free-path lengths.

nonlinear superposition (reflection and interaction) properties. Shock-waves are generally associated with explosions, high-speed impacts, laser ablation and other uncontrolled and irreversible processes involving very high-energy density states caused by the very fast deposition of any form of energy. Although shock-waves are indeed irreversible, the process is well understood and can be controlled in the laboratory to produce a desired response. Shock-waves are also a common phenomenon in nature on Earth and under certain conditions are produced during volcanic eruptions and earthquakes. Other striking natural shock-wave phenomena include thunder and the fall of meteors. Cosmic shock phenomena reach enormous dimensions compared to terrestrial ones, such as those encountered during stellar explosions (supernovae). The shock-wave of the largest imaginable dimensions would be the Big Bang, the "shock of all shocks", which resulted about 14 billion years ago from a gigantic explosion of a highly concentrated mass of gaseous matter at a single point in space. Shock-wave effects have in general been observed in all four states of matter, and also in media composed of multiple phases. It is now generally recognised that shock-waves play a dominant role in most mechanical high strain-rate phenomena. Furthermore, shock-waves can exist in all proportions, ranging from the microscopic regime to cosmic dimensions.

One practical means of getting a useful survey on the development of shock-wave physics is to classify the large number of milestones and shock-wave-related-disciplines in terms of states of matter, that is shock-waves in gases, liquids, solids and plasmas. Only the third of these categories, that is the propagation of shock-waves in solid-state condensed matter, will be considered within the scope of this introduction, and indeed throughout the duration of the entire thesis. Understanding the dynamic lattice response of solids under the extreme

conditions of pressure, temperature and strain-rate is a scientific quest that spans more than a century [15, 139]. Historically, solid-state shock-wave physics is an outgrowth of classical percussion, which was established in the 17th century, but the main push into this new area of research came from the 19th century pioneers of classical shock-wave theory [210]. These pioneers did not in fact limit their analyses to fluids, but had also considered the peculiarities involved in the propagation of shock-waves in solids. In his famous classic treatise "On the thermodynamic theory of waves of finite longitudinal disturbance" published in 1869 [199], the Scottish civil engineer William J.M. Rankine clearly states that the original relations he derived are valid "for any substance, gaseous, liquid or solid". Ensuing authors, such as Christoffel, Hugoniot, Duhem, Hadamard, and Jouguet, addressed the shock-compressed solid state in more detail. The most important (largely theoretical) works on shock waves in condensed matter dating from the period 1808-1949 have been brought together into a single collection [114]. Important papers from 1948 to the present were later added to this original collection [115], allowing researchers and historians to trace the major events leading to the establishment of the field of shock-compression in solids. Contrary to the rapid and steady progress of shock-wave physics in gaseous matter since the 1870s, research in shock-compressed solids has evolved slowly. The main reason was certainly the need for very challenging high-speed instrumentation and diagnostics for detecting and recording physical parameters of interest, which require sub-microsecond resolution and which were not available until after World War II (and were even then initially confined to only a few laboratories).

Solid-state shock-wave physics therefore did not evolve as a significant and independent field of research until the end of World War II, partly as an outgrowth

of nuclear weapon research imposed by the Manhattan Project. Contrary to the foundations of gas dynamics, which were built mainly in Europe, the foundations of modern solid-state shock-wave physics were laid independently in military laboratories in the United States and the former Soviet Union, motivated exclusively by military requirements. In its early days, the primary objective of shock-wave laboratory experiments was in fact the determination of wide-range equations of state of materials and the parameters of detonation of high explosives for predicting the effects of explosions and high-velocity collisions typical of military armaments. It was only many years later that the power and the potential of shock-waves as a scientific probe for gaining insight into the fundamental structural and mechanical response properties of high-pressure crystal structures, and as a machining tool for their technological treatment, was realised [140]. This particular application of shock-waves provided for the first time a dynamic alternative to the static loading techniques, such as DACs, that had until then been the norm for interrogating the effects of high compressions on crystal lattices. This complementarity can be understood both in terms of the pressures attainable during shock-compression, which vastly exceed the order Mbar pressure threshold in DAC experiments, and in terms of the breadth and depth of its applications, which are broadened by the dynamic time-resolving abilities of shocks for investigating the picosecond time-scales characteristic of the fundamental mechanical phenomena in solids. Modern investigations of shock waves in solids revealed rather complex behaviour in comparison to fluids, and theories describing the solid state under shock-compression taking into account structural properties are still in development today. Furthermore, the range of related fields associated with shock-waves in condensed matter is much wider than those in fluids. The

majority of shock-wave studies in solid materials has in fact been pursued with material science applications in mind and not in the wave behaviour itself [140]. More than a thousand solid materials have been studied experimentally so far to determine their shock-wave properties, including almost all solid elements, a large number of technically relevant metal alloys, as well as many common minerals [26, 155].

The first publicly-available paper on the experimental study of shock-wave propagation in solids, which was entitled "The Propagation of Shock Waves in Steel and Lead", was published in 1948 by D.C. Pack and co-workers [183]. The first review article on the progress of shock-wave research in solids was not given until 1955 [74]: the American physicist R.W. Goranson, who in 1945 initiated a programme at Los Alamos National Laboratory to systematically study the equations of state of various materials, presented the first data on the dynamic compressibility of metals. This allowed the first quantitative comparisons with Bridgman's static measurements. The classic, most widely cited work in this new field of science was published in 1958 by three Los Alamos scientists, Rice, Walsh and McQueen [203]. Their pioneering paper "Compression of Solids by Strong Shock Waves" represents a landmark in the evolution of solid-state shock-wave physics. Almost overnight, ordnance laboratories throughout the world were able to convert technology developed for weapons into technology for visionary studies of matter in an entirely new range of pressures. Swords forged for nuclear weapon development were beaten into high-pressure science ploughshares. Other significant names in the post-war American condensed matter shock-wave research community include G.E. Duvall, R.A. Graham and L. Davison. A general comprehensive guide to the early literature documenting progress in solid-state

shock-wave physics can be found in the introduction of Ref. [40]. Independently of the research conducted in this field throughout the duration of the Cold War in the American National Laboratories, primarily the Los Alamos, Lawrence Livermore, Sandia and Oakridge National Laboratories, similar work was also initiated in the Soviet Union's Nuclear Centre located in Arzamas-16 (now Sarov). This institution (now the Russian Federal Nuclear Centre of the All-Russian Scientific Research Institute of Experimental Physics) was from its conception up to 1996 in many senses a "hidden world", where a multi-disciplinary team of scientists made significant contributions to defence and fundamental research. Of particular eminence are the Soviet Physicists Y.B. Zel'dovich, S.B. Kormer and L.V. Al'tshuler. The first Soviet results on dynamic equations of state for a number of metals were not published in the open literature until 1958. In 1965, Al'tshuler, the patriarch of Russian solid-state shock-wave physics, published another important review paper on the use of shock-waves in high-pressure physics [6].

As mentioned earlier, very high-energy density states of matter are necessary to produce high-pressure shock-waves in condensed media. Methods of generating shock-waves in condensed matter can be divided into two broad categories [58]. One is the direct contact of some media in a high-energy density state with the surface of the sample under investigation. The high-energy density media can be a high-temperature plasma, gaseous products of high explosive charges, etc. The other procedure involves the impact of a high-speed projectile accelerated by some means, whereby at least half of the kinetic energy of the projectile is converted into the internal energy of the collided material. Overall, the detonation of high-explosive charges in contact with the sample, electrical explosion of foils, laser pulses or particle-beam generators can be used to induce shock-waves

in condensed matter. If any of these methods are used to accelerate a projectile to high velocity (usually of order of several km/s) it is also possible to realise the second type of shock generation. A common method to accelerate a projectile to high velocity is to use a propellant, such as a volume of compressed gas. A device designed to accelerate a projectile and to perform the impact experiment is called a gun. Examples include compressed gas guns, powder guns, and two-stage gas guns, all of which were first developed in the 1940s and are now established experimental techniques for generating shock-waves. Much of the presently available shock-wave data of materials is derived from either explosives of gas-gun work. The nose part of the projectile to be collided with the target assembly is called the flyer plate. To generate a plane shock-wave in solids and to measure the shock propagation, a relatively thin plate must be used. The target assembly essentially consists of the driver plate and specimen plate, which is typically several millimetres thick. A high-pressure plane shock-wave can be induced through a precisely controlled head-on collision of the flyer plate with the driver plate. Using plates as all components of the impact shock experimental assembly guarantees that all strains are strictly one-dimensional and that the resulting shock-wave is therefore planar.

One of the major objectives of shock-compression experiments is to obtain information on the high-pressure state attained during the shock-loading process. The simplest way to do this is to measure the shock velocity and particle velocity simultaneously in one shot. The time history of some physical variables such as pressure and density is also normally measured. This kind of measurements are crucial in most shock-compression experiments, as profiles of the quantities contain information on the dynamic structural phenomena occurring inside the

shock-loaded sample, such as elastic-plastic transition and the onset of crystal defects accompanying the plastic flow, pressure-induced polymorphic phase transitions, shock-induced melting, relaxation due to the stress release etc. Many experimental methods have been developed to monitor the evolution of the shock and particle velocities, and of other physical quantities. Several kinds of in-material gauges were for example developed to measure the stress profile with time. The most established and popular method for monitoring the particle velocity history is the VISAR technique introduced by Barker and Hollenbach [11]. VISAR is an acronym for Velocity Interferometer System for Any Reflector. The underlying physical principle of the method is a wide-angle Michelson Interferometer with delay leg. The reflected light by the surface of the sample is divided into two paths, one of which is delayed through a delay leg. Interference of these two beams provides information on the change in the Doppler shift due to the moving velocity of the surface. VISAR can measure the acceleration-sensitive signals from which very precise velocity history of the surface can be determined. The Rankine-Hugoniot relationships, which relate the thermodynamic state of the medium behind the shock front to its initial state, the shock-wave velocity and the particle velocity, also proved most useful in the further evolution of solid-state shock-wave physics, allowing many more variables to be derived from the experimentally-measured ones.

The entire research field of shock generation in solid matter was propelled to a new dimension by the advent of high-power laser systems in the late 1960s and early 1970s [68, 105]. This marked a radical departure, in terms of effectiveness, manageability and versatility, from all approaches for generating shock-compressed solid targets in laboratory experiments considered previously, which

had relied primarily on the use of explosive charges or the afore-mentioned driving of flyer plates into the sample. The most commonly used class of lasers in the field of laser-induced shock-waves consists in Neodymium glass lasers, which emit at a wavelength of 1.053 μm, although this frequency can then be doubled or tripled following its generation for more effective coupling with the target material through the use of anharmonic non-linear optic conversion crystals. The fields of high-power lasers and laser-matter interaction are vast and active areas of research in their own right, and will not be discussed further here. In the context of this presentation, it suffices to know that when short pulses of high intensity laser radiation typical of these high-power laser systems, with duration of order a few nanoseconds and containing tens or even hundreds of Joules of energy, impinge on the solid target after having been focussed by huge lenses down to focal spots with diameters of order a few hundred microns (with corresponding irradiances of order 10^{10} to 10^{15} Wcm^{-2}), a very high temperature plasma is generated on the target surface upon impact and deposition of the beam energy [168]. The subsequent rapid expansion of this hot plasma away from the solid surface and into the surrounding vacuum chamber, where these types of experiments are typically held, results in a force being exerted on the rest of the target (by conservation of momentum) and gives rise to a rapid rise in pressure of the sample, which is in turn mediated by the formation and propagation of a shock wave. In general, the higher the energy contained in the laser pulse, the stronger the resulting pressure of the shock wave in the material. The relation between the shock-induced pressure into the target sample P and intensity of the drive laser beam I_L is approximately of the form $P \sim I_L^{2/3}$. Shock pressures between 10 and 1000 GPa are now easily accessible through direct ablative laser drive. In experiments involv-

ing laser-induced shock waves, the solid targets typically consist in single crystal samples, although polycrystalline materials offering a more realistic portrayal of real engineering materials can also be studied. Most of these high-power lasers were originally developed in the context of the research for generation of electrical energy by Inertial Confinement Fusion [194], the same physical process that fuels stars and offers the hope to provide a clean and virtually inexhaustible source of nuclear energy for meeting future energy demands, if proven feasible. Beside its applications in nuclear fusion, the achievement via laser-induced shock waves of pressures reproducing the same physical environments as found in planetary cores paved the way for major breakthroughs to be accomplished in the field of geophysics, allowing in particular new phases of the material constituents of the Earth's various internal structural layers to be identified and studied. Notable examples include the $MgSiO_3$ perovskite, thought to be the major component of the Earth's mantle, and the $\alpha - \epsilon$ phase transition in iron, which is believed to be the main component of the Earth's solid inner core [87, 121, 122].

At the end of the 19th century, the British engineer C. Parsons, inventor of the multistage steam turbine, and the French chemist H. Moissan, a professor at the University of Paris, first attempted to use shock-waves to induce polymorphic phase transformations in solids, especially in carbon to produce artificial diamonds. However, their efforts proved for the large part inconclusive. An important step forward towards this goal were the later results of static high-pressure investigations on a large number of liquid and solid substances carried out by the American experimental physicist P.W. Bridgman at Harvard College, in a long-term campaign spanning several decades from the start of the 20th century that showed that many crystals transform to new structures under the influence of

static pressure and that formed the foundations for our understanding of the behaviour of matter under static high pressures [20]. These results aroused the interest of the shock-physics community about how substances would behave under dynamic pressures. There is now a large body of experimental and theoretical evidence that many pressure-induced phase transitions occur during shock compression [53]. This is a remarkable result, given that the time scale over which the loading pressure is applied to the sample under investigation in shock experiments is many orders of magnitude shorter than in the static experiments. The most well known, and indeed most thoroughly studied of these shock-induced transformations, is the α-ε phase transition in iron, where the body-centred cubic (bcc) lattice in which iron crystallises under ambient conditions transforms to hexagonal closed packed (hcp). Iron has traditionally been held at great importance by the high-pressure physics research community, being a material of crucial importance in the development of human civilisation, as well as being the principal element within the Earth's core. The first attempt at detecting the α-ε transition under shock conditions came half a century ago, when Walsh reported data on the propagation of high-pressure shock waves in Armco iron that were in disagreement with Bridgman's original static compressibility measurements. A possible explanation for this discrepancy was offered by Bancroft, Peterson, and Minshall [10] when they observed a multiple-wave shock structure within a shocked single-crystal sample, which they interpreted as the elastic-plastic response followed by a transformation of the material to a different phase. Analysis of the wave profiles implied that the onset of the phase transition occurred at a pressure of 13 GPa. Originally it was assumed that this was a transition to the face-centred cubic γ phase, which can be observed statically by raising the temperature to

around 1000 K at standard pressure. It was only several years later that crystallographic evidence for a transition from equilibrium bcc to a previously unknown ε phase in the hcp structure at 13 GPa was obtained in static X-ray diffraction experiments by Jamieson and Lawson [108]. Direct evidence of the equivalence of the statically and shock-compressed phases came in 2005 during the nanosecond X-ray diffraction studies from laser-shocked single-crystal targets by Kalantar et al [121]. This data was also found to be in remarkable agreement with large scale molecular dynamics simulations of the shock-induced phase transition reported by Kadau and co-workers [117, 118, 119]. The confirmation that the same phase transition occurs under static conditions at an almost identical pressure to that encountered in earlier shock-wave measurements has long been regarded as one of the major breakthroughs in the history of the field of shock-wave physics. The fact that the transition pressure is essentially unaltered by the different conditions encountered in dynamic compression compared to the static case is by itself a remarkable result. The shear stress experienced by crystals under the two different techniques is in fact radically different: in static measurements the crystals are compressed hydrostatically, whereas in planar shock-wave experiments, the crystal sample undergoes uniaxial straining. Hydrostatic conditions occur during shock-compression only if the shear stress is relieved by significant plastic flow or by the onset of a phase transition. Even then the material will retain some degree of shear stress due to the material strength. Thus in general there are very significant differences between the conditions experienced by a shock loaded and a hydrostatically compressed sample. Other early spectacular investigations in the field of shock-induced polymorphic phase transitions include the work on possible ice modifications of shock-compressed water by Rice and Walsh [237], on

shock-induced transformations of quartz into high-pressure polymorphs by Chao et al. [29], on the detection of the well-known Bi I to Bi II shock-induced transition by Duff and Minshall [49], and on shock-induced transformation of graphite into diamond by DeCarli and Jamieson [42]. This latter experiment in particular demonstrated the power of shock-induced polymorphic transitions as a tool for new material synthesis. Today dynamic and static high-pressure methods of generation, calibration and measurement do not compete with one another, but rather are used to complement each other, as the example of the discovery of the α-ε phase transition in iron demonstrates.

1.2 Computational techniques in solid-state shock-wave physics

The high cost and complexity of the experiments described in the previous section makes it an imperative to have computational simulation techniques at the disposal of the shock-wave research community for emulating from first principles, or "ab-initio", the mechanical response properties and X-ray diffraction signals of solids subject to compressive loading by laser-induced shock waves at the microscopic atomistic level [220]. This type of ab-initio simulation work is useful for both predicting *a priori* the outcome of experiments, and for generating comparative benchmarks for substantiating *a posteriori* experimental results. One computational approach which has proven to be of particular usefulness in the simulation of shock-wave propagation and induced mechanical effects in crystalline matter is the technique of classical Molecular Dynamics (MD) [92, 93, 94, 216],

such as implemented by the software package LAMMPS [196]. This method involves setting up large systems of atoms modelling real single-crystal and poly-crystalline samples, and giving the particles at one end of the system an initial uniaxial velocity representative of a shock-wave propagating through the sample. Moreover, the mutual electrostatic interactions between all particles in the ensemble can be accounted for through the choice of a specific parametric form for the inter-atomic potential. Numerous different flavours of potentials, often semi-empirical in nature, have been developed with time and are currently available for simulating most materials in the Periodic Table, the most notable examples being the Lennard-Jones pairwise interaction potentials [66] and Embedded-Atom Model (EAM) many-body potentials [41]. The latter class of potentials is particularly efficient for the modelling of metallic samples [23, 110, 111, 170]. The term "classical" in the description of this MD technique is reminiscent of the fact that the particles in the system are allowed to evolve dynamically with time upon calculation of their trajectories by simple integration of Newton's classical equations of motion, without consequently the need to account for the quantum mechanical nature of their interactions. The recent technological advances in supercomputer processing power, coupled with the development of techniques for the massive parallelisation of computer codes [82], have allowed classical MD simulations comprising over a billion atoms, corresponding to model sample lengths of order microns (comparable to real targets) and evolving over time-scales of order nanoseconds, to be executed and post-processed at the microstructural level in reasonable times [21, 22]. Furthermore, the visualization of atomic positions at any time step allows for the detection and tracking of the time evolution of microscopic structural features of the crystal induced by the shock-loading, such

as defects [21] and phase transitions [118].

The principal source of uncertainty in MD simulations typically lies in the choice of the interatomic potential, the element of the simulation which embodies all the most drastic approximations on the nature of the interatomic forces governing the conduct of matter. Even though most MD potentials are parametrised by accounting for several empirical bulk properties of the material under investigation, most commonly the lattice parameter, bulk modulus and elastic tensor components, they can remain of doubtful accuracy under certain physical conditions, and in particular under the high compressive strains characteristic of simulated shock-waves which lie at the core of our research interests. As a means to authenticate and complement the results already readily obtainable by classical MD simulations, the alternative computational technique of Density Functional Theory (DFT), a powerful and fully quantum-mechanical alternative ab-initio approach to the solution of complex many-body problems in solid-state and condensed-matter physics, can be of great help [216]. This class of computational methods, and in particular its formulation in terms of plane-waves and pseudopotentials, has recently emerged as an extensive and burgeoning area of active research interest, owing in particular to its efficiency, ease of implementation and continuously improving accuracy in performing electronic structure calculations and predicting from first principles the physical properties for a broad variety of systems, ranging from isolated atoms and molecules to extended crystalline solids and chemical compounds [116]. When assessing the reliability of DFT simulations for reproducing the effects of shock-loading on solids, an important distinction must however be drawn between the dynamic and irreversible conditions characteristic of shock-waves, which in real shock experiments lead to high strain rates

and rapid heating of the sample, and the quasi-static, reversible and adiabatic fashion in which DFT simulations such as those discussed in this thesis are normally performed. Despite the fundamental differences in the principles governing these two regimes, the estimates for material properties, such as the transition pressures and elastic limits, delivered by static ab-initio simulations often compare favourably with experimental observation on shock-compressed solids. This is a direct consequence of the fundamental nature of these quantities, which makes them only weakly dependent on the particular approach employed for attaining the relevant pressure regimes.

1.3 Role of the Author

As is customary in scientific research, many of the results presented in this thesis have been obtained through collaborative efforts with other members of Prof. Justin Wark's group and beyond. In this section, the contributions made individually by the author in obtaining these results are clearly outlined. Throughout the entire length of the thesis, references made to work performed by other researchers in deriving these results will be clearly labelled.

- Chapter 2 - The chapter following the present one reviews the relevant general background theory necessary for understanding the new material presented throughout the duration of the entire thesis. Most of this theoretical work has been appropriately reproduced from general reference textbooks and review articles. In particular, the main references consulted in writing each section in this chapter are Ref. [7] for section 2.1, Ref. [165] for section 2.2, Refs. [225, 245] for section 2.3, and finally Ref. [156] for section 2.4.

- Chapter 3 - The first problem confronted in this thesis consisted in investigating, using DFT techniques, the magnitude of the transition pressure and enthalpy barrier of the pressure-induced solid-solid polymorphic phase transition in single-crystal silicon from its equilibrium cubic-diamond (*cd*) structure to its first stable high-pressure phase, which lies in the so-called β-Sn structure. The initial part of the research presented in this chapter closely mirrors the work performed by Strauch and Gaál-Nagy [65] in a previous DFT investigation, one of the few in which the properties of the *cd* to β-Sn phase transition in silicon were studied through ab-initio DFT techniques under non-hydrostatic pressure conditions, and the first to analyse the influence of such conditions specifically on the enthalpy barrier. The reader is therefore referred to this paper for a direct comparison of the results presented throughout this chapter. In a first instance we have reproduced the same results as in this paper with our own versions of the computational and data analysis codes involved. The subsequent extrapolation of these results to the conditions of uniaxial compression characteristic of the propagation of shock-waves in the sample is an original idea of the author.

- Chapter 4 - The development of this chapter was motivated mainly by the problem of how to determine phase equilibrium for phase transitions occurring under non-hydrostatic stress which was encountered during the course of the work performed in the previous chapter. Due to the scarcity of consistent and reliable methods for tackling this problem available in the literature, the majority of the results presented in this chapter are original

ideas of the author.

- Chapter 5 - This final chapter of new work is devoted to exploring the behaviour of single-crystal silicon under shock-compression as modelled with classical Molecular Dynamics techniques, in connection in particular with the occurrence of the shock-induced phase transition from the equilibrium *cd* structure to the high-pressure *Imma* phase. Previous computational investigations, such as the work by Lane and Thompson [145], have considered the possibility of phase transitions as a mechanism for the relief of shear stress in shocked semiconductors. However the work presented in this chapter for the first time provides a detailed model for how this relief of shear stress is accommodated by the sample at the microscopic lattice level. Furthermore, a quantitative thermodynamical analysis successfully explains the occurrence of the phase transition in terms of minimisation of the enthalpy of the system. Both aspects of the investigation of the phase transition have been conceived and implemented by the author, and the results of this work have been accepted for publication in Physical Review B, with the author of this thesis the primary author of this paper [172].

- Chapter 6 - This chapter is simply a summary of the most important results of the previous three chapters, and also offers suggestions of further work.

Chapter 2

Theoretical Background

2.1 Fundamentals of Crystallography

This section is aimed at equipping the reader with the essential knowledge of crystallography deemed necessary to gain a better understanding of the various crystal structures considered in this thesis. For a full introduction to the theory of crystals, the reader is referred to one of the many textbooks on condensed matter physics [7, 45, 84, 154].

2.1.1 Bravais Lattices

The most fundamental concept in the description of crystalline solids is the *Bravais Lattice*, which explains the geometry of the underlying periodic structure of atoms in a crystal, regardless of what the actual chemical composition of the crystal may be. There are two equivalent definitions of a Bravais Lattice:

1. A Bravais lattice is an infinite periodic array of abstract discrete lattice points with an arrangement and orientation that appears exactly the same

from whichever of the points the array is viewed. This is to say that all lattice points are equivalent, and the array is therefore periodic.

2. A three-dimensional Bravais lattice consists of the set of all lattice points with positions vectors $\overrightarrow{R}$ relative to one of the points of the form -

$$\overrightarrow{R} = n_1\overrightarrow{a_1} + n_2\overrightarrow{a_2} + n_3\overrightarrow{a_3} \tag{2.1}$$

which are known as Bravais Lattice Vectors. The three $\overrightarrow{a}$ vectors must not lie in the same plane, and the n coefficients are integers. The $\overrightarrow{a}$ vectors are known as primitive translation vectors and are said to generate or span the Bravais Lattice. $\overrightarrow{R}$ corresponds to the displacement vectors between any two Bravais lattice points , that is the sum or difference of any two Bravais lattice vectors, including the Bravais lattice vectors themselves.

An important property of all Bravais Lattices is that they have translational symmetry, and therefore are invariant under a translation by a displacement vector $\overrightarrow{R}$ between any two Bravais Lattice points. $\overrightarrow{R}$ therefore represents the periodicity of the Bravais lattice. As a result, any local physical property of the crystal is invariant (periodic) under $\overrightarrow{R}$, such as the charge concentration, electron number density, or magnetic moment density. For any given Bravais lattice the set of primitive vectors is not unique, and there are infinitely many nonequivalent choices, just like basis sets in linear algebra for vector spaces. Hence the most convenient set is typically chosen. There are two Bravais lattices, in addition to the simple cubic (sc) lattice, that are of enormous importance since a great variety of solids crystallise in these forms with a repeating unit like a molecule or atom at each lattice site, and serve to illustrate many of the general features of

Bravais lattices which have just been outlined. These are the body-centred cubic (bcc) and face-centred cubic (fcc) Bravais Lattices:

1. bcc lattices are formed by adding to the sc lattice an additional point at the centre, as shown in Fig. 2.1. The bcc lattice can be easily shown to have more than one set of primitive vectors. If the original sc lattice is generated by primitive vectors $a\hat{x}, a\hat{y}, a\hat{z}$, where $\hat{x}, \hat{y}, \hat{z}$ form an orthonormal basis set and a is the length between points in the lattice, then a symmetric set of primitive vectors for the bcc lattice is -

$$\overrightarrow{a_1} = \frac{a}{2}(\hat{y} + \hat{z} - \hat{x}) \qquad \overrightarrow{a_2} = \frac{a}{2}(\hat{z} + \hat{x} - \hat{y}) \qquad \overrightarrow{a_3} = \frac{a}{2}(\hat{x} + \hat{y} - \hat{z}) \quad (2.2)$$

2. fcc lattices are obtained by adding to the sc lattice an additional point in the centre of each square face, as shown in Fig. 2.1. A symmetric set of primitive vectors for the fcc lattice is -

$$\overrightarrow{a_1} = \frac{a}{2}(\hat{y} + \hat{z}) \qquad \overrightarrow{a_2} = \frac{a}{2}(\hat{z} + \hat{x}) \qquad \overrightarrow{a_3} = \frac{a}{2}(\hat{x} + \hat{y}) \qquad (2.3)$$

The points in a Bravais lattice that are closest to a given lattice point are called its nearest neighbours. Because of the periodic nature of a Bravais Lattice, each point has the same number of nearest neighbours. This number is thus a property of the Bravais lattice, and is referred to as the coordination number of the lattice. The sc lattice has coordination number of 6, bcc lattice of 8, and a fcc lattice of 12.

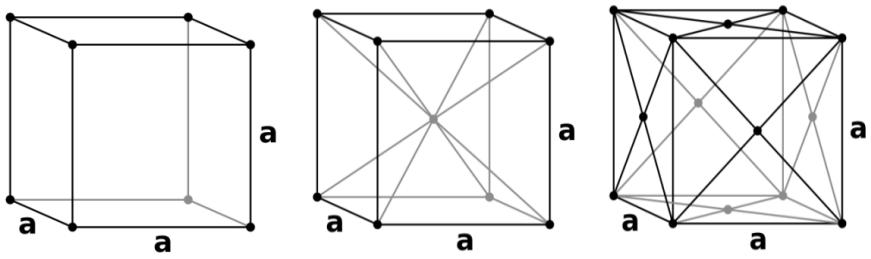


Figure 2.1: From left to right: the sc, bcc and fcc Bravais lattices. The solid lines indicate the bonds between the atoms. The lattice constant a (same on all sides) is also indicated. (Figure reproduced from Ref. [1].)

2.1.2 Unit Cells

The unit cell of a Bravais lattice is defined as a parallelepiped-shaped volume which, when reproduced by close-packing in 3D, gives the whole Bravais lattice. The shape of a parallelepiped is completely defined by the lengths of the three sides a, b and c, known as the crystal axes (or lattice constants) of the unit cell, and the values of the three angles α, β and γ, such that α lies between the b and c axes, β between the a and c axes, and γ between the a and b axes. Most Bravais lattices can have many possibilities for a unit cell, which differ between them in the set of translations necessary to fill the whole space without either overlapping or leaving voids.

There are two main choices for unit cells, the primitive unit cell and the conventional unit cell. The main difference is that primitive unit cells contain only one lattice point, whereas the conventional ones contain more than one lattice point. It can be deduced that the representations of the bcc and fcc lattices in Fig. 2.1 correspond to conventional unit cells containing two and four lattice points respectively, while that of the sc lattice can be thought of

as being either primitive or conventional, since the two are equivalent in this special case. In general, conventional unit cells are more useful since they convey more readily the overall symmetry of the underlying lattice. It follows that the conventional unit cell is normally the most symmetrical among all the possible choices for a unit cell, such that they contain all the symmetry elements of the lattice that they represent. Primitive unit cells on the other hand are always minimum-volume cells, which is a property of the Bravais lattice. Even with this definition however there is still no unique way of choosing a primitive unit cell for a given Bravais lattice. The obvious primitive unit cell to associate with a particular Bravais lattice is the parallelepiped whose sides are delineated by the three primitive translation vectors, used to define the Bravais lattice points, applied to the lattice point occupying one of the eight corners. The Primitive unit cell has often the disadvantage of not displaying the full symmetry of the Bravais lattice. For example the primitive unit cells of the bcc and fcc lattices for the choice of primitive vectors of Eq. (2.2) and Eq. (2.3) respectively are oblique parallelepipeds, and therefore do not have the full cubic symmetry of the lattices in which they are embedded.

2.1.3 Miller index labelling system for crystal planes

The orientation of a crystal plane is determined by three points in the plane, provided that they are not collinear. We can specify the orientation of a plane by the indices determined according to the following rules:

1. We first find the intercepts of the plane with the three crystal axes a, b and c, in the units of the crystal axes themselves. The axes may be those of a

primitive or non-primitive unit cell, as long as a consistent set of axes is used to interpret the indices unambiguously. When the Bravais lattice is cubic for example, the simple cubic crystal axes of the conventional unit cell are invariantly used.

2. We then take the reciprocals of these intercepts and reduce them to the smallest three integers with no common factors. The result, enclosed in parentheses (hkl), are called the *Miller indices* of the plane.

3. For an intercept of infinity, that is if the plane is parallel to a given axis, the corresponding index is zero.

4. If a plane crosses the origin, then it suffices to take any parallel plane not passing through the origin to find its indices.

5. The indices may denote a single plane or a whole family of parallel lattice planes (since parallel planes in general have proportional intercepts).

6. If a plane cuts an axis on the negative side of the origin, the corresponding index is negative, indicated by placing a bar above the index like so: $\left(h\overline{k}l\right)$.

7. The Miller indices depend on the choice of crystal axes and hence are related to a particular unit cell. They are therefore not uniquely defined for a given crystal face. However, no matter which unit cell is chosen, one can always find a set of Miller indices for each face.

There is also a notation for planes that are equivalent by virtue of the symmetry of the crystal, which can be denoted by curly brackets around the indices. For example, the faces of a cubic crystal are (100), (010), (001), $\left(\overline{1}00\right)$, $\left(0\overline{1}0\right)$ and

$(00\bar{1})$. Collectively, these planes are referred to as the $\{100\}$ planes. In general, one uses $\{hkl\}$ to refer to the (hkl) planes and all those that are equivalent to them by virtue of the crystal symmetry.

An index system also exists to label directions in crystals. The indices $[uvw]$ of a direction in a crystal are the set of the smallest integers that have the ratio of the components of a vector in the desired direction. A particular choice of crystal axes $\overrightarrow{a_1}$, $\overrightarrow{a_2}$ and $\overrightarrow{a_3}$ serves as the basis set, such that they lie in the [100], [010] and [001] directions respectively. Thus in general the lattice point $n_1\overrightarrow{a_1} + n_2\overrightarrow{a_2} + n_3\overrightarrow{a_3}$ lies in the direction $[n_1n_2n_3]$ from the origin. In cubic crystals the direction $[hkl]$ is perpendicular to a plane (hkl) having the same indices, but this is not generally true in other crystal systems. The notation used to label directions related by symmetry collectively (as is done for lattice planes) is to enclose the indices in triangular brackets $\langle uvw \rangle$. Hence for example the [100], [010], [001], $[\bar{1}00]$, $[0\bar{1}0]$ and $[00\bar{1}]$ directions in a cubic crystal are referred to, collectively, as the $\langle 100 \rangle$ directions.

2.1.4 Lattice with a basis: crystal structures

A physical crystal is described by its underlying Bravais lattice together with its basis (or repeated structural unit). The basis describes the arrangement and composition of the chemical unit (be it an atom or molecule) associated with each lattice point in the Bravais lattice. A basis of atoms is attached to every lattice point, with every basis identical in composition and orientation. The basis does not have to be centred on the lattice point, as it can also be displaced relative to it. In general, the basis can consist of a single type of atom (the crystalline

elements), groups of atoms, molecules (as in organic crystals), groups of molecules or ions. The atoms or molecules in the basis in particular can be different from one another. The fact that many atoms can be associated with a lattice point means that even a primitive unit cell can contain many atoms. The basis convolved with the underlying Bravais lattice therefore gives the physical *crystal structure* of the crystalline solid, consisting in identical copies of the same basis located at the locations of all the points of a Bravais lattice.

It is possible for one compound to adopt more than one crystal structure under different conditions of crystallisation (such as different rates of crystallisation, different temperatures or pressures, different solvents). This phenomenon is called polymorphism, and is important because different crystal structures can have drastically different physical and chemical properties. In the context of the research presented in this thesis, an important example of crystal structure which will be considered is the cubic diamond crystal structure portrayed in Fig. 2.2. The cubic diamond structure consists of two interpenetrating fcc Bravais lattices , displaced along the body diagonal of the cubic cell by one quarter the length of the diagonal. Hence it corresponds to a single fcc lattice with a two atom basis at atomic positions (000) and $\left(\frac{1}{4}\frac{1}{4}\frac{1}{4}\right)$ relative to the crystal axes of the conventional cubic unit cell. Its coordination number is consequently 4, with the four nearest neighbours of each point forming the vertices of a regular tetrahedron. The diamond structure is not a Bravais lattice, because the environment of any point differs in orientation from the environments of its nearest neighbours. The structure bears its name from the crystal structure of diamond, where the two-atom basis consists of carbon atoms.

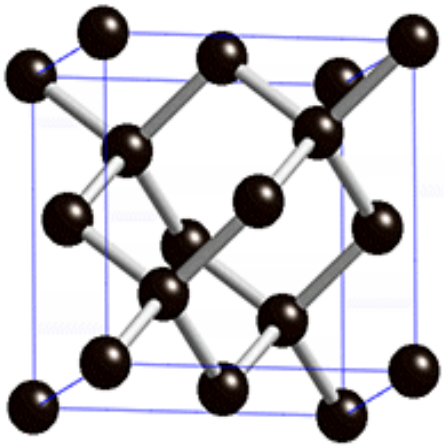


Figure 2.2: Conventional cubic unit cell of the cubic diamond crystal structure, with the nearest-neighbour bonds drawn between the atoms. (Figure reproduced from Ref. [1].)

2.1.5 Point groups and space groups

There are two kinds of symmetry in crystallography: external, which relates to crystal macroscopic shapes, and internal, which relates to the atomic arrangement in the underlying unit cells. Clearly the symmetry of a macroscopic crystal as a whole is inherently connected with the symmetry of the constituent unit cells. All the symmetry elements of the crystal are in fact guaranteed to be always found in its unit cells. From the point of view of symmetry, a Bravais Lattice/Crystal Structure is characterised by all rigid operations that transform the lattice into itself, and under which the lattice is therefore invariant. In this context rigid means operations that preserve the distance between all lattice points. When a rigid operation transforms the lattice into itself, it is known as a symmetry transformation or symmetry element of the Bravais lattice/Crystal structure. The set of all symmetry transformations of a Bravais lattice/Crystal structure is known as the *symmetry group* or *space group* of the Bravais lattice/Crystal

structure [1]. Even though symmetry elements apply to the whole lattice, we can consider just a single unit cell that exhibits the full symmetry of the Bravais lattice and that therefore has the same symmetry elements of the full space group of the Bravais lattice. This is known as a symmetry unit cell, and often consists in a conventional and not primitive unit cell.

In general any symmetry operation of a Bravais lattice can be compounded out of two other symmetry operations: a translation through a Bravais lattice vector $\overrightarrow{R}$ and a rigid operation leaving at least one lattice point fixed (the translation by itself leaves no point fixed). These are known as point operations, and include all symmetry operations that are not translations. The types of point operations are Inversion, Reflection, Rotation and Rotation-Inversion. The subset of all point symmetry operations is known as the *point group* of the Bravais lattice. There turn out to be only seven distinct point groups that a Bravais lattice can have, known as *crystal systems*. When one relaxes the restriction to point operations and considers the full symmetry group of the Bravais lattice (including therefore translational symmetries), there turn out to be 14 distinct symmetry groups that a Bravais lattice can have. Thus from the point of view of symmetry there are 14 different kinds of Bravais lattices. A summary of the names and structural properties of the conventional unit cells (which also correspond to the symmetry unit cells) of these 14 Bravais lattices is presented in Fig. 2.3. Lines connect the lattice points to clarify the relationships between them. In the absence of any symmetry, the three axes of these conventional unit cells have different lengths and the three angles are different from each other and from 90°. In the presence

[1] In general a crystal structure does not necessarily have the same set of symmetry elements as its underlying Bravais lattice.

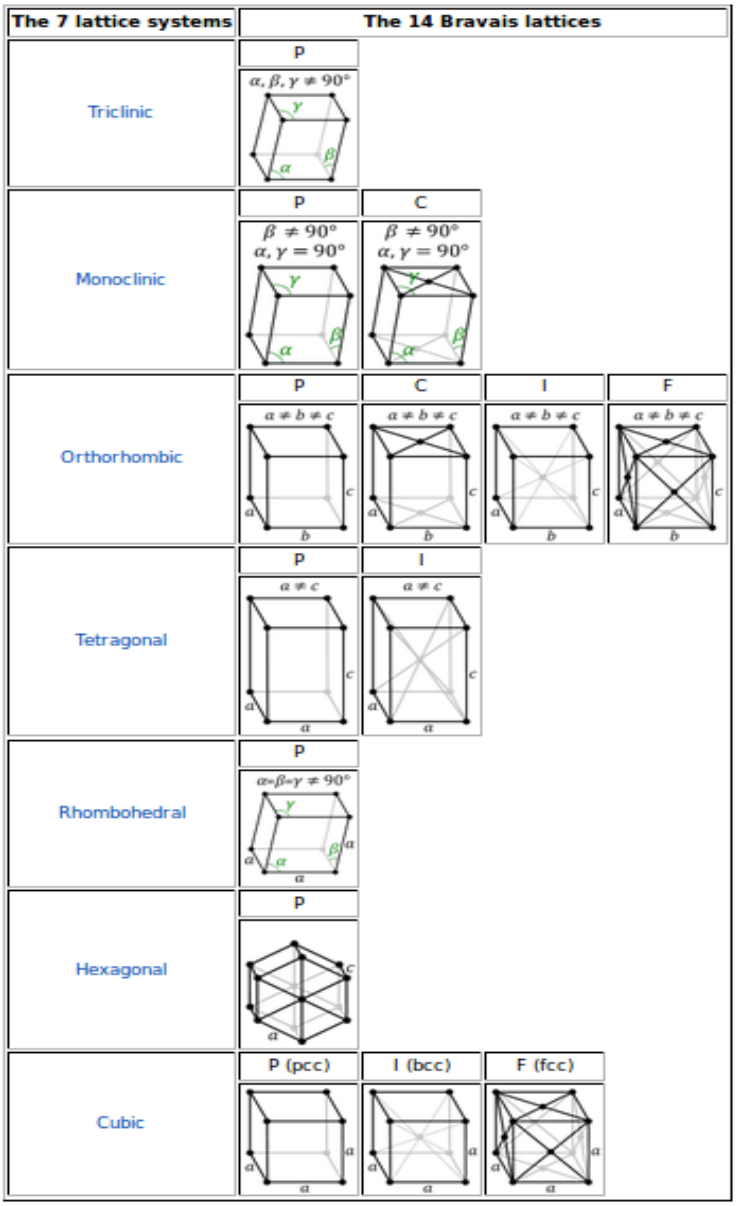


Figure 2.3: The seven crystal systems and 14 Bravais lattices, as defined from the symmetry elements that they possess. The geometry and type of conventional unit cell is indicated for each Bravais lattice. The symmetry of the crystal systems increases moving down the table. (Figure reproduced from Ref. [1].)

of symmetry elements, there are restrictions and special values of the unit cell parameters.

We now perform a similar analysis not on Bravais lattices but on general crystal structures. We take as the basis of the crystal structure an arbitrary object, and try to classify the symmetry groups of the crystal structure so obtained. The symmetry transformations that transform the crystal structure into itself now depend both on the symmetry of the object (internal symmetry of the basis) and the symmetry of the underlying Bravais lattice. Because the objects no longer have the maximum spherical symmetry like the individual lattice points of a Bravais lattice, the number of symmetry transformations and possible symmetry groups is greatly increased. There turn out to be 230 different space groups that a lattice with a basis can have.

2.1.6 The reciprocal lattice

The lattice reciprocal to a Bravais lattice (the reciprocal lattice) plays a fundamental role in the analysis of how periodic structures behave under diffraction by, for example, X-rays. The definition of reciprocal lattice stems from considering a set of Bravais lattice vectors $\overrightarrow{R}$ constituting a Bravais lattice, and a plane wave $e^{i\overrightarrow{k}\cdot\overrightarrow{r}}$. For a general wave vector $\overrightarrow{k}$ such a plane wave will not of course have the periodicity of the Bravais lattice, but for certain special choices it will. The reciprocal lattice of a Bravais lattice embodies the set of all wave vectors $\overrightarrow{K}$ (or $\overrightarrow{G}$) that yield plane waves with the periodicity of a given Bravais lattice. The $\overrightarrow{K}$ vectors are then known as the reciprocal lattice vectors. Analytically, $\overrightarrow{K}$ belongs to the reciprocal lattice of a Bravais lattice of points $\overrightarrow{R}$ provided that the relation

-

$$e^{i\overrightarrow{K}\cdot\left(\overrightarrow{r}+\overrightarrow{R}\right)} = e^{i\overrightarrow{K}\cdot\overrightarrow{r}} \tag{2.4}$$

holds for any $\overrightarrow{r}$, and for all $\overrightarrow{R}$ in the Bravais lattice. Factoring out $e^{i\overrightarrow{K}\cdot\overrightarrow{r}}$, we can characterise the reciprocal lattice as the set of wave vectors $\overrightarrow{K}$ satisfying -

$$e^{i\overrightarrow{K}\cdot\overrightarrow{R}} = 1 \tag{2.5}$$

for all $\overrightarrow{R}$ in the Bravais lattice. It must be emphasised that a reciprocal lattice is always defined with reference to a particular Bravais lattice. The Bravais lattice that determines a given reciprocal lattice is then referred to as the direct lattice, when viewed in relation to its reciprocal. It must also be noted that, given the above definition, the reciprocal lattice lies in the Fourier (reciprocal) space associated with the crystal. $\overrightarrow{r}$ and $\overrightarrow{k}$ therefore constitute a pair of reciprocal (conjugated) coordinates. In particular, if vectors in the direct lattice have the dimensions of [length], vectors in the reciprocal lattice have the dimensions of [1/length].

The reciprocal lattice is itself a Bravais lattice, according to both definitions of Bravais lattice. The proof of this provides us with an explicit algorithm for constructing the reciprocal lattice. Let $\overrightarrow{a_1}$, $\overrightarrow{a_2}$ and $\overrightarrow{a_3}$ be a set of primitive translation vectors for the direct lattice. Then it can be shown that the reciprocal lattice can be generated by the following three reciprocal primitive translation vectors -

$$\begin{aligned}
\overrightarrow{b_1} &= 2\pi\frac{\overrightarrow{a_2}\times\overrightarrow{a_3}}{\overrightarrow{a_1}\cdot(\overrightarrow{a_2}\times\overrightarrow{a_3})} \\
\overrightarrow{b_2} &= 2\pi\frac{\overrightarrow{a_3}\times\overrightarrow{a_1}}{\overrightarrow{a_1}\cdot(\overrightarrow{a_2}\times\overrightarrow{a_3})} \\
\overrightarrow{b_3} &= 2\pi\frac{\overrightarrow{a_1}\times\overrightarrow{a_2}}{\overrightarrow{a_1}\cdot(\overrightarrow{a_2}\times\overrightarrow{a_3})}
\end{aligned} \tag{2.6}$$

To verify that the above set of equations gives a set of primitive vectors for the

reciprocal lattice, one first notes that the $\overrightarrow{b_i}$ vectors satisfy -

$$\overrightarrow{b_i} \cdot \overrightarrow{a_j} = 2\pi\delta_{ij} \tag{2.7}$$

where $\delta_{ij} = 0$ if $i \neq j$, or $\delta_{ij} = 1$ if $i = j$. Since the set of $\overrightarrow{b_i}$ vectors form a complete basis set in reciprocal space, any vector $\overrightarrow{k}$ in reciprocal space can be written as a linear combination -

$$\overrightarrow{k} = k_1\overrightarrow{b_1} + k_2\overrightarrow{b_2} + k_3\overrightarrow{b_3} \tag{2.8}$$

If $\overrightarrow{R}$ is a Bravais lattice vector, then -

$$\overrightarrow{R} = n_1\overrightarrow{a_1} + n_2\overrightarrow{a_2} + n_3\overrightarrow{a_3} \tag{2.9}$$

where the n_i coefficients are integers. Hence the dot product of $\overrightarrow{k}$ with $\overrightarrow{R}$ is given by -

$$\overrightarrow{k} \cdot \overrightarrow{R} = 2\pi\left(k_1n_1 + k_2n_2 + k_3n_3\right) \tag{2.10}$$

where we have made use of the results of Eq. (2.7). For $e^{i\overrightarrow{k}\cdot\overrightarrow{R}}$ to be unity for all $\overrightarrow{R}$ as required for a reciprocal lattice, $\overrightarrow{k} \cdot \overrightarrow{R}$ must be 2π times an integer for any choices of the integers n_i. This requires the coefficients k_i to be integers. Thus the condition that $\overrightarrow{K}$ be a reciprocal lattice vector is satisfied by just those vectors for which -

$$\overrightarrow{K} = k_1\overrightarrow{b_1} + k_2\overrightarrow{b_2} + k_3\overrightarrow{b_3} \tag{2.11}$$

where the k_i coefficients are integers. This demonstrates that the reciprocal lattice is a Bravais lattice and that the $\overrightarrow{b_i}$ vectors can be taken as the reciprocal primitive

translation vectors. Since the reciprocal lattice is itself a Bravais lattice, one can in theory construct its reciprocal, but this turns out to be nothing but the original direct lattice. A further important property of reciprocal lattices is that, if v is the volume of a primitive unit cell in the direct lattice, then the primitive cell of the reciprocal lattice has a volume of $(2\pi)^3/v$. Some important examples of reciprocal lattices are:

1. Simple Cubic Bravais lattice, with cubic unit cell of side a, has as its reciprocal a simple cubic lattice with cubic unit cell of side $2\pi/a$.

2. The fcc Bravais lattice with a cubic conventional unit cell of side a has as its reciprocal a bcc lattice with cubic conventional unit cell of side $4\pi/a$.

3. The bcc lattice with cubic conventional unit cell of side a has as its reciprocal lattice a fcc lattice with cubic conventional unit cell of side $4\pi/a$.

2.2 The physics of shock-waves in one-dimensional planar geometries

Only the surface of the vast and active area of research that is the study of shock-induced compression of solid materials will be scratched within the scope of this short introduction. For a more comprehensive overview, the reader is referred to the numerous introductory review textbooks on the subject [165, 246]. In addition, Springer offers a comprehensive collection of textbooks on shock-compression of condensed matter as part of its "Shock Wave and High Pressure Phenomena" series [39, 59, 77, 128, 248]. Further comprehensive coverage of

the field is given in the "Handbook of shock-waves" series of three volumes [15]. Finally, a more concise introduction to the subject is offered in the review paper by Davison and Graham [40].

2.2.1 Rankine-Hugoniot jump conditions

Planar shock waves in solid crystalline materials are defined as propagating disturbances giving rise to a discontinuity in the material's pressure, temperature (or internal energy) and density, thus resulting in an intense uniaxial dynamic compression of the internal crystal structure of the material along the shock propagation direction. A "shock-wave" is then the term which is used to denote the interface of this discontinuity. The circumstances that surround the propagation of shock waves in condensed matter are made unique by the extreme physical conditions that can be attained, together with their exceptionally high rates of variation. These are typically characterised by pressures ranging from $\sim$ 100 MPa up to several hundreds of GPa (and up to ten TPa in some unique experiments), and temperatures up to tens of thousands of degrees Kelvin, coupled with durations of the load application varying from 10^{-9} to 10^{-5} s.

The concept of shock-wave propagation can be very easily understood and derived by means of a simplified conceptual framework involving a cylinder of unit cross-sectional area onto which a piston penetrates. This is shown in Fig. 2.4. Initially the piston is at rest. It then is pushed into the compressible material, initially at a pressure P_0 and having density ρ_0, at a velocity U_p. After a time t_1, the highly compressed region ahead of the piston has moved forward by a distance equal to $U_S t_1$, where U_S is the velocity of propagation of the disturbance ahead

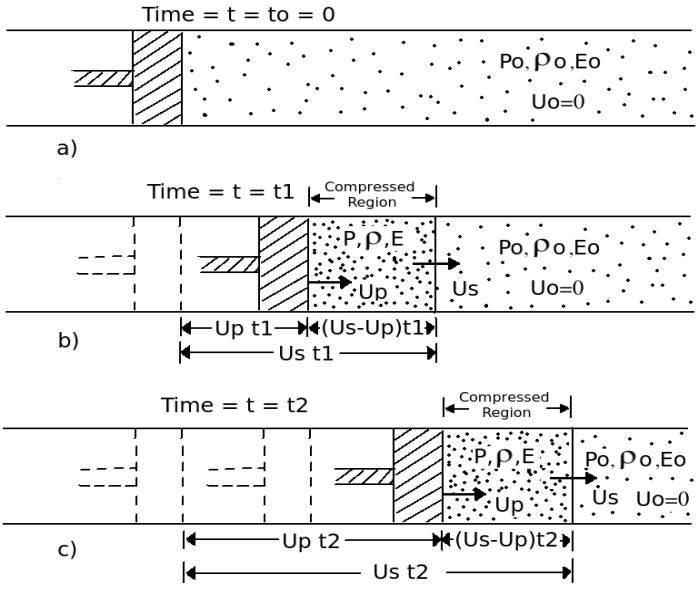


Figure 2.4: Successive positions of an idealised piston moving into a cylinder with a compressible fluid inside.

of the piston. The compressed region has a pressure P and a density ρ, and the particles within it move at a velocity U_p equal to that of the piston. A shock front can be visualised as a plane discontinuity separating moving from stationary fluid in a cylinder with a moving piston. The velocity U_S of the shock-wave is greater than the piston velocity U_p.

The mathematical theory of shock-waves was originally developed by Rankine and Hugoniot for fluids [102, 199]. The development of the Rankine-Hugoniot equations relies on several assumptions, most notably that the shear modulus of the material is zero, such that it responds to the wave as a fluid, that body forces (such as gravitational forces) and heat conduction at the shock front are negligible, and finally that there is no elastoplastic behaviour or phase transitions. The Rankine-Hugoniot equations can be easily developed by considering regions immediately ahead of and behind the shock front. Ahead of the front, the pressure

is P_0, the density is ρ_0, and the temperature is T_0; behind it they are P, ρ and T respectively. The velocity of the front is U_S. At the front and behind it, they are moving at a velocity U_p. This displacement of particles is responsible for the pressure build-up. If one considers the centre of reference as the shock front and moves with it at a velocity U_S into a region of particle velocity $U_p = U_0$ and density ρ_0, then the apparent velocity of the fluid moving towards the centre of reference is $U_S - U_0$. At the same time, the material leaving the front or receding from the centre of reference is moving at a velocity $U_S - U_p$. With this in mind, we will set up the Rankine-Hugoniot equations embodying the principles of conservation of mass, momentum and energy.

The equation of conservation of mass stems from the fact that the mass moving toward the front in time dt, given by $A\rho_0 (U_S - U_0)\, dt$ must be equal to the mass moving away from the front, given by $A\rho (U_S - U_p)\, dt$. Hence, if $U_0 = 0$, we have -

$$\rho_0 U_S = \rho (U_S - U_p) \tag{2.12}$$

This is the equation for the conservation of mass.

The conservation of momentum requires that the difference in momentum, given by the product of mass and velocity, be equal to the impulse Fdt acting in time dt per unit cross sectional area. The difference in momentum across the shock front is therefore given by -

$$\underbrace{\rho A (U_S - U_p)\, dt}_{mass}\ \underbrace{U_p}_{velocity} - \underbrace{\rho_0 A (U_S - U_0)\, dt}_{mass}\ \underbrace{U_0}_{velocity} \tag{2.13}$$

The impulse on the other hand is given by -

$$Fdt = (PA - P_0A)\,dt \tag{2.14}$$

Then, equating change in momentum with impulse, we obtain -

$$\rho_0\,(U_S - U_0)\,(U_p - U_0) = P - P_0 \tag{2.15}$$

If $U_0 = 0$ -

$$(P - P_0) = \rho_0 U_S U_p \tag{2.16}$$

This is the equation for the conservation of momentum, and the quantity $\rho_0 U_S$ is often called the shock impedance.

The conservation of energy is obtained by setting up an equation in which the work done by P minus the work done by P_0 is equal to the difference in the total energy (kinetic plus internal) between the two sides of the front. The difference of work done by P and P_0 is given by -

$$\Delta W = \underbrace{(PA)}_{force}\underbrace{(U_p dt)}_{distance} - \underbrace{(P_0A)}_{force}\underbrace{(U_0 dt)}_{distance} \tag{2.17}$$

The difference in total energy (kinetic plus internal) per unit mass is equal to the final minus the initial energy -

$$\begin{aligned}\Delta E = {} & \tfrac{1}{2}\left[\rho A\,(U_S - U_p)\,dt\right]U_p^2 + EA\rho\,(U_S - U_p)\,dt \\ & - \left\{\tfrac{1}{2}\left[\rho_0 A\,(U_S - U_0)\,dt\right]U_0^2 + E_0 A\rho_0\,(U_S - U_0)\,dt\right\}\end{aligned} \tag{2.18}$$

So, equating ΔW to ΔE and taking $U_0 = 0$ yields -

$$PU_p = \frac{1}{2}\rho\left(U_S - U_p\right)U_p^2 - E_0\rho_0 U_S + E\rho\left(U_S - U_p\right) \tag{2.19}$$

If $1/\rho = V$ then, using conservation of mass and momentum derived previously, it can be shown that one obtains -

$$E - E_0 = \frac{1}{2}\left(P + P_0\right)\left(V_0 - V\right) \tag{2.20}$$

Eq. (2.20) is the more common form of the conservation of energy. Equations (2.12), (2.16), (2.20) are, in essence, the Rankine-Hugoniot conservation equations for a material in which a pressure discontinuity propagates. These equations apply to a piston moving into a compressible medium (gas) and can be extended to a shock-wave propagating into gas, liquid, or solid or to a detonation wave.

In the three conservation equations of mass, momentum and energy, equations (2.12), (2.16), (2.20), there are five variables: pressure P, particle velocity U_p, shock velocity U_S, specific volume V or density ρ, and energy E. Hence, an additional equation is needed if one wants to determine all parameters as a function of one of them. This fourth equation, which can be conveniently expressed as the relationship between shock and particle velocities, has to be experimentally determined. A polynomial equation with parameters C_0, S_1, S_2, S_3..... empirically describes the relationship between U_S and U_p -

$$U_S = C_0 + S_1 U_p + S_2 U_p^2 + ... \tag{2.21}$$

Eq. (2.21) is often known as the equation of state (EoS) of a material. Here,

S_1 and S_2 are empirical parameters and C_0 is the sound velocity in the material at zero pressure. For most metals, S_2 is very close to zero, and Eq. (2.21) thus reduces to a linear relationship -

$$U_S = C_0 + S_1 U_p \tag{2.22}$$

This linear relationship between U_S and U_p describes fairly well the shock response of materials not undergoing phase transitions and with no porosity.

2.2.2 Conditions for shock-wave formation

Shock-waves are characterised by a steep front in the form of a discontinuous surface with no apparent thickness and require in a first instance a state of uni-axial strain along the shock-propagation direction (no lateral flow of materials) which allows the build-up of the shear component of stress to high levels. The requirement for the formation of shock-waves can be understood by considering the case of an ideal gas being compressed isentropically by a high-pressure disturbance travelling through it. The corresponding equation of state for the process is given by -

$$PV^{\gamma} = K = \text{constant} \tag{2.23}$$

By differentiating the above we obtain -

$$\gamma P V^{\gamma-1} dV + V^{\gamma} dP = 0 \rightarrow \frac{dP}{dV} = -\gamma \frac{P}{V} \tag{2.24}$$

Furthermore, it can be shown that the velocity of the disturbance in the gas, assuming a one-dimensional configuration, is given by -

$$u = \left(\frac{d\sigma/d\varepsilon}{\rho}\right)^{1/2} = \left(\frac{dP/dV}{\rho}\right)^{1/2} = |K|^{1/2} \tag{2.25}$$

where K is the bulk modulus of the gas. Hence the velocity of the disturbance is proportional to $(dP/dV)^{1/2}$. Since the value of P/V increases with pressure, it can be concluded from Eq. (2.24) that high-pressure amplitude isentropic disturbances travel faster than low-amplitude ones in gases. Hence a disturbance front will "steepen up" as it travels through the material because the higher amplitude regions of the front travel faster than the low amplitude regions. This is the fundamental requirement for the establishment of a shock-wave, that the velocity of the pulse, U, increases with pressure, that is -

$$\left(\frac{\partial^2 P}{\partial U^2}\right) > 0 \tag{2.26}$$

as P and U increase. Fig. 2.5 demonstrates the steepening of a ramp as it travels into a sample. The higher pressure components advance faster and catch up to the low pressure leading edge to form an increasingly steep front with time, which eventually results in the formation of a shock-wave. The opposite case on the other hand, where the velocity of the disturbances is inversely proportional to the pressure amplitude, leads to the dispersion of the wave, which makes it impossible for the shock-wave to be steady.

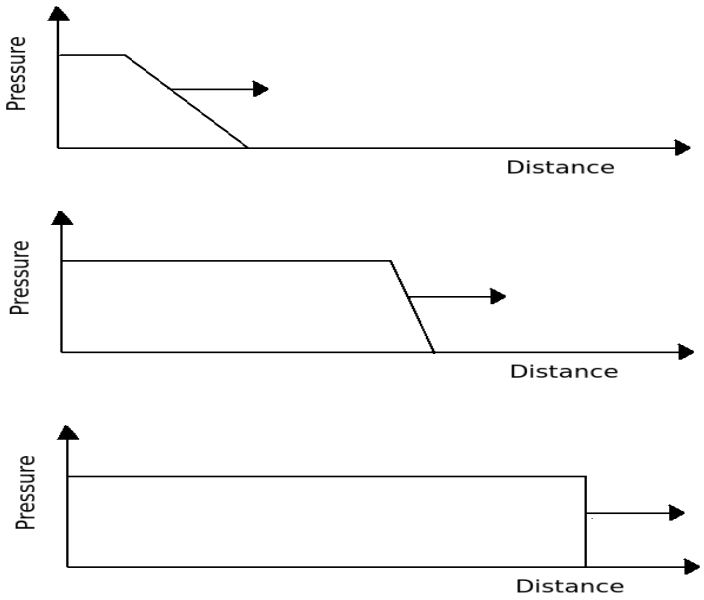


Figure 2.5: A schematic of the steepening of a ramped compression launched into a material sample.

2.2.3 The Hugoniot curve

Eq. (2.20), derived from the conservation of energy, establishes a relation between P and ρ immediately behind the shock-front. This pressure-density relationship is usually known as the Rankine-Hugoniot equation, or simply the "Hugoniot", and in graphic form is shown in Fig. 2.6 as a $P - V$ curve. The Hugoniot is therefore defined as the locus of all shocked states in a material and essentially describes the material properties. The straight line joining (P_0, V_0) and (P_1, V_1) is known as the Rayleigh line and refers to the shock state at P_1.

It is very important to realise that when pressure is increased in a shock front, it does not follow the Hugoniot curve. Rather, it changes discontinuously from its initial value P_0 to its value P_1 as defined by the Rankine Hugoniot relationships. This discontinuity is explained by the slope of the Rayleigh line

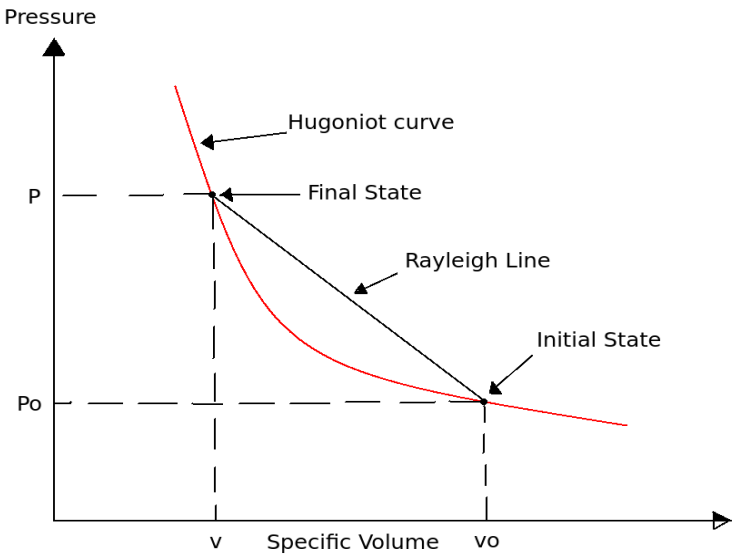


Figure 2.6: Hugoniot $(P - V)$ curve denoting all the shocked states that can be attained in a material. The Rayleigh line connecting the initial to the final states is also shown.

that is proportional to the square of the velocity U_S of the shock-wave -

$$\frac{P - P_0}{V - V_0} = -\rho_0^2 U_S^2 \tag{2.27}$$

One sees clearly that the higher the pressure, the higher the magnitude of the slope and the higher the velocity of the wave.

2.2.4 Real shock-wave profiles and the Hugoniot Elastic Limit

While an ideal shock-wave profile would predict a discontinuity at the front, a plateau at the top, and a gradual return to zero pressure, real shock-waves exhibit a number of peculiarities that are material and pressure dependent. The profiles

of idealised and realistic shock-waves are shown in Fig. 2.7. The most important difference is that the pressure-volume curve for a real material is not the same as the ideal Hugoniot curve because of the deviatoric component of stress present in the former. The difference between the two curves is shown in Fig. 2.8. Firstly, the rate of rise of stress with volume of the real material's curve is much higher in the elastic range. Secondly, when the elastic limit under the imposed stress and strain-rate conditions is reached above some limit of the value of the deviatoric stress, a dynamic yield point known as the Hugoniot Elastic Limit (HEL), the pressure-volume curve of the real material exhibits a change in slope and curves downward. The value of stress at the HEL is a material-specific parameter that specifies the elastic-to-plastic transition. The steady-state HEL of metals is fairly low, and these effects are relatively unimportant. However, in ceramics this is not the case. For example, the HEL of sapphire is close to 20 GPa, whereas that of alumina is around 6-8 GPa. The position of the HEL separating the elastic portion of the wave from the plastic portion is shown in the realistic time profile of Fig. 2.7. This elastic portion, below the HEL, travels at a velocity higher than the plastic wave in the weak-shock regime. The propagation velocity of the elastic wave is equal to the longitudinal sound velocity.

At this point we are in a position to explain all the phenomena observed in Fig. 2.7(b). The leading wave is an elastic shock limited in amplitude by the shear strength of the material. In an ideal elastic-plastic solid, after the initial steep rise in pressure (or particle velocity), this elastic wave attains the HEL of the material. Permanent plastic deformation occurs through a splitting of the leading elastic precursor wave into two waves, an elastic wave and a slower plastic wave. At higher pressures, the plastic wave velocity exceeds the elastic wave velocity, and

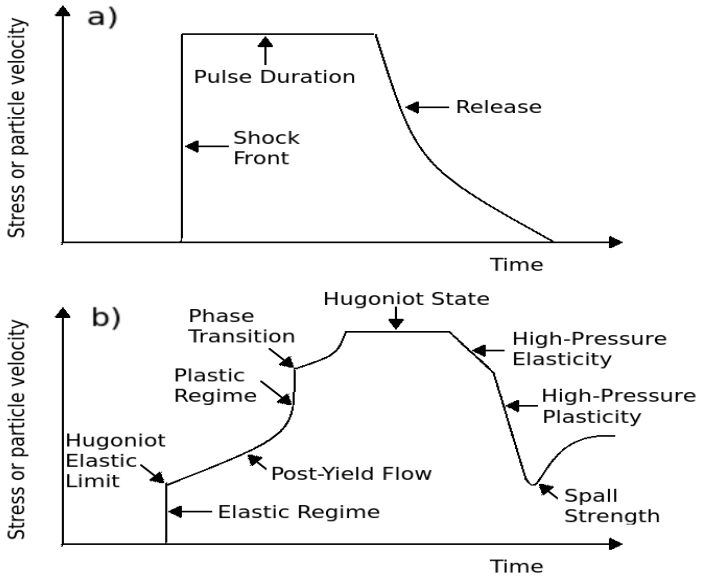


Figure 2.7: Idealised (a) and "generic" realistic (b) shock-wave stress or particle velocity profiles. In the latter case, the positions of the features in the profile characteristic of the onset of various types of material behaviour are labelled. This variety of material behaviour is explained in the text of this subsection.

we reach the so-called strong-shock regime, comprising a single plastic wave. The latter wave is what gives rise to the plastic behaviour. The ensuing rate of rise of the pressure is dictated by the constitutive behaviour of the material. In general, the rise becomes steeper as the shock-induced pressure increases. If there is a phase transition following the regime of plastic deformation, it is accompanied by a clear signal in the wave profile, which normally consists in the further splitting into two of the wave. The phase transition occurs via the arrival of the phase transition wave resulting from this splitting, and goes to completion if the driving pressure is large enough. For weak shocks, this phase transition wave travels even more slowly than the plastic wave, which in turn travels more slowly than the elastic precursor. At the top of the plot of Fig. 2.7(b) we have the pulse duration

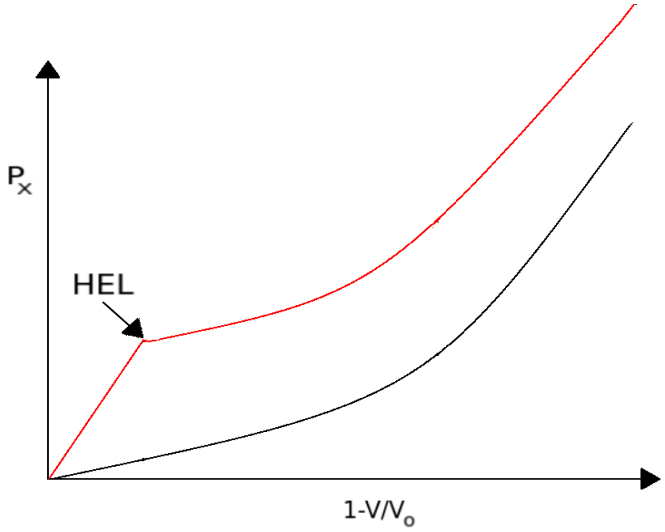


Figure 2.8: Representation of the pressure-volume curves for a real material (red) compared to that of an idealised material (black). The position of the HEL in the former is labelled.

plateau labelled as the Hugoniot state, since this represents the endstate which is attained on the characteristic pressure-volume curve of the material. When unloading starts following this plateau, it occurs initially elastically and then plastically. This elastoplastic transition in unloading leaves a signal analogous to the signal left by the HEL on loading. This signal is normally referred to as the release or rarefaction wave, and returns the material to something approaching its original state. At the end of the unloading process, the wave reflects from the back surface of the sample and this phenomenon, known as spalling, can result in the fracturing of the material.

Finally, we analyse the response of the shock-loaded sample at the microstructural level of the underlying crystal lattice. It is widely accepted that the material morphology and timescales of atomistic phenomena have a profound impact on

bulk properties, such as plasticity, phase transformations, and damage. Fig 2.9 shows the various stages of development of the shock-induced deformation of the crystal structure put in direct correlation with the various features of the real-material wave profile of Fig. 2.7. In the case of a planar shock considered here, the initial response of the crystalline lattice to shock-loading is a uniaxial, one-dimensional compression of the crystal along the direction of shock propagation. This uniaxial response can remain elastic, that is once the disturbance is removed, the lattice will relax back to its original configuration. Furthermore, this uniaxial compression leads to the accumulation of strong levels of shear stress in the lattice. Under high-stress conditions and given sufficient time, the lattice will undergo an irreversible (permanent) deformation. Various morphologies of permanent deformation can occur, consisting in either plasticity, melting, resolidification, or solid-solid structural transformations. These atomistic changes can have dramatic and important consequences to most macroscopically observable behaviour such as the materials thermodynamic state (pressure, temperature, density), strength, and failure. If the shock-wave propagating through the lattice exceeds the HEL of the material, the shear stress accumulated during the elastic phase of the compression leads to nucleation and propagation of dislocations, allowing the lattice to plastically relax to a quasi-hydrostatic, three-dimensional state of compression on some characteristic timescale. A fully 3D relaxed state is ideally defined as having zero shear stress and hydrostatic compression. The rate of relaxation to hydrostatic conditions is controlled by the nucleation rates and mobility of dislocations, which in turn depend upon microstructural parameters such as grain boundaries, barriers, etc. Under shock compression, solids can also exhibit a rich variety of solid-to-solid polymorphic phase transformations,

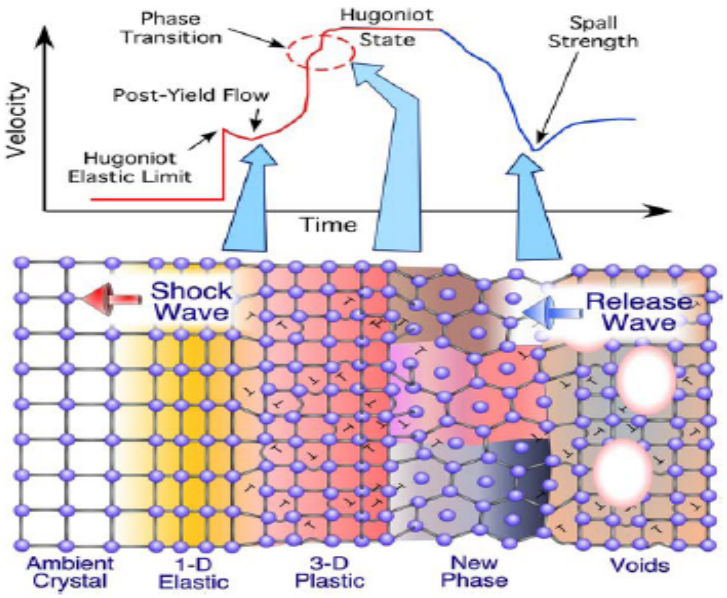


Figure 2.9: A schematic diagram of a shocked crystalline solid, linking microstructural processes to the bulk behaviour measured by inspection of the pressure or particle velocity wave profile. The rearrangement of the atoms as the lattice relaxes plastically or undergoes a phase-transition alters the response of the material, causing the corresponding change in the wave profile. (Figure reproduced with permission from Ref. [150].)

some of which are metastable and, due to the uniaxial and ultrafast nature of the compression, may differ from those encountered under longer timescale and more hydrostatic conditions such as during static DAC-based experiments. During these transformations, the lattice structure changes to a more stable configuration for the pressure and temperature realised by the strong shock-compression. Phase transitions can provide an alternative microscopic mechanism for the relief of shear stress from plastic deformation. Solid-to-melt transformations can also occur under sufficiently strong shocks.

2.3 Classical Molecular Dynamics

2.3.1 Elements of Molecular Dynamics simulations

A general definition of classical Molecular Dynamics (MD) simulations [200, 220, 245] is a computation technique by which the atomic trajectories of a system of N particles are generated by numerical integration of Newton's equation of motion (within a given statistical ensemble). This integration is performed in conjunction with the operation of a specific interatomic potential to calculate the forces on each atom, and with certain initial conditions (IC) and boundary conditions (BC). MD simulations can be structured into four main steps, very much like experiments: system setup, equilibration, simulation run and output. In the equilibration step, we fine-tune the system until it reaches the desired conditions, such as for example temperature T and pressure P, and then in the simulation step we perform property averages, for example calculating the radial distribution function $g(r)$ or thermal conductivity.

There are five key ingredients to a MD simulation, which are boundary conditions, initial conditions, force calculation, integrator/ensemble, and property calculation. A brief overview of each one of these elements will now be given.

There are two major types of boundary conditions: isolated boundary condition (IBC) and periodic boundary condition (PBC). IBC is best suited for studying clusters and molecules, while PBC is suited for studying bulk liquids and solids. There can also be mixed boundary conditions such as slab or wire configurations for which the system is assumed to be periodic in some directions but not in the others. In IBC, the N-particle system is surrounded by vacuum. These particles are still able to interact among themselves, but they are so far

away from everything else in the universe that no interactions with the outside occur expect perhaps responding to some well-defined external forcing. In PBC on the other hand, the motion of the N particles in the supercell are followed, but the supercell is surrounded by infinitely replicated, periodic images of itself. Therefore a particle may interact not only with particles in the same supercell, but also with particles in adjacent image supercells. IBC can in fact often be well reproduced by a large enough PBC supercell such that the images do not interact among themselves.

Since Newton's equations of motion are second-order ordinary differential equations (ODE), specifying the initial conditions basically means specifying $\mathbf{x}^{3N}(t=0)$ and $\dot{\mathbf{x}}^{3N}(t=0)$, the initial particle positions and velocities. $\mathbf{x}^{3N}(t=0)$ can for example be a perfect fcc crystal, or an interface between two crystalline phases.

Two approximations are employed in the classical equation of motion to describe the motion of the atoms -

$$m_i \frac{d^2\mathbf{x_i}(t)}{dt^2} = \mathbf{f_i}, i = 1, ..., N \tag{2.28}$$

The first is the Born-Oppenheimer approximation, which assumes that the electronic state couples adiabatically to nuclei motion. The second is that the nucleus motion is far removed from the Heisenberg uncertainty lower bound: $\Delta E \Delta t \gg \hbar/2$. If we insert $\Delta E = k_B T/2$, the kinetic energy, and $\Delta t = 1/\omega$, where ω is a characteristic vibrational frequency, we obtain $k_B T/\hbar\omega \gg 1$. In solids, this means that the temperature should be significantly greater than the Debye temperature. The evaluation of the right-hand side of Eq. (2.28) is usu-

ally the most computationally-expensive step in a MD simulation, so its efficiency is of crucial importance. There exist special algorithms to break up long range Coulomb interactions into two contributions, a short-range interaction and a smooth field-like interaction, both of which can be computed efficiently in separate ways.

Eq. (2.28) is a set of second-order ordinary differential equations, which can be strongly non-linear. By converting them to first-order ordinary differential equations in the $6N$-dimensional space of $\{\mathbf{x}_N, \dot{\mathbf{x}}_N\}$, general numerical algorithms for solving ordinary differential equations such as the Runge-Kutta method can be applied. However, these general methods are rarely used in MD, because the existence of a Hamiltonian allows for more accurate integration algorithms, including the family of predictor-corrector integrators and the family of symplectic integrators. Integrators will be discussed in more detail in the next section. Ensembles such as the micro-canonical, canonical and grand-canonical are concepts in statistical physics that refer to the distribution of initial conditions. However, ensemble and integrator are often grouped together because it is possible to generate the desired ensemble distribution via time integration.

One of the great powers of classical MD is that it provides a nearly complete amount of information at the atomistic level. All properties that are well defined in classical mechanics and statistical mechanics can in principle be computed from the positions and velocities of constituent atoms [85, 205]. The only limiting factors are the accuracy of the calculations, which is limited by the choice of the interatomic potential, and the computational efficiency. The material properties that can be calculated by MD can be roughly grouped into four categories. Firstly, we have structural characterisation, which includes for example the cal-

culation of radial distribution functions and dynamic structure factors. Secondly, we have equation of state calculations, which includes the calculation of free energy functions, phase diagrams, and static response functions like the thermal expansion coefficient. A third type of calculations are those which pertain to the transport properties of the material, which includes for example viscosity, thermal conductivity, correlation functions and diffusivity. Finally, MD is capable of calculating the non-equilibrium response of the sample, which includes such phenomena as plastic deformation and pattern formation.

2.3.2 Integrators

An integrator is defined as the algorithm which advances the trajectory of the atoms in the MD simulation over small time increments Δt -

$$\mathbf{x}^{3N}(t_0) \rightarrow \mathbf{x}^{3N}(t_0 + \Delta t) \rightarrow \mathbf{x}^{3N}(t_0 + 2\Delta t) \rightarrow ... \rightarrow \mathbf{x}^{3N}(t_0 + L\Delta t) \tag{2.29}$$

where L usually ranges from 10^4 to 10^7. For illustrative purposes, we will now give a brief overview of the most basic type of integrator known as the Verlet integrator [232]. A complete list of the various types of integrators can be found in Ref. [245].

In the Verlet algorithm, assuming the $\mathbf{x}^{3N}(t)$ trajectory is smooth, we perform the Taylor expansion -

$$\mathbf{x}_i(t_0 + \Delta t) + \mathbf{x}_i(t_0 - \Delta t) = 2\mathbf{x}_i(t_0) + \ddot{\mathbf{x}}_i(t_0)(\Delta t)^2 + \mathcal{O}\left((\Delta t)^4\right) \tag{2.30}$$

Since $\ddot{\mathbf{x}}_i(t_0) = \mathbf{f}_i(t_0)/m_i$ can be evaluated given the atomic positions $\mathbf{x}^{3N}(t_0)$ at

$t = t_0$, $\mathbf{x}^{3N}(t_0 + \Delta t)$ in turn may be approximated by -

$$\mathbf{x}_i\left(t_0 + \Delta t\right) = -\mathbf{x}_i\left(t_0 - \Delta t\right) + 2\mathbf{x}_i\left(t_0\right) + \left(\frac{\mathbf{f}_i\left(t_0\right)}{m_i}\right)\left(\Delta t\right)^2 + \mathcal{O}\left(\left(\Delta t\right)^4\right) \tag{2.31}$$

By discarding the $\mathcal{O}\left(\left(\Delta t\right)^4\right)$ term, we obtain a recursion formula to compute $x^{3N}\left(t_0 + \Delta t\right), x^{3N}\left(t_0 + 2\Delta t\right), ...$ successively, which is the Verlet algorithm. The velocities do not appear in the recursion but are needed for property calculations. They are given approximately by -

$$\mathbf{v}_i\left(t_0\right) \equiv \dot{\mathbf{x}}_i\left(t_0\right) = \frac{1}{2\Delta t}\left[\mathbf{x}_i\left(t_0 + \Delta t\right) - \mathbf{x}_i\left(t_0 - \Delta t\right)\right] + \mathcal{O}\left(\left(\Delta t\right)^2\right) \tag{2.32}$$

We now investigate to what degree the above recursion reproduces the real trajectory $\mathbf{x}^{3N}(t)$. If the $\mathbf{x}_i(t_0)$ and $\mathbf{x}_i(t_0 - \Delta t)$ terms in Eq. (2.31) are exact, and assuming the computer employed is perfect and has no machine errors in storing the numbers or carrying out floating-point operations, the computed $\mathbf{x}_i(t_0 + \Delta t)$ would still be different from the real $\mathbf{x}_i(t_0 + \Delta t)$ by $\mathcal{O}\left(\left(\Delta t\right)^4\right)$, which is defined as the local truncation error (LTE). LTE is an intrinsic error of the Verlet algorithm. In addition to LTE, there is a round-off error due to the computer's finite precision.

2.3.3 The Tersoff Potential

The semi-empirical interatomic potentials employed in MD simulations permit the calculation of structural properties and energetics of complex systems. In particular interatomic potentials give the total energy E of a set of particles as an explicit mathematical function of the set $\{\mathbf{r}\}$ of particle coordinates. If this

function is sufficiently easy to calculate, and if it gives a sufficiently accurate description of the real physical system of interest, then one can perform realistic calculations of the properties of relatively large systems. Of course the accuracy delivered by such potential-based calculations will always inevitably be worse than that characteristic of truly quantum-mechanical ab-initio methods such as Density Functional Theory or Quantum Molecular Dynamics. Most MD potentials are created by fitting the adjustable parameters to ambient bulk properties of the material under investigation. Common material properties used for fitting empirical potentials include lattice parameter, bulk modulus and elastic tensor components.

Pair potentials, like the notable Lennard-Jones potential and the exponential Morse potential, have long been used to describe rare-gas atoms, simple metals, and highly ionic systems. These potentials describe the interaction of atoms as a function of their separation, including only two-body interactions. Such potentials can be directly applied to a completely arbitrary configuration of atoms but do not accurately describe any but the simplest closed-shell systems. In particular, pair-potentials are completely inapplicable to strongly covalent systems such as semiconductors, which assume more open structures. This pair potential approach corresponds to the leading term in a mathematical expansion of the energy, viewed as a function of the atomic positions. The energy of N interacting particles may be written as -

$$E = \sum_i V_i(\mathbf{r}_i) + \sum_{i<j} V_2(\mathbf{r}_i, \mathbf{r}_j) + \sum_{i<j<k} V_3(\mathbf{r}_i, \mathbf{r}_j, \mathbf{r}_k) + ... \tag{2.33}$$

where $\mathbf{r}_n$ is the position of the n-th particle and the function V_m is called an m-

body potential. The first (one-body) term corresponds to an external potential. The first term which describes the interactions between the particles is the second (two-body) term, which when taken alone constitutes a pair potential. Thus, in this expansion, the pair potential is the simplest possible model for the interaction of a set of particles.

The more recent Tersoff scheme [223, 224, 225, 226] offers a new approach for constructing potentials affording for a improved description of covalent materials such as semiconductors like silicon and other interesting materials such as ceramics, polymers and refractory metals. For describing covalent systems, a natural first step was to include the next term in the expansion of Eq. (2.33), and therefore obtain a three-body potential. This additional term could stabilise more open structures. However, it was found that a three-body potential was inadequate for accurately describing the cohesive energy of silicon over a wide range of bonding geometry and coordination. However, at the same time, a general form for a four- or a five-body potential would probably prove intractable, and would contain far too many free parameters. As an alternative, the Tersoff approach [223, 224, 225, 226] was introduced going beyond the three-body potential. In attempting to construct an accurate and tractable potential, it abandons the use of a general N-body form and attempts to identify the relevant physics and to build it directly into the form of the potential. The central idea behind Tersoff is that, in real systems, the bond order (that is, the strength of each bond) depends upon the local environment. In particular, an atom with many neighbours forms weaker bonds than an atom with few neighbours. For covalent materials, this dependence is sufficient to stabilise structures with low atomic coordination number. Including this dependence explicitly in the Tersoff scheme appears to

solve some of the most serious problems of describing covalent systems without introducing any major increase in computational complexity. Tersoff appears to be particularly suited for modelling silicon, which represents a particular challenge because it has many polymorphs with qualitatively different bonding which, nevertheless, have similar cohesive energies. For this reason, Tersoff is by far the most widely employed potential for modelling silicon.

Because of the crucial role of bond order and its dependence upon local geometry, Tersoff includes an environment-dependent bond order explicitly into the potential in the following way -

$$\begin{aligned} E &= \sum_i E_i = \tfrac{1}{2} \sum_{i \neq j} V_{ij} \\ V_{ij} &= f_C\left(r_{ij}\right)\left[a_{ij} f_R\left(r_{ij}\right) + b_{ij} f_A\left(r_{ij}\right)\right] \end{aligned} \tag{2.34}$$

Here E is the total energy of the system, which is decomposed into a site energy E_i and a bond energy V_{ij}. The indices i and j run over the atoms of the system, and r_{ij} is the distance from atom i to atom j. The function f_R represents a repulsive pair potential and f_A represents an attractive pair potential associated with bonding. The extra term f_C is merely a smooth cutoff function, to limit the range of the potential, since for many applications short-ranged functions permit a significant reduction in computational expense. The function b_{ij} is the only novel feature of the Tersoff potential. It represents a measure of the bond-order, and is assumed to be a monotonically decreasing function of the coordination of atoms i and j. Determining a satisfactory form for b_{ij} is by far the most difficult part of applying the Tersoff approach.

The functions f_R, f_A, f_C, a_{ij} and especially b_{ij} still need to be determined.

The choice of exponential functions for f_R and f_A, as in a Morse potential, proves to be a convenient one -

$$\begin{aligned} f_R(r) &= A\exp(-\lambda_1 r) \\ f_A(r) &= -B\exp(-\lambda_2 r) \end{aligned} \tag{2.35}$$

The cutoff function is simply taken as -

$$f_C(r) = \begin{cases} 1, & r < R - D \\ \frac{1}{2} - \frac{1}{2}\sin\left[\frac{\pi}{2}(r-R)/D\right], & R - D < r < R + D \\ 0, & r > R + D \end{cases} \tag{2.36}$$

which has continuous value and derivative for all r, and goes from 1 to 0 in a small range around R. R is chosen to include only the first-neighbour shell for most structures of interest. The parameters R and D specify the position and the width of the cutoff region. The short range of the potential is numerically advantageous in many applications. Furthermore, b_{ij} is taken to have the following form -

$$\begin{aligned} b_{ij} &= \left(1 + \beta^n \xi_{ij}^n\right)^{-1/2n} \\ \xi_{ij} &= \sum_{k \neq i,j} f_C(r_{ik})\, g(\theta_{ijk}) \exp\left[\lambda_3^3 (r_{ij} - r_{ik})^3\right] \\ g(\theta) &= 1 + c^2/d^2 - c^2/\left[d^2 + (h - \cos\theta)^2\right] \end{aligned} \tag{2.37}$$

where θ_{ijk} is the bond angle between bonds ij and ik. Finally, the form proposed by Tersoff for a_{ij} is -

$$\begin{aligned} a_{ij} &= \left(1 + \alpha^n \eta_{ij}^n\right)^{-1/2n} \\ \eta_{ij} &= \sum_{k \neq i,j} f_C(r_{ik}) \exp\left[\lambda_3^3 (r_{ij} - r_{ik})^3\right] \end{aligned} \tag{2.38}$$

with α taken sufficiently small that $a_{ij} \simeq 1$ unless η_{ij} is exponentially large, which will only occur for atoms outside the first-neighbour shell. The terms a_{ij} and b_{ij} contain the three-body interactions and modify the strengths of the repulsive and attractive terms according to the bonds local environment. The resulting Tersoff potential has performed quite well in describing many properties of silicon [211].

The Tersoff potential was further refined by Erhart and Albe [56] for the cases of silicon, carbon and silicon carbide with the addition of some new free parameters. The cohesive energy is now written as a sum over individual bond energies -

$$E = \sum_{i>j} f_C\left(r_{ij}\right) \left[V_R\left(r_{ij}\right) - \underbrace{\frac{b_{ij} + b_{ji}}{2}}_{\overline{b_{ij}}} V_A\left(r_{ij}\right) \right] \tag{2.39}$$

with the pairwise attractive and repulsive contributions given by -

$$V_R\left(r\right) = \frac{D_0}{S-1} \exp\left[-\beta\sqrt{2S}\left(r - r_0\right)\right] \tag{2.40}$$

and -

$$V_A\left(r\right) = \frac{SD_0}{S-1} \exp\left[-\beta\sqrt{2/S}\left(r - r_0\right)\right] \tag{2.41}$$

where D_0 and r_0 are the dimer energy and bond length. β and S are adjustable free parameters of the potential. The cutoff function is the same as that of the general Tersoff potential. The bond-order is given by -

$$b_{ij} = \left(1 + \chi_{ij}\right)^{-1/2} \tag{2.42}$$

with -

$$\chi_{ij} = \sum_{k \neq i,j} f_C\left(r_{ik}\right) \exp\left[2\mu\left(r_{ij} - r_{ik}\right)\right] g\left(\theta_{ijk}\right) \tag{2.43}$$

and the angular function -

$$g\left(\theta\right) = \gamma\left(1 + \frac{c^2}{d^2} - \frac{c^2}{d^2 + \left[h + \cos\theta\right]^2}\right) \tag{2.44}$$

The three-body interactions are determined by the parameters 2μ, γ, c, d, and h, which leads in total to up to nine adjustable parameters, all of them depending on the type of atoms i and j. This new bond-order potential for silicon, carbon and silicon carbide reproduces well the elastic, thermal and point defect properties.

2.4 Density Functional Theory

The most salient and relevant aspects of the mathematical formalism and computational implementation of Density Functional Theory (DFT) are reviewed in this section. For a more thorough description of the theoretical and computational principles underlying DFT, the reader is referred to any of the standard introductory textbooks [54, 137, 156, 214] and review articles [116, 186] on the subject.

2.4.1 The Kohn-Sham formulation of Density Functional Theory

The *raison d'etre* of DFT is the solution of the many-body Hamiltonian for a system of N electrons and M positively-charged nuclei (or ions) in a crystalline

solid, the starting point for nearly all problems in solid-state physics. Neglecting all relativistic and magnetic effects, this Hamiltonian can be written as -

$$\begin{aligned}\widehat{H_N} = &-\frac{\hbar^2}{2m_e}\sum_{i=1}^{N}\nabla_i^2 - \sum_{i,I=1}^{N,M}\frac{Z_I e^2}{4\pi\varepsilon_0\left|\mathbf{r_i}-\mathbf{R_I}\right|} + \frac{1}{2}\sum_{i,j}^{i\neq j}\frac{e^2}{4\pi\varepsilon_0\left|\mathbf{r_i}-\mathbf{r_j}\right|} \\ &-\sum_{I=1}^{M}\frac{\hbar^2}{2M_I}\nabla_I^2 + \frac{1}{2}\sum_{I,J}^{I\neq J}\frac{Z_I Z_J e^2}{4\pi\varepsilon_0\left|\mathbf{R_I}-\mathbf{R_J}\right|}\end{aligned} \tag{2.45}$$

where the electrons are denoted by lower case subscripts and the nuclei, with charge Z_I and mass M_I, by upper case subscripts. The terms in this Hamiltonian represent, from left to right, the kinetic energy of the electrons, the attractive potential acting on the electrons due to the nuclei, the repulsive electron-electron interaction, the kinetic energy of the nuclei and finally the repulsive internuclear electrostatic interaction. In practice, such an elementary equation as Eq. (2.45) is impossible to solve analytically for all but the most trivial systems because of the enormously complicating effects of the interactions between electrons, which leads to coupling between the electronic coordinates in the system. This coupling manifests itself under the well-known phenomena of inter-electron exchange and correlation interactions in Quantum Mechanics . The issue central to the theory of electronic structure is therefore the development of approximate methods using simplifying physical ideas to treat electronic interactions and correlations with sufficient accuracy such that, starting from Eq. (2.45), one can still gain insight into the diverse array of electronic properties and phenomena exhibited by real solid matter.

One initial simple approximation involves setting the mass of the ions M_I to infinity, which is tantamount to saying that the positions of the ions are assumed

fixed to their corresponding lattice points within the crystal structure. This so-called Born-Oppenheimer, or adiabatic, approximation in electronic structure calculations allows the ionic kinetic energy term in Eq, (2.45) to be ignored, which is an excellent approximation for most intent and purposes. Neglecting also the final inter-ionic electrostatic interaction term, which is essential in total energy calculations but reduces to a simple classical additive term within the Born-Oppenheimer approximation, the initial problem of solving the electronic structure for the entire crystalline solid is consequently simplified to the treatment of the crystal electron cloud exclusively. The corresponding N-electron Schroedinger equation can be rewritten as -

$$\left[\sum_{i=1}^{N}\left(-\frac{\hbar}{2m_e}\nabla_i^2 + V_{ion}\left(\mathbf{r_i}\right)\right) + \frac{1}{2}\sum_{i,j}^{i\neq j}\frac{e^2}{4\pi\varepsilon_0|\mathbf{r_i}-\mathbf{r_j}|}\right]\Psi_N\left(\mathbf{r_1},\sigma_1;\mathbf{r_2},\sigma_2;....\mathbf{r_N},\sigma_N\right)$$
$$= E_N\Psi_N\left(\mathbf{r_1},\sigma_1;\mathbf{r_2},\sigma_2;....\mathbf{r_N},\sigma_N\right) \tag{2.46}$$

where $V_{ion}(\mathbf{r_i}) = -\sum_{I=1}^{M}\frac{Z_I e^2}{4\pi\epsilon_0|\mathbf{r_i}-\mathbf{R_I}|}$ represents the combined ionic potential acting on each electron, E_N is the total electronic energy and $\Psi_N\left(r_1,\sigma_1;r_2,\sigma_2;....r_N,\sigma_N\right)$ is the N-electron wavefunction expressed in terms of the spatial ($\mathbf{r_i}$) and spin (σ_i) quantum numbers for the i^{th} electron in the material.

Historically, an important milestone for going beyond the independent-electron approximation, embodied by the Sommerfeld free-electron model, and incorporating approximately the effect of inter-electron interactions in solids was the development of the Hartree-Fock equations [1]. Even though they were the first technique which allowed for a neat separation between electron exchange and

[1] For an introduction to the mathematical formalism of Hartree-Fock theory, see for example page 332 in Ref. [7].

correlation effects, in practice their treatment remains difficult and requires careful further approximations. The need for more accurate, widely-applicable and easy-to-implement methods for calculating the ground state properties of many-body molecules and solid-state systems from first-principles, or "ab-initio", while still accounting for the effects of inter-electron exchange and correlation interactions, provided an incentive for P. Hohenberg and W. Kohn to conceive the current modern formulation of DFT in 1964 [91]. In this pioneering work, the authors demonstrated that the density $n(\mathbf{r})$ of particles in the ground state of a quantum many-body system can be assigned a special role and considered as a "fundamental" variable, and that all properties of the system under investigation, including the effects of interactions and correlations among the particles, can be considered to be unique *functionals* of this fundamental quantity. It follows from this crucial conjecture that the ground state electron density can be used as an effective replacement for the ground state many-body wavefunction $\Psi_G\left(r_1, \sigma_1; r_2, \sigma_2; ....r_N, \sigma_N\right)$ appearing in Eq. (2.46), thus significantly simplifying the scale and complexity of the problem from the full $3N$ degrees of freedom for N electrons embodied by Ψ_G.

This reformulation of the many-body problem is encapsulated by two cardinal theorems, known as Hohenberg-Kohn (HK) theorems, which together establish the theoretical foundations of all modern formulations of DFT. Apart from encompassing the important role assigned to the ground state density in DFT mentioned previously, the HK theorems also provide insight in the relation between the ground state density of a system of mutually-interacting electrons and any general external potential $V_{ext}\left(\mathbf{r}\right)$ acting upon it (for example, the Coulomb potential due to the nuclei in the periodic crystal structure of a material). The HK

theorems, which will be stated here without proof [1], can be expressed as follows:

1. **Theorem 1**: For any system of interacting particles bathed in an external potential $V_{ext}(\mathbf{r})$, the potential $V_{ext}(\mathbf{r})$ is determined uniquely, except for a constant, by the ground state particle density $n_o(\mathbf{r})$.

   Corollary 1: Since the Hamiltonian of the system is thus fully determined, except for a constant shift of the energy, it follows that the many-body wave-functions for all states (ground and excited), and consequently all internal properties of the system, are completely determined from the solution of the corresponding Schroedinger equation given only the ground state density.

2. **Theorem 2**: Any internal property of the system, including its total energy, can be expressed as a unique functional of the density $n(\mathbf{r})$, valid for any external potential $V_{ext}(\mathbf{r})$. For any particular $V_{ext}(\mathbf{r})$ the exact ground state energy of the system is the global minimum value of the functional of the total energy $E[n]$, and the density $n(\mathbf{r})$ that minimises the functional is the exact ground state density $n_o(\mathbf{r})$.

   Corollary 2: The functional $E[n]$ alone is sufficient to determine only the exact ground state energy and density. In general, excited states of the electrons must be determined by other means.

The challenge posed by the Hohenberg-Kohn theorems is how to make use of the reformulation of many-body theory in terms of functionals of the density. Such a functional for the total ground-state energy of the system can be written

[1] For a formal proof of the HK theorems, consult for example section 6.2 in Ref. [156].

in general as -

$$E_N\left[n(\mathbf{r})\right] = T_S\left[n(\mathbf{r})\right] + E_{Hartree}\left[n(\mathbf{r})\right] + E_{XC}\left[n(\mathbf{r})\right] + \int d^3\mathbf{r} V_{ext}(\mathbf{r}) n(\mathbf{r}) + E_{II} \quad (2.47)$$

where E_{II} is the interaction energy of the nuclei among themselves, and $T[n]$, $E_{Hartree}[n]$ and $E_{XC}[n]$ represent respectively the kinetic, classical Coulomb interaction (Hartree) and exchange-correlation energies of the electron cloud, all of which are internal properties of the electron system and are therefore expressible as functionals of the density according to the second HK theorem. At this stage however we are still left with the problem of finding explicit forms for the constituent functionals in Eq. (2.47). While on one hand there exists a simple expression linking the Hartree potential energy to the density -

$$E_{Hartree}\left[n\right] = \frac{1}{2} \int d^3\mathbf{r} d^3\mathbf{r}' \frac{n\left(\mathbf{r}\right) n\left(\mathbf{r}'\right)}{4\pi\epsilon_0 \left|\mathbf{r} - \mathbf{r}'\right|} \quad (2.48)$$

this task is more problematic for the kinetic energy term $T[n]$, for which there is no known direct connection to the density, and for the exchange-correlation energy functional $E_{XC}[n] = E_X[n] + E_C[n]$ incorporating all the complex many-body exchange ($E_X[n]$) and correlation ($E_C[n]$) effects, which cannot be modelled analytically.

A significant step forward from this impasse was accomplished by the seminal work performed in 1965 by W. Kohn and L.J. Sham [138], which lead to the now well-established Kohn-Sham (KS) approach to DFT . The defining *Ansatz* of the KS formulation of DFT was to map the difficult interacting many-body system obeying the Hamiltonian of Eq. (2.46) to a different fictitious auxiliary system of

non-interacting particles that can be solved more easily, with the condition that its ground state density be equal to that of the original interacting system and consequently that its internal physical properties be equivalent. Even though it has never been proven formally that this auxiliary system is capable of reproducing precisely all the physical properties of the original interacting problem, this basic assumption yields excellent approximations for the problems of greatest practical interest, and in particular for ground-state calculations which are by far the most widespread applications of DFT.

Solution of the KS auxiliary system for the ground state can be viewed as the problem of minimisation of the total ground state energy functional of Eq. (2.47) with respect to small variations in the density $\delta(n(\mathbf{r},\sigma))$. One of the major qualities of the KS approach is that it allows the electronic density of the independent-particle auxiliary system to be expressed as a simple sum of the probability densities associated with each single-particle wavefunction $\psi_i^\sigma(\mathbf{r})$ -

$$n\left(\mathbf{r}\right) = \sum_{\sigma} n(\mathbf{r},\sigma) = \sum_{\sigma}\sum_{i=1}^{N^\sigma} \left|\psi_i^\sigma\left(\mathbf{r}\right)\right|^2 \tag{2.49}$$

The establishment of such a relation between density and wavefunctions allows in turn the functional for the kinetic energy in Eq. (2.47) to be kept expressed in terms of the single-particle orbitals, without therefore the need to find an explicit dependence on the density -

$$T_s = -\frac{\hbar^2}{2m_e}\sum_{\sigma}\sum_{i=1}^{N^\sigma}\left\langle \psi_i^\sigma \mid \nabla^2\psi_i^\sigma\right\rangle = -\frac{\hbar^2}{2m_e}\sum_{\sigma}\sum_{i=1}^{N^\sigma}\left|\nabla\psi_i^\sigma\right|^2 \tag{2.50}$$

Given that all other functionals of the density in Eq. (2.47) can now also be

expressed in terms of the independent-particle orbitals $\psi_i^\sigma(\mathbf{r})$ via Eq. (2.49), the problem of minimising Eq. (2.47) to find the ground-state energy of the system can be reformulated in terms of variations of the orbitals via the chain rule, which yields the following variational equation -

$$\frac{\delta E_N}{\delta \psi_i^{\sigma *}(\mathbf{r})} = \frac{\delta T_S}{\delta \psi_i^{\sigma *}(\mathbf{r})} + \left[\frac{\delta E_{ext}}{\delta n(\mathbf{r},\sigma)} + \frac{\delta E_{Hartree}}{\delta n(\mathbf{r},\sigma)} + \frac{\delta E_{XC}}{\delta n(\mathbf{r},\sigma)} \right] \frac{\delta n(\mathbf{r},\sigma)}{\delta \psi_i^{\sigma *}(\mathbf{r})} = 0 \tag{2.51}$$

subject to the orthonomalization constraint on each of the single-particle orbitals -

$$\left\langle \psi_i^\sigma \,\middle|\, \psi_j^{\sigma'} \right\rangle = \delta_{i,j}\delta_{\sigma,\sigma'} \tag{2.52}$$

Using expressions (2.50) and (2.49) for calculating the derivatives involving the kinetic energy and the density -

$$\frac{\delta T_S}{\delta \psi_i^{\sigma *}(\mathbf{r})} = -\frac{1}{2}\nabla^2 \psi_i^\sigma(\mathbf{r}); \;\; \frac{\delta n^\sigma(\mathbf{r})}{\delta \psi_i^{\sigma *}(\mathbf{r})} = \psi_i^\sigma(\mathbf{r}) \tag{2.53}$$

and the Lagrange multiplier method for constrained minimisation, we obtain the following set of Schroedinger-like equations, one for each of the N single-particle orbitals in the auxiliary system -

$$\begin{gathered} \left(H_{KS}^\sigma - \varepsilon_i^\sigma\right) \psi_i^\sigma(\mathbf{r}) = 0 \\ \{\psi_i^\sigma : i = 1, N\} \end{gathered} \tag{2.54}$$

where the Lagrange parameters ϵ_i represent the possible eigenvalues. It is important to stress that these eigenvalues do not correspond to the single-particle energies as in a normal Schroedinger equation, and in fact have no obvious physical meaning except for the highest one, which corresponds to the ionization energy

of the system. H_{KS} on the other hand represents the effective KS Hamiltonian -

$$H^{\sigma}_{KS}(\mathbf{r}) = -\frac{\hbar^2}{2m_e}\nabla^2 + V^{\sigma}_{KS}(\mathbf{r})$$
$$\text{where } V^{\sigma}_{KS}(\mathbf{r}) = \frac{\delta E_{ext}}{\delta n\,(\mathbf{r},\sigma)} + \frac{\delta E_{Hartree}}{\delta n\,(\mathbf{r},\sigma)} + \frac{\delta E_{XC}}{\delta n\,(\mathbf{r},\sigma)} = V^{\sigma}_{ext}(\mathbf{r}) + V^{\sigma}_{Hartree}(\mathbf{r}) + V^{\sigma}_{XC}(\mathbf{r}) \tag{2.55}$$

Equations (2.54) and (2.55), collectively referred to as the *Kohn-Sham equations*, represent the culminating point of the entire KS formulation of DFT. By diagonalising and solving the equations self-consistently (in practice by numerical means) one can first compute all the single-particle KS eigenstates $\psi^{\sigma}_i(\mathbf{r})$, and from there the ground-state density and total ground-state energy of the original interacting system from equations (2.49) and (2.47) respectively, with an accuracy limited only by the approximations in the exchange-correlation functional (given that all other functionals in Eq. (2.47) can be computed exactly within the KS approach). The next section in this document is devoted to the description of the approximations for this functional most entrenched in the condensed-matter physics community.

2.4.2 The Local Density and Generalized Gradient approximations for the exchange-correlation energy functional

Already in their seminal paper [138], Kohn and Sham pointed out that solids can often be considered as close to the limit of the homogeneous electron gas. In this limit, it is known that the effects of exchange and correlation are rather local in character, and they proposed making the local density approximation (LDA) in

which the exchange-correlation energy is simply an integral over all space, with the exchange-correlation energy density $\epsilon_{XC}([n], \mathbf{r})$ at each point $\mathbf{r}$ assumed to be the same as in a homogeneous electron gas of interacting electrons with the same local density -

$$E_{XC}^{LDA}[n] = \int d^3\mathbf{r} n(\mathbf{r}) \varepsilon_{XC}^{\text{hom}}(n(\mathbf{r})) = \int d^3\mathbf{r} n(\mathbf{r}) \left[\varepsilon_X^{\text{hom}}(n(\mathbf{r})) + \varepsilon_C^{\text{hom}}(n(\mathbf{r}))\right] \quad (2.56)$$

The corresponding exchange-correlation potential appearing in the KS equations is consequently given by -

$$V_{XC}^{\sigma}(\mathbf{r}) = \frac{\delta E_{XC}^{LDA}[n]}{\delta n(\mathbf{r}, \sigma)} = \left[\varepsilon_{XC}^{\text{hom}} + n\frac{\partial \varepsilon_{XC}^{\text{hom}}}{\partial n^{\sigma}}\right]_{\mathbf{r},\sigma} \quad (2.57)$$

The only information needed within the LDA approximation is therefore the exchange-correlation energy of the homogeneous gas as a function of density. Since the exchange energy of an homogeneous electron gas can be calculated analytically within Hartree-Fock theory, and is given by [1] -

$$\varepsilon_X^{\text{hom}} = -\frac{3}{4}\frac{e^2 k_F}{\pi} = -\frac{3e^2}{4\pi a_o}(k_F a_o) \quad (2.58)$$

where k_F is the Fermi wavevector and a_o the Bohr radius, the LDA simply boils down to fitting numerical correlation energies for the homogeneous gas, for example by Monte Carlo total energy calculations [27, 191]. A variety of LDA expressions for the correlation energy have been proposed with time, and the most celebrated are summarised in Appendix B of Ref. [156]. The LDA is expected to give the best results for solids close to a homogeneous electron gas in which

[1] A derivation of this expression can be found in Chapt. 17 of Ref. [7].

the charge density is slowly varying (like a nearly-free-electron metal) and worst for very inhomogeneous cases, like for the case of atoms where the density must go continuously to zero outside the atom, or indeed in any general covalently-bound solid. However, experience has proved the LDA to be a surprisingly good approximation for a wide variety of solid-state systems.

The remarkable success of the LDA in most applications has stimulated ideas for the development of various Generalized Gradient Approximations (GGAs) [187, 188, 190], with marked improvement over LDA in many cases. Within the the context of the GGA, it is convenient to generalise the expression for the exchange-correlation functional given by Eq. (2.56) to include explicitly the dependence on the various orders of the density gradient $|\nabla^m n^\sigma(\mathbf{r})|$ -

$$\begin{aligned} E_{XC}^{GGA}[n] &= \int d^3r n(r)\varepsilon_{XC}\left(n, |\nabla n|, \left|\nabla^2 n\right| ..... |\nabla^m n|\right) \\ &\equiv \int d^3r n(r)\varepsilon_X^{\text{hom}}(n)F_{XC}\left(n, |\nabla n|, \left|\nabla^2 n\right| ..... |\nabla^m n|\right) \end{aligned} \tag{2.59}$$

where F_{XC} is a dimensionless function, known as the enhancement factor of the exchange-correlation functional, and $\epsilon_x^{hom}(n)$ is the exchange energy density of the homogeneous electron gas given by Eq. (2.58). An expression for the exchange-correlation potential appearing in the KS equations can also be found by calculating the change $\delta E_{XC}[n]$ to linear order in δn and $\delta\nabla n = \nabla\delta n$ -

$$V_{XC}^\sigma(\mathbf{r}) = \frac{\delta E_{XC}^{GGA}[n]}{\delta n(\mathbf{r},\sigma)} = \left[\varepsilon_{XC} + n\frac{\partial\varepsilon_{XC}}{\partial n^\sigma} - \nabla\left(n\frac{\partial\varepsilon_{XC}}{\partial\nabla n^\sigma}\right)\right]_{\mathbf{r},\sigma} \tag{2.60}$$

2.4.3 Computational self-consistent solution of the Kohn-Sham equations: the plane-wave pseudopotential method

In order to solve in practice the eigenvalue problem presented by the KS equations (2.54), the single-particle eigenstates $\psi_i^\sigma(\mathbf{r})$ must be expanded in some orthogonal basis set. The simplest and most popular choice for this basis is to use orthogonal plane-wave functions, under the so-called orthogonalised planewave (OPW) method [89, 141, 214] . These plane-waves can be expressed as [1] -

$$\psi_{\mathbf{k}}^i(\mathbf{r}) = \sum_{\mathbf{G}} c_{\mathbf{k}}^n(\mathbf{G}) e^{i(\mathbf{k}+\mathbf{G})\cdot\mathbf{r}} \tag{2.61}$$

where $\mathbf{k}$ is the crystal momentum and the sum is over all Bravais lattice vectors $\mathbf{G}$ of the reciprocal lattice of the system under investigation. This discrete basis set can in theory be made infinite in size by application of periodic boundary conditions to the problem, but in practice a finite number of plane-wave basis states is normally sufficient to converge systematically most physical quantities of interest in typical computational problems. As explained in Fig. 2.10, in order to truncate the basis set, the sum term in Eq. (2.61) is limited to a set of reciprocal lattice vectors encompassed by a sphere with radius defined by the cutoff kinetic energy, E_{cut} -

$$\frac{\hbar^2 \left|\mathbf{k}^2 + \mathbf{G}^2\right|}{2m} \leqslant E_{cut} \tag{2.62}$$

[1] This form for the plane-wave functions can be shown to be the most general solution satisfying Bloch's Theorem for periodic boundary conditions in a crystal lattice.

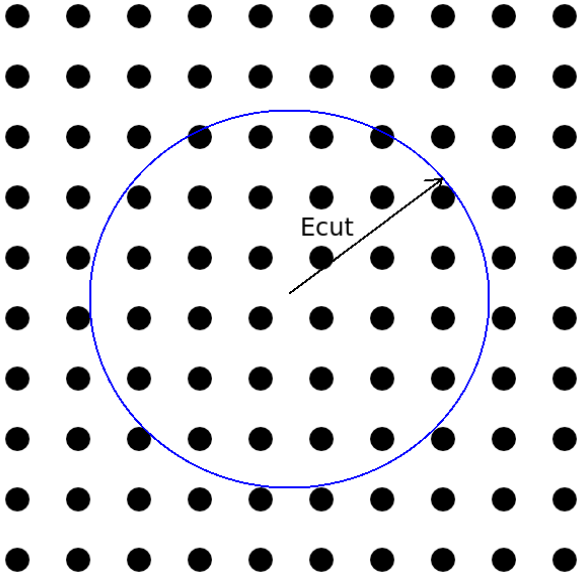


Figure 2.10: Truncation of the plane wave basis states expansion at a sphere of radius E_{cut} in reciprocal space. The black dots represent the discrete reciprocal lattice vectors available for the expansion.

so that the entire set of plane-waves can be defined by this maximum kinetic energy component. More recently, the OPW method has been reformulated and adapted to modern techniques for calculation of total energy, forces and stress under the so-called Projector-Augmented Wave (PAW) method [17], which introduces projectors and auxiliary localised functions for a more efficient solution of the KS eigenvalue problem.

The choice of plane waves as basis set however requires to be operated in conjunction with the implementation of pseudopotentials [33, 34, 195] in order to limit the size of this expansion to computationally-feasible proportions for the solution of realistic systems. Pseudopotentials allow for a neat separation between the treatment of core electrons in an atom, that is those electrons which are tightly-bound to the nucleus and are therefore not involved in the interac-

tions between atoms, and the valence electrons, which on the other hand are more loosely bound and consequently dictate the chemical properties of the material. As a direct consequence of the orthogonality requirement on the single-electron wavefunctions, the superposition of the valence and core electron wavefunctions results in a many-electron wavefunction exhibiting strong-oscillations in the region near the nucleus, as illustrated in Fig. 2.11. These oscillations become inevitably quite difficult to model using a plane-wave basis set, requiring many plane-waves for an accurate description. It therefore becomes convenient to ignore altogether the region in the immediate surroundings of the nucleus, and this is indeed the approach adopted by the pseudopotential approximation, where only the valence electrons of atoms are explicitly considered and the screening effects of the inner core electrons contained within the cutoff nuclear radius r_c indicated in Fig. 2.11 are integrated within a new effective ionic potential (the pseudopotential). The remaining smoother variation of the all-electron valence wavefunction in the outskirts of the nuclear region beyond r_c can be modelled accurately with a much more restricted size for plane-wave basis set, with the consequent sharp gain in computational efficiency. The pseudopotential approach turns out to be an excellent approximation for practical calculations since, as mentioned previously, this region remains almost completely shielded from all neighbouring interactions, and the oscillations are consequently of very little consequence for the electronic structure of the solid.

When constructing a new pseudopotential, the main goals that need to be attained are threefold: firstly, the pseudopotential should be as soft as possible, meaning that it should allow expansion of the valence pseudo-wavefunctions using as few plane-waves as possible. Secondly, it should be as transferable as possible,

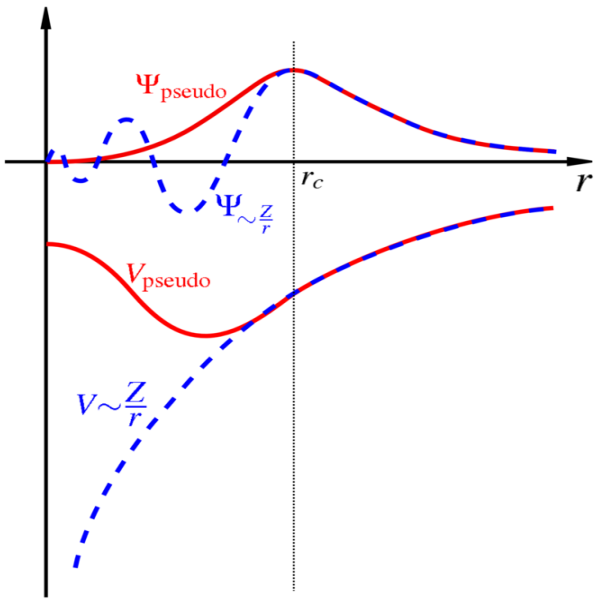


Figure 2.11: Schematic representation of the concept of pseudopotential. Ψ labels the true all-electron wavefunction, while Ψ_{pseudo} the all-electron pseudowavefunction which results from substituting the true bare Coulombic nuclear potential Z/r with the modified pseudopotential V_{pseudo} incorporating the screening effects of the inner core electrons. The smooth variation of Ψ beyond the core radius r_c implies that an accurate emulation of the atomic interaction with Ψ_{pseudo} requires only a limited plane-wave basis expansion, thus making the pseudopotential a very efficient approximation for most atomic systems. (Figure reproduced from Ref. [1].)

in the sense that a pseudopotential generated for a given atomic configuration should accurately reproduce others. This helps to ensure that its application in solid-state systems, where the overall crystal potential is inevitably different from an atomic potential, be capable of reliable results. Finally, the pseudo-charge density, that is the charge density constructed using the pseudo-wavefunctions, should reproduce the valence charge density of the atom under consideration as accurately as possible. The concept of *norm-conservation* in pseudopotential theory [83] provided the first systematic solution for reconciling these conflicting

goals. Within norm-conserving pseudopotentials, the pseudo-wavefunctions are designed and constructed to be equivalent to the actual valence wavefunctions outside the core radius r_c. Inside r_c on the other hand, the pseudo-wavefunctions are allowed to differ from the true wavefunctions, but their norm is constrained to be the same.

A radical departure from the concept of norm-conservation in pseudopotentials was eventually proposed by Vanderbilt and co-workers [230]. In this approach, which became to be known as the *ultra-soft* pseudopotential method, the pseudo-wavefunctions are required to be equal to the all-electron wavefunctions outside r_c as with norm-conserving pseudopotentials, but inside r_c they are allowed to be as soft as possible, which is accomplished by removing the norm-conservation constraint. Even though the use of non-normalised wavefunctions complicates the solution of the KS equations, this approach offers the major advantage of greatly reducing the required plane-wave cutoff without sacrificing the accuracy of the calculation, which explains its popularity for use in large-scale calculations. The computational work presented in this thesis was no exception.

One final aspect of the computational implementation of DFT worth mentioning is the techniques used for determining the charge density and other quantities which can be extracted from DFT calculations such as total energy and atomic forces. The evaluation of all these quantities require summations to be performed over the occupied states, which for crystals translate into integrals over the Brillouin zone. Exploiting the symmetry properties of the crystal, this integration can then be limited to the symmetry-irreducible wedge of the zone (IBZ). In practice, these integrals are calculated numerically using wavefunctions and eigenvalues at a finite number of **k**-points in the electronic bandstructure of the IBZ. This leads

to the so-called *special points method* for Brillouin-zone integration [9, 28, 57], the most commonly used approach for this type of calculations, in which integrations are performed as weighted sums over a grid of representative, or special, **k**-points chosen to yield optimum convergence for smoothly varying functions of **k**. This application of the special points method however proves problematic for the case of metals, where electronic bands intersect the Fermi energy E_f. This leads to discontinuities in the electronic occupation numbers and therefore in the integrands at the Fermi surface, thus yielding slower convergence for a given number of **k**-points. This difficulty can be overcome by the introduction of an artificial temperature-induced and convergence-accelerating broadening of the Fermi surface corresponding to a smoother electron distribution function than the original step function, such as a finite-temperature Fermi distribution. Care must however be taken to ensure that the introduction of such broadening factor does not affect physical quantities of interest.

Chapter 3

Ab-initio investigation of the cubic-diamond $\rightarrow$ β-tin phase transition in Si and Ge

3.1 Motivation

Crystalline silicon, together with its fellow group IV A elemental semiconductor germanium with which it shares many physical and chemical qualities, has progressively emerged as a material of paramount importance in the microelectronics industry since the early advent of Integrated Circuit Technology in the early 60's [182, 213]. Nowadays it has come to underpin the circuitry of the most widespread technological devices, from simple LEDs and transistors to complex microprocessors and solar cells. Furthermore, silicon has traditionally been of inherent research interest within the fields of high-pressure and planetary physics due to its relative abundance in the Earth's crust, and more recently it has gar-

nered attention also for its excellent mechanical properties as a brittle material in a wide range of applications in electro-mechanical systems and ultra-precision machining [193].

This chapter concerns itself with the first of two pieces of research presented in this thesis based on ab-initio computational methods which aim at furthering our understanding of the mechanical response properties of monocrystalline semiconducting materials with equilibrium cubic diamond (*cd*) crystal structure (in particular silicon and germanium) under the effects of shock-wave compression. The fundamental reason behind why we are interested in studying these two materials, Si and Ge, is that to this day a lattice-level understanding of the fundamental mechanism underpinning the relief of shear stress following the initial stage during shock-wave loading of elastic uniaxial compression has remained elusive. The bulk of the experimental and computational research effort devoted to these materials has in fact so far revolved on the effects of static/hydrostatic compression. These shortcomings are part of a generalised pattern of poor understanding of the behaviour of solid matter under dynamic compression at the fundamental microstructural lattice-level nanoscale, which has persisted to this day despite the considerable theoretical, computational and experimental advances of recent years [150, 201, 202].

In the present chapter we aim at redressing this balance, and the main emphasis will be put on the role played by the occurrence of the particular process in solid-state shock physics of shock-induced polymorphic solid-solid phase transitions [53]. In particular we investigate, through ab-initio Density Functional Theory (DFT) computational techniques, the particular issue of the polymorphic pressure-induced phase transition from the equilibrium *cd* crystal structure

which both crystalline silicon and germanium have in common at ambient pressures and temperatures, to their first stable high-pressure phase, which is known as the β-Sn (or white-tin) phase. This phase transition occurs at a pressure of around 120 and 100 kbar for Si and Ge respectively when the compression is applied hydrostatically and the temperature is maintained at atmospheric levels. In addition to entailing a transformation in the structure of the crystal, the *cd* to β-Sn phase-transition manifests itself also as a drastic increase in the electrical conductivity from the semiconducting levels characteristic of silicon and germanium at ambient pressure, to levels comparable to those of "poor" metals such as Ni, Al, Zn, Pb and Mo. This phenomenon of pressure-induced metallisation of originally semiconducting crystals resulting from the closure of the band gap, which besides Si and Ge also concerns the elements Se (at 20 GPa), Te (4 GPa), Br (100 GPa), I (17 GPa) and Xe ($\sim$ 160 GPa), is of practical interest in several applications concerning the generation and governing of electromagnetic energy flows in high power systems [16, 233], on top of being a phenomenon of obvious inherent intrigue.

In a wider context, this phase transition represents only the first step in order of ascending pressure in the sequence of structural transformations connecting the equilibrium *cd* phase to other high-pressure phases. Both silicon and germanium are now known to exhibit a plethora of 11 stable and metastable solid crystalline structural phases at high pressures [3, 175]. These distinct high-pressure phases were progressively identified experimentally through static loading techniques in the context of pressure applied hydrostatically, for example by DACs, diamond indentation and high pressure X-ray synchrotron diffraction experiments. None of the pressure-induced phase transitions linking any two of these phases has a

sharply defined boundary, such that two-phase coexistence regions exist over a wide range of pressures. A comprehensive tabulation of their crystal properties, pressure ranges over which they exist and conventional labelling with Roman numbers can be found in Refs. [103, 227], and in the references cited therein. Only two of these phases turn out to be semiconducting, the ambient-pressure *cd* (Si-I) phase and the Si-IV phase, while all remaining phases have metallic conductivity. Furthermore, all phases except for Si-IV do not require heating above room-temperature in conjunction with the increase in pressure in order to be observed. Single-crystal germanium was also observed to follow precisely the same series of structural changes as silicon and to have in general an essentially identical pressure-temperature phase diagram [25], the only difference being the absolute values of the transition pressures and temperatures.

The pressure-induced *cd* to β-Sn phase transition in monocrystalline silicon is by now one of the best understood in condensed-matter physics, as a result of having been thoroughly studied experimentally in connection with its emergence under hydrostatic compression for the case of both silicon [79, 100, 101, 120, 234], and germanium [13, 43, 163, 198]. Despite having been under the spotlight of the high-pressure physics research community ever since its original discovery through static loading techniques in the early 60s [47, 107, 242], a quantitative understanding of how exactly this phase transition fits within the overall framework of the mechanical and dynamical response properties of silicon and germanium to shock-wave loading is still not fully understood. This research attempts at casting some light over these shortcomings, although as explained in the concluding section the results presented here are still far form conclusive and leave much scope for further investigation.

3.2 The mechanical response properties of silicon and germanium under shock-compression: the current state of research

A first attempt at a characterisation of the mechanical response properties of single-crystal silicon under the effects of dynamic loading by planar shock-waves was carried out in the seminal experimental investigation by Pavlovskii [185] for shock-induced compressions directed along the ⟨111⟩ crystallographic axis. The shock-induced behaviour of the very closely related case of single-crystal germanium was on the other hand investigated experimentally for the first time in another landmark paper by Graham *et al.* [76], again for the case of shocks propagated along the ⟨111⟩ axis.

By making use of the inclined-prism technique for the continuous measurement of free-surface velocities, Gust and Royce [80, 81] subsequently expanded these original findings to shock-induced compressions along the two other main-symmetry directions ⟨100⟩ and ⟨110⟩ in each of the two materials. In both cases, the authors observed a break-up of the leading elastic precursor front into several successive waves during the course of its propagation through the target sample. The first wave following the break-up was speculated to consist in a slower plastic wave responsible for stressing the loaded sample up to its Hugoniot Elastic Limit (HEL), the dynamic yield point marking the transition of the material's internal response from the initial regime of elastic uniaxial straining along the shock-propagation direction, to a subsequent state of plastic flow characterised by permanent three-dimensional hydrostatic deformation. This type of defect-

mediated plasticity typically provides a mechanism for the relief of the shear stress that, as the solid gets uniaxially compressed, is progressively accumulated in the underlying lattice until the point of rupture of the covalent bonds between atoms and the consequent complete loss of shear strength. For the case of the $\langle 100 \rangle$ shock orientation that is of interest to us in the context of the research presented herein, the HEL of the silicon and germanium single-crystal samples were measured at 92 ± 10 kbar and 58 ± 8 kbar respectively. The values of the HEL for shocking along the other directions were in general observed to be significantly lower, hovering around 50 kbar in all cases, suggesting a marked anisotropy in the response of both materials to the external loading. Furthermore, the ensuing higher pressure waves were recognised by the authors as succeeding transition waves (with the exception of the final pressure release wave), each giving rise to a distinct shock-induced polymorphic phase transition to a high-pressure phase. Just one of these phase transition waves, resulting in an overall three-wave structure, was resolved and identified with certainty for shocking along the $\langle 100 \rangle$ direction, and the corresponding transition stress was recorded at 140 ± 4 kbar for silicon and 117 ± 10 kbar for germanium. With just these wave-profile measurements, the authors were not in a position to carry out a structural analysis of this newly emerged phase, although the possibility of a β-Sn structure was deemed implausible on the grounds of density estimations performed on the final recovered sample.

Following these initial discoveries, Goto *et al.* [75] performed a second complete investigation on the dynamic shock compression of single-crystal silicon oriented along the same three main symmetry axes, again by making use of the inclined mirror technique for the wave profile measurements operated in conjunc-

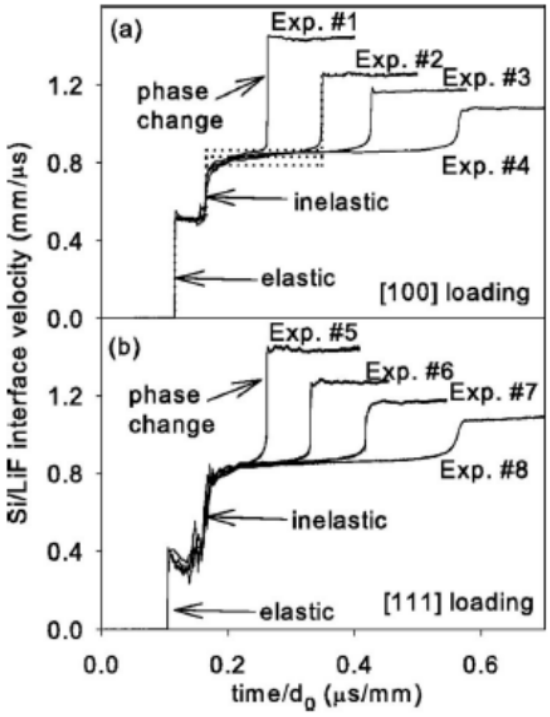


Figure 3.1: Particle velocity profiles recorded in the experiments by Turneaure and Gupta [228, 229], showing the break-up of the leading elastic precursor into an inelastic and then phase transition waves, for the case of shock-wave loading along ⟨100⟩ (top) and ⟨111⟩ (bottom) (figure reproduced with permission from Ref. [228]).

tion with the impacting of flyer plates for driving the shock waves into the sample. They reported, among their other results, an HEL of 84 kbar and a phase transition stress of 134 ± 2 kbar for ⟨100⟩ loading, both results being in agreement with those of Gust and Royce [80, 81] within the quoted error bars. The result for the HEL was again positively corroborated in a further flyer plate impact experiment by Turneaure and Gupta [228, 229], which yielded a value of about 90 kbar. Fig. 3.1 shows the break-up of the leading elastic wave observed in this last experiment.

A radical new approach for probing the high-pressure phase of ⟨100⟩ silicon was implemented by Gilev and Trubachev, who conducted a series of time-resolved measurements on the electrical response of the material during the shock-loading process [69, 70, 71]. As shown in Fig. 3.2, they reported a steep monotonic increase in the electrical conductivity by five orders of magnitude as a function of increasing normal stress, with an onset of metallic-type behaviour at about 100 kbar and a definitive stabilization of the conductivity at a "plateau"-level typical of "poor" metals like Lead at around 120 kbar. These results appear to be correlating the metallisation of silicon indicative of the phase-transition to the β-Sn structure more closely with the HEL rather than the phase-transition signal. Other conductivity experiments by Rosenberg [207] and Coleburn *et al.* [35] arrived at similar conclusions after detecting a sharp peaking in the conductivity to metallic levels in the neighbourhood of the HEL for the case of loading along the ⟨111⟩ axis. Attempts at identifying the final transformed high-pressure structure emerging from the ensuing phase-transition wave were also made, with results supportive of either the orthorhombic *Imma* phase [71] or the next higher-lying simple-hexagonal phase [228].

Single-crystal silicon has moreover been the object of a comprehensive set of laser-based experiments [90, 123, 124, 125, 126, 133, 136, 152, 177, 238, 240, 241], which made use of the structural diagnostic technique of time-resolved *in situ* X-ray diffraction (TXRD) [219, 239] for taking real-time "snapshots" of transient lattice dynamics effects in crystals undergoing laser-induced shock-compression. This technique commonly employs a "pump-probe" setup based on a two-beam geometry whereby a first nanosecond-duration high-power pulsed laser beam is used to directly drive the shock-wave into the target sample by laser ablation

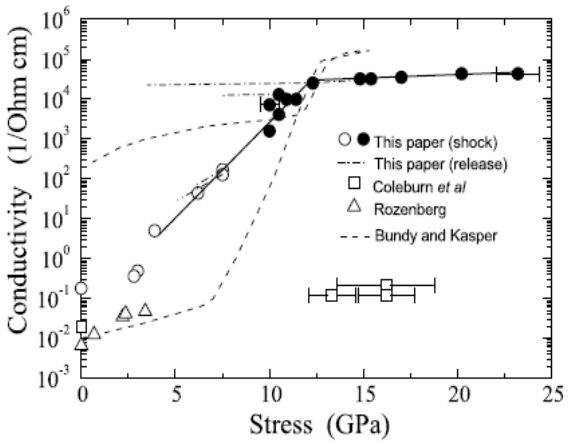


Figure 3.2: Increase in conductivity as a function of shock-induced stress in shocked single-crystal silicon reported by Gilev and Trubachev [71]. The results reported in the shock experiments by Rosenberg [207] and Coleburn *et al.* [35] are also shown, as well as the static compression measurements by Bundy and Kasper [24] (figure reproduced with permission from Ref. [71]).

and subsequent expansion of the resulting plasma created at the surface into the surrounding vacuum. A second delayed (typically by a few nanoseconds) "back-lighting" beam is then made to irradiate a thin metal foil placed very close to the target in order to generate an ultrafast (nanosecond or picosecond duration) and powerful burst of X-ray radiation (which can be either nearly-monochromatic or white-light-like depending on the composition of the metal foil) by plasma line emission [176]. This X-ray source can then be adopted as a structural probe to interrogate the response of the sample to the passage of the shock-wave at the microscopic lattice level by recording the corresponding time-resolved X-ray diffraction patterns under various reflection and transmission geometries on a set of image plates placed around the target, thus effectively mapping the dynamics of the reciprocal lattice of the crystal with a temporal resolution characteristic of the picosecond-duration vibration period of phonons and consequently of most

microstructural phenomena in solid-state physics [206]. Of particular interest in this kind of experiments are the interplanar lattice spacings oriented longitudinally and transverse to the shock-propagation direction, whose shock-induced compression provide respectively a measure of the degree of uniaxial elastic compression, and of the onset of hydrostatic-like plastic deformation or new structural phases.

However, even within the subset of these TXRD experiments in which laser-induced pressures exceeding the nominal value of the HEL for the particular orientation under consideration were achieved, and in which the X-rays diffracted from lattice planes perpendicular to the shock direction were actively monitored [124, 125, 136, 152], the use of TXRD proved inconclusive in identifying any evidence of plastic deformation, with the target exhibiting a purely elastic response under all loading circumstances with no observable shifts in the diffraction signals corresponding to the lattice spacings perpendicular to the shock propagation direction. One exception was the experiment by Kishimura *et al.* [136], in which a superior time and angle resolution allowed for the identification of microscopic mosaic blocks with inclined orientations in the final state of the sample, allegedly caused by the initial elastic compression and the subsequent pressure release during relaxation. This type of spalling effect remains however unrelated to conventional plasticity. This "anomalous" elastic response was originally rationalised [124, 152] in terms of the characteristic time-scales for the propagation of dislocations in Si and Ge, which were believed to determine the corresponding plastic strain rates. These were estimated to be of order of microseconds, in marked contrast with the nanosecond and picosecond durations of laser-induced shock waves and associated TXRD bursts of X-rays. This slow dislocation velocity would have

explained why the experiments were unable to capture the effects of dislocation-mediated plasticity for this particular case, while at the same time successfully doing so with other materials such as Cu in which the dislocation velocity can be as much as six orders of magnitude faster than that in Si according to theoretical predictions.

Finally, the residual structure of recovered samples of laser-shocked single-crystal silicon, following complete relaxation from shock pressures exceeding the transition pressures of the first few high-pressure phases, was itself investigated in a series of measurements by X-ray diffraction, Raman spectroscopy and Scanning Tunnelling Microscope techniques [134, 135]. Similarly to the aforementioned TXRD studies however, these surveys proved unsuccessful in detecting evidence for the formation of stable high-pressure phases, suggesting that any phase transition that could have possibly taken place during the loading process was in fact only temporary, and was consequently followed upon pressure release by a rapid collapse back to the original *cd* structure in a highly-polycrystalline and compressed state. This suggests that the high-pressure phases of silicon can still turn out to be metastable upon application of dynamic compression, even when they are observed to remain stable under static pressure loading.

The case of single-crystal germanium on the other hand has attracted a far less comprehensive record of experiments concerned with its behaviour under shock-wave loading. Beside the aforementioned researches by Graham and Gust and Royce, we are aware of only two other experimental investigation in which single crystals of germanium were laser-shocked above the HEL and the lattice deformation due to shock compression probed by TXRD, both carried out by Nakamura and co-workers [177, 178]. Similarly to the case of silicon, the response

of germanium was in both cases purely elastic due allegedly to the elastic-plastic transformation taking a much longer time than the order picosecond duration of laser-induced shocks.

Considering all the above-mentioned results, there remains an ambiguity in the precise nature of the fundamental mechanism underpinning the relief of shear stress and the onset of inelastic behaviour at the reported value of around 90 kbar and 60 kbar for silicon and germanium respectively following the initial state of elastic uniaxial compression. It also remains uncertain how the phase-transition from the ambient pressure *cd* phase to the metallic β-Sn crystal structure fits exactly within the overall panorama of the mechanical response properties of silicon and germanium under shock-compression. There is strong evidence for polymorphic phase transitions taking place at higher pressures, although as explained previously it appears unlikely that these bear any relation to the β-Sn structure itself. Most of the experiments have to this day based their conclusions on the assumption of an intermediate state of conventional plasticity triggered by the attainment of the material's HEL preceding the final phase-transition wave. No evidence, such as a rigorous assessment of the structural evolution of the crystal lattice, has however been provided to back up this hypothesis. In particular any comparison with materials such as Cu, in which the onset of shock-induced plastic flow mediated by the nucleation of defects is a well-established phenomenon corroborated by many independent investigations [167, 169, 218], seem far-fetched. On the other hand, measurements such as the shock-induced rise in electrical conductivity appear to correlate the metallisation of silicon indicative of the phase-transition to the β-Sn structure more closely with the HEL rather than the reported phase-transition wave signal itself, which was indeed

observed to match more closely the properties of other higher-pressure phases. These observations suggest a scenario in which the phase-transition to β-Sn caters directly for the relief of shear stress in the crystal structure of shock-compressed silicon, without consequently the need for an intermediate transient state of plastic deformation, a possibility which has not been carefully considered before for this particular material.

Alongside the conduction of experimental campaigns such as those described so far in this section, there has been a growing interest among the high pressure physics research community, motivated on one hand by the dramatic advances in computational processing power achieved in recent times [82] and on the other by the high costs and complexity of laser-based experiments, in trying to model the mechanical properties of crystalline solids at the atomistic level under the effects of uniaxial (or more generally non-hydrostatic) compression from first principles, or "ab-initio", and in particular through the implementation of DFT computational codes relying on plane-waves and pseudopotentials. Both silicon [30, 31, 51, 63, 65, 88, 112, 146, 147, 148] and germanium [50] have not been excluded from the developments of this relatively young but burgeoning branch of theoretical research, in connection in particular with the properties of the *cd* to β-Sn phase transition. Interest in non-hydrostatic loading conditions in fact originated as an extension to the simpler case of hydrostatic compression which was dealt with in all earlier ab-initio computational investigations (see for example Ref. [175] for a review of these early computational efforts). This extension was for the most part motivated by an attempt to model more realistically the environment found inside DACs, where inhomogeneities in the pressure-transmitting medium often lead to compressive geometries at the position of the sample which

are not perfectly isotropic.

Regardless of the peculiarities of each individual computational simulation among this accumulated body of knowledge, a general consensus has emerged that the *cd* to β-Sn phase transition in silicon and germanium exhibits a significant lowering of the transition pressure, together with the enthalpy barrier, as a function of increasing non-hydrostatic pressure conditions, which include the case of uniaxial straining encountered in the initial stage of shock-compression. The physical origin of this decreasing trend was already offered by Durandurdu [50, 51] in terms of the applied non-hydrostatic stress breaking the symmetry of the originally cubic lattice of silicon to a general orthorhombic configuration since the very start of the loading process, before the phase transition to β-Sn has even begun to occur. A direct connection between this lowering of the transition pressure and the response of silicon to shock-compression however has never been established. This theoretical prediction raises a new possibility whereby, under the conditions of strong uniaxial dynamic compression along the shock propagation direction characteristic of shock-wave loading, the transition pressure might in fact be lowered to levels previously associated with the HEL. It follows that what has so far been believed to consist in the onset of conventional shock-induced plastic flow might in fact correspond to the *cd* to β-Sn phase transition itself, the same new hypothesis supported by the experimental evidence as explained previously. Relief of shear stress in single crystals by a direct transition from the initial state of uniaxial elastic compression to a new stable high-pressure structural phase, without consequently the occurrence of an intermediate transient state of defect-mediated plastic deformation, is not after all unheard of in shock-compression science, having already been ascertained for the alternative

case of single-crystal iron shocked along $\langle 100 \rangle$ which, according to predictions made with MD simulations, also exhibits a lack of transient plastic flow when it undergoes its own shock-induced phase transition from the equilibrium α phase to the high-pressure ϵ phase [118]. The remainder of this chapter is dedicated to establishing the likelihood of this new hypothesis.

In particular, the research presented in this report closely mirrors the initial work performed by Strauch and Gaál-Nagy [65] in a previous ab-initio DFT investigation, the first to analyse the influence of non-hydrostatic pressure conditions specifically on the enthalpy barrier of the phase transition. The reader is therefore referred to their paper for a direct comparison of the results presented throughout the remainder of this chapter. We began our endeavour by first reproducing all of their results implementing our own versions of the computational codes involved, and we subsequently expanded upon them to gain better understanding of the mechanical response properties of single-crystal Si and Ge under shock-wave compression, in which strong non-hydrostatic conditions persist throughout the entire duration of the phenomenon. As will be explained in more detail in the next chapter however, we encountered fundamental problems when applying their definition of enthalpy to our analysis in that we observed the results to be path-dependent, in contradiction with the fundamental definition of enthalpy as a path-independent function of state. In the next chapter, we will propose a correction to these results relying on a new tentative method based on the concept of Availability in thermodynamics.

3.3 The cubic diamond to β-tin phase transition

3.3.1 Crystallographic properties of the two phases

The cubic-diamond (*cd*) crystal structure in which both silicon and germanium crystallise under ambient pressures and up to their melting temperatures is characterised by an underlying face-centred cubic (fcc) Bravais lattice with experimental lattice constant a of about 5.431 Å for Si and about 5.658 Å for Ge at room temperature [217]. Each lattice point in the unit cell is associated with a two-atoms basis located at the origin $(0, 0, 0)$ and at atomic position $a(1/4, 1/4, 1/4)$ relative to a reference system centred on the lattice point itself. This implies that the conventional unit cell of the *cd* structure contains a total of eight atoms. The overall symmetry of the resulting crystal structure corresponds to that of Space group No. 227 (O_h^7, $Fd\bar{3}m$).

The β-Sn phase on the other hand lies in a compressed body-centred tetragonal (bct) Bravais lattice. In the customarily-used unit cell of this lattice system, which is different from the conventional eight-atom cubic-diamond-like unit cell, the minor lattice constant c lies perpendicular to the square base of sides the major lattice parameter a. For Si, c and a have experimental lengths of approximately 2.572 Å and 4.665 Å respectively at 103 kbar pressure and at room temperature [162]. The corresponding crystal structure is obtained by adding the two-atom basis at the origin $(0, 0, 0)$ and at atomic position $(0, 0.5a, 0.25c)$ relative to each lattice point as shown in Fig. 3.3, which inserts a total of four atoms in the unit cell and collocates the overall crystal structure to the lower-symmetry

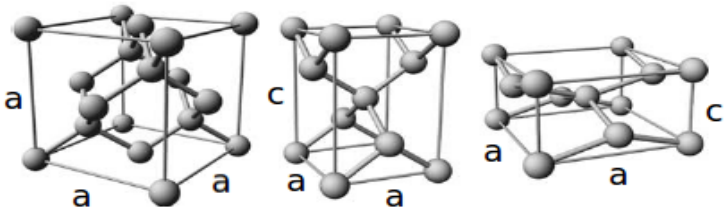


Figure 3.3: From left to right: the conventional unit cells of the equilibrium *cd* crystal structure of Si and Ge, of the same *cd* structure represented in a bct lattice with c/a ratio of precisely $\sqrt{2}$, and finally of the compressed bct crystal structure of the β-Sn phase, where instead c/a is a degree of freedom. The distinction between the a and c lattice parameters is shown in each case. (Figure reproduced with permission from Ref. [61].)

space group No. 141 ($D_{4h}^{19}, I4_1/amd$). As explained in Fig. 3.3, the whole crystal structure of the *cd* phase in its conventional eight-atom unit cell portrayal can be mapped, with no change in the absolute atomic positions, into a four-atom bct unit cell enclosed between two such *cd* unit cells and rotated relative to them by 45° about its c axis, which (contrary to the β-Sn bct unit cell) now represents the major lattice constant and is of same length as the a parameter of the original *cd* structure. The base lattice parameters a in the four-atom unit cell are instead smaller by a factor of $\sqrt{2}$ compared to those in the eight-atom unit cell. In order for this new bct geometrical representation to reproduce exactly the crystal structure of the original *cd* unit cell, its lattice parameter ratio c/a is constrained to remain fixed at precisely $\sqrt{2}$ by symmetry arguments. As explained later in this section, this transformation has important practical implications for our DFT calculation. From the order of the two point groups involved in the transition, one can finally infer the order of the phase transition [63] connecting the β-Sn phase to the equilibrium *cd* structure, which turns out to be of first order.

3.3.2 Thermodynamics of first-order pressure-induced phase transitions

In addition to the transition pressure p^t, a second quantity of interest in connection with the investigation of the phase transition from ab-initio theoretical arguments is the Gibbs free energy G, the thermodynamic potential whose minimisation determines phase stability in high-pressure systems under conditions of fixed pressure and temperature as will be explained in more detail in the next chapter [4] -

$$G = E + pV - TS \tag{3.1}$$

where E is the total internal energy, p the pressure, T the temperature, S the entropy, and V the volume. In the context of the present investigation, T was consistently taken to be 0K so that all zero-point motion thermal effects could be neglected, even though a slight dependence of the phase transition on the temperature, in the form of a decrease of the transition pressure with increasing T, has been reported both in experiments [234] and ab-initio simulations [62]. This approximation can be justified on the basis that the *cd* to β-Sn transition is both silicon and germanium is quite energetic in terms of the relatively large size of its enthalpy barrier, as will be demonstrated later. With $T = 0$, the phase stability criterion on G reduces to the minimisation of another thermodynamic potential, the enthalpy H -

$$H = E + pV \tag{3.2}$$

Consequently, the transition pressure p^t can be determined from the intersection of the enthalpy as a function of pressure curves corresponding to the two phases

$H^{cd}(p)$ and $H^{\beta-tin}(p)$, such that $H^{cd}(p^t) = H^{\beta-tin}(p^t)$. Isothermal first-order phase transitions are also accompanied by a collapse ΔV in the volume of the unit cell and the overcoming of a discontinuity, in the form of a barrier, in the enthalpy of height ΔH located between the two phases.

3.3.3 Mechanics of non-hydrostatic lattice deformations

With the ultimate aim of extracting the two quantities p^t and ΔH across the phase transition first for hydrostatic, and subsequently for non-hydrostatic pressuring conditions relevant for the realistic portrayal of shock-loading in solids, a numerical multiphase Equation of State (EoS) for Si, in the form of a continuous, multi-valued function $V(p)$ connecting the volume V to the pressure p, was calculated by performing total ground state energy calculations on a single primitive unit cell of Si an Ge in turn with its corresponding two-atom basis, representative of a real single-crystal sample of each material, for a variety of compressed lattice configurations encompassing the deformation path between the *cd* and the β-Sn phases. In order to minimise the energy offset between the structures of the two phases, which may have arisen from using different cells, the *cd* phase was described within the same bct unit cell as the β-Sn phase using the geometrical construction explained previously. The structures of the *cd* and β-Sn phases within this bct unit cell will henceforth be referred to as CD and BCT respectively. This bct unit cell was successively deformed away from its *cd* equilibrium state, and for each configuration the resulting components of the stress tensor describing its internal response to the applied distortion were extracted together with the ground state energy. The stress tensor σ acting on

a general lattice geometry can in general be written as the following symmetric matrix [166, 209] -

$$\begin{aligned}\sigma &= \begin{pmatrix} \sigma_{11} & \sigma_{12} & \sigma_{13} \\ \sigma_{21} & \sigma_{22} & \sigma_{23} \\ \sigma_{31} & \sigma_{32} & \sigma_{33} \end{pmatrix} \xrightarrow{ORTH.} \begin{pmatrix} \sigma_{11} & 0 & 0 \\ 0 & \sigma_{22} & 0 \\ 0 & 0 & \sigma_{33} \end{pmatrix} \\ &= \begin{pmatrix} -p_x & 0 & 0 \\ 0 & -p_y & 0 \\ 0 & 0 & -p_z \end{pmatrix}\end{aligned} \tag{3.3}$$

where the above equation also shows how the overall matrix can be diagonalised relative to the principal axes in orthogonal crystal structures such as the bct unit cell considered here, and in the last equality how the components of the stress tensor are related to those of the pressure.

It can also be deduced that, for the bct unit cell under consideration, $p_x = p_y$ for all types of pressure-induced distortions. This component notation for the pressure also allows the condition of hydrostaticity to be defined as $p_x = p_y = p_z = p$, where p is the total external pressure, showing how hydrostatic conditions imply a configuration of local equilibrium for the structure whereby the sum of internal and external forces caused by the pressure is zero. The more general non-hydrostatic conditions on the other hand occur whenever $p_x = p_y \neq p_z$. For both classes of conditions, the total average pressure p_o can in general be expressed in terms of its components as -

$$p_0 = \frac{1}{3}\left(p_x + p_y + p_z\right) = -\frac{1}{3}\mathrm{tr}\sigma \tag{3.4}$$

which reduces again to p for hydrostatic conditions.

The application of non-hydrostatic stress on a solid significantly complicates its thermodynamical treatment. The scope of Eq. (3.2) is in fact entirely restricted to the calculation of the enthalpy when the pressure p exerted on the solid is applied hydrostatically. As soon as $p_x = p_y \neq p_z$, then it becomes necessary to account the full anisotropy of the strain tensor ε, in addition to that of the stress tensor σ considered previously. Similarly to σ, for orthogonal structures such as the bct unit cell under investigation ε reduces to the following diagonal form [166, 209] -

$$\varepsilon = \begin{pmatrix} \varepsilon_{11} & 0 & 0 \\ 0 & \varepsilon_{22} & 0 \\ 0 & 0 & \varepsilon_{33} \end{pmatrix} = \begin{pmatrix} \varepsilon_x & 0 & 0 \\ 0 & \varepsilon_y & 0 \\ 0 & 0 & \varepsilon_z \end{pmatrix} \tag{3.5}$$

where ε_x, ε_y and ε_z are the components directed along each of the Cartesian crystal axes. An infinitesimal normal strain component $d\varepsilon_{jj}$ is defined by the change in length of the lattice parameter x_j in the $j = x, y$ or z direction -

$$d\varepsilon_j = \frac{dx_j}{x_j} \tag{3.6}$$

Gaál-Nagy *et al.* state [65] that the inclusion of strain effects allows the enthalpy of the solid at an infinitesimal non-hydrostatic deformation away from an original equilibrium configuration of volume V_o (the *cd* phase) to be expressed in terms of a combined stress-strain term [144] -

$$H = E - V_0 \sum_{j=x,y,z} \sigma_j \varepsilon_j + pV_o = E + V_0 \sum_{j=x,y,z} p_j \varepsilon_j + pV_o \tag{3.7}$$

Being valid only across small deformations, where the linear version of the theory of elasticity holds, they say Eq. (3.7) can be used in conjunction with the linearised small-strain, or engineering, approximation for the components of the strain tensor -

$$\varepsilon_{jj} = \frac{x_j^{'} - x_j^0}{x_j^0} \tag{3.8}$$

where x_j^0 is the initial (equilibrium) length of the lattice parameter in the $j = x, y$ or z direction, and $x_j^{'}$ its current strained length. The total enthalpy at a finite deformation away from the initial equilibrium configuration of the solid can thus be found via Eq. (3.7) by recursively re-defining the equilibrium position across small deformational steps. This yields the iterative scheme described by Eq. (3.9), which can then be integrated numerically on the energy surface [65] -

$$\begin{aligned} H^i = H^{i-1} + \left(E^i - E^{i-1}\right) + V^{i-1} \sum_{j=x,y,z} \frac{x_j^i - x_j^{i-1}}{x_j^{i-1}} p_j^i \\ + V^{i-1}\left(p_0^i - p_0^{i-1}\right) \end{aligned} \tag{3.9}$$

where p_0 is the average pressure for non-hydrostatic conditions defined by Eq. (3.4), and the i index labels the step number. Eq. (3.9) follows naturally from the definition of finite enthalpy change -

$$\Delta H = \Delta E + \Delta\left(pV\right) = \Delta E + \left(pV - p_o V_o\right) = \Delta E + p\Delta V + V_o \Delta p \tag{3.10}$$

From Eq. (3.9), an integrated value for the enthalpy can therefore be obtained at any non-hydrostatic point on the energy surface upon selection of a suitable integration path. It can also be shown that from the numerical integration approach of Eq. (3.9) the normal expression $H = E + pV$ is recovered when conditions

are again set to be hydrostatic. The physical origin of Eq. (3.7) conceived by Gaál-Nagy *et al.* [65] and the issues associated with it will the object of detailed consideration in the next chapter.

3.4 Density Functional Theory calculation

The plane-wave pseudopotential computational formulation of DFT, employed to perform the total ground state energy and total pressure calculations, was implemented with the Vienna ab-initio simulation package (VASP) [141]. The Generalized Gradient Approximation (GGA) for the exchange-correlation energy functional was given preference in this study upon recommendation by Moll *et al.* [173], and by Del Corso *et al.* [38]. As explained in these papers, and as experienced first-hand in various ab-initio researches [61, 88, 179], the tendency of the alternative Local Density Approximation (LDA) to overbind the cohesive energy in solids leads in fact to a significant underestimation of the transition pressure relative to experimental observation. A Vanderbilt-class ultrasoft pseudopotential [230], as supplied by Kresse and Hafner [142], was chosen to model the interaction of the four valence electrons in the atoms of Si and Ge with their respective ion cores in order to adhere as closely as possible to the approach adopted in Ref. [65]. This ultra-soft pseudopotential was parametrised and generated according to the GGA exchange-correlation energy functional by Perdew *et al.* [189]. Finally, metallic conditions were imposed for all geometrical configurations of the unit cell encountered throughout the course of the simulation, including on the *cd* phase which in reality is semiconducting, since it is not possible to predict a priori whether a given configuration at any point in the distortion path between

the two phases yields a metallic or semiconducting phase. Metallic behaviour was accounted for by inclusion in our calculation of the electronic smearing scheme by Methfessel and Paxton [164] for accelerating the convergence of integrations of quantities in the Brillouin zone across the Fermi energy.

It is common practice to commence all DFT calculations by first performing a series of preliminary convergence studies of the total ground state energy in the surroundings of the energy wells associated with the phase equilibria, in order to ensure that the appropriate accuracy is reached in the ultimate application of the calculation. The convergence parameters under investigation are, in turn, the kinetic energy cutoff in the plane-wave expansion of the single-electron Kohn-Sham orbitals *ecut* and the total size ($kgrid \times kgrid \times kgrid$) of the grid of special **k**-points needed for integration of quantities across the symmetry-Irreducible wedge of the Brillouin Zone (IBZ) of the unit cell, as explained in section 2.4.2. The latter convergence parameter was investigated together with variations in the artificial thermal smearing parameter in the electronic distribution *tsmear*, as it is customary in convergence studies. The particular method for the selection of special **k**-points implemented in VASP is that developed by Monkhorst and Pack [174]. In all cases, the accuracy sought in the energy was of the order of 1 meV. The final values of the convergence parameters that yielded the desired accuracy in the energy in each of Si and Ge, and that were as a result employed in the final simulation, are summarised in table 3.1. The error in the calculated pressure according to the Pulay Stress [197] was also monitored and was observed to be negligible in all cases.

Following this preliminary convergence study, the total ground state energy calculation as a function of unit cell compression was performed for different bct

Table 3.1: Convergence parameters used the final computation of the total ground state energy of Si and Ge that were deemed sufficient to achieve an accuracy of order meV. The total number of **k**-points in the IBZ corresponding to the selected dimensions of the Monkhorst-Pack mesh is also indicated.

	ecut (eV)	kgrid	Points in IBZ	tsmear (eV)
Si	270	18	864	0.2
Ge	410	24	1962	0.2

unit cell configurations encompassing the deformation path between the *cd* and β-Sn phases. The final outcome was the generation of complete energy $E(c/a, V)$ and total average pressure $p_0(c/a, V)$ surfaces, where the ratio of conventional unit cell parameters c/a and the primitive unit cell volume $V = (1/2)a^2c$ are used to uniquely label the geometry of the bct unit cell at each point across the surface. The energy surfaces for Si and Ge within the GGA are shown in Fig. 3.4 in the form of color contour plots. The same energy contours are shown overlaid with the pressure surface in Fig. 3.5. Except for the points located along the trajectory of the hydrostatic line shown in this latter figure, conditions are everywhere non-hydrostatic. The two local energy minima corresponding to the *cd* and β-Sn phase equilibria are located at the intersection point between the hydrostatic line and the contour of zero p_0, such that at these two positions $p_x = p_y = p_z = p_0 = 0$ in agreement with the definition of phase equilibrium. Clearly visible is also the energy saddle that separates them and gives rise to the enthalpy barrier ΔH of the phase transition. Furthermore, inspection of the plots in Fig. 3.5 reveals that the ideal *cd* structure has been identified fairly accurately, at least from the point of view of its lattice parameter ratio c/a, which is predicted by theory to be exactly $\sqrt{2}$ as mentioned previously.

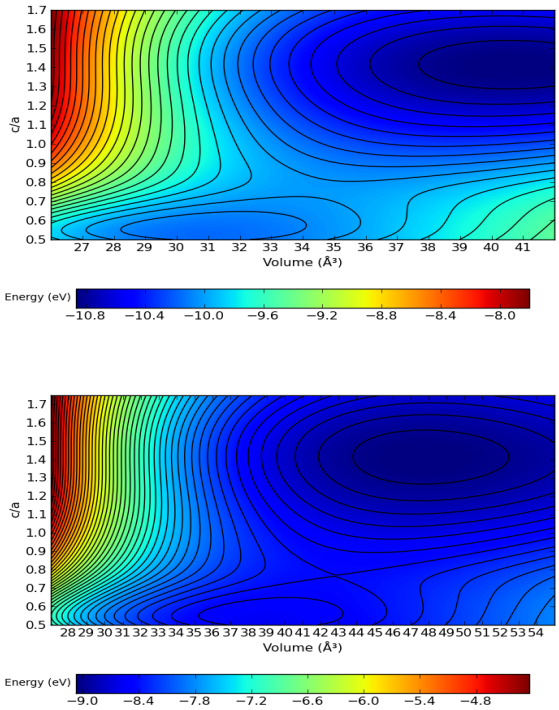


Figure 3.4: Colour-coded contour plots of the total ground state energy $E(c/a, V)$ for Si (top) and Ge (bottom). The scale of the color maps is shown below each figure. Shown in each case is the regions of minimum energy enclosing the positions of the two phase equilibria at the top-right (cd) and bottom-left (β-Sn) corners (the precise positions of the phase equilibria are more easily identifiable in Fig. 3.5). The color mapping also allows for a clear visualisation of the saddle in the energy separating the two phases. The spacing between the contours is everywhere 100 meV.

3.5 Numerical Analysis

3.5.1 Transition pressure and enthalpy barrier at hydrostatic conditions

In order to derive the multi-phase EoS $V(p)$ for the $cd \rightarrow \beta$-Sn phase transition, and to extract the values of the transition pressure p^t and enthalpy barrier ΔH in

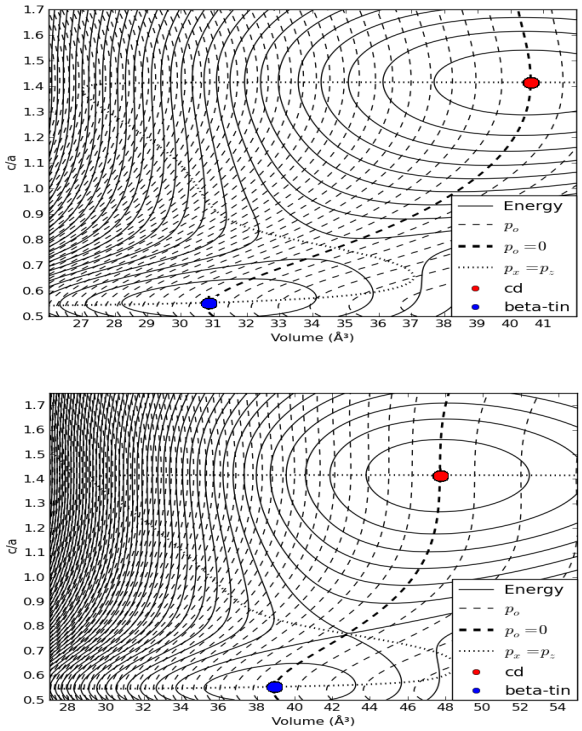


Figure 3.5: Combined pressure-energy contour plot for Si (top) and Ge (bottom), highlighting in each case the precise location of the two phase equilibria (shown as a red dot for *cd* and blue dot for β-Sn). These are given by the intersection of the hydrostatic line (dotted line), tracing all points along which the condition $p_x = p_y = p_z$ applies, with the $p_0 = 0$ contour (bold dashed line). The position of the energy saddle is located at the center of the plot at the third point of intersection between these two contours. The energy and pressure contours at all points are shown as solid and thin dashed lines respectively. The spacing between the contours is 100 meV for the energy and 20 kbar for the pressure.

Si and Ge under hydrostatic conditions, we followed the same procedure as in Ref. [65], whose reliability had already been tested against an alternative approach developed by the same authors [63]. Firstly, the values of the total energy E, external pressure $p = p_0$ and primitive unit-cell volume V at the positions traced by the hydrostatic line $p_x = p_z$ in Fig. 3.5 were extracted, and secondly the corresponding enthalpy values were calculated using Eq. (3.2). The results are

portrayed in Figures 3.6 and 3.7, which show respectively the variation of the enthalpy as a function of hydrostatic pressure $H(p)$, and the same variation for the enthalpy barrier $\Delta H(p)$, with each plot separated into the three regions of the hydrostatic line overarching the *cd* phase, the intermediate energy saddle and the β-Sn phase respectively, as labelled in the legends. In Fig. 3.6, the values of $H(p)$ were plotted as reduced enthalpies after subtraction of a linear baseline $f(p) = -10.17p + 0.02$ in order to better discern the three branches of the plot from one another, giving a quantity which we shall refer to as reduced enthalpy. From this curve, the $\Delta H(p)$ plot of Fig. 3.7 was then calculated as the differences between the enthalpy curve of the intermediate saddle and those for each of the *cd* and β-Sn phase, which represent the enthalpy barrier encountered in moving across the energy surface in the *cd* $\rightarrow$ β-Sn and β-Sn $\rightarrow$ *cd* directions respectively

-

$$\Delta H^{CD}(p) = H^{SADDLE}(p) - H^{CD}(p) \tag{3.11}$$

$$\Delta H^{BCT}(p) = H^{SADDLE}(p) - H^{BCT}(p) \tag{3.12}$$

Inspection of this last figure reveals that at zero applied pressure there is still an enthalpy barrier left for the β-Sn $\rightarrow$ *cd* transition. This is a direct consequence of the irreversibility of the *cd* $\rightarrow$ β-Sn phase transition, whereby no spontaneous transition can occur from β-Sn back to *cd*.

The transition pressure p^t could be identified in Fig. 3.6 as the pressure at which the CD and BCT branches of the enthalpy plot $H^{cd}(p)$ and $H^{\beta-tin}(p)$ intersect, such that $H^{cd}(p^t) = H^{\beta-tin}(p^t)$, and its numerical value is listed in Table 3.2 together with that of the volume change ΔV and of the enthalpy barrier ΔH across the phase transition. The latter quantity is given by the value of the

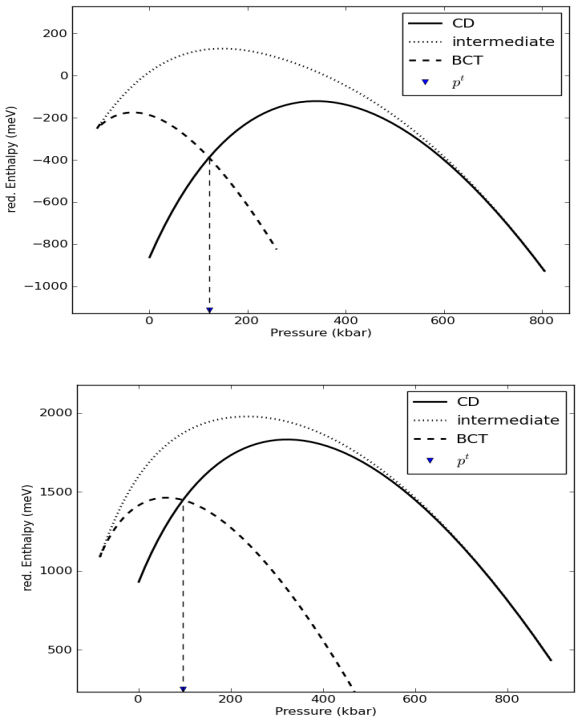


Figure 3.6: Reduced enthalpy of the bct primitive unit cell as a function of hydrostatic pressure for Si (top) and Ge (bottom). The position of the transition pressure p^t, given by the intersection of the CD with the BCT lines, is highlighted.

$\Delta H(p)$ plot of Fig. 3.7 at p^t, which again coincides with the crossing between the CD and BCT branches of the plot.

From the results summarised in Table 3.2, we can conclude that our results for the phase transition parameters under hydrostatic conditions are in perfect agreement with those reported previously by Gaál-Nagy and co-workers in Ref. [65], and also in their other paper [61] in which very similar values were obtained through a slightly different approach, thus confirming the accuracy and fidelity of our DFT simulation and of the resulting energy surface. Experimental observation of this phase transition under static loading techniques such as DACs [13, 43, 79, 101, 120, 163, 198, 234, 243] also support these findings, although in

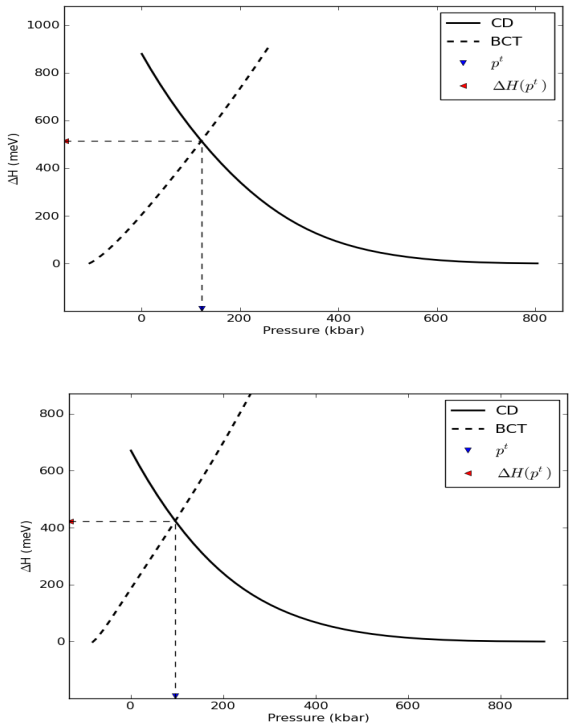


Figure 3.7: The enthalpy barrier ΔH, calculated as described in the text, as a function of hydrostatic pressure for Si (top) and Ge (bottom). The positions of the transition pressure p^t, equivalent to that already found in Fig. 3.6, and of the corresponding enthalpy barrier $\Delta H(p^t)$ are indicated.

this case the spread in the final results reported in the literature tends to be quite large. Measurements of the transition pressure in Si for instance have yielded results ranging from the 103 kbar measured by McMahon and Nelmes [162] up to the 133 kbar reported by Werner *et al.* [243]. This appears to suggest that at least some of these nominally hydrostatic experiments were affected by the presence of slight anisotropies in the applied load, due for example to non-homogeneities in the pressure-transmitting medium enveloping the DAC, which as mentioned previously has the effect of altering the transition pressure.

Table 3.2: Transition pressure p^t, volume change ΔV and enthalpy barrier ΔH for the *cd* to β-Sn phase transition in Si and Ge.

	Si	Ge
p^t (kbar)	121.71± 0.01	96.00 ± 0.01
ΔV (Å^3)	8.32 ± 0.01	7.56 ± 0.01
ΔH (meV)	514.37 ± 0.01	423.42 ± 0.01

3.5.2 Extension to non-hydrostatic conditions

In this section we use the method of Gaál-Nagy *et al.* [65] (Eq. (3.7)) to determine the transition pressures and enthalpy barriers for non-hydrostatic pressure conditions for which $p_x = p_y \neq p_z$. The shortcomings of this approach will be discussed in Section 3.6. In particular, we are interested in extracting the phase transition parameters as a function of increasing shear stress $p_z - p_x$ away from the hydrostatic case $p_z - p_x = 0$. The procedure of Ref. [65] for doing so is identical to that described in the previous section for hydrostatic compression except that, as explained in Section 3.3.3, this time care needs to be taken to apply the more advanced formulation of the enthalpy in terms of the full anisotropy of the stress and strain tensors, as represented by Eq. (3.7). As was already pointed out in Ref. [65], one cannot in fact re-apply the same simple expression $H = E + p_0 V$ when the values of E, p_0 and V are obtained under non-hydrostatic conditions, as experiment-contradicting results such as an increase of the transition pressure for $p_z > p_x$ would otherwise be obtained. From the numerical realization of Eq. (3.7), Eq. (3.9), an integrated value for the enthalpy can then be obtained at any point along contours of constant shear stress $p_z - p_x = d \neq 0$ (where d is a constant) upon selection of a suitable integration path. This path was chosen to lie along the constant shear stress contour itself for convenience reasons, starting

from the zero-strain position of the equilibrium *cd* phase and ending at the point on the contour whose enthalpy is being sought. Fig. 3.8 shows some examples of contour lines of constant shear stress for the case of Si. We shall henceforth consider only positive values of the shear stress, since we exclude stretching the crystal along the z axis. Inspection of Fig. 3.8 reveals that for shear stresses greater than about 22 kbar, the contours become broken in the lower-right corner within the range covered by the plot, and in fact it can be shown by extending the simulation to higher volumes that they never merge again. Since the iterative scheme of Eq. (3.9) remains valid only when the integration steps are executed across small strains, it becomes necessary to circumvent this broken section by continuing the integration along the straight line connecting its endpoints. An example of a full integration path along the +40 kbar shear stress contour, showing the bypass across the broken section, is depicted in green in Fig. 3.8.

By repeating the evaluation of the enthalpy barrier at the phase transition for a range of values of the shear stress d, the plot in Fig. 3.9, showing the evolution of the enthalpy barrier $\Delta H(p_0^t)$ as a function of d, was obtained for both Si and Ge. The same evolution for the transition pressure p_0^t is shown in Fig. 3.10, together with that of its constituent components in the x and z directions, $p_x^t = p_y^t$ and p_z^t, which are given by $p_x^t = p_o^t - d/3$ and $p_z^t = p_o^t + (2/3)d$ respectively. As already observed in Ref. [65], from the decrease in the transition pressure for $p_z^t > p_x^t$ visible in this latter plot one can deduce that the crystal is more stable and resistant against compression along the x and y axes when the external pressure is applied non-hydrostatically. This behaviour is also reflected in the sharp decrease in the enthalpy barrier of the phase transition for large values of $d = p_z - p_x$, as shown in Fig. 3.9. Both set of curves are in general in

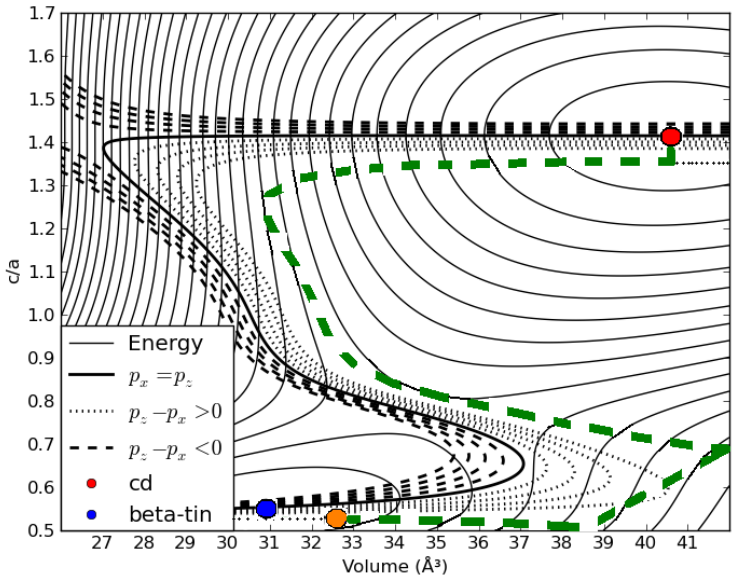


Figure 3.8: The same $E(c/a, V)$ energy surface for Si as that of Fig. 3.5, where this time however the emphasis is put on the non-hydrostatic contour lines of constant shear stress $p_z - p_x = d$. Four shear stress contours are shown on each side of the hydrostatic line $p_z - p_x = 0$ (bold solid line), corresponding to either positive values of $d = +5, +10, +15$ and $+20$ kbar (dotted lines) or to negative values $-5, -10, -15$ and -20 kbar (dashed lines). Highlighted as the thick dashed green contour is an example of integration path starting at the equilibrium position of the *cd* phase for calculating the enthalpy at the arbitrary point labelled in orange on the +40 kbar shear stress contour. As explained in the text, a detour along a straight line needs to be taken where the contour is discontinuous in the lower-right region of the plot.

perfect agreement with those reported in Ref. [65], and in both cases the results for hydrostatic conditions $p_z - p_x = 0$ derived in section 3.5.1 are reproduced correctly, thus indicating that all the analysis of the DFT data has so far been carried out correctly. In particular, it is worth emphasising that both p_0^t and $\Delta H(p_0^t)$ exhibit the expected decline with increasing shear stress already observed in all previous ab-initio simulations.

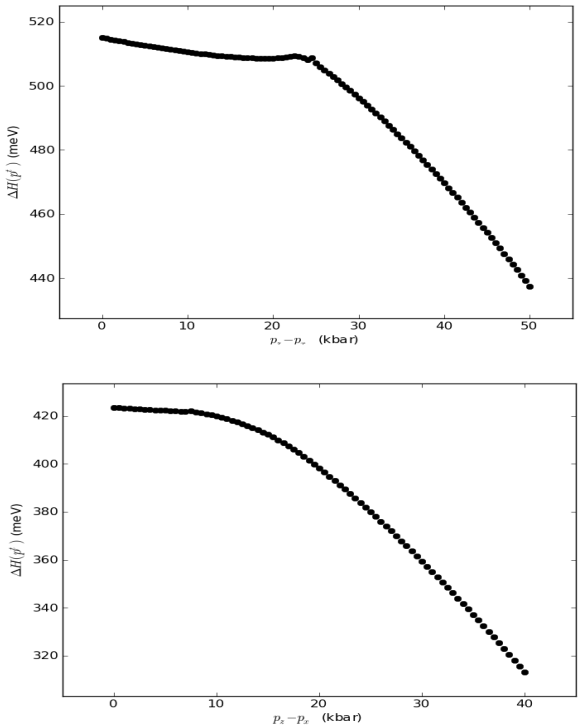


Figure 3.9: Evolution of the enthalpy barrier for the $cd \rightarrow \beta$-Sn phase transition as a function of shear stress $d = p_z - p_x$ for Si (top) and Ge (bottom).

3.5.3 Applications to shock-wave loading

Finally, the above analysis of the properties of the cd to β-Sn phase transition under non-hydrostatic conditions was applied to our ultimate intent which, as explained earlier in Section 3.2, consists in predicting its onset under the conditions of shock-wave loading. As described there, immediately after the passage of the shock wavefront a single-crystal sample responds in a first instance by elastically straining uniaxially along the shock propagation direction. Without loss of generality, this direction can be taken to lie along the c axis of our simulation bct unit cell representative of axial pressure loading along the $\langle 001 \rangle$ direction. For this case, the initial elastic response of the system can be represented by the

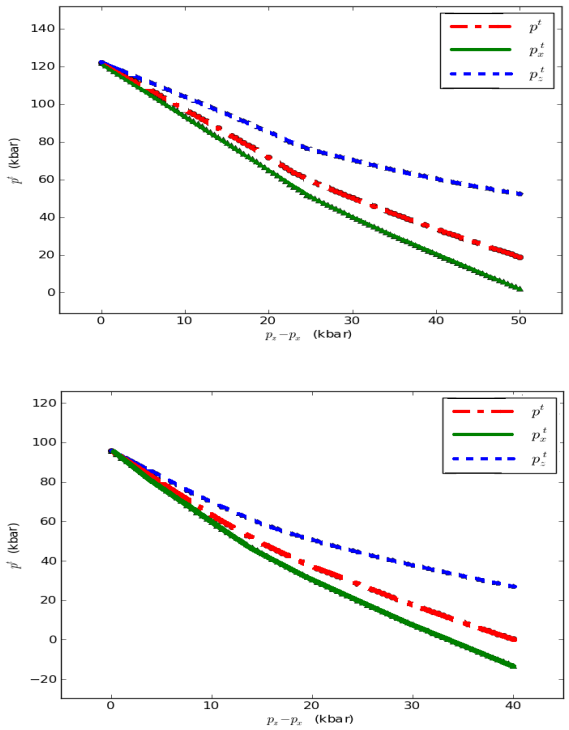


Figure 3.10: Evolution of the transition pressure p_0^t and its components p_x^t and p_z^t as a function of shear stress $d = p_z - p_x$ for Si (top) and Ge (bottom).

line of uniaxial compression along the c axis, as portrayed in red in Fig. 3.11 for the case of Si. At all points along this line, $\varepsilon_x = \varepsilon_y = 0$, and consequently the a parameter of the bct unit cell remains constant at its equilibrium cd value a_{cd}.

The initial stage in the axial Hugoniot of the material, describing the material's elastic response to shock compression as predicted by the DFT calculation in the form of a pressure-volume diagram, can be obtained by extracting the z component of the average pressure $p_o^z(a = a_{cd})$ along the line of uniaxial compression (on which in general $p_o^x(a = a_{cd}) \neq 0$ and consequently $p_o^z(a = a_{cd}) \neq p_o(a = a_{cd})$, since uniaxial strain does not necessarily correspond to uniaxial stress). Fig. 3.12 shows the axial Hugoniot plotted together with the p_z^t curve calculated ear-

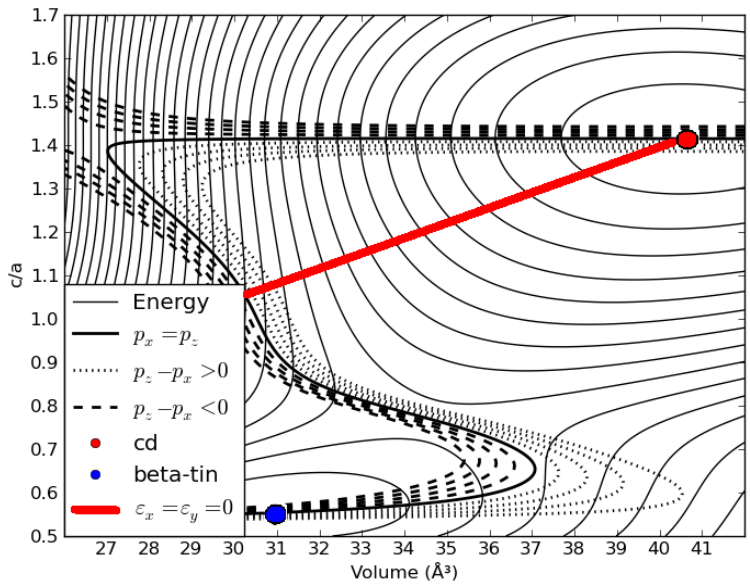


Figure 3.11: The same energy surface of Si as shown previously in Fig. 3.8, including depicted in red the line of uniaxial compression along c starting from the equilibrium position of the *cd* phase. At all points along this line, $\varepsilon_x = \varepsilon_y = 0$ and $a = a_{cd}$.

lier in Fig. 3.10, both as a function of increasing uniaxial shear stress $p_z - p_x$ and decreasing compressive volume ratio V/V_0 from the equilibrium volume of the *cd* phase V_0. This construction provides an effective mean to compare the internal response properties of the system under investigation, as embodied by $p_o^z(a = a_{cd})$, with the properties of the phase transition itself (p_z^t). It follows from this consideration that the point of intersection between the two lines coincides with the state at which the enthalpy barrier of the phase transition is finally overcome, and at which the shear-stress relieving mechanism underpinning the onset of the transformation to β-Sn is finally triggered, thus marking an end to the initial state of uniaxial elastic compression. This point therefore provides an estimate of the transition stress as encountered under uniaxial shock compression

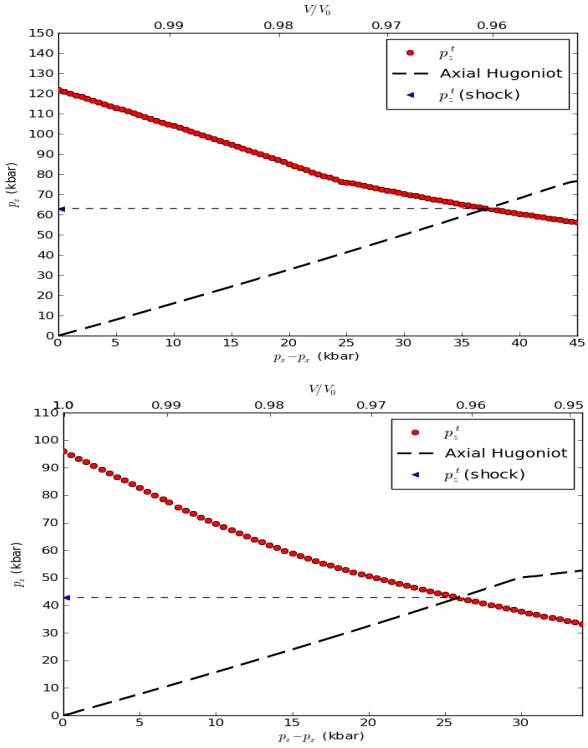


Figure 3.12: The axial Hugoniot $p_o^z(a = a_{cd})$ of single-crystal Si (top) and Ge (bottom), describing the material's response to uniaxial compression as induced by shock-loading, plotted against the axial component of the transition pressure p_z^t. The intersection between the two lines corresponds to the transition stress under the conditions of uniaxial shock compression $p_z^t(shock)$.

$p_z^t(shock)$.

Furthermore, we plotted the evolution of the Poisson ratio υ, defined as the ratio of the transverse strain to the axial strain, along the line of elastic uniaxial compression. This method allows to directly estimate the shear stress corresponding to the experimental results for the axial component of the transition pressure reported by Gust and Royce [80, 81]. Experiments do not in fact customarily report any of the transverse components. For small strains, for which we can take the Poisson ratio υ to be constant, we can relate the shear stress to the

stress acting in the axial direction as a result of the applied shock σ_z -

$$d = \sigma_z - \sigma_x = \sigma_z \frac{(1-2\upsilon)}{(1-\upsilon)} \tag{3.13}$$

To verify the validity of this approximation, we compare the results for the shear stress along the line of elastic uniaxial compression extracted directly from the energy surface on one hand, and calculated by assuming a constant value of $\upsilon = 0.27$ for both Si and Ge on the other, which roughly corresponds the unstrained value of the Poisson ratio for both of these materials [99]. The results of this comparison are shown in Fig. 3.13. It can be deduced that the agreement, despite deteriorating at higher compressions, remains relatively good.

By inverting Eq. (3.13), we can also directly infer the value of υ from the DFT calculations -

$$\upsilon = \frac{\sigma_z - d}{(2\sigma_z - d)} \tag{3.14}$$

The results corresponding to the above formula are shown in Fig. 3.14. The value of υ does therefore remain roughly constant for both materials at around 0.27, thus justifying our previous assumption. The results of Fig. 3.13, together with those of Fig. 3.14, justify employing Eq. (3.13) for calculating the shear stress corresponding to the results from Gust and Royce [80, 81] using a constant value of $\upsilon = 0.27$. The results for the axial component of the transition pressure of silicon (92 ± 10 kbar) therefore yield a corresponding shear stress of 58 ± 6 kbar, whereas for the case of germanium for which the transition pressure was reported at 58 ± 8 kbar the shear stress is 36.5 ± 5 kbar.

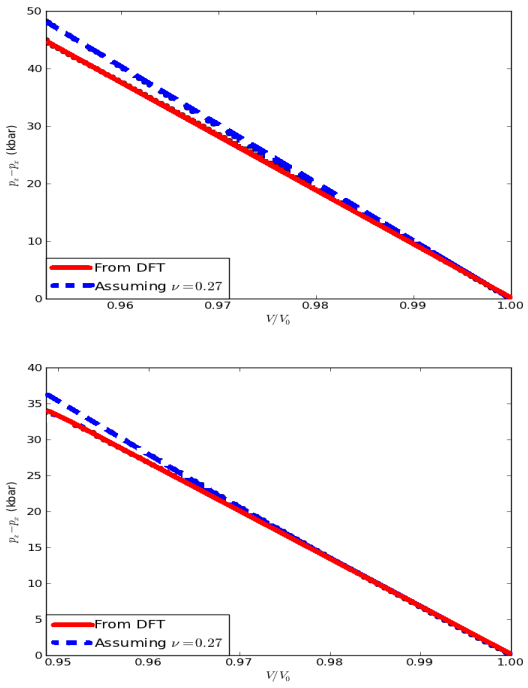


Figure 3.13: Shear stress along the line of uniaxial compression as extracted directly form the energy surface calculated by DFT, compared to the results of applying Eq. (3.13) assuming a constant value of $\upsilon = 0.27$, for Si (top) and Ge (bottom).

3.6 Discussion of the results

From the results portrayed in Figures 3.12, we can draw the conclusion that the phase transition to the β-Sn structure under the conditions of uniaxial elastic compression characteristic of shock-wave loading according to the method of Ref. [65] is predicted by our DFT simulation to occur at a pressure $p_z^t(shock)$ of about 63 ± 1 kbar for Si and around 43 ± 1 kbar for Ge, which corresponds to a shear stress of around 37 ± 1 kbar and 26 ± 1 kbar respectively. The two estimates for $p_z^t(shock)$ are to be compared with the measurements of the HEL of the two materials which, as described in Section 3.2, have been agreed upon by the

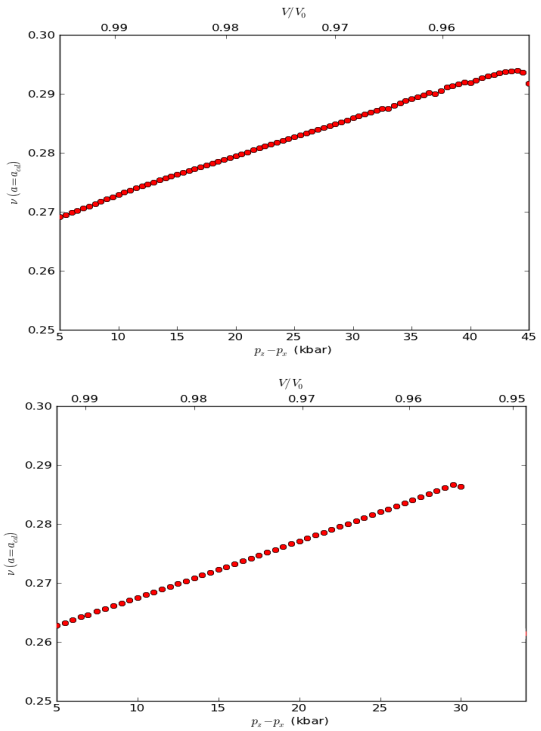


Figure 3.14: Evolution of the Poisson ratio υ as a function of uniaxial compression for Si (top) and Ge (bottom).

shock-wave research community to lie at around 90 and 58 kbar for Si and Ge respectively. Hence, we deduce that both results for $p_z^t(shock)$ calculated using this method are lower than the experimental values for the HEL, and for the case of Si the discrepancy is especially significant.

This discrepancy lead us to reconsider the validity of the approach of Ref. [65] for enthalpy determination under non-hydrostatic conditions. When the above calculations were performed their enthalpy extraction method was to our knowledge the only proposed approach for accessing information on the enthalpy barrier. However, a second distinct method for the extraction of the transition *pressure* under anisotropic stress was proposed by Cheng *et al.* [30, 31], and

then reproduced also by Hennig *et al.* [88]. The derivation of this alternative procedure follows directly from the second law of thermodynamics, which embodies the principle of increase of entropy. Under conditions of $p_x = p_y$ and at $T = 0$ K (which was the condition of their simulations), they derived the following expression for the enthalpy phase-stability condition -

$$\begin{aligned} &[(E_2 - E_1) + p_x (V_2 - V_1)] + \left[(p_z - p_x) \int_1^2 l_x l_y dl_z\right] \\ &= \Delta H + \bar{\Delta} W = \bar{\Delta} H \leq 0 \end{aligned} \tag{3.15}$$

in which E_1 and E_2 are the internal energies of phases 1 and 2, and l_x, l_y and l_z are the lattice constants of the crystal phases 1 and 2 under the pressure components p_x, p_y and p_z. According to this condition, the inequality holds when phase 2 is relatively more stable than phase 1, and the equality corresponds to the transition pressure. Note that there is a term $\bar{\Delta} W$ which is not present under hydrostatic conditions, and whose magnitude depends on the path of integration (whereas the term ΔH is path-independent). Cheng and co-workers did acknowledge the presence of this path-dependent term, but at the same time proposed that the most physical path employed by the system during the phase transition is also the shortest path involving simultaneously compressing the c axis and expanding the a axis of the crystal, and thus the errors incurred by this path-dependence are minimised. This shortest path of deformation can be expressed as -

$$\begin{aligned} l_x &= (1 - \alpha)\, a_x^{cd} + \alpha a_x^{\beta} - Sn \\ l_z &= (1 - \alpha)\, a_z^{cd} + \alpha a_z^{\beta} - Sn \end{aligned} \tag{3.16}$$

where $0 < \alpha < 1$ (such that $\alpha = 0$ corresponds to the cd phase and $\alpha = 1$ to

β-Sn) and a_i^j is the lattice parameter along the i-th direction for the conventional eight-atom unit cell of phase j. Substituting these two expressions for l_x and l_z into the integral of Eq. (3.15) and integrating with respect to α, we get the following expression for $\bar{\Delta}W$ -

$$\bar{\Delta}W = \frac{1}{3}\left(p_z - p_x\right)\left(a_z^{\beta} - a_z^{cd}\right)\left(\left(a_x^{\beta}\right)^2 + a_x^{\beta}a_x^{cd} + \left(a_x^{cd}\right)^2\right) \tag{3.17}$$

Hence Eq. (3.15) can be solved for the transition pressure, where it becomes an equality. The resulting expression for the component of the transition pressure p_x^t in terms of the shear stress $d = p_z - p_x$ is -

$$p_x^t = \frac{(E_1 - E_2)}{(V_2 - V_1)} - \frac{d}{(V_2 - V_1)}I \tag{3.18}$$

where -

$$I = \frac{1}{3}\left(a_z^{\beta} - a_z^{cd}\right)\left(\left(a_x^{\beta}\right)^2 + a_x^{\beta}a_x^{cd} + \left(a_x^{cd}\right)^2\right) \tag{3.19}$$

The results for the transition pressure are shown in Fig. 3.15. Whilst this alternative approach produced very similar results concerning the behaviour of the transition pressure as a function of shear stress, it does not however provide any information on the intermediate state comprising the energy saddle which is crucial for the evaluation of the enthalpy barrier.

Given that Cheng *et al.* [30, 31] identify a path-dependent $\bar{\Delta}W$ term, we re-evaluated the enthalpy formula of Gaál-Nagy *et al.* [65] (Eq. (3.7)). In doing so, we found that Eq. (3.7) also yields path-dependent results in a series of tests which will be presented in the next chapter. This appears to be in contradiction with the standard definition of enthalpy as a path-independent function of

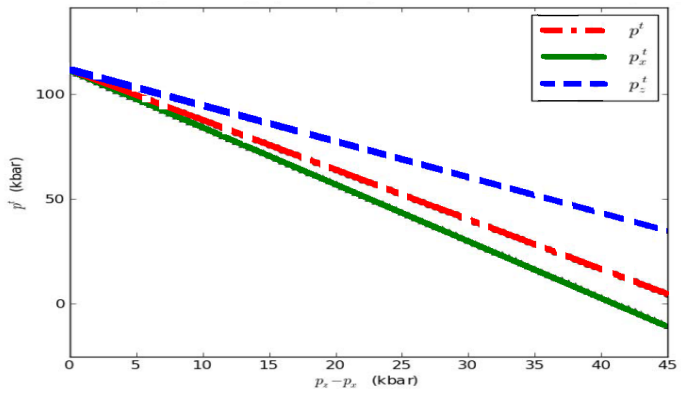


Figure 3.15: Evolution of the transition pressure in Si as a function of shear stress obtained with the method developed by Cheng *et al.*. The results presented here are to be compared with those of Fig. 3.10.

state. A more rigorous understanding of the mathematical formalism of thermodynamical potentials subject to finite and anisotropic stresses, within a general characterization of the thermodynamical properties of solids under the effects of dynamic shock-compression, is worth a separate investigation. In the next chapter, we offer an analysis of this problem and propose some alternative (tentative) solutions.

A second problem with the approach of Ref. [65] is that it relies on contours of constant shear stress as deformation paths, and consequently assumes that both the transition pressure and enthalpy barrier (even if calculated correctly) are unique functions of the shear stress. The assumption of the phase transition occurring at constant shear stress does not necessarily correspond to the dynamics encountered under real shock-compression. The boundary conditions encountered in real a real shock-wave environment will be the object of further discussion in chapter 5, where we make use of the alternative computa-

tional technique of classical Molecular Dynamics (MD) to model the dynamic and high strain-rate non-equilibrium conditions encountered in shock-waves and the induced mechanical effects more realistically.

3.7 Conclusions

In summary, the computational technique of DFT was employed to investigate from first principles the first-order pressure-induced polymorphic phase transition from the equilibrium cubic diamond crystal structure, in which both single-crystal silicon and germanium crystallise under atmospheric conditions, to their first stable high-pressure phase, which lies in the metallic β-Sn structure. Using the definition of enthalpy of Ref. [65], the simulation predicts a significant lowering of the transition pressure and enthalpy barrier under the effects of uniaxial compression. However we have identified several problems with the approach of Ref. [65]. Firstly, we have discovered a fundamental flaw with the formulation of enthalpy employed in the current thermodynamical analysis, in that the results of the corresponding numerical integration scheme have been observed to yield path-dependent results. Secondly, the boundary conditions encountered in real shock-wave environments do not necessarily correspond to the conditions of constant shear stress assumed in Ref. [65]. Both of these issues will be addressed further in the forthcoming chapters of this thesis, and in the next chapter in particular we consider the basic thermodynamics that pertain under non-hydrostatic conditions.

Chapter 4

The role of the Gibbs free energy in pressure-induced phase transitions under non-hydrostatic stress

4.1 Theory of first-order phase transitions

In this section we aim to highlight the importance of the concept of Gibbs free energy in the theory of first-order phase transitions [4, 18, 129]. Solids exist in many structures, and the change from one structure to the other is governed by thermodynamics and kinetics. Furthermore, phase stability is governed by external factors such as pressure and temperature and internal factors such as compositions and internal stresses due to defects (dislocations, point defects, interfaces). Let us start our analysis by considering a system whose chemical

composition is uniform but in which more that one phase is present, such as for example a liquid in contact with its own vapour. In this system, we require that both the pressure p and the temperature T be uniform throughout and constant, and therefore common to both phases. Furthermore, we will only assume the case of work done by hydrostatic pressure. Suppose that the masses present in each phase are m_1 and m_2 and that their specific Gibbs functions are g_1 and g_2, which in general are given by $g_i = e_i - Ts_i + pv_i$ for phase i (where lowercase letters denote the corresponding specific quantities for that phase). Then the total Gibbs free energy of the system is given by -

$$G = m_1 g_1 + m_2 g_2 \tag{4.1}$$

Since p and T are constant, the condition for equilibrium reduces to the condition of minimisation of G, as will be explained later in Section 4.4 -

$$dG = g_1 dm_1 + g_2 dm_2 = 0 \tag{4.2}$$

As we are considering a closed system in which mass is conserved this is subject to the constraint -

$$dm_1 + dm_2 = 0 \tag{4.3}$$

Hence the condition of equilibrium between phases reduces to -

$$g_1 = g_2 \tag{4.4}$$

This argument can be generalised to cases where more than two phases are present, with the result that for equilibrium the specific Gibbs functions must all be equal. It can be shown that this conditions holds whatever the external constraints, even though it was derived for the case of constant pressure and temperature.

The conditions for which two phases of the same substance coexist in equilibrium define the phase boundary on a phase diagram $p(V,T)$, along which their specific Gibbs functions are equal according to the condition (4.4). The gradient of this phase boundary on a p-T phase diagram is given by the well known Clausius-Clayperon equation -

$$\frac{dp}{dT} = \frac{\Delta S}{\Delta V} = \frac{L}{T\Delta V} \tag{4.5}$$

where ΔS and ΔV are the changes in entropy and volume across the phase transition respectively, and L is the latent heat absorbed. Usually, dp/dT is positive for all phase transitions across the phase diagram [1]. An example of such p-T phase diagrams encompassing the solid, vapour and liquid phases of a material is shown in Fig. 4.1.

It must be noticed that the Clausius-Clayperon equation applies to all changes of phase in which ΔS and ΔV across the transition are both discontinuous. Phase transitions that satisfy these two conditions are called *first-order* phase transitions. Examples of first-order transformations are the martensitic transformation (usually, a few percent volume increase), melting (usually a volume increase), and solidification (usually, volume decrease). It follows from these conditions

[1] A notable exception is the solid-liquid phase boundary in water, which has a negative gradient.

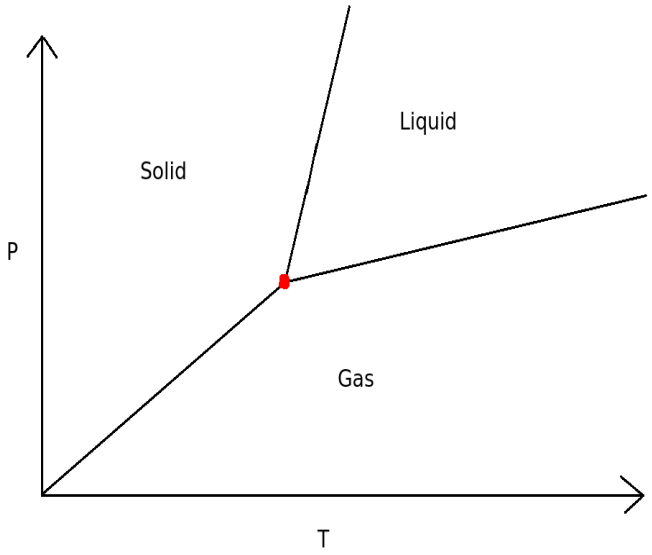


Figure 4.1: Typical appearance of a p-T phase diagram between the three phases of a generic material. The solid lines indicate the phase boundaries along which the various phases coexists in equilibrium, and along which their specific Gibbs functions are equal. The central point indicated in red where the three phase boundaries meet is called the Triple Point of the substance.

that the first derivative of the Gibbs function of a material with respect to its proper variables p and T is discontinuous across a first-order phase transition, and that the Gibbs function itself therefore exhibits a kink at the transition point as a result of the intersection between the two g surfaces [1]. This can be seen from

[1] In the case of second-order phase transitions on the other hand, the two surfaces $g_1(p,T)$ and $g_2(p,T)$ do not intersect, but rather are tangent to each other. The first derivative of G is therefore continuous across the transition pressure, and the second derivative is the one that becomes discontinuous

the fundamental definition of G -

$$\begin{aligned} G &= U - TS + pV \\ \rightarrow dG &= -SdT + V\,dp \\ &= \left(\frac{\partial G}{\partial T}\right)_p dT + \left(\frac{\partial G}{\partial p}\right)_T dp \end{aligned} \tag{4.6}$$

Hence the partial derivatives of G are defined as -

$$\left(\frac{\partial G}{\partial T}\right)_p = -S \qquad \left(\frac{\partial G}{\partial p}\right)_T = V \tag{4.7}$$

Thus, the values of the first derivative with respect to pressure at the transition pressure gives the change in volume accompanying the transformation, while that with respect to temperature gives the change in entropy. In general the order of a phase transition is defined as the order of the lowest differential of G which exhibits a discontinuity at the transition point. These considerations, together with the condition for equilibrium between phases which asserts that along the phase boundary where the two phases are in equilibrium we have $g_1 = g_2$, while away form it the phase with the lower g will be the stable one at constant p and T, allow us to sketch a complete Gibbs free energy surface for a material undergoing a first-order phase transition between two of its phases. This surface will in general be three-dimensional of the form $G(P, T)$. Plotted in the form of a section in the plane of constant T, it has the appearance of Fig. 4.2.

The discontinuities in the volume and the entropy define an isothermal and isobaric *mixed-phase* region in p-V-T space where the two phases coexist in equilibrium [52, 53]. The appearance of this mixed-phase region in this three-

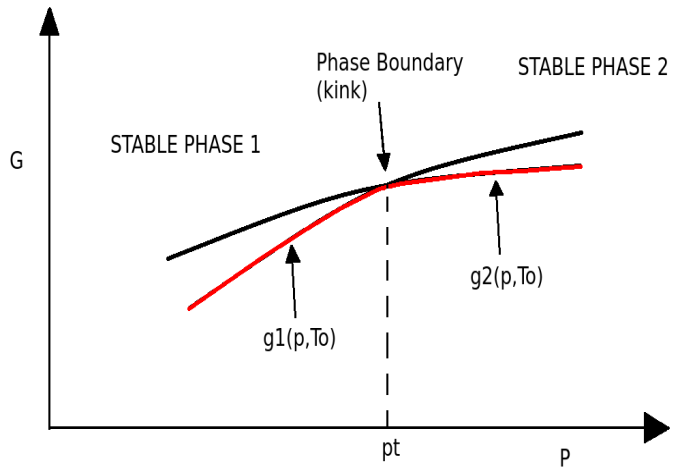


Figure 4.2: Section in plane of constant $T = T_o$ of the Gibbs free energy surface of a material undergoing a first-order phase transition. The Gibbs surfaces of the two phases are labelled, together with that of the material overall draw in red. For given p and T, the stable state is that with the lowest g. The position of the phase boundary where the two surfaces meet at the transition pressure p_t is also indicated. From Eq. (4.7), we see that the gradients of g in a constant T plane must always be positive (in a constant p plane they would always be negative).

dimensional space for the case of a normal polymorphic transition for which $\Delta S < 0$, $\Delta V < 0$ and $dp/dT > 0$, is illustrated in Fig. 4.3.

If the pressure is non-hydrostatic, the thermodynamic condition of transformation cannot be satisfied in general by equating the Gibbs functions of the two phases. The Gibbs equality in fact only applies in a very restricted set of cases. One such condition is the case of uniaxial elastic strain. Let us consider the case of a slab of material being compressed between two slabs of the other phase, with the overall system in a state of uniaxial elastic strain (say along the z axis). Since the component of the pressure along this direction p_z is common to both phases (together with the temperature), the same Gibbs equality principle as Eq. (4.4)

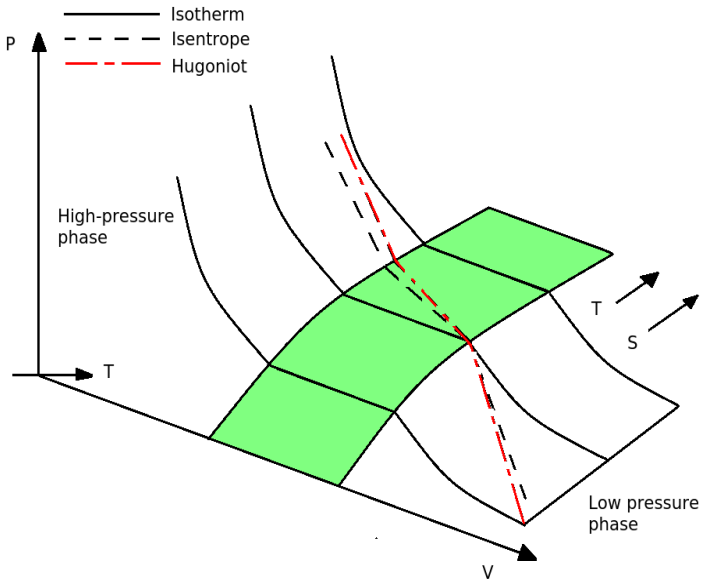


Figure 4.3: p-V-T surface of a conventional polymorphic first-order phase transition, in which the position of the mixed-phase region is demarcated in green. The solid lines represent the isotherms, which cross the mixed-phase region at constant p, the dashed line represents the isentrope, and finally the red line is the Hugoniot curve of the material. Both the isentropes and the Hugoniot exhibit a break in slope at the boundaries of the mixed region marking the onset of transformation.

applies, with the pressure p replaced with p_z [52, 147] -

$$g_1 = e_1 - Ts_1 + p_z v_1 = e_2 - Ts_2 + p_z v_2 = g_2 \tag{4.8}$$

This gives the condition of equilibrium between phases under uniaxial strain along z. In general, the equilibrium position can be significantly affected by this change.

4.2 The problem of how to formulate the Gibbs free energy under non-hydrostatic stress

The issue of how to formulate the Gibbs free energy under generic non-hydrostatic stress conditions introduced in the previous chapter has been the object of considerable research interest since the original seminal work by Gibbs himself [67] in 1906. Most of the early research on this subject was done with geological applications in mind in the context of how rocks and ice deform in regional metamorphism. Such rocks have in many cases undergone deformation beyond their elastic limit, and this deformation has consequently taken the form of a plastic flow of the rock. A necessary condition for plastic flow to take place is that the rock be under a non-hydrostatic stress. Non-hydrostatic stress are also the conditions which prevail in the microstructures and physical properties of rocks in the Earths crust, mantle and core. Hence the interests of geologists to develop general thermodynamical theories of elastic bodies under such conditions [73, 78, 104, 127, 143, 153, 157, 158, 159, 160, 212, 222, 231]. A good general reviewing summary of many of these theories is offered by Paterson [184].

In general many of these theories have been found to be mutually-contradicting, and a proper formulation of the thermodynamic theory of non-hydrostatically stressed solids has been the object of considerable dispute throughout the development of the field. A common feature to most of this early and subsequent work was the attempt to formulate the Gibbs free energy for non-hydrostatically stressed solids, on the grounds that such a quantity is necessary for the consideration of phase equilibrium. These attempts may be classified into two types. The first one, which includes the theories developed by Gibbs [67], Kamb [127],

McLellan [157, 158, 159, 160], Ida [104] and Paterson [184] revolve around the concept of "local equilibrium" at each point on the phase interface, which gives a variable expression for the Gibbs free energy as a function of surface orientation, even in a uniform stress field. The second, which includes the theories of Goranson [73], Verhoogen [231], MacDonald [153] and Kumazawa [143] treats a thermodynamic function describing absolute equilibrium of the form -

$$G = U - TS - V_o \sum_i \sum_j \sigma_{ij}\varepsilon_{ij} \tag{4.9}$$

The ideas behind the derivation of the above equation were summarised by Landau and Lifshitz in their famous book on the theory of elasticity [144], which is part of a collection on theoretical physics. Eq. (4.9) is a generalisation of the usual expression $G = U - TS + pV$ under hydrostatic conditions, although it can be seen that it reduces to only $G = U - TS + p(V - V_o)$ when conditions are set to hydrostatic, where $V - V_o$ is the volume change resulting from the deformation. Hence this definition of G is missing a term pV_o compared to the usual definition $G = U - TS + pV$ which, as will be explained throughout this chapter, is the source of significant complications when conditions are reverted back to non-hydrostatic.

At $T = 0$ K, Eq.(4.9) reduces to the definition of enthalpy of Ref. [65] which we made use of in the analysis of the DFT calculations presented in the previous chapter. As was explained there, the formulation of the enthalpy across infinitesimal deformations given in Ref. [65] is -

$$H = E - V_0 \sum_{j=x,y,z} \sigma_j\varepsilon_j + pV_o = E + V_0 \sum_{j=x,y,z} p_j\varepsilon_j + pV_o \tag{4.10}$$

This formulation of the enthalpy however suffers from the fundamental flaw that its numerical integration yields results which are path-dependent. This is in contradiction with the fundamental definition of enthalpy as a path-independent function of state. This path-dependence can be verified empirically by comparing the outcome of integrating Eq. (4.10) across different paths on the zero-temperature ground state energy surface of silicon encompassing the deformational configurations between the equilibrium cubic-diamond (*cd*) structure and the first high-pressure β-Sn stable phase, as was calculated by ab-initio Density Functional Theory (DFT) techniques in the previous chapter. This energy surface is reproduced in Fig. 4.4, with the integration paths considered in this work plotted overlaid.

The results of the numerical integration of Eq. (4.10) across each of the three paths explained in Fig. 4.4 for the case of the points along the contour of +40 kbar are shown in Fig. 4.5 to Fig. 4.7. As can be deduced by inspecting these figures, the final results for the enthalpy are very different in each case, thus demonstrating that Eq. (4.10) is indeed path-dependent and that therefore this formulation of the enthalpy under non-hydrostatic stress cannot be correct in this form.

We have identified the source of the error in Eq. (4.10) which gives rise to this path-dependence in the last term, pV_o. As was already pointed out by Landau and Lifshitz [144], the inclusion of this term can in fact be rationalised theoretically only when the pressure conditions are reverted back to hydrostatic ($p_x = p_y = p_z = p$), in which case one recovers the usual formulation $H = U + pV$. The term pV_o cannot however justifiably be included in a formula for the enthalpy under generic non-hydrostatic ($p_x \neq p_y \neq p_z$) stress conditions. This problem was

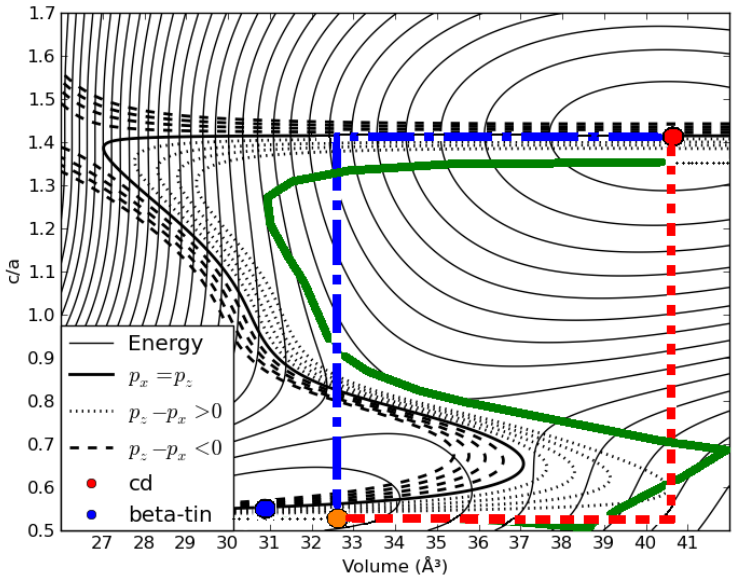


Figure 4.4: The ground-state energy surface of silicon $E(c/a, V)$. Highlighted as the continuous green contour is the same integration path as the one considered in Fig. 3.8 starting at the equilibrium position of the *cd* phase for calculating the enthalpy at the arbitrary point labelled in orange on the +40 kbar shear stress contour. Also shown are the two other paths considered in this work for comparing the results of the numerical integration of the enthalpy: the first one, shown as the dashed red path, connects the position of the *cd* phase to the orange point by advancing first vertically and then horizontally, whereas the second, shown as the dot-dashed blue path, proceeds the other way around.

already noted by Jeong and Kitamura [112], who decided to omit the problematic pV_o term altogether in their atomistic simulation under non-hydrostatic stress, and proceed with what they referred to as a "free-energy-like" term in all their ensuing analysis. A second distinct formulation for the enthalpy under anisotropic stress was proposed by Cheng *et al.* [30, 31] as introduced in the previous chapter, which however also yields path-dependent results.

Hence it appears that both the definitions of enthalpy of Ref. [65] and Refs. [30, 31] are path-dependent. Even though these quantities might still have some

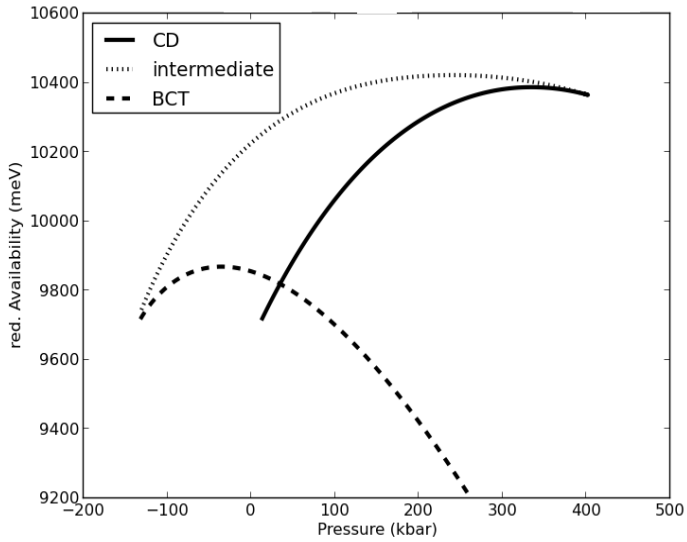


Figure 4.5: Results of the numerical integration of Eq. (4.10) from the equilibrium *cd* phase to the points along the +40 kbar shear stress contour proceeding along the green integration path of Fig. 4.4 along the contour itself. The enthalpy curve is subdivided between the three regions of the shear stress contour overarching each of the *cd* phase (solid line), the intermediate energy saddle located between the two phases (dotted line), and the β-Sn phase (dashed line).

physical meaning, they cannot be thermodynamic potentials which can be used for the determination of thermodynamic equilibrium, which by definition have to be path-independent functions of state. The most recent review of the problem of how to formulate the Gibbs function in the context of phase transformations under non-hydrostatic stress conditions was offered by Johnson at the 2011 APS topical conference on Shock Compression of Condensed Matter [113]. In this review, the author confirmed the persistence of this problem to this day. The fact that the condition of equality of the Gibbs free energies between solid phases at equilibrium is valid only for a few simple geometries, morphologies and stress distributions was also emphasised. Two such cases are the case of uniaxial compression and uniaxial

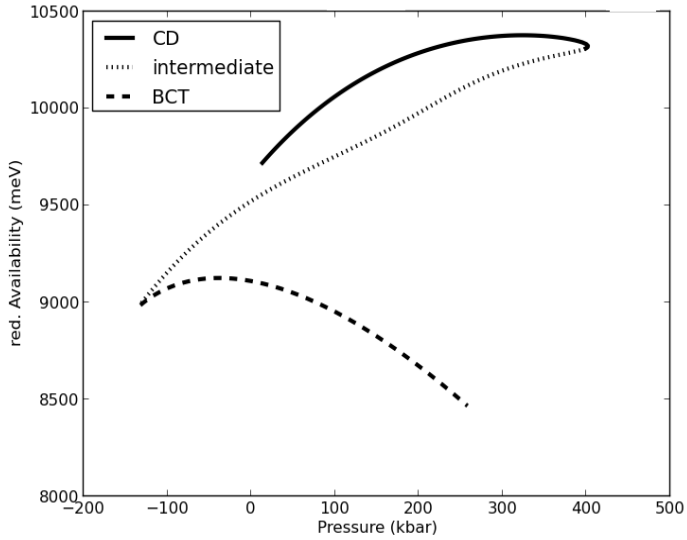


Figure 4.6: The same enthalpy results as in Fig. 4.5, but this time obtained by integrating along the red path of Fig. 4.4.

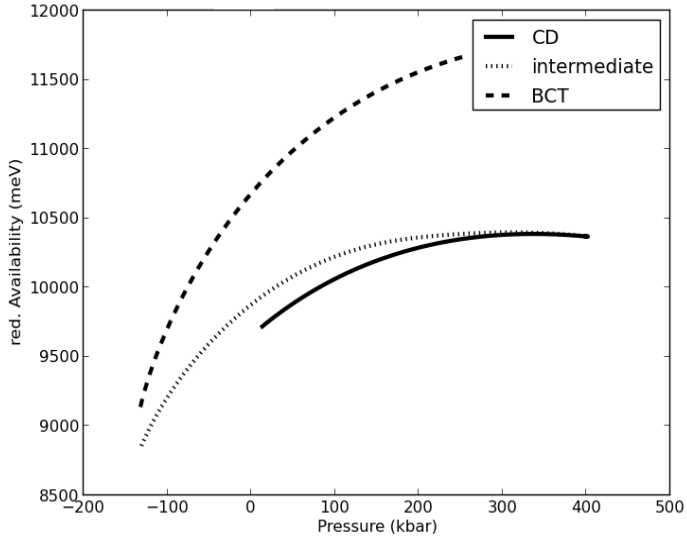


Figure 4.7: The same enthalpy results as in Fig. 4.5, but this time obtained by integrating along the blue path of Fig. 4.4.

stress. Furthermore, this applies to more complex geometries such as a simple laminate of alternating composition of phases, and the case of two concentric elastic spheres. The underlying reason for this limited applicability of the Gibbs equality condition is that in general, under non-hydrostatic conditions, all points on all interfaces between two solid phases are potentially different, such that the condition for thermodynamical equilibrium for solids produces in general a complex spatial stress distribution.

We now put forward our own approach, based on the concept of Availability (otherwise known as Exergy) in thermodynamics, for determining phase stability in elastic solids (of at most tetragonal symmetry) subject to finite (that is within the non-linear realm of the theory of elasticity) and non-hydrostatic deformations. This approach appears to reconcile both needs of finding a thermodynamic quantity that is physically meaningful in the context of phase transitions since it affords for the determination of phase equilibrium conditions under any constraint, and which can be expressed in a form that is path independent. We must stress however that the approach presented herein is still very much in the tentative phase, and we do not exclude the possibility that future research will find it to be more restricted in its scope of application than it is believed to be here. Before embarking in the investigation of Availability however, it is worth revisiting the concept of thermodynamical work and in particular its definition under non-hydrostatic stress.

4.3 Work under non-hydrostatic stress conditions

It is always possible to express the work done on a system in terms of quantities pertaining to the properties of the system if the changes during which the work is performed are reversible. When changes take place reversibly, the work done on a system is in general given by -

$$dW = \sum_i X_i dx_i \tag{4.11}$$

where X_i and x_i are the intensive forces and their conjugate extensive displacements respectively. To understand the form that this equation takes when the work is done by hydrostatic pressure, we consider a fluid contained in a cylinder by a frictionless, tight fitting piston. Let the surface area of the piston be A and the pressure exerted by the fluid p. It follows that the force which is exerted on the piston to contain the fluid is $F = pA$. If the piston is now moved into the fluid by a small distance $d\xi$, the work done on the fluid is -

$$dW = Fd\xi = pAd\xi = -pdV \tag{4.12}$$

where dV is the change in volume of the fluid. The sign convention is as follows: when the volume of the fluid increases and dV is therefore positive, the fluid does work on the surroundings and the work is therefore negative. If conversely the volume of the fluid decreases and dV is negative, work is done on the fluid and the work is positive. Thus for work done on a system by hydrostatic pressure in

a reversible fashion we always have [4, 18] -

$$dW = -pdV \tag{4.13}$$

To find the total work during a given change in the system, we need to integrate Eq. (4.13) according to the pressure-volume relation which pertains to the change taking place.

So far we have restricted ourselves to the analysis of a fluid under hydrostatic compression. For fluids, this is the only possible pressure loading configuration owing to their zero shear strength. In the case of solids on the other hand, their finite shear strength means that non-hydrostatic pressure configurations can be supported. In order to obtain a more general expression for the work done during such non-hydrostatic stress loadings, we refer back to Eq. (4.11) and notice that during any given displacement along the i-th direction, only the force acting in that given direction performs work. In the case of uniaxial compression, three pressure components need to be applied simultaneously in each step, one acting normally to apply the uniaxial compression and two acting transversely to prevent any lateral expansion of the solid resulting from its finite Poisson Ratio. However only the pressure component acting in the direction of the compression does work.

We further notice that any general non-hydrostatic deformation of a solid (of at most orthorhombic symmetry) can be accomplished by three subsequent uniaxial compressions along each of the x, y and z orthogonal axes in turn. The corresponding expression for the work done in performing this generic non-

hydrostatic deformation is therefore given by -

$$dW = -F_x dl_x - F_y dl_y - F_z dl_z = -p_x dV_x - p_y dV_y - p_z dV_z \tag{4.14}$$

where F_i is the force exerted in the i-th direction that achieves displacement dl_i along the l_i lattice parameter of the solid. In the second expression for the work in terms of the pressure components, dV_i represents the volume change under uniaxial compression along the i-th direction. Integrating this expression for the work differential across three subsequent uniaxial compressions, we obtain for the total work ΔW -

$$\Delta W = -b_0 c_0 \int_{a_0}^{a} p_x dl_x - a c_0 \int_{b_0}^{b} p_y dl_y - ab \int_{c_0}^{c} p_z dl_z \tag{4.15}$$

where a_0, b_0 and c_0 represent the initial values of the lattice parameters of the solid, while a, b and c represent their final values at the end of the deformation.

Whether Eq. (4.15) is path-independent and therefore independent of the order in which the three subsequent uniaxial compressions are performed depends on the conditions under which the compressions are applied. One obvious example in which ΔW turns out to be a path-independent function of state is when the changes are adiabatic, such that from the First Law of Thermodynamics [4, 18] -

$$dU = dW + dQ \tag{4.16}$$

it follows that ΔW is always equal to the change in internal energy ΔU (a function of state) when the exchange of heat dQ is zero. A possible way to implement

this condition in practice is to elastically compress a sample at T =0 K, such that all the work done on the sample is converted into internal potential strain energy with no friction and net heat dissipation. Being elastic, this type of compression represents a reversible process since the sample is able to recover its original shape once the pressure is released, with all the strain energy being returned to the surroundings. This type of elastic compression provides us with a way to verify the validity of Eq. (4.15), which if correct should exactly reproduce the change in internal energy ΔU of the compressed sample. Being equal to ΔU, the result of Eq. (4.15) should also be independent of the order in which the three subsequent uniaxial compressions are performed. These assertions are easily verified by setting up a T =0 K simulation box in equilibrium and displacing it uniaxially three subsequent times along each lattice side in turn. The LAMMPS Molecular Dynamics code [196] was employed for performing this test, and single-crystal silicon was adopted as the model material using the semi-empirical modified bond-order Tersoff-like potential as parametrised by Erhart and Albe [56] to model the interatomic interactions. A large number of states were calculated across each uniaxial compression for performing the numerical integration of the pressures in Eq. (4.15). The results of performing the three subsequent uniaxial compressions in each of the six possible orders is presented in Table 4.1 and the resulting work calculated through Eq. (4.15) is put into comparison with the corresponding change in internal energy in each case. The agreement to within an order of 10^{-4} meV between the works calculated across the six different permutations of the order of compression, and the essentially exact agreement between each of these six values for the work and the total change in internal energy of the solid, establishes the validity of Eq. (4.15) for

calculating the work under any generic non-hydrostatic deformation. This result will prove to be of paramount importance in our development of the approach of phase transitions under non-hydrostatic stress, given that uniaxial compression represents the only case in which the pressure components acting on a solid and the resulting volumetric strain can be directly related to each other to obtain a measure of the corresponding work done.

Finally, we can confirm that Eq. (4.15) agrees with the hydrostatic limit when all the states reached during the integration are hydrostatic -

$$\Delta W = \int_1^2 p_x dV_x + \int_2^3 p_y dV_y + \int_3^4 p_z dV_z = \int_1^4 p dV \tag{4.17}$$

where the last equality applies when $p_x = p_y = p_z = p$. The result for the total work under three subsequent uniaxial compressions considering the left-hand side of the above expressions was of 458.5135482 meV to reach a compressed cubic hydrostatic state with lattice constant of 5.0 Å starting from equilibrium. The result of calculating the work across a single hydrostatic compression step to reach the same final state using the right-hand side of Eq. (4.17) was on the other hand 458.5135459 meV. Hence the agreement between the two methods of compression is excellent, confirming that Eq. (4.15) can be correctly reconciled with the hydrostatic limit.

Table 4.1: Results of the total work done ΔW for the six different orders in which the three uniaxial compressions that take the system from the equilibrium configuration into a generic non-hydrostatic strain state $\left(a = 5.2\ \text{Å}, b = 5.0\ \text{Å}, c = 4.8\ \text{Å}\right)$ can be applied. The total work ΔW at the end of the three deformational steps given by Eq. (4.15) is listed at the bottom of the corresponding entry in the table, together with the total change in internal energy ΔU. U represents the internal energy per unit atom of the sample.

strain dir. and step no.	U (meV)	a (Å)	b (Å)	c (Å)	ΔW_{step} (meV)
Equilibrium	-4628.4147	5.42888	5.42888	5.42888	0.0
x, 1	-4609.0028	5.2	5.42888	5.42888	19.4119005
y, 2	-4501.2433	5.2	5.0	5.42888	107.7594563
z, 3	-4148.7076	5.2	5.0	4.8	352.5357068
ΔW_{tot} (meV)	479.707064				
ΔU (meV)	479.7071				
y, 1	-4558.5466	5.42888	5.0	5.42888	69.8680205
x, 2	-4501.2433	5.2	5.0	5.42888	57.30334497
z, 3	-4148.7076	5.2	5.0	4.8	352.5357068
ΔW_{tot} (meV)	479.707072				
ΔU (meV)	479.7071				
z, 1	-4475.0096	5.42888	5.42888	4.8	153.4050655
x, 2	-4394.1164	5.2	5.42888	4.8	80.89328850
y, 3	-4148.7076	5.2	5.0	4.8	245.4087587
ΔW_{tot} (meV)	479.7071128				
ΔU (meV)	479.7071				
x, 1	-4609.0028	5.2	5.42888	5.42888	19.41190051
z, 2	-4394.1164	5.2	5.42888	4.8	214.8864468
y, 3	-4148.7076	5.2	5.0	4.8	245.4087587
ΔW_{tot} (meV)	479.7071061				
ΔU (meV)	479.7071				
y, 1	-4558.5466	5.42888	5.0	5.42888	69.86802050
z, 2	-4279.1055	5.42888	5.0	4.8	279.4411494
x, 3	-4148.7076	5.2	5.0	4.8	130.3979022
ΔW_{tot} (meV)	479.7070722				
ΔU (meV)	479.7071				
z, 1	-4475.0096	5.42888	5.42888	4.8	153.4050655
y, 2	-4279.1055	5.42888	5.0	4.8	195.9041234
x, 3	-4148.7076	5.2	5.0	4.8	130.3979022
ΔW_{tot} (meV)	479.7070911				
ΔU (meV)	479.7071				

4.4 The concept of Availability in the theory of phase-transitions

Similarly to the derivation by Cheng *et* al. [30, 31], the definition of Availability also follows directly from the law of increase of entropy coupled with the First Law of Thermodynamics. When a generic system interacts with its surroundings with a net inward heat flow, the entropy change dS of the system across any infinitesimal change is related to the heat flow dQ according to [4, 18] -

$$dQ \leq T_o dS \tag{4.18}$$

where T_o is the temperature of the surroundings at which heat is supplied to the system [1] and the equality sign necessarily holds when the change is reversible. For a system which is thermally isolated, $dQ = 0$. It follows from Eq. (4.18) that under these conditions we have $dS \geq 0$. This general result is known as the law of increase of entropy, which states that the entropy of an isolated system cannot decrease. This law can be used to determine the equilibrium configuration of an isolated system. Since in approaching equilibrium the entropy of the system can only increase, the final equilibrium configuration is that for which the entropy is maximised. This simple law has far reaching consequences in the determination of phase equilibrium during phase transitions, as will be explained later. If, in addition to exchanging heat with the system, the surroundings also exert a pressure p_o and this pressure component is the only source of work, then the

[1] Only when the source of heat is in thermal equilibrium with the system as a whole does it become the temperature of the system also.

external work done by the surroundings dW is -

$$dW = -p_o dV \tag{4.19}$$

where dV is the corresponding volume change of the system. Making use of the First Law of Thermodynamics, namely that the change in internal energy dU of a system as a result of its interaction with the surroundings is related to the work dW and the heat flow dQ by -

$$dU = dQ + dW = dQ - p_o dV \tag{4.20}$$

then Eq. (4.18) becomes -

$$dU \leq T_o dS - p_o dV \tag{4.21}$$

or equivalently -

$$dA = dU - T_o dS + p_o dV \leq 0 \tag{4.22}$$

where the *Availability* A of the system is defined as [4, 18, 236] [1] -

$$A = U + p_o V - T_o S \tag{4.23}$$

The corresponding expression for the finite change is given accordingly by -

$$\Delta A = \Delta U - T_o \Delta S + p_o \Delta V \tag{4.24}$$

[1] The Availability bears its name from the fact that it gives a measure of the maximum amount of work which may be extracted from a system in given surroundings.

or, for the case of zero temperature which will be of interest to us, by -

$$\Delta A = \Delta U + p_o \Delta V \tag{4.25}$$

Alternatively, the Availability differential of Eq. (4.22) can be re-defined by making use of the First Law as applied to the system -

$$dU = TdS - pdV \tag{4.26}$$

which yields -

$$dA = (T - T_o)\, dS - (p - p_o)\, dV \tag{4.27}$$

It must be emphasised that p_o and T_o here refer to the pressure and the temperature of the surroundings, which are fixed quantities and may be quite different from those of the system. In future we shall however deal only with situations in which the external pressure components exerted by the surroundings and the internal response of the system (which will always be of at most orthorhombic symmetry) are in equilibrium with one another and are therefore equal and opposite in magnitude. The external pressure and the corresponding internal pressure component acting on the same side of the solid can therefore be used interchangeably. It must also be noted that the expression for ΔA in Eq. (4.25) includes only the corresponding changes in energy and volume of the system, but not those in the external pressure since it is this pressure which exerts the work on the system and drives its volume (and consequently its Availability) change in the first place. Eq. (4.22) embodies the restatement of the law of increase of entropy that in any natural change the Availability of a system cannot increase. It follows directly

that the general condition for thermodynamic equilibrium of a system in given surroundings is that the Availability be a *minimum*, in which case we have -

$$dA = dU + p_o dV - T_o dS = 0 \tag{4.28}$$

for all possible reversible (infinitesimal) displacements from equilibrium. This principle lies at the basis for the treatment of phase transition which is at the centre of our attention in this thesis.

The alternative condition for equilibrium expressed in terms of the minimisation of the Gibbs free energy can be derived as a special case of this general law of minimisation of the Availability. This can be seen by considering a system interacting with its surroundings and exploring how A varies when the system is displaced reversibly from equilibrium. For A to be a minimum and for equilibrium to be achieved, both terms in Eq. (4.27) must be zero in an infinitesimal displacement since they represent independent degrees of freedom. When the system is not thermally isolated and is held at constant pressure (isobaric system), in general its entropy may change so that for the first term of Eq. (4.27) to be zero we must have $T = T_o$, and therefore $dT = 0$ in any infinitesimal reversible change. Furthermore, since the volume may change, for the second term to be zero we require $p = p_o$, or $dp = 0$ in any reversible change. Under these two conditions, Eq. (4.22) reduces to the condition of minimisation of the Gibbs free energy G for determining phase stability -

$$dA = dU - TdS + pdV = dG = 0 \tag{4.29}$$

which applies under the constraints of constant T ($dT = 0$) and constant p ($dp = 0$). It must be noted that these two constraints represent the constancy of the two proper variables of G which represent the two degrees of freedom of the system. This condition of minimisation of G is entirely analogous to that of A since they both stem originally from the law of increase of entropy. It just happens to be a more convenient way to formulate the condition for thermodynamic equilibrium when the system is subject to constant temperature and constant pressure, since these two constraints are automatically embodied in the condition. The principle of minimisation of A remains instead applicable under all circumstances since it is independent of any constraints.

4.5 Some illustrative examples of the principle of minimisation of Availability

4.5.1 Hydrostatic compression of the system

If the internal response of the system to the externally applied pressure p_o is hydrostatic, and furthermore if this internal hydrostatic pressure p remains constant between the start and the end of the phase transition, then we effectively have a situation where we can replace all instances of the external pressure p_o in the formula for the Availability with the internal hydrostatic pressure p, since these two pressures balance each other in both phases. The internal and external pressures do not necessarily have to be equal during the progress of the phase transition itself, but only at the end states. However the details of how the relation between the internal and external pressures varies during the phase transition need

not concern us, since as we will show later the Availability is a function of state in this case, and consequently the magnitude of its change depends only on the end states of the phase transition and not on the actual path employed between them. Considering the case where the temperature is everywhere zero, such as is the case in our ab-initio DFT simulations, the change in Availability across the phase transition from phase 1 to phase 2 under these circumstances is given by Eq. (4.25) -

$$\Delta A\,(1 \rightarrow 2) = \Delta U + p_o \Delta V = (U_2 - U_1) + p\,(V_2 - V_1) \leq 0 \tag{4.30}$$

where as explained earlier we can replace the external pressure p_o with the internal hydrostatic pressure p. The last inequality is satisfied if phase 2 is relatively more stable than phase 1 and the phase-transition pressure occurs when the equality condition is met and the Availabilities of the two phases are equal, since this marks the phase equilibrium point where changes between the two phases are reversible.

Eq. (4.35) can be compared with the corresponding expression for the enthalpy change between the two phases -

$$\Delta H\,(1 \rightarrow 2) = \Delta U + p\Delta V + V_1 \Delta p = \Delta U + p\Delta V \tag{4.31}$$

Hence it can be deduced that under conditions of constant pressure between the two phases ($\Delta p = 0$) and constant zero temperature, the Availability reduces to the enthalpy change of the system. Phase equilibrium in isobaric and isothermal phase changes at absolute zero is therefore given by the minimisation of the

enthalpy of the system, such that at any given pressure the stable phase is that with the lowest enthalpy while at the transition pressure the enthalpies of the two phases are the same. This quantity is clearly a function of state since all variables on the right-hand side of Eq. (4.35) are themselves functions of state (a formal mathematical proof of this statement will be provided in the next section). It is worth noticing that the $p\Delta V$ appearing in Eq. (4.31) is not the work done in transforming between the two phases, which is instead still given by $\int_1^2 pdV$ integrated along the hydrostat (along which the pressure is not constant). ΔH is therefore not equal to the heat exchange ΔQ, which is always null for isothermal processes at absolute zero given that at this temperature the system has no heat content. Alternatively, this equivalence between the enthalpy and availability under isobaric and isothermal phase changes at absolute zero can be deduced by invoking the Third Law of Thermodynamics, which states among other things that at absolute zero all isothermal processes are isentropic. Furthermore, the entropy of a pure crystalline substance at absolute zero is always zero. Hence dS in Eq. (4.27) is always zero. For the other term in Eq. (4.27) to be zero we require $p = p_o$, or $dp = 0$, in any infinitesimal reversible change, since the volume can in general change. Therefore the expression for dA reduces to $dA = dU + pdV = dH = 0$ since p is constant.

The evolution of ΔA, or equivalently of ΔH, between the cubic-diamond and the β-Sn hydrostatic phases of single-crystal silicon as a function of hydrostatic pressure, as predicted by the DFT ground-state energy surface calculated in the previous chapter, is presented in Fig. 4.8. It can be deduced that the point where the two phases have the same enthalpies and therefore $\Delta H = 0$ corresponds exactly to the transition pressure under hydrostatic compression of around 121.7

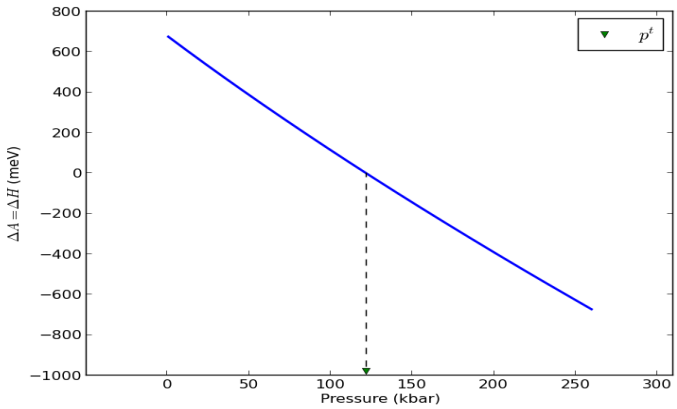


Figure 4.8: Evolution of the difference in Availability (or equivalently enthalpy) between the *cd* and β-Sn phases in silicon as a function of hydrostatic pressure. The point where $\Delta H = \Delta A = 0$ corresponds to the transition pressure under such hydrostatic pressure conditions.

kbar already estimated in the previous chapter. At higher pressures, where $\Delta H < 0$, the β-Sn phase is more stable, whereas at pressures lower than the transition pressure the *cd* phase is more stable. Hence we can conclude that the principle of minimisation of Availability correctly reproduces the phase transition parameters of the *cd* to β-Sn phase transition in silicon under hydrostatic pressure.

4.5.2 Uniaxial compression of the system

We now consider the alternative case in which the system gets uniaxially compressed along for example the z direction by the externally applied pressure p_o. Physically, this corresponds to the situation already introduced in Section 4.1 in which the material of phase 2 grows as a uniaxially compressed slab between two uniaxially compressed slabs of material in phase 1. This two-phase configuration is illustrated in Fig. 4.9. In this case, the internal pressure component p_z is common to both phases and equal in magnitude to the external pressure p_o, so

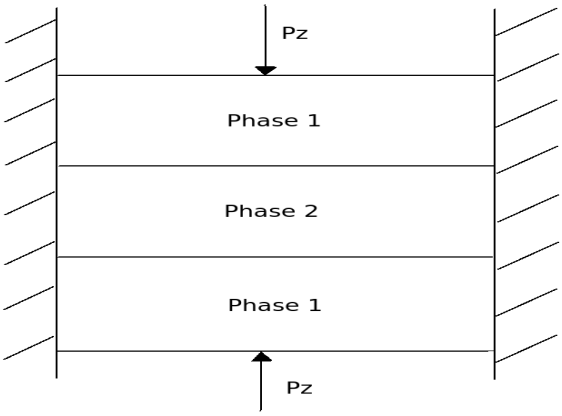


Figure 4.9: Phase transformation from phase 1 to phase 2 under uniaxial strain. The p_z pressure component is constant throughout the material.

that the analysis of the previous subsection can be repeated by replacing p with p_z. In particular, p_z is the only pressure component doing work for uniaxial compression along z, so that the expression for the change in Availability between the two phases at $T = 0$ K is this time given by -

$$\Delta A\,(1 \to 2) = \Delta U + p_o \Delta V = (U_2 - U_1) + p_z\,(V_2 - V_1) \leq 0 \tag{4.32}$$

Similarly to the case of hydrostatic compression, this expression for the Availability change under uniaxial strain can be compared with that for the enthalpy change of the system under the same conditions. As explained earlier, the expression for the enthalpy under uniaxial compression along z is -

$$H = U + p_z V \tag{4.33}$$

Hence the enthalpy change between the two phases is given by -

$$\Delta H\,(1 \rightarrow 2) = \Delta U + p_z \Delta V + V_1 \Delta p_z = \Delta U + p_z \Delta V \tag{4.34}$$

Once again, under conditions of constant p_z between the two phases ($\Delta p_z = 0$) and constant zero temperature, the Availability change under uniaxial compression reduces to the enthalpy change of the system. Furthermore, this quantity is also a function of state, given that all quantities in terms of which it is defined are themselves functions of state (when the total average pressure p is a function of state, its components p_x, p_y and p_z necessarily are too).

Using this simple model, we can obtain an estimate of the transition pressure for the *cd* to β-Sn phase transition in single-crystal silicon under conditions of uniaxial compression along the c axis of the crystal for both phases (note once more, and as will be discussed in Chapter 5, this assumption does not necessarily pertain to the physical conditions under shock compression). Fig. 4.10 shows the trajectories of the lines of uniaxial compression along z starting from the equilibrium positions of the *cd* and β-Sn phases on the ground-state energy surface of silicon. By extracting the values of p_z, V and U along each of these lines, the evolution of ΔA, or equivalently of ΔH, between the cubic-diamond and the β-Sn uniaxially-compressed phases of single-crystal silicon as a function of uniaxial stress p_z could be plotted. The results are presented in Fig. 4.11. The point where the two phases have the same enthalpies and therefore $\Delta H = 0$ corresponds to a transition pressure p_z^t under uniaxial compression of around 118 kbar, that is only slightly below the hydrostatic transition pressure of 121.7 kbar estimated in the previous subsection. The x component of the transition pressure p_x^t on the

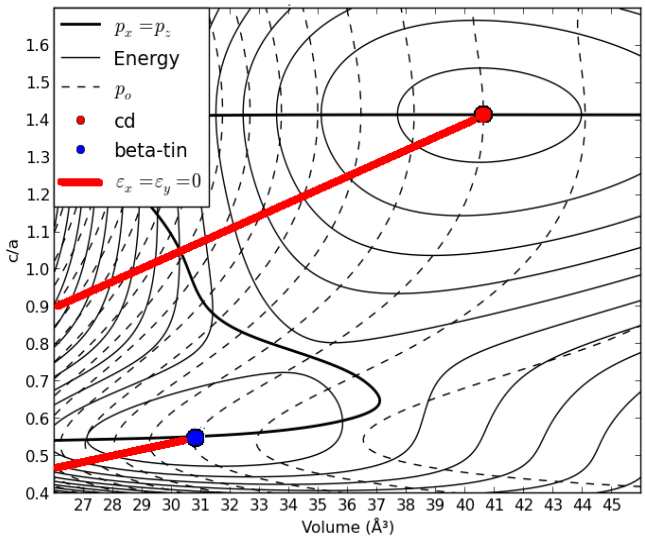


Figure 4.10: Ground state energy surface of silicon, showing in red the lines of uniaxial compression along the c axis of the crystal starting from the equilibrium positions of the two phases.

other hand is markedly lower than the hydrostatic transition pressure at around 55 kbar.

4.5.3 System held at constant volume

Finally, we consider the case in which the phase transition between phase 1 and phase 2 occurs at constant volume of the system, and in which both phase 1 and 2 are subject to hydrostatic pressure. Physically, this corresponds to the case in which the external pressure p_o does zero work in driving the phase transition. The expression for the change in Availability between the two phases at $T = 0$ K in this case is given by -

$$\Delta A\,(1 \rightarrow 2) = \Delta U + p_o \Delta V = (U_2 - U_1) \leq 0 \tag{4.35}$$

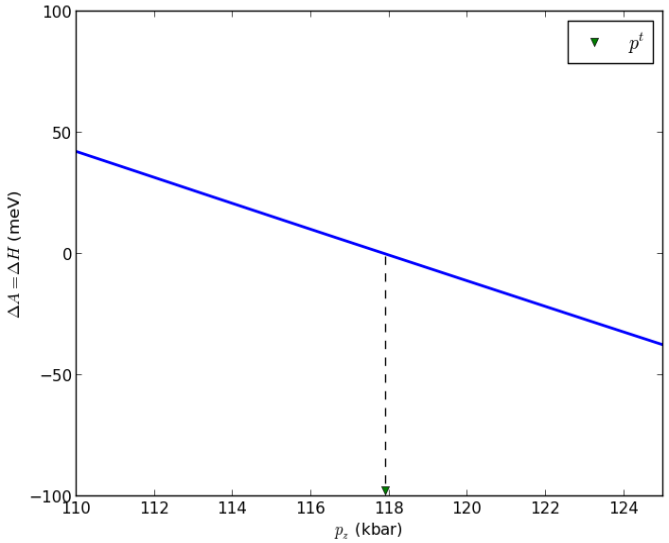


Figure 4.11: Evolution of the difference in Availability (or equivalently enthalpy) between the *cd* and β-Sn phases in uniaxially-compressed silicon. The point where $\Delta H = \Delta A = 0$ corresponds to the transition pressure under such uniaxial strain conditions.

Hence, under conditions of constant volume between the two phases ($\Delta V = 0$) and of constant zero temperature, the Availability change reduces to the internal energy change of the system, which is of course a function of state by definition. Phase stability in isochoric and isothermal at absolute zero (and therefore isentropic) phase changes is therefore given by the minimisation of the internal energy, such that at any given volume the stable phase is that with the lowest internal energy and at the transition volume the internal energies of the two phases are the same. At this stage, we can draw up a list of all the conditions for phase equilibrium encountered so far, each of which represents a restatement of the principle of minimisation of Availability under given constraints. This list is presented in Table 4.2. There exist many other conditions for equilibrium corresponding to other combinations of constraints, as found on page 110 in Ref.

[4], but the conditions listed in Table 4.2 undoubtedly represent the most useful and most frequently occurring ones in the context of ab-initio modelling of phase transitions.

Table 4.2: Conditions for stable equilibrium under the given set of constraints, as derived from the principle of minimisation of Availability. When phase transitions occur at $T = 0$ K such as is the case in all DFT ab-initio simulations presented in this thesis, conditions are isentropic (constant S) and therefore the minimisation of U and H are the only relevant phase stability conditions.

Variables held constant	Equilibrium condition
T , p	G minimum
T , V	F minimum
S , V	U minimum
S , p	H minimum

Finally, it is worth investigating how first-order phase transitions are defined when U is the thermodynamic potential determining phase stability. As explained in Section 4.1, the order of a phase transition is defined as the order of the lowest differential of the potential determining phase stability which exhibits a discontinuity at the transition point. Hence in the case of H at $T = 0$ K, whose differential is given by -

$$dH = Vdp = \left(\frac{\partial H}{\partial p}\right)_S dp \tag{4.36}$$

first-order phase transitions are accompanied by a discontinuity in the volume of the system. In the case of U at $T = 0$ K on the other hand, whose differential is -

$$dU = -pdV = \left(\frac{\partial U}{\partial V}\right)_S dV \tag{4.37}$$

first-order phase transitions are associated with a discontinuity in the pressure of the system. Hence, instead of dealing with a transition pressure and volume discontinuity, as we have customarily been doing so far in the context of isobaric and isentropic phase transitions, when dealing with isochoric and isentropic phase transitions we are now faced with a transition volume and pressure discontinuity. Even though this represents an inherently interesting case to study, for practical purposes isochoric conditions are not usually encountered in experiments, where isobaric conditions represent the norm instead. Therefore the results presented in this subsection are not immediately useful for understanding the real-life experimental behaviour of materials, but will be presented regardless for completeness.

The above theory for isochoric, isentropic phase transitions can once again be applied to the *cd* to β-Sn phase transition in single-crystal silicon. Along the hydrostatic contour, we can calculate the internal energy across each phase and, by locating the intersection between the two resulting energy surfaces where $\Delta U = 0$, we can obtain an estimate of the transition volume under hydrostatic conditions in a similar fashion to how the transition pressure was measured from the intersection of enthalpy surfaces in the previous chapter. The result of this analysis is presented in Fig. 4.12. The result for the transition volume under such hydrostatic conditions is 32.27 Å^3. Finally, it is worth noticing that the pressure discontinuity across the phase transition is around 375 kbar.

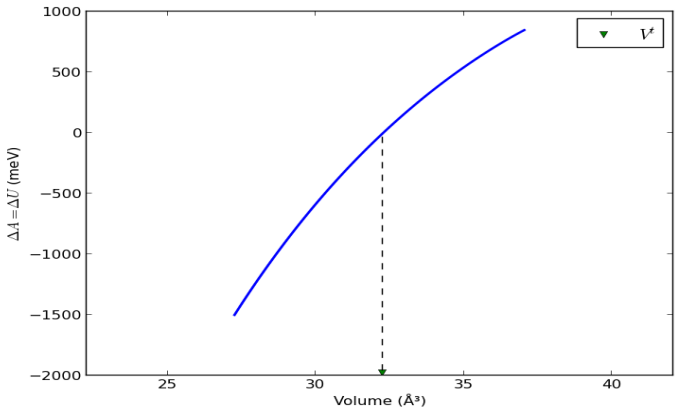


Figure 4.12: Evolution of the difference in Availability (or equivalently the internal energy) between the *cd* and β-Sn phases in single-crystal silicon held at constant volume under hydrostatic stress. The point where $\Delta U = \Delta A = 0$ corresponds to the transition volume under such isochoric conditions.

4.6 Availability under general non-hydrostatic stress conditions

So far we have limited ourselves to special pressure loading configurations (hydrostatic, uniaxial and isochoric compressions) in which the Availability reduced to well-defined thermodynamic potentials which were also functions of state. We now aim to generalise our results to general non-hydrostatic pressure conditions. For simplicity, we will consider crystal geometries of tetragonal symmetry, although the results presented here should be easily extendible to orthorhombic lattices. General non-hydrostatic pressure conditions are therefore defined as $p_x = p_y \neq p_z$. The main complication when dealing with general non-hydrostatic pressure conditions arises from there now being multiple pressure components doing work on the system at the same time. In all cases analysed previously in fact, we only had to deal with one unique pressure component performing work

at a time, be it the total pressure p for the case of hydrostatic compression or the uniaxial pressure p_z in the case of uniaxial strain of the system. To understand how multiple pressure components can be organised together in a unique expression for the total external work, we refer back to the expression for the total work ΔW done in three subsequent uniaxial compressions derived in section 4.3 (Eq. (4.15)) -

$$\Delta W = -b_0 c_0 \int_{a_0}^{a} p_x dl_x - a c_0 \int_{b_0}^{b} p_y dl_y - ab \int_{c_0}^{c} p_z dl_z \tag{4.38}$$

Given that any generic non-hydrostatic strain deformation can be achieved in three subsequent uniaxial steps, the above expression represents a general way of writing the total internal work done whenever $p_x \neq p_y \neq p_z$. In particular, we re-emphasise the fact that each pressure component only does work when it lies along the same direction as the uniaxial compression being performed in the current deformational step.

A rigorous approach for deriving the work differential under non-hydrostatic stress consists in starting from the expression for the total volume differential dV in terms of variations of the lengths l_x and l_z of the sides of the unit cell -

$$dV = \left(\frac{\partial V}{\partial l_x}\right)_{l_z} dl_x + \left(\frac{\partial V}{\partial l_z}\right)_{l_x} dl_z \tag{4.39}$$

where $V = l_x^2 l_z$ for tetragonal lattices. Hence -

$$dV = 2 l_x l_z dl_x + l_x^2 dl_z \tag{4.40}$$

Adding the pressure components to the corresponding uniaxial displacements, we

obtain the expression for the differential of the work done on the system -

$$dW = -p_x \left(\frac{\partial V}{\partial l_x}\right)_{l_z} dl_x - p_z \left(\frac{\partial V}{\partial l_z}\right)_{l_x} dl_z = -2p_x l_x l_z dl_x - p_z l_x^2 dl_z \tag{4.41}$$

This definition of dW can be directly inserted in the expression for the Availability differential at $T = 0$ K -

$$dA = dU - dW = dU + 2p_x l_x l_z dl_x + p_z l_x^2 dl_z \leq 0 \tag{4.42}$$

As a first attempt, in parallel with the derivation of Availability with only one pressure component doing work outlined in Section 4.4, we can assume that the external pressure components p_x and p_z appearing in Eq. (4.41) are constant between the two phases of the phase transition. This was indeed the approach adopted by Cheng *et al.* [30, 31]. Even before performing the integration of dW to obtain an expression for the finite change in A, we notice that there is a fundamental problem with this definition of dW under constant external pressure components which makes it inconsistent with the requirement for A to be a well defined function of state across the phase transition. This problem can be understood by revisiting the fundamental definition of path-independent work line integrals in terms of conservative force vector fields. In general, a force vector field $\boldsymbol{F}(x, y, z)$ that has continuous partial derivatives in a simply connected region R is conservative if, and only if, any of the following is true [204]:

- The work line integral $\Delta W = \int_A^B \boldsymbol{F} \cdot d\boldsymbol{r}$, where A and B lie in the region R, is independent of the path from A to B. Hence the integral $\oint_C \boldsymbol{F} \cdot d\boldsymbol{r}$

around any closed loop in R is zero.

- There exists a single-valued function ϕ of position such that $\boldsymbol{F} = \nabla\phi$.
- $\nabla \times \boldsymbol{F} = \boldsymbol{0}$.
- $\boldsymbol{F} \cdot d\boldsymbol{r}$ is an exact differential.

Furthermore, it can be shown that the validity or otherwise of any of these conditions implies the same for the other three. The last of the four conditions is particularly resourceful for assessing the path-independence of Eq. (4.41). Exact differentials in general are defined as differentials that can be integrated directly. It is naturally of interest to investigate which properties of a differential make it exact. Consider the general differential containing two variables -

$$df = A\,(x, y)\,dx + B\,(x, y)\,dy \tag{4.43}$$

We see that -

$$\frac{\partial f}{\partial x} = A\,(x, y) \qquad \frac{\partial f}{\partial y} = B\,(x, y) \tag{4.44}$$

and, considering the property of second partial derivatives -

$$\frac{\partial^2 f}{\partial x \partial y} = \frac{\partial^2 f}{\partial y \partial x} \tag{4.45}$$

we therefore require -

$$\frac{\partial A}{\partial y} = \frac{\partial B}{\partial x} \tag{4.46}$$

This is in fact both a necessary and sufficient condition for the differential to be exact [204]. In Eq. (4.41) the A and B coefficients are defined as $A = 2p_x l_x l_z$ and

$B = p_z l_x^2$. Hence we see that the condition (4.46) is not fulfilled and consequently Eq. (4.41) is not in general an exact differential -

$$\frac{\partial A}{\partial l_z} = 2p_x l_x \neq \frac{\partial B}{\partial l_x} = 2p_z l_x \tag{4.47}$$

The only case when Eq. (4.41) is directly an exact differential and consequently ΔW is a path-independent function of state is when $p_x = p_z$, that is when the stress conditions are hydrostatic as analysed in subsection 4.5.1. In this case the work differential becomes pdV. Otherwise, under general non-hydrostatic pressure conditions, ΔW and consequently ΔA are not functions of state under the condition of constant pressure components. This is the origin of the path-dependence in Cheng's formula for the enthalpy change [30, 31]. We therefore conclude that those of constant external pressure components do not represent suitable conditions to derive a well-defined, path-independent formulation of Availability as we require.

The work differential of Eq. (4.41) can however be re-expressed in terms of the external force components F_x and F_z, which in fact represents the most fundamental definition of work -

$$dW = -2F_x dl_x - F_z dl_z \tag{4.48}$$

where the relation between the force and the pressure components is -

$$F_x = p_x l_x l_z \qquad F_z = p_z l_x^2 \tag{4.49}$$

It can be easily deduced that when the external force components F_x and F_z in

Eq. (4.48) are constants, the corresponding force vector field is a conservative one. This can be seen from both the $\nabla \times \boldsymbol{F} = \boldsymbol{0}$ requirement, in which all the derivatives in the definition of curl -

$$\nabla \times F = \begin{vmatrix} \boldsymbol{i} & \boldsymbol{j} & \boldsymbol{k} \\ \partial/\partial l_x & \partial/\partial l_y & \partial/\partial l_z \\ F_x & F_y & F_z \end{vmatrix} \tag{4.50}$$

identically vanish in the case of constant force components, and the $\boldsymbol{F} \cdot d\boldsymbol{l}$ being an exact differential requirement, for which we have -

$$\frac{\partial F_x}{\partial l_z} = 0 = \frac{\partial F_z}{\partial l_x} \tag{4.51}$$

in the case of constant force components. It follows that the expression for the work given by Eq. (4.48) is now a path-independent function of state, as required in the definition of Availability. Hence those of constant external force components appear to be the correct conditions that yield a suitable path-independent formulation for the Availability -

$$dA = dU - dW = dU + 2F_x dl_x + F_z dl_z \leq 0 \tag{4.52}$$

These conditions are in agreement with the fundamental definition of Availability as a thermodynamic potential which is defined in terms of fixed external properties of the surroundings. Internal force components are readily output by the DFT code employed in this thesis, and the contours of constant shear force $F_z - F_x$ on the ground state energy surface of silicon have an appearance which

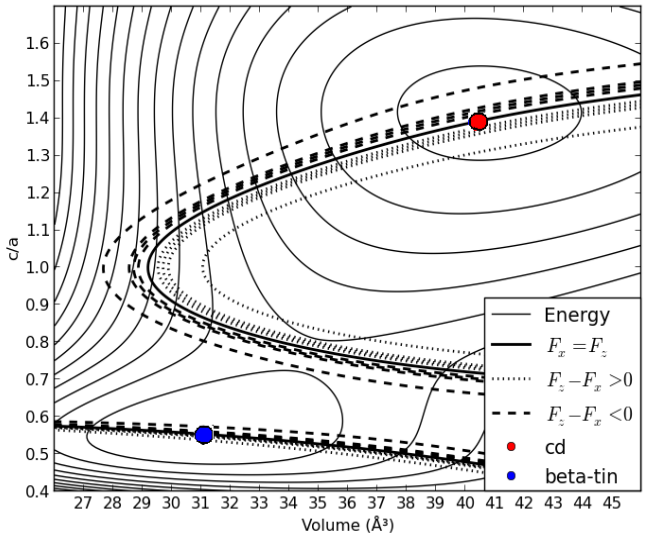


Figure 4.13: Appearance of the constant shear force contours on the DFT ground state energy surface of single-crystal silicon.

is very similar to that of the contours of constant shear stress $p_z - p_x$ considered previously, as can be deduced from Fig. 4.13.

Let us now integrate Eq. (4.52) between the two phases involved in the phase transition. We again require that the internal and external force components be in equilibrium at each phase, but we are not ultimately concerned with how the relationships between the two sets of forces varies during the progress of the integration since Eq. (4.52) expressed in terms of constant external force components is suitably a function of state, and consequently the magnitude of its change does not ultimately depend on the path of integration but only on the endstates. Given that the force components remain constant between the two phases but the lattice dimensions do not, we deduce that the pressure components will also be different between the two phases. The finite change in Availability

across the phase transition will in general be given by -

$$\Delta A = (U_2 - U_1) + 2F_x \left(l_x^2 - l_x^1\right) + F_z \left(l_z^2 - l_z^1\right) \leq 0 \tag{4.53}$$

The values of the forces at the transition point occur when the equality condition is met. Outside of phase equilibrium, the inequality is satisfied if phase 2 is relatively more stable than phase 1. In practice, this condition for phase stability can be implemented by plotting the function $A = U + 2F_x l_x + F_z l_z$ for the two phases along each contour of constant shear force as a function of F_z. The values of this function on the ground-state energy surface of silicon are shown in Fig. 4.14. At any given value of F_z, the difference between the two curves will be given by Eq. (4.53). The value of F_z where the two curves meet therefore provides us with an estimate of the transition force F^t at that value of shear force. The results of repeating this analysis as a function of varying shear force for the case of the *cd* to β-Sn phase transition in silicon are presented in Fig. 4.15. It can be deduced that all components of the transition force exhibit a decreasing trend with increasing degree of non-hydrostatic conditions. These results appear to be in agreement with the premise that the *cd* to β-Sn phase transition in silicon becomes more accessible by moving away from perfectly hydrostatic loading conditions. We note however that these results are not directly comparable with those obtained in the previous section under conditions of hydrostatic and uniaxial compression, since the conditions of constant average pressure p and uniaxial pressure p_z across the phase transition which apply in each of these two loading configurations respectively do not in fact represent special limiting cases of the constant force components condition considered here. This can be understood by

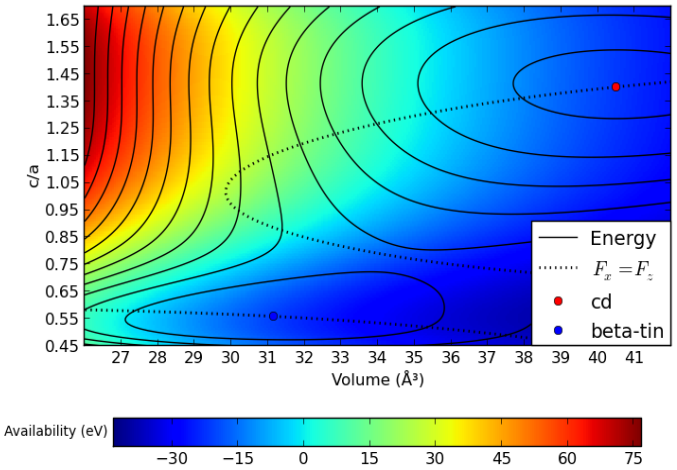


Figure 4.14: Colour plot of the values of the Availability $A = U + 2F_x l_x + F_z l_z$ on the DFT ground-state energy surface of silicon.

realising that if the two phases have the same pressure, then due to their different lattice dimensions they will in general have different force components, and vice-versa.

4.7 Evidence in support of the Availability formulation: pressure-induced phonon softening in silicon

We now focus on one particular aspect of the theory of the ideal strength of initially perfect crystalline metals whereby the fundamental microscopic mechanism responsible for imposing a limit upon its value is directly correlated with the appearance in reciprocal space of instabilities in the acoustic phonon spectra.

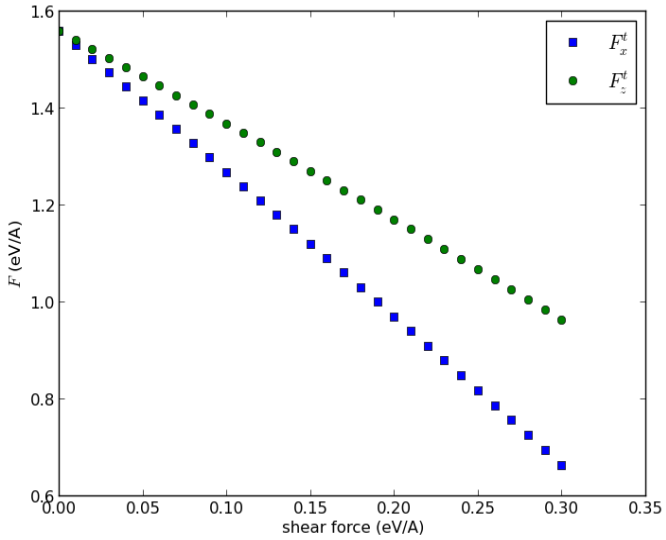


Figure 4.15: Evolution of the components of the transition force, F_x^t and F_z^t, for the *cd* to β-Sn phase transition in silicon as a function of non-hydrostatic shear force $F_z - F_x$.

Mechanical stability requires that the energies of phonons be positive and real for all wave vectors in the Brillouin zone. This can be understood by considering the simplest possible descriptive form for a phonon mode as a travelling mechanical wave inducing lattice vibrations within the crystal, and characterised by a spatial wave-vector $\mathbf{q}$ and a wave-vector dependent (dispersive) lattice vibrational frequency $\omega(\mathbf{q})$ -

$$A(\mathbf{r}, t) = A_0 e^{-i(\mathbf{r}\cdot\mathbf{q}+\omega(\mathbf{q})t)} \tag{4.54}$$

It can be seen that if $\omega(\mathbf{q})$ were to become imaginary, the amplitude of the wave would as a result grow exponentially, thus giving rise to an instability in the entire material. Unstable phonon waves of this type are commonly referred to as *soft*-phonon modes. A direct connection between mechanical instability and the onset of soft phonon modes in simple perfect crystalline metals was established only

recently through the ab-initio computational work of Clatterbuck and co-workers on aluminium under tension and shear [32]. This soft-phonon-mediated stability criterion was subsequently found by Kimminau *et al.* to be applicable also to the closely-related case of single-crystal copper subject to uniaxial compression along the $\langle 001 \rangle$ crystallographic axis and undergoing plastic deformation [132].

By implementing the small-displacement method for ab-initio phonon frequency computation [5], we observed a similar softening of the acoustic phonon modes in single-crystal silicon in the *cd* structure subject to both hydrostatic and uniaxial compression. This suggests that for the pressure range in which soft phonons are observed the material is structurally and mechanically unstable, thus paving the way for the phase transition to β-Sn to take place. The appearance of soft phonon modes with imaginary frequency therefore appears to constitute the fundamental driving mechanism underlying the occurrence of the phase transition. In particular, their point of onset in the high pressure *cd* structure provides us with an alternative indicator for estimating the transition pressure to β-Sn which is completely independent of any thermodynamical consideration, and which can therefore be used to corroborate the Availability-based transition force estimates derived in the previous section. Previous ab-initio investigations [62, 64, 244] appear to have missed this soft phonon phenomenon in silicon as a result of having been restricted to high-symmetry positions in the Brillouin zone only, whereas in the present study the complete phonon dispersion curve across the entire Brillouin zone of the crystal was explored.

The small-displacement method was implemented by making use of the PHON code [5] operated in conjunction with the VASP [141] DFT package for calculating the atomic forces required for the evaluation of the force-constant matrix

elements. During the course of this investigation, a $2 \times 2 \times 2$ super-cell (16 Si atoms in total), representative of a defect-free silicon single-crystal sample at 0 K, was adopted as the main simulation environment. The same DFT pseudopotential as the one employed in the previous chapter for performing the total ground state energy calculations was considered. The following input parameters were employed for the DFT-based force calculation: a plane-wave cutoff of 400 eV and a $2 \times 2 \times 2$ grid of special $\mathbf{k}$ points. The point of onset of the soft-phonons under high-pressure compression turned out to be very sensitive on the electronic smearing scheme being implemented, which in turn depends on the position $(c/a, V)$ on the ground state energy surface of silicon at which the phonon calculation is performed. For this reason, the parameters of the electronic smearing scheme were chosen upon calibration against the transition pressure of silicon under uniaxial compression, which is known to lie at around $p_z = 118$ kbar from enthalpy stability arguments, as explained in Section 4.5.2. In particular, the choice of a simple Gaussian smearing with smearing parameter of 0.03 eV resulted in the soft phonon modes appearing at a pressure of $p_z = 115.92$ kbar and hence in excellent agreement with the thermodynamic transition pressure. This combination of input parameters also yields results for the phonon dispersion curve at zero pressure which are in relatively good agreement with experiment, as can be deduced from Fig. 4.16.

The phase transition from *cd* to β-Sn under uniaxial compression occurs at the point $(c/a, V) = (1.31089, 37.67056)$. Due to the sensitivity of the electronic smearing parameters for reproducing the point of onset of the soft phonons on the location on the $(c/a, V)$ phase diagram of silicon, only contours of constant shear force whose corresponding phase transition point lies very close to that

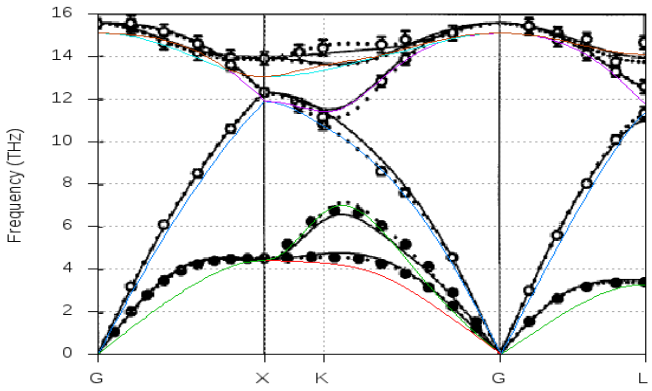


Figure 4.16: Complete phonon dispersion curve of silicon along high-symmetry directions in the Brillouin zone at ambient pressure calculated with the small-displacement method (coloured lines). The results are in good agreement with the experimental results reported in the literature shown in the background. In particular, the open circles are neutron scattering data from Ref. [44], and the closed circles are neutron data from Ref. [180]. The solid and dotted curves are derived from a best fit to the neutron and X-ray scattering data of Ref. [96]. The small discrepancies between the theoretical and experimental results, in particular across the transverse acoustic branch of the dispersion curve, are likely the result of the difference in temperature (all the experimental measurements were performed at room temperature at 300 K, whereas the ab-initio theoretical calculations of this thesis have been performed at 0 K) (background figure reproduced with permission from Ref. [96]).

under uniaxial compression can be directly analysed with this choice of input parameters. One such contour is that of +0.3 eV/Å, for which the phase transition can be predicted from the Availability construction to occur at force components of $F_x^t = 0.66206$ eV/Å and $F_z^t = 0.96206$ eV/Å (see Fig. 4.15), which corresponds to a position on the phase diagram of $(c/a, V) = (1.31055, 37.66047)$. The onset of soft-phonons for this particular contour of constant shear force was detected at force components of $F_z^t = 0.95955$ eV/Å and $F_x^t = 0.65955$ eV/Å, that is in excellent agreement with the aforementioned Availability-based esti-

mate of the transition force components. Furthermore, the soft phonon modes were observed to grow as the applied force components were increased beyond these transition values, as can de deduced from Fig. 4.17, signifying an increasing degree of instability of the *cd* structure beyond the phase transition point. Hence we conclude that the Availability formula proposed in the previous section for predicting transition forces under generic non-hydrostatic conditions correctly reproduces the point of onset of soft phonons for the case of constant shear force of +0.3 eV/Å . Unfortunately only one such test could be performed due to the lack of other contours of constant shear force whose transition point lies close to the case of uniaxial compression (this also applies to the transition point along the hydrostat), and therefore despite being supportive of the Availability method proposed in this chapter this test is not conclusive. However at the same time the possibility of a simple coincidence as an explanation for the agreement between the transition force results is unlikely.

4.8 Conclusions

We believe we have derived a valid and path-independent expression for the Availability in terms of force components, embodied by Eq. (4.53), which is valid under deformational conditions which are both non-hydrostatic and finite in nature. The significance of this conclusion in the theory of phase transitions under such conditions can be understood in the light of the role that the concept of Availability plays in the determination of phase equilibrium and consequently of the transition parameters of phase transitions. In particular, we have observed that this expression for the Availability correctly reproduces the point of onset of soft

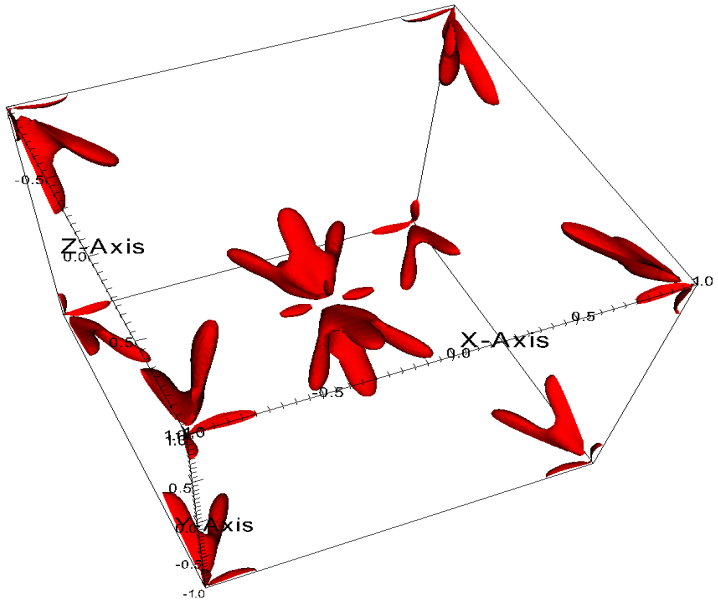


Figure 4.17: Appearance of the stress-induced soft phonon modes (shown as phonons with negative frequency enclosed within the red zero-frequency isocontour) in the Brillouin zone of silicon compressed along the +0.3 eV/Å constant shear force contour at a force of $F_x = 0.81414$ eV/Å and $F_z = 1.11414$ eV/Å. The unit cube enclosing the plot and labelling its orientation corresponds to the conventional unit cell of the reciprocal lattice of silicon. This type of plot can therefore deliver a complete overview of the entire Brillouin zone. The axis labelled as z represents the direction of uniaxial compression.

phonon instabilities for the case of the contour of constant +0.3 eV/Å shear force in single-crystal silicon. We do not however wish to label our results as definitive due to the lack of alternative research on this topic that could provide us with a comparative benchmark for our results.

Chapter 5

Molecular Dynamics simulations of the cubic diamond to *Imma* shock-induced phase transition in silicon

5.1 Introduction

The computational technique of classical Molecular Dynamics (MD) has already in the past proven an invaluable tool for modelling the response of condensed matter under the simulated effects of shock-compression [92, 93, 94], affording fully dynamic and time-resolved insight on the conduct of matter at the atomistic level. Beside the correct reproduction of the salient features of shock-induced phase-transitions in materials other than silicon, such as the $\alpha-\epsilon$ phase transition in single-crystal iron [117, 118, 119], recent accomplishments of MD simulations

of phenomena occurring during the propagation of shock-waves in solid matter include for example the modelling of the nucleation and propagation of crystalline defects such as dislocation and stacking faults in face-centred cubic materials undergoing plastic deformation [21, 23, 66, 95, 221], and the observation of shock-induced melting [14].

In the context of the research presented in this chapter, we aim to gather more evidence in support of the hypothesis advanced in this thesis that the mechanism behind the relief of shear stress in shock-compressed monocrystalline silicon could be provided directly by a shock-induced phase transition, without the need for an intermediate transient state of conventional plastic deformation as was believed previously. In particular, we aim to show that the overall microstructure of the mixed-phase region ensuing after the initial state of elastic uniaxial compression is consistent with this hypothesis, and that its onset and evolution as a function of increasing shock-wave velocity is in turn consistent with a simple thermodynamical analysis of the relative phase stability. Despite the simplicity of the arguments employed, this is the first time that such considerations have been applied to the case of a shock-induced polymorphic phase transition.

We are aware of only several previous publications in which the shock compression of crystals with the diamond cubic structure has been investigated with classical MD techniques, and in which the results obtained are directly comparable with the work presented here. On one hand, Oleynik and co-workers [181] performed a set of shock-propagation simulations in single-crystal silicon along the $\langle 100 \rangle$, $\langle 110 \rangle$ and $\langle 111 \rangle$ directions in the range of piston velocities from 1 to 4 km/s, in which they reported four different regimes of material response as the shock strength increased: simple elastic compression below the HEL, shock-

wave splitting into a second plastic wave, anomalous elastic response above the HEL justified in terms of a non-monotonic dependence of shear stress on uniaxial compression of the material, and a single over-driven plastic wave inducing amorphisation or chemical reactions. No mention was made of the possibility of a direct transition from elasticity to phase-transformation. On the other hand, Lane and Thompson [145] performed a similar set of simulations of germanium, in which this time they identified the onset of the phase transition to a new body-centred tetragonal structure and the consequent complete relief of shear stress as the driving mechanism without an intermediate state of plastic deformation, in agreement with the premise of this thesis. However their analysis still warrants further investigation since the explanations offered were generally-speaking mostly qualitative and grounded on macroscopic observations of the simulations rather than from the perspective of the response of the underlying crystal lattice, which is instead the approach we intend to take here. Similar results were reported by Lin, Perriot and co-workers [149, 192] for the case of diamond.

In the work discussed here we extend certain of the results outlined above. We present MD simulations of single-crystal silicon shock-compressed along the $\langle 001 \rangle$ direction. In agreement with other work on germanium and diamond [145, 149, 192] we find elastic response up until a critical stress, above which the shear stress is relieved by a fraction of the material undergoing a phase transformation. As in the germanium case described by Lane and Thompson [145], in our simulations of shock-compressed silicon we also identify a body-centred lattice in the new phase. However, a reciprocal space analysis of the sample provides more detailed information, and allows us to identify the new phase predicted by this potential to be *Imma*, rather than β-Sn. We demonstrate that the shock conditions under

which the transformation occurs within the simulations can be readily understood in terms of the relative enthalpy of the sample when compressed uniaxially, to that within the mixed phase region, assuming the material in the mixed phase is close to being in a hydrostatic condition. Furthermore, as the transition is inelastic rather than plastic (in the sense that the shear stress is not relieved by defect generation and motion), not only can the fractions of the phases in the mixed phase region be readily predicted, but the morphology of the banding structure between the two phases can be understood by considering the lattice parameters of the two phases in the mixed phase region and the condition of zero transverse strain. However, whilst our analysis provides a more detailed picture of what occurs at the atomic level within the simulations of shock-compressed silicon, it is the case, as with previous simulations, that the predicted onset of inelastic behaviour occurs at stresses considerably higher than those seen in experiment [80]. This may indicate that the potentials being used are still not yet capable of capturing the full pertinent physics, even if the mechanisms being revealed may be hinting at the underlying physics that occurs within such materials under shock compression. The work presented within this Chapter has been accepted for publication in Physical Review B [172].

5.2 Molecular Dynamics simulations

Two sets of multi-million atom MD simulations of uniaxial shock-wave propagation along the $\langle 001 \rangle$ direction in perfect single-crystal samples of silicon (modelled as microcanonical, or NVE, ensembles) were executed simultaneously in the context of the research presented in this chapter, differing only in the overall size

of the sample. On one hand the first set of smaller simulations, which we shall henceforth refer to as Set I, was considered for those tasks in which the final results sought were deemed to be relatively size-independent, and therefore the speed of the simulation was of high priority, whereas the second set (Set II) were much larger simulations, employed when the overall stability of the wave profiles was the most important criterion. Shock propagation along the two other main symmetry directions in the sample, $\langle 011 \rangle$ and $\langle 111 \rangle$, has not been considered in the context of the research presented in this chapter, and is indeed worthy of future investigation. The software package employed to perform the simulations was the freely-available LAMMPS code [196], which was run on massively-parallel supercomputing clusters. In both sets of simulations, shock-waves with propagation velocity U_s were launched into the system for interrogation through the impact of a piston only a few unit cells wide and with constant atomic velocity U_p ($< U_s$), following the initial thermalisation of the bulk sample at 300 K for 3 ps. Furthermore, periodic boundary conditions were imposed on the two dimensions transverse to the shock-propagation direction. The interatomic interactions in the sample were modelled with a modified semi-empirical bond-order Tersoff-like potential for silicon [223, 224, 225, 226], as parametrised by Erhart and Albe [56], which has in the past been compared with alternative potentials [8, 37, 211] and has proven successful in describing various structural properties of crystalline silicon such as elastic constants [106] and general thermodynamic properties [247], as well as the properties of the *cd* to β-Sn phase-transition under both hydrostatic and uniaxial compression [112, 146, 171]. In Set I, the sample cross-section was 30×30 unit cells, and 390 unit cells along the shock-wave propagation direction (the z -axis), corresponding to a total of 2,809,800 atoms. For all values of U_p, the

elastic shock-front reached the rear end of the sample and underwent reflection just after 23 ps from the start of the simulations, and unless otherwise stated 23 ps is the time when results from the Set I simulations are presented in everything that follows. In Set II, the sample dimension was of $100 \times 100 \times 1500$ unit cells, corresponding to 120,020,000 atoms in total. Piston velocities between $U_p = 1.4$ km s^{-1} and $U_p = 2.5$ km s^{-1} in steps of 0.1 km s^{-1} were explored in both cases. Finally, it is worth emphasising that all samples considered in this work have been modelled as perfect defect-free crystals, given that silicon can be manufactured with essentially zero defect density [215].

These simulations predict the onset of a high-pressure mixed-phase region ensuing directly after the initial region of elastic uniaxial compression, consisting on one hand of nearly-hydrostatically compressed silicon in a high-pressure *cd* structure and of material in the high-pressure *Imma* phase [161, 162] on the other. This *Imma* phase ensues directly after β-Sn in the sequence of structural phase transitions of silicon in order of ascending pressure at about 140 kbar under hydrostatic compression, and lies in a body-centred orthorhombic (bco) Bravais lattice with experimental lattice parameters a, b and c of 4.737 Å, 4.502 Å and 2.550 Å respectively at 130 kbar [162]. The corresponding crystal structure has a two-atom basis with atoms at the origin $(0, 0, 0)$ and at atomic position $\left(0, \frac{1}{2}, \Delta\right)$, where Δ is an extra degree of freedom which ranges between 0.25 and 0.5 and further distinguishes it from the β-Sn crystal structure, in which Δ takes the special value of 0.25. The significance of this Δ parameter relative to the customarily-used four-atom unit cell of the *Imma* phase is shown in Fig. 5.1. A summary of the special values that the four parameters of this cell, a, b, c and Δ, take in each of the *cd*, *Imma* and β-Sn phases in this four-atom unit cell

representation is presented in Table 5.1. The identity of the two phases in the mixed-phase region was confirmed by separating them by internal energy per atom (they can also be readily separated by the Centro-Symmetry Parameter (CSP)[1] [130]), calculating the Fourier Transform (FT) of the atomic co-ordinates, and analysing the resulting diffraction pattern in reciprocal space [131]. The lifting of symmetry in the basis of *Imma* leads to a reappearance of peaks in the FT which are forbidden by the cubic diamond (and by extension β-Sn) structure factor. The presence of these peaks in the FT confirms that the transformed material lies in the *Imma* phase, not the closely related β-Sn. Fig. 5.2 shows the position of the (002) diffraction spot in the observed pattern, which represents an example of a diffraction peak which would be forbidden by the β-Sn structure factor but is allowed by the *Imma* structure factor. The identity of the *Imma* phase was also confirmed independently by calculating the radial distribution functions from the real-space positions of the atoms in the simulations, as well as fitting simulated powder diffraction patterns. The real-space analysis of the atomic positions in particular provided us with an estimate of the c lattice parameter, and from there of the Δ parameter, of the *Imma* unit cell. These were measured respectively to be around 2.47 Å and 0.295 in the Set I simulations for the case of shock propagation at 1.6 km/s. The value of Δ is therefore not very different from the special case

[1] In solid-state systems the Centro-Symmetry Parameter is a useful measure of the local lattice disorder around an atom and can be used to characterise whether the atom is part of a perfect lattice, a local defect (e.g. a dislocation or stacking fault), or at a surface. This parameter is computed using the following formula from Kelchner [130], $CSP = \sum_{i=1}^{N/2} \left| \overrightarrow{R_i} + \overrightarrow{R}_{i+N/2} \right|^2$, where the N nearest neighbours for each atom are identified and R_i and $R_{i+N/2}$ are vectors from the central atom to a particular pair of nearest neighbours. There are $N(N-1)/2$ possible neighbour pairs that can contribute to this formula. The quantity in the sum is computed for each, and the $N/2$ smallest are used. This will typically be for pairs of atoms in symmetrically opposite positions with respect to the central atom; hence the $i + N/2$ notation.

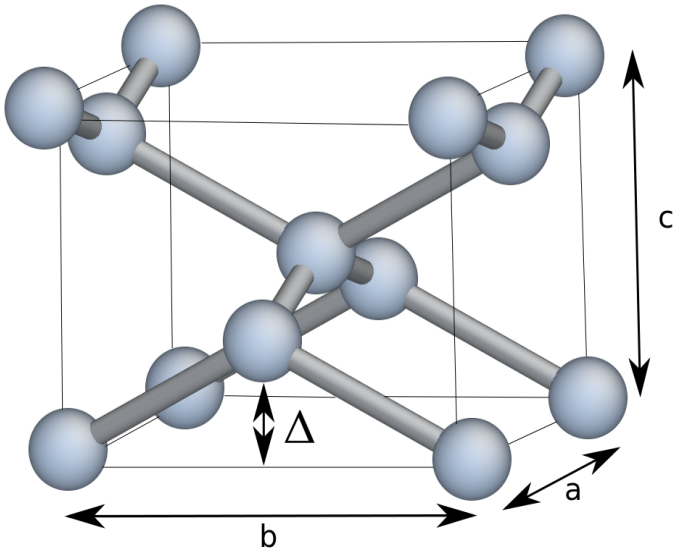


Figure 5.1: Four-atom unit cell of the orthorhombic *Imma* phase, where a, b and c are the lattice parameters and Δ is the degree of freedom in the atomic position of the second atom in the two-atom basis at $\left(0, \frac{1}{2}, \Delta\right)$.

of β-Sn of 0.25. Furthermore, the estimate of c is in reasonable agreement with the values extracted from the position of the diffraction spots in the FT of the *Imma* phase, which are listed in Fig. 5.3 as a function of piston velocity. The values of the a and b parameters will be shown later in this chapter.

The potential considered in this work does not in fact quite capture the phase transition to β-Sn, which should have preceded *Imma* had the potential been con-

Table 5.1: Crystallographic structural parameters of the four-atom unit cell for the three phases considered in this work.

Structure	b/a	c/a	Δ	Space Group
Cubic Diamond	1	$\sqrt{2}$	0.25	$Fd\bar{3}m$
β-Sn	1	free	0.25	$I4_1/amd$
Imma	free	free	free	*Imma*

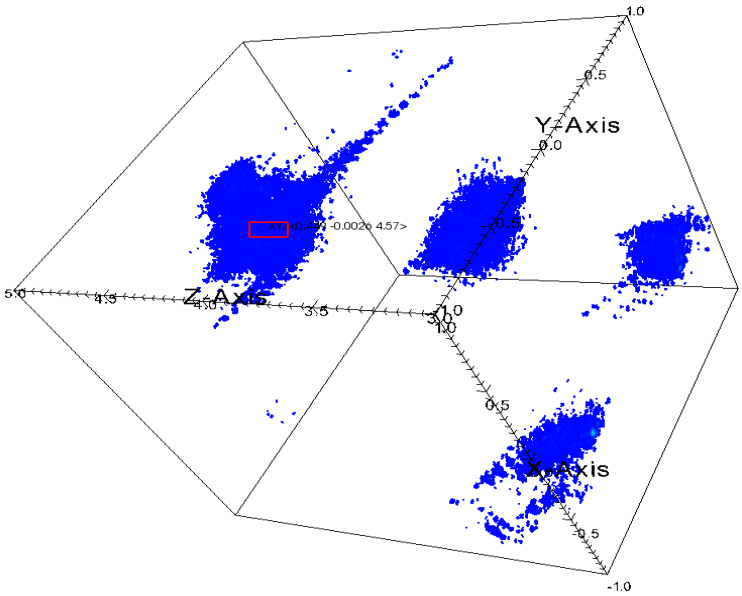


Figure 5.2: Position of the (002) diffraction spot in the observed diffraction pattern of the *Imma* phase. As shown in the figure, the position of the centre of the spot is roughly at $x = 0.449, y = -0.0026, z = 4.57$ in reciprocal space, which corresponds to a value of the c lattice parameter of 2.365 Å. This is in good agreement with the estimates of c provided in Fig. 5.3.

sistent with the sequence of structural phase transitions of Si in order of ascending pressure. This shortcoming of the potential however is relatively unimportant in the context of the present study given the similarities in both structure and dimensions between the bct and bco lattices of the two phases.

A typical simulation from Set I for a particle velocity of 1.6 km s^{-1} is shown in Fig. 5.4, where the atoms have been colour-coded according to their CSP [130]. An elastic precursor is observed, followed by a region of bands of interlocking parallelepipeds composed of material in the *Imma* phase, and lying inclined at an angle relative to the sides of the simulation box across the (111) crystallographic plane of the compressed sample. Only two such planes of the banding structure are activated in the Set I simulations due to the deliberately restrictive size of

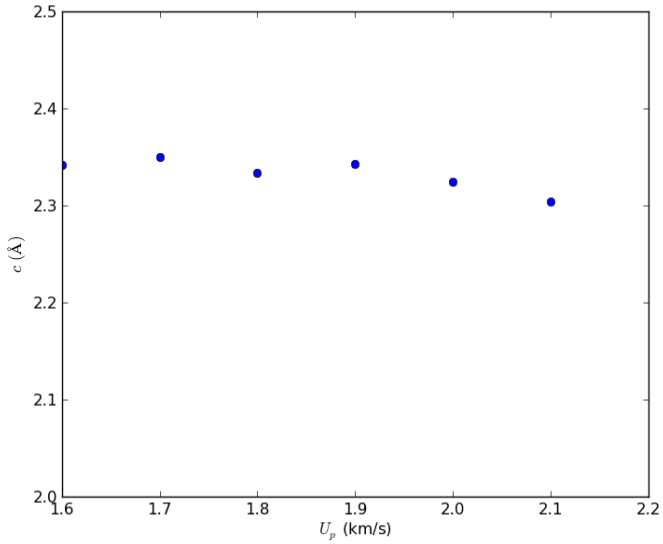


Figure 5.3: c lattice parameter of the *Imma* unit cell as a function of U_p. It can be seen that its value stays roughly constant at around 2.35 Å.

the cross-sectional area, whereas in the larger Set II simulations all four planes have been observed to be activated as shown in Fig. 5.8. The Set I simulations therefore afford for a cleaner and simpler picture of the banding structure, and for this reason much of the ensuing analysis of the microstructure of the phase transition presented in the remainder of this chapter will be performed on these smaller simulations. The larger Set II simulations on the other hand are not readily amenable for structural analysis due to the complicated nature of the banding structure observed there. Qualitatively however, the same phenomena are observed to occur in the two sets of simulations, including the shock-induced phase transition and the ensuing relief of shear stress, and both sets therefore offer the same degree of physical insight into these phenomena. The onset of the mixed-phase banding structure was first detected at a particle velocity of 1.6 km s^{-1} in the Set I simulations, and slightly lower at 1.5 km s^{-1} in the Set II

simulations. It was then observed to dominate the response of the sample up to around 2.1 km s^{-1}, at which point it started to be gradually eroded by shock-induced melting (which was confirmed by the onset of considerable diffusion of individual atoms). In most of the results that follow (unless otherwise stated) we will therefore restrict the analysis to values of U_p below 2.3 km s^{-1}, before melting becomes significant.

The two types of material behaviours predicted by the simulations, elasticity and inelastic phase-transitioning, together give rise to a two-wave profile for the shock-loading process. The two-wave profile in the stress due to the phase transformation is shown in Fig. 5.5, together with the evolution of the residual shear stress as a function of distance, for a shock of particle velocity 1.9 km s^{-1}. We find that the degree of relief of the shear stress increases as a function of particle velocity U_p, as shown in Fig. 5.6, until it eventually vanishes altogether at the onset of the shock-induced melting. The shock Hugoniot of the material in the form of a plot of pressure P against specific volume $1/\rho$ is also shown in Fig. 5.7 for completeness. As explained earlier, the Set I simulations were used to perform most of the analysis on the microstructure due to the simplicity of the banding structure there. In particular, the region of the simulations encompassing the stable part of the pressure and particle velocity profiles, with a typical width of 300 Å, was considered for performing this analysis. Longer simulations were used to confirm that the final states reached were indeed stable on the timescales accessible to simulation. We have also made a spot check of the normal component of the pressure on either side the interface between the two phases and found that they agree within 3%, further confirming that the mixed phase system is close to equilibrium (if the normal pressures were different, one phase would still continue

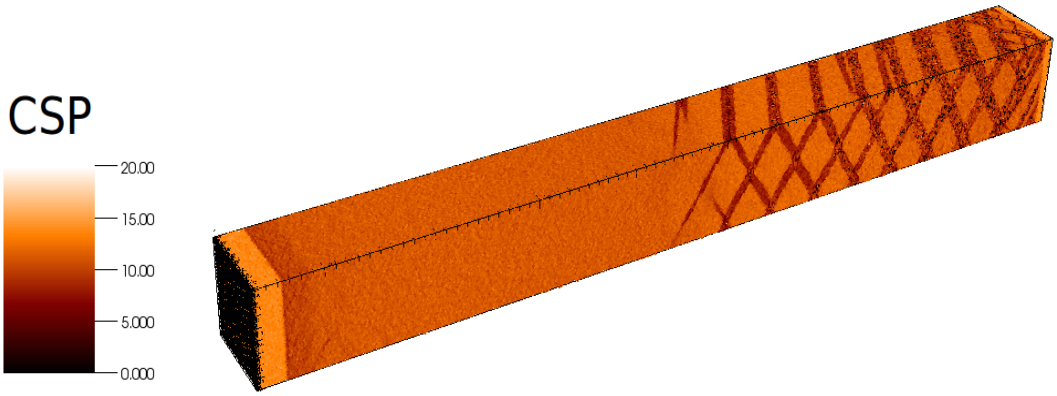


Figure 5.4: Example of a Set I simulation of shock-wave propagation (from right to left) in single-crystal Si at a particle velocity of 1.6 km s^{-1}, and 23 ps after the start of the simulation. The atoms are color-coded according to their CSP [130]. The CSP is higher for the material in the *cd* phase depicted in light orange (around 11.5 $Å^2$) than for the remaining *Imma* phase shown in darker red (around 6 $Å^2$). Note that at the points where the bands of *Imma* phase intersect the value of CSP drops to nearly zero (coloured in black), possibly as a result of stress-concentration effects. The structure of intersecting parallelepipeds of *Imma* material that constitutes the mixed-phase region is clearly visible, together with the region of elastic compression that precedes it.

to grow at the expense of the other).

The overall appearance of the banding of this mixed-phase region is qualitatively very similar to the results reported by Lane and Thompson [145] in their simulations of shock-compressed germanium. In agreement with their results, we find that rather than defect-mediated plasticity, it is the phase transition itself that relieves the shear stress in the uniaxially-compressed lattice - what might be termed an inelastic, rather than plastic response. Conversely, the relief of shear stress can be thought of as the mechanism driving the phase transition. Exactly how this relief is accommodated within the morphology of the banding structure will be the object of the next section. An analysis of the mixed phase

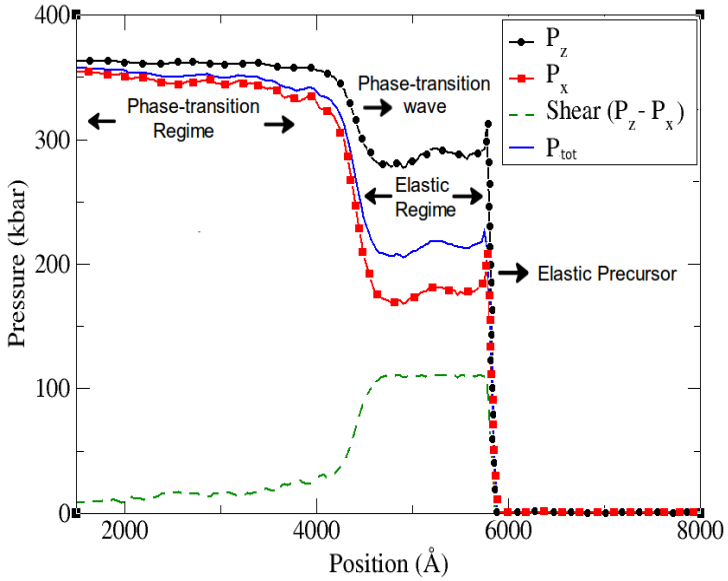


Figure 5.5: Wave profiles as a function of position in the sample of the pressure components P_x and P_z, together with those of the total pressure $P_{tot} = \frac{1}{3}(P_x + P_y + P_z)$ and the shear stress $P_z - P_x$, for the Set II simulation at $U_p = 1.9$ km s^{-1}. The positions of the elastic precursor front and the ensuing phase transition wave are indicated.

region in reciprocal space shows its usefulness in distinguishing between defect-mediated plasticity, and inelastic behaviour. As the material is compressed under conditions of uniaxial strain, the total strain transverse to the shock propagation direction is zero. For any general material response, this means that the total strain transverse to the shock, $\epsilon^{\mathrm{T}}_{\mathrm{Tot}}$, composed in principle of both elastic strain, $\epsilon^{\mathrm{T}}_{\mathrm{e}}$, and plastic strain, $\epsilon^{\mathrm{T}}_{\mathrm{p}}$, is zero. That is to say $\epsilon^{\mathrm{T}}_{\mathrm{Tot}} = \epsilon^{\mathrm{T}}_{\mathrm{e}} + \epsilon^{\mathrm{T}}_{\mathrm{p}} = 0$. In the case of defect-mediated plasticity in the absence of a phase transition, it is the finite plastic strain, $\epsilon^{\mathrm{T}}_{\mathrm{p}}$, caused by the generation and motion of defects, that gives rise to a negative elastic strain transverse to the shock propagation (i.e. a compression of the mean spacing of the lattice in this direction). As the lattice is already compressed along the direction parallel to the shock propagation, this

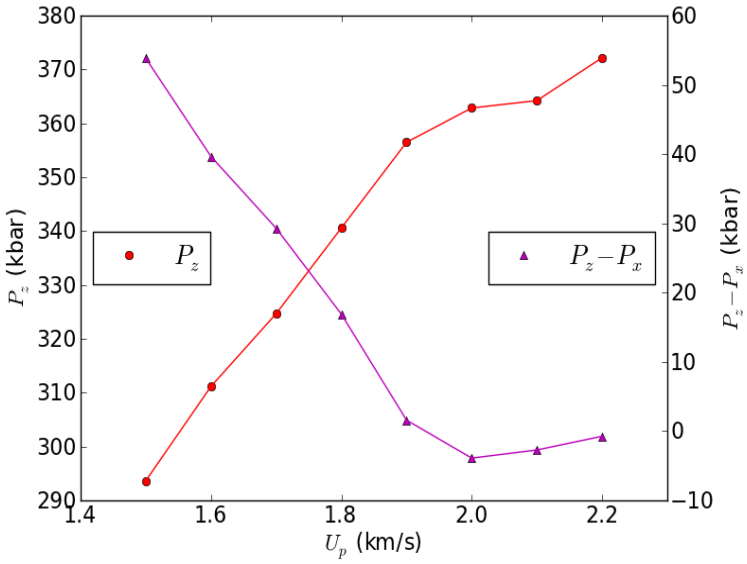


Figure 5.6: Values from the Set II simulations of the pressure component P_z and of the residual shear stress $P_z - P_x$ across the stable part of the phase transition wave. The magnitude of the shear stress at the end of the phase transformation process gradually decreases from the first occurrence of the phase transition at 1.5 km s^{-1}, until it is essentially fully relieved by $U_p = 2.0$ km s^{-1} as a result of the onset of the new liquid phase.

results, for an initially cubic material, in the average unit cell changing from being tetragonal (under elastic compression) back to cubic yet further compressed - and thus the material is closer to the hydrostat. As with X-ray diffraction, an FT of the material reveals the elastic strain (owing to the random nature of the defects, which thus do not contribute in large amplitude to the FT signal).

The mechanism behind the inelastic behaviour observed here is qualitatively different. In this case, there is no defect mediated plasticity, and thus $\epsilon_{\mathrm{p}}^{\mathrm{T}}$, and hence $\epsilon_{\mathrm{e}}^{\mathrm{T}}$, are both zero. The relief of the shear stress occurs directly due to the phase transition. The new phase (in this case *Imma*) has a lattice spacing in the transverse direction which is larger than the lattice spacing of the unshocked *cd*

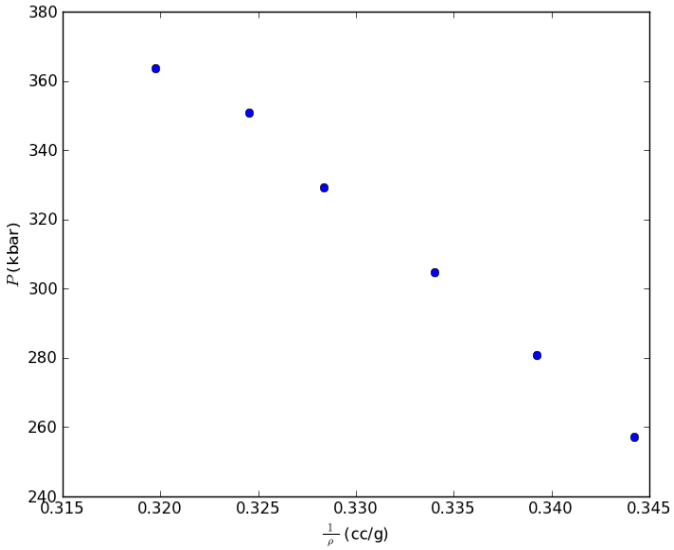


Figure 5.7: Inelastic branch of the Shock Hugoniot curve of the sample obtained from the pressure P and specific volume $1/\rho$ data-points across the stable part of the phase-transition wave as calculated in the Set II simulations for the range of U_p between 1.5 km/s to 2.0 km/s.

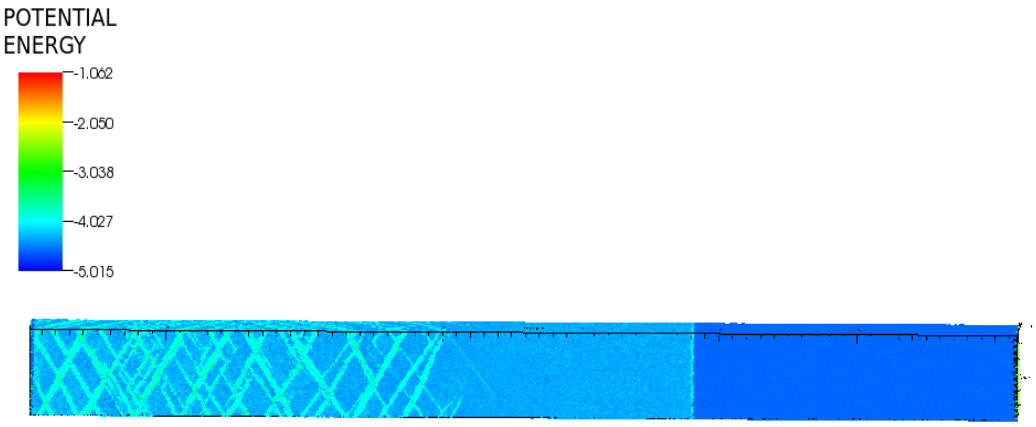


Figure 5.8: Example of a large Set II simulation of shock-wave propagation in single-crystal Si at a particle velocity of 1.6 km s^{-1}. The atoms are color-coded according to their potential energy. The complicated nature of the mixed-phase region compared to that observed in the smaller Set I simulation of Fig. 5.4 is clearly visible.

phase, and thus the transformation of material to the *Imma* phase necessitates a reduction in the lattice spacing of the *cd* phase, driving it towards the hydrostat. We can decompose the total elastic strain in the transverse direction into the elastic strain within the *Imma* and *cd* phases, $\epsilon^{\mathrm{T}}_{\mathrm{e,Imma}}$ and $\epsilon^{\mathrm{T}}_{\mathrm{e,cd}}$, where now $\epsilon^{\mathrm{T}}_{\mathrm{e,Imma}} + \epsilon^{\mathrm{T}}_{\mathrm{e,cd}} = 0$.

This interpretation is readily borne out by an analysis of the mixed-phase region in reciprocal space. Fig. 5.9 shows a slice through reciprocal space (k-space) across the $k_z = 0$ plane. Note that each of the original (220) reflections has split in two, and are located either side of the position of the (220) reflection of the unshocked material (which we have confirmed is also the position of the peak for the material in the region which is elastically compressed). The generation of this FT using only atoms in the *Imma*, and then *cd*, phase, confirms that the intensity in reciprocal space further from the origin is due to the atoms in the *cd* phase (their lattice spacing has reduced in real space, thus increased in reciprocal space), whereas the intensity closer to the origin is due to the *Imma* phase. Inelastic behaviour, as discussed above, is confirmed by the fact that the weighted mean of the intensity remains at the original (220) position, which would not be the case in a situation of defect-mediated plasticity (as observed by Bringa and co-workers for Cu [21]).

5.3 Morphology of the mixed-phase region

As noted above, we find that the shear stress in the mixed-phase region is relieved due to the phase transformation: a contraction of the lattice parameter of the *cd* material transverse to the shock is accommodated by the larger lattice parameter

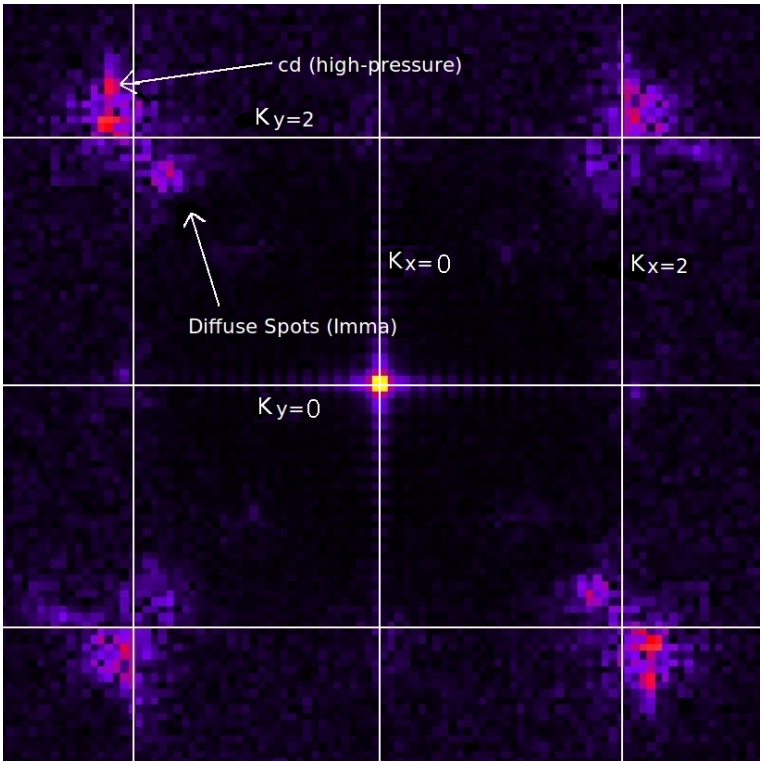


Figure 5.9: Fourier Transform image of the real-space atomic positions in the mixed-phase region. The region shown is the $k_z = 0$ plane between the $k_x \pm 3$ and $k_y \pm 3$ limits (the k-axes of the reciprocal plane are in units of $2\pi/a_o$, where a_o is the lattice constant of the uncompressed cubic diamond structure). The equilibrium positions of the {220} diffraction spots are highlighted. The signals corresponding to the two phases on both sides of each of these spots are also labelled.

in this direction of the *Imma* phase, with the total number of unit cells transverse to the shock propagation direction remaining constant. In this model, a greater fraction of the new phase will allow for a larger accommodation of shear strain, and as such, the fraction of *Imma* will increase with pressure.

We now establish the relation between the condition of relief of shear stress across the mixed-phase region and its microstructure, and in particular the dimensions of the elementary unit cells of the various phases involved. In the context

of the analysis presented here, we will refer to the coordinate system explained in Fig. 5.10 to describe the orientation of the planar surfaces of a single representative parallelepiped of *Imma* phase in the mixed-phase banding structure. We will also assume for simplicity that all individual unit cells have their sides aligned with the axes of this coordinate system, thus neglecting for the moment the effects of lattice rotations which will be discussed later. It follows from this that the inclination of the parallelepipeds relative to the sides of the containing box, described by the two angles θ and ϕ , results from the *Imma* unit cells being stacked in steps along both of these dimensions, with atoms being shared at the corners of the unit cells to avoid atom-duplication. The angles θ and ϕ are therefore related to the lattice parameters a, b and c of the orthorhombic unit cell of the *Imma* phase as shown in the inset of of Fig. 5.10. This yields the following relations which effectively establish a direct connection between the overall macroscopic morphology of the banding structure and the microscopic dimensions of the constituent unit cells -

$$\begin{aligned} \tan\theta &= \tfrac{b}{c} \qquad (a) \\ \tan\phi &= \tfrac{a}{c} \qquad (b) \\ \sin\theta &= \tfrac{b}{\sqrt{b^2+c^2}} \qquad (c) \\ \cos\theta &= \tfrac{c}{\sqrt{b^2+c^2}} \qquad (d) \end{aligned} \tag{5.1}$$

Let us assume full relief of shear stress within the cubic diamond phase, i.e. that $a_{cd} = b_{cd}$ (note that henceforth, *cd* should be understood to refer to the high-pressure cubic diamond material unless otherwise stated). At this stage we are therefore left with the following three degrees of freedom that the parallelepipeds can adopt to accommodate the relief of shear stress: angles θ and ϕ, and the

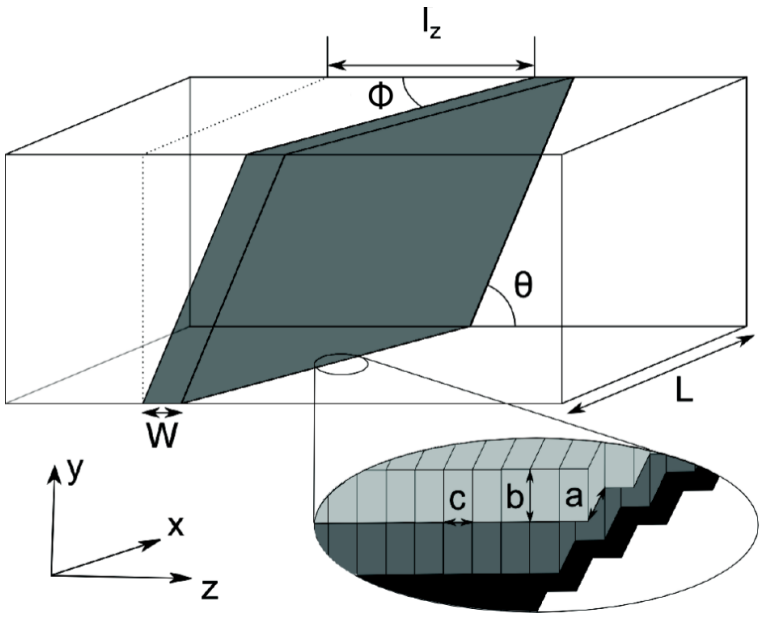


Figure 5.10: Reference system employed in this study to describe the orientation of a parallelepiped of *Imma* material (shown in dark grey): x,y,z are the orthogonal Cartesian axes, θ and ϕ are the angles that the parallelepiped makes to the sides of the simulation box containing it, W is the thickness of the parallelepiped, and L is the square cross-sectional dimension of the box. The inset below the figure shows how the individual *Imma* unit cells are stacked on top and next to each other. Only one parallelepiped is shown here for representative purposes, but in the actual simulations the box, of length l_z along the z-axis, contains the volume of exactly four such parallelepipeds.

band width W, as defined by Fig. 5.10. In order to pin-down any microscopic relation between them that can be reconciled with the overall morphology of the banding structure exhibited empirically in the simulations, we shall now consider the square cross-sectional area of the sample across the $x-y$ plane transverse to the shock-propagation direction, and impose on it those structural constraints that apply during the entirety of the shock-wave loading process, namely conservation of transverse length (width) of the sample and conservation of transverse number of unit cells. The physical origin of both of these constraints stems intu-

itively from the fact that the external loading force exerted on the sample by the piston, and then in turn by the shock-front, is directed entirely uniaxially along the shock-propagation direction, which effectively precludes any net mass flow in the form of atom movement from occurring transversely to this direction out of the original area of the cross-sectional plane (which therefore behaves effectively as an isolated system containing only the internal response forces of the sample). Hence the lateral dimensions of the sample are bound to remain fixed, and since all phases involved contain eight atoms in their conventional unit cells, the total number of unit cells also remains fixed in any transverse direction. It also follows that these two constraints do not apply to the longitudinal direction, along which there is a net external force. The model presented here does not therefore provide any information about the z dimension of the sample and the c lattice parameter of the unit cells. In what follows, we shall use the term φ to denote the angular direction of a generic vector on the $x-y$ plane, since in general the two constraints apply along any direction on the transverse plane, although the final answer will ultimately emerge from considering just the x ($\varphi = 0°$) and y ($\varphi = 90°$) directions independently. The first condition of conservation of transverse length between the initial un-shocked lattice in the equilibrium *cd* structure and the final mixed-phase state can be expressed simply as -

$$N_I(\varphi)\, a_I(\varphi) + N_{cd}(\varphi)\, a_{cd}(\varphi) = N_o(\varphi)\, a_o(\varphi) \Rightarrow L_I(\varphi) + L_{cd}(\varphi) = L_0(\varphi) \quad (5.2)$$

where all quantities depend on φ in general. N_I, N_{cd} and N_0, a_I, a_{cd} and a_0, and L_I, L_{cd} and L_0 are respectively the number of unit cells, lattice parameter ad total length for the *Imma* phase, *cd* phase and the un-shocked material along the

transverse direction φ. Eq. (5.2) can be more neatly expressed in terms of the fraction of number of unit cells f_i for phase i relative to the total initial number N_o -

$$f_i(\varphi) = \frac{N_i(\varphi)}{N_o(\varphi)} \tag{5.3}$$

which is done by dividing Eq. (5.2) through by $N_o(\varphi)$ -

$$\begin{aligned} &\tfrac{N_I(\varphi)}{N_o(\varphi)} a_I(\varphi) + \tfrac{N_{cd}(\varphi)}{N_o(\varphi)} a_{cd}(\varphi) = a_o(\varphi) \\ &\rightarrow f_I(\varphi)\, a_I(\varphi) + f_{cd}(\varphi)\, a_{cd}(\varphi) = a_o(\varphi) \end{aligned} \tag{5.4}$$

The number fraction f_i must be distinguished from the length fraction for phase i, which we shall denote as f_i^l instead -

$$f_i^l(\varphi) = \frac{N_i(\varphi)\, a_i(\varphi)}{\sum_i N_i(\varphi)\, a_i(\varphi)} = \frac{N_i(\varphi)\, a_i(\varphi)}{N_o(\varphi)\, a_o(\varphi)} \tag{5.5}$$

It follows from Eq. (5.2) that this definition of length fraction f_i^l is already properly normalised, in that $\sum_i f_i^l(\varphi) = 1$. The same is not true to the number fraction f_i at this stage, for which we first need to introduce the second constraint, namely that the number of unit cells along any transverse direction is also conserved across the shock -

$$N_o(\varphi) = N_I(\varphi) + N_{cd}(\varphi) \tag{5.6}$$

from which it follows that $\sum_i f_i(\varphi) = 1$. From their definitions, the length and

number fractions are related to each other as follows -

$$f_i(\varphi) = f_i^l(\varphi) \frac{a_o(\varphi)}{a_i(\varphi)} \tag{5.7}$$

Before proceeding any further with imposing the above constraints on the shape of the parallelepipeds, we need to evaluate the intersection of the parallelepipeds with the $x-y$ plane. This requires deriving first the equations of their planar surfaces. For simplicity we shall make use of the elementary form for the equation of a plane in Cartesian geometry relative to the coordinate system explained in Fig. 5.10 -

$$n_x x + n_y y + n_z z + d = 0 \tag{5.8}$$

in which $d = D\sqrt{n_x^2 + n_y^2 + n_z^2}$, with D being the distance of the plane to the origin. From the geometry of Fig. 5.10, D corresponds to -

$$D = \frac{W}{2} \sin\theta \tag{5.9}$$

Let's restrict our attention to just one of the two surfaces of the parallelepiped of Fig. 5.10 with span vectors $\overrightarrow{s_1}$ and $\overrightarrow{s_2}$, and normal vector $\overrightarrow{n}$ given by their cross-product -

$$\begin{aligned} \overrightarrow{s_1} &= \left(1, 0, \tfrac{1}{\tan\phi}\right) \\ \overrightarrow{s_2} &= \left(0, 1, \tfrac{1}{\tan\theta}\right) \\ \overrightarrow{n} &= \left(\tfrac{1}{\tan\phi}, \tfrac{1}{\tan\theta}, -1\right) \end{aligned} \tag{5.10}$$

The corresponding equation of the plane given by Eq. (5.8) therefore is -

$$\left(\frac{1}{\tan\phi}\right)x+\left(\frac{1}{\tan\theta}\right)y-z-\frac{W\sin\theta}{2\tan\phi\tan\theta}\sqrt{\tan^2\theta+\tan^2\phi+\tan^2\phi\tan^2\theta}=0 \tag{5.11}$$

The intersection between the above plane and the $x-y$ plane ($z=0$) consequently lies along the following line -

$$y=-\frac{\tan\theta}{\tan\phi}x+\frac{W\sin\theta}{2\tan\phi}\sqrt{\tan^2\theta+\tan^2\phi+\tan^2\phi\tan^2\theta} \tag{5.12}$$

It can be shown that the other side of the parallelepiped, together with the second parallelepiped bisecting it, give rise to similar intersection lines on the other quadrants of the $x-y$ plane expressed by the following set of four equations corresponding to all $\pm$ sign combinations -

$$y=\pm\frac{\tan\theta}{\tan\phi}x\pm\frac{W\sin\theta}{2\tan\phi}\sqrt{\tan^2\theta+\tan^2\phi+\tan^2\phi\tan^2\theta} \tag{5.13}$$

Hence the overall intersection pattern between the two parallelepipeds and the $x-y$ plane is as shown in Fig. 5.11. The symmetry of the pattern stems from the original choice of the origin of the coordinate system in Fig. 5.10 at the centre of the parallelepipeds. This is the most convenient choice since as a result all four quadrants of the $x-y$ plane are equivalent to each other, which means that we can restrict our analysis to just one of them.

In order to derive an expression for the length fraction of the *Imma* phase along any generic transverse direction φ, we need to find the intersection between Eq. (5.12) and the line at an angle φ to the x-axis described by the equation $y=\tan\varphi x$. For $\varphi<45°$, this vector is of length $L(\varphi)=l\sqrt{1+\tan^2\varphi}$, whereas

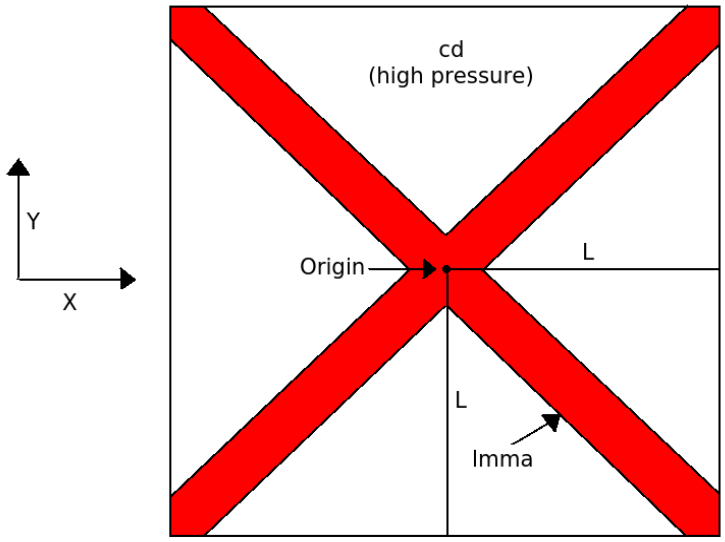


Figure 5.11: Slice through a pair of bisecting parallelepipeds of *Imma* structure as seen on the $x-y$ plane. Each side of the resulting X-pattern corresponds to one of the four equations in Eq. (5.13).

for $\varphi > 45°$ it is of length $L(\varphi) = l\sqrt{1+\frac{1}{\tan^2\varphi}}$. Calculating the intersection between this vector and Eq. (5.12), and subsequently dividing the result by the total transverse length $L(\varphi)$ yields the following expressions for the length fraction of the *Imma* phase -

$$\begin{aligned} f_{I^l}(\varphi) &= \frac{W}{2l}\frac{\sin\theta}{(\tan\varphi\tan\phi+\tan\theta)}\sqrt{\tan^2\theta+\tan^2\phi+\tan^2\phi\tan^2\theta}\,(\varphi<45°) \\ &= \frac{W}{2l}\frac{\tan\varphi\sin\theta}{(\tan\varphi\tan\phi+\tan\theta)}\sqrt{\tan^2\theta+\tan^2\phi+\tan^2\phi\tan^2\theta}\,(\varphi>45°) \end{aligned} \tag{5.14}$$

The number fractions of *Imma* unit cells f_I along the special cases of the x and y axes can be found by substituting $\varphi = 0°$ and $\varphi = 90°$ in the above formulae for the length fraction f_I^l, and then making use of Eq. (5.7) to convert between f_I^l and f_I. Finally, all terms involving the angles θ and ϕ can be replaced with the lattice parameters of the *Imma* unit cell through the set of relations in Eq.

(5.1). The final result is the same for both the x and y directions -

$$f_I\left(\varphi = 0°, 90°\right) = \frac{W}{2l}\frac{a_o}{a}\frac{1}{\sqrt{b^2+c^2}}\sqrt{b^2+a^2+\frac{a^2b^2}{c^2}} \tag{5.15}$$

The above result represents the total fraction for all *Imma* material present in the banding structure along these two special directions, even though it was derived by considering just one of the two intersecting parallelepipeds. This can be understood upon inspection of Fig. 5.11.

We now revert our attention back to the original issue of under which conditions the parallelepipeds in the banding structure satisfy the two constraints of conservation of transverse length of the sample and transverse number of unit cells within their empirical morphology exhibited in the simulations. The former constraint is inherently satisfied, for the parallelepipeds always manifest themselves within the original bounds of the simulation box, and therefore does not by itself impose any limits on the combination of values that θ, ϕ and W can adopt. The exercise therefore reduces to imposing the constraint of conservation of transverse number of unit cells on the shape of the parallelepipeds. It suffices to consider the two special directions along x and y in turn, for which the shape of the parallelepipeds is expressed by Eq. (5.15), and solve the resulting system of two simultaneous equations. In both cases the first step involves expressing the constraint in terms of the total length L_i of the material of phase i. For the

case of the x direction ($\varphi = 0°$), the procedure is as follows -

$$\begin{aligned} & N_{cd} + N_I = N_o \\ \rightarrow & \tfrac{L_{cd}}{a_{cd}} + \tfrac{L_I}{a} = \tfrac{L_o}{a_o} \\ \rightarrow & \tfrac{(l-L_I)}{a_{cd}} + \tfrac{L_I}{a} = \tfrac{l}{a_o} \\ \rightarrow & \tfrac{L_I(a_{cd}-a)+la}{a_{cd}a} = \tfrac{l}{a_o} \end{aligned} \tag{5.16}$$

where for $\varphi = 0$, L_I is given by -

$$L_I = \frac{W}{2}\frac{1}{\sqrt{b^2+c^2}}\sqrt{b^2+a^2+\frac{a^2b^2}{c^2}} \tag{5.17}$$

For the alternative case of the y direction ($\varphi = 90°$), the equivalent of the above analysis yields -

$$\frac{L_I\,(a_{cd}-b)+lb}{a_{cd}b} = \frac{l}{a_o} \tag{5.18}$$

where this time L_I is given by -

$$L_I = \frac{W}{2}\frac{b}{a}\frac{1}{\sqrt{b^2+c^2}}\sqrt{b^2+a^2+\frac{a^2b^2}{c^2}} \tag{5.19}$$

It can be shown that solving Eq. (5.18) and (5.16) simultaneously together with their corresponding expressions for L_I yields the final answer that $a = b$ for the *Imma* unit cell. This is the special condition according to which the parallelepiped structure satisfies the constant unit cell number constraint along x and y simultaneously. Even with $a = b$ however the *Imma* unit cell remains different from that of β-Sn due to the Δ factor in Fig. 5.1, which remains a free-parameter. A simple geometrical realization of this result, as shown in Fig. 5.12, follows by noticing that the x and y dimensions are not completely independent,

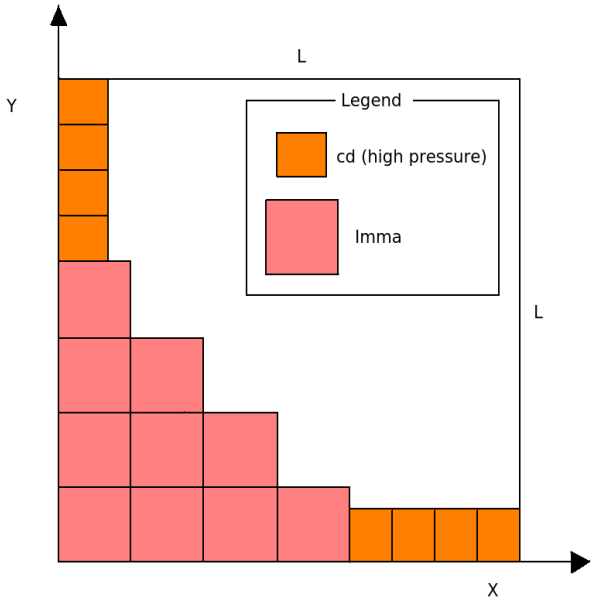


Figure 5.12: View of the intersection pattern between a single parallelepiped of *Imma* phase and the $x-y$ plane, broken into its constituent unit cells. From the slope of Eq. (5.12), it can be deduced that the x and y dimensions must have the same number of *Imma* unit cells. Applying the constraint of conservation of transverse number of unit cells along x and y, it also follows that the number of *cd* unit cells must also be the same in these two directions. At the same time we assume that the *cd* structure is hydrostatic and that $a_{cd} = b_{cd}$, implying that the *cd* fraction along each of x and y is of the same length. Consequently the *Imma* fraction must also be of equal length on both dimensions upon application of the second constraint of conservation of transverse length. The equivalence of the length fraction and number of unit cells of the *Imma* phase between x and y establishes the final result that $a = b$.

but are linked by the slope of Eq. (5.12), which in turn is linked to the ratio b/a of the lattice parameters of the *Imma* unit cell.

It must be emphasised that the picture of the lattice offered in Fig. 5.12 is drastically simplified. The interface between the two phases in particular is likely to be significantly more complicated than the simple stacking of unit cells shown in the picture, which in fact could be contested to be unphysical simply on the grounds of the duplication of atoms that it generates at the corners of the unit

cells. That of crystal interfaces between structural phases with different lattice dimensions is a complex topic, which often involves the mediation of dislocations and other interface defects similar to those which occur in the epitaxial growth of crystals on substrates of a different material. A detailed analysis of these interface effects in the context of the banding structure model presented here lies however beyond the scope of this investigation, and we shall therefore consider Fig. 5.12 as our final approximative model.

The theoretical prediction that $a = b$ in the *Imma* unit cell is also supported by empirical evidence in the MD simulations. On one hand, the values of the angles θ and ϕ estimated by graphically inspecting the external appearance of the simulations agree very closely as shown in Fig 5.13, in agreement with the idea that $a = b$ as predicted by Eq. (5.1). If the *Imma* phase lay precisely on the hydrostat, then $c_I/a_I \approx 0.55$ for all piston velocities, and we would predict that $\theta = \phi \approx 62°$ according to Eq. (5.1). In practice, we find that owing to the finite residual shear stress present in the simulations, θ and ϕ range from around 55° to around 60° as the particle velocity is increased from 1.6 km s^{-1} to 2.1 km s^{-1}. Moreover, the values of a and b of the *Imma* unit cell extracted directly from the position of the (220) diffraction spot in the FT of the *Imma* phase are also in excellent agreement at a value of around 6.7 Å in all simulations, as portrayed in Fig. 5.14.

A further test of the model presented above can be performed by comparing the volume fraction of the *Imma* phase f_I^V relative to the total volume of the mixed-phase region as predicted theoretically by the model and as measured directly in the simulations. In the former case, we first require a "first-principles" expression for f_I^V in terms of the fundamental lattice parameters a and b of the

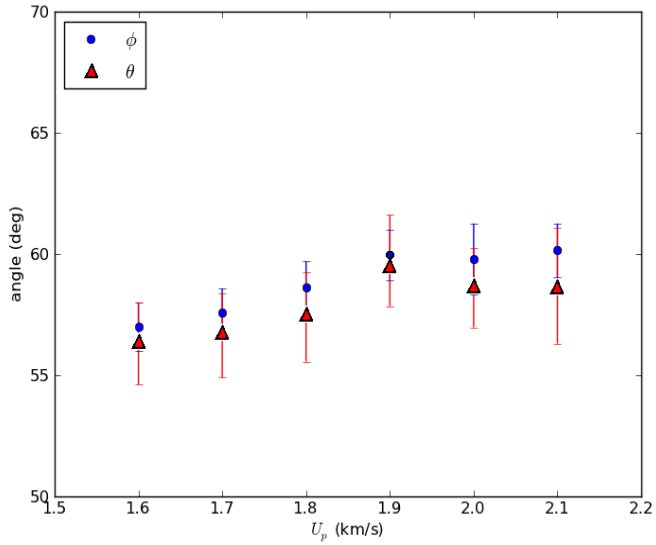


Figure 5.13: Angles θ and ϕ determined by visually inspecting the inclination of the bands of *Imma* phase observed in the Set I simulations.

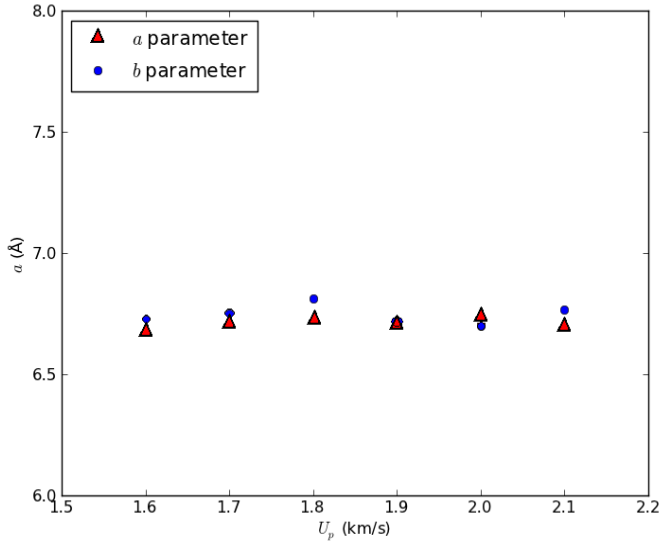


Figure 5.14: Values of the lattice parameters a and b of the *Imma* unit cell estimated by the position of the (220) diffraction spot in the corresponding FT pattern of the Set I simulations between $U_p = 1.6$ km/s and $U_p = 2.1$ km/s.

Imma unit cell. The volume of a single parallelepiped is in general given by -

$$V_I = \left|(\overrightarrow{s_1} \times \overrightarrow{s_2}) \cdot \overrightarrow{W}\right| = l^2 W \tag{5.20}$$

Hence the volume fraction of a parallelepiped of *Imma* material relative to the volume of the box enclosing it of length l_z along the z-axis (as defined in Fig. 5.10) and therefore of total volume $V_{TOT} = l^2 l_z$ is -

$$f_I^V = \frac{V_I}{V_{TOT}} = \frac{W}{l_z} \tag{5.21}$$

If we apply the above equation to the geometry of Fig. 5.10, in which l_z amounts to -

$$\begin{aligned} l_z &= \tfrac{l}{\tan\theta} + \tfrac{l}{\tan\phi} \\ &= \tfrac{N_o a_o}{\tan\theta} + \tfrac{N_o a_o}{\tan\phi} \\ &= \tfrac{c}{a}\left(2N_o a_o\right) \end{aligned} \tag{5.22}$$

the corresponding value of f_I^V then is -

$$f_I^V = \frac{W}{l_z} = \frac{W}{(2N_o a_o)}\frac{a}{c} \tag{5.23}$$

In order to find the expressions for N_o and W to substitute into the above, we solve the constraints of conservation of length (Eq. (5.2)) and number of unit cells (Eq. (5.6)) along the transverse x and y directions simultaneously, using the result obtained earlier that $a = b$ in the *Imma* unit cell (together with the fact

that $a_{cd} = b_{cd}$). The final result is -

$$\begin{aligned} N_{cd} &= N_o \tfrac{(a-a_o)}{(a-a_{cd})} \\ N_I &= N_o \tfrac{(a_o-a_{cd})}{(a-a_{cd})} \end{aligned} \tag{5.24}$$

It can also be shown from Eq. (5.15) that an expression for the width W of the bands is -

$$W = N_I \sqrt{\frac{a^2+c^2}{2+a^2/c^2}} \tag{5.25}$$

Substituting Eq. (5.25) and Eq. (5.24) into Eq. (5.23) yields the following final result for the *Imma* volume fraction of a single parallelepiped within the volume of the box of Fig. 5.10 -

$$f_I^V = \frac{(a_o - a_{cd})\, a}{2\,(a - a_{cd})\, a_o} \frac{\sqrt{a^2+c^2}}{\sqrt{2c^2+a^2}} \tag{5.26}$$

Note that the above formula was derived for the case of a single parallelepiped. In reality the mixed-phase banding structure contains four times the volume of such parallelepiped within the container box of Fig. 5.10. An expression for f_I^V accounting for this is given by -

$$\left(f_I^V\right)_{TOT} = \left(\frac{2\,(a_o - a_{cd})\, a}{(a - a_{cd})\, a_o} \frac{\sqrt{a^2+c^2}}{\sqrt{2c^2+a^2}} \right) \tag{5.27}$$

A test on the validity of the theoretical model presented in this chapter was conducted by considering the fraction of number of atoms (as opposed to the volume fraction) in the *Imma* phase f_I^N. In order to find an expression to convert between f_I^V and f_I^N, we look back at their definitions. The total volume of each of the two phases in the mixed-phase region, *Imma* and *cd*, in terms of these two

types of fractions is given by -

$$\begin{aligned} f_N^I \rho_{TOT} V^I &= f_V^I \\ \left(1 - f_N^I\right) \rho_{TOT} V^{cd-hp} &= \left(1 - f_V^I\right) \end{aligned} \tag{5.28}$$

where $\rho_{TOT} = N_{TOT}/V_{TOT}$ is the total number density, and where we have made use of the fact that both types of fractions add up to unity. Solving the two equations in Eq. (5.28) simultaneously yields the following results -

$$\begin{aligned} f_V^I &= \frac{f_N^I V^I}{f_N^I V^I + V^{cd-hp} - V^{cd-hp} f_N^I} \\ f_N^I &= \frac{f_V^I V^{cd-hp}}{V^I - f_V^I V^I + f_V^I V^{cd-hp}} \end{aligned} \tag{5.29}$$

The second in the above set of equations can be used to obtain the number fraction of atoms in the *Imma* phase f_N^I from the total volume fraction predicted by Eq. (5.27). The results can then be compared with the number fractions measured directly in the simulations. An effective method for counting the number of atoms in each phase from the MD simulations is by binning according to internal energy. Once plotted, the distribution of internal energy appears as a well-defined double-peaked distribution, with each peak corresponding to one of the two phases. Also present at the highest values of the internal energy in the overall profile is a smooth distribution of atoms identified as lying at the boundaries between the two phases. These atoms have the highest energy because they are in the most highly strained environments. The number of atoms in each phase was estimated by fitting a function in the form of the sum of three Voigt profiles, with two profiles encompassing the two main peaks corresponding to the two phases, and the third one centred across the distribution of atoms at

the boundaries. The overall result was an accurate fit to the potential energy profile. In counting the number fraction of the *Imma* phase, the number of atoms under the corresponding peak was divided by the total number of atoms across the entire internal energy profile, including therefore the number of atoms at the boundaries, due to these atoms being non-negligible in number. The upper limit in the value of the number fraction for each piston velocity was estimated by assuming that all atoms at the boundaries belong to the *Imma* phase, whereas the lower limit was obtained conversely by assuming that all boundary atoms lie in the *cd* phase. The results of the comparison between the theoretical prediction of Eq. (5.29) and the direct counting of the atoms in the MD simulations with the method outlined above is presented in Fig. 5.16. The lattice parameters used in Eq. (5.29) were derived from an analysis of the reciprocal space plots for the two phases. By considering a sample of around 20 diffraction spots in reciprocal space for each phase, a statistical analysis on the values of these lattice parameters was performed, with the error bars shown representing the derived standard deviation in number fraction. It can be seen that the values obtained from the model and the MD simulations are consistent for all values of U_p, thus confirming the validity and accuracy of the model presented in this section despite the simplicity of some of the arguments implemented.

Despite the consistency between the model and the simulations, it should be noted that the arguments put forward above do not take into account a number of factors. Firstly, we have neglected the effects of lattice rotations, which have been observed in the FT of both phases. These rotations amount to roughly 10° about the y-axis for the *cd* phase, and up to around 18° in the opposite sense for the *Imma* phase. We have also neglected the effects of inter-facial strains

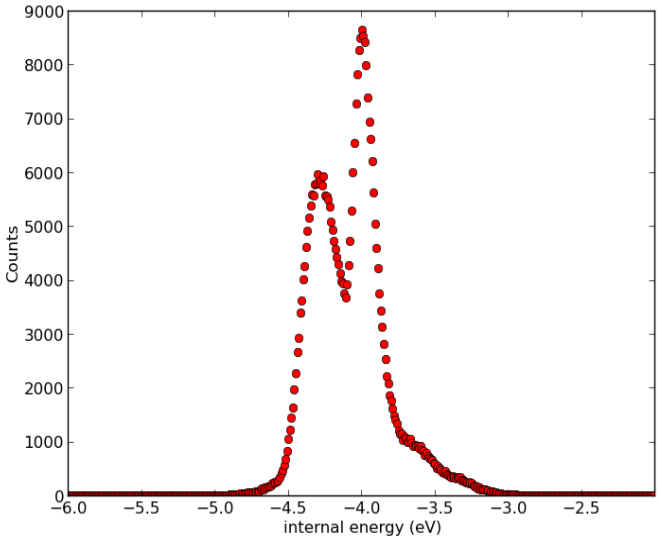


Figure 5.15: Example of the internal energy distribution in the Set I simulation with $U_p = 1.6$ km/s, showing how the profile peaks at the positions of the two phases at internal energy values of around -4 eV for *Imma* and around -4.3 eV for *cd*.

occurring at the boundary between *cd* and *Imma* phases mentioned previously. The mismatch in lattice parameters of these two phases will necessarily lead to an incommensurate boundary which could lead to distortion of the simple structures discussed above. However, the highly disordered nature of this boundary material (typically accounting for around 10-15% of the atoms) makes characterisation of these regions highly challenging. In addition, similar issues are encountered at intersections between bands, where once again detailed analysis is hindered by the small number of atoms (rendering reciprocal space analysis ineffective), as well as inherent disorder and strain gradients. We therefore conclude that although quantitative agreement is not to be expected, the qualitative trend exhibited is indicative of the underlying mechanisms conforming to those forming the basis of Eq. (5.29).

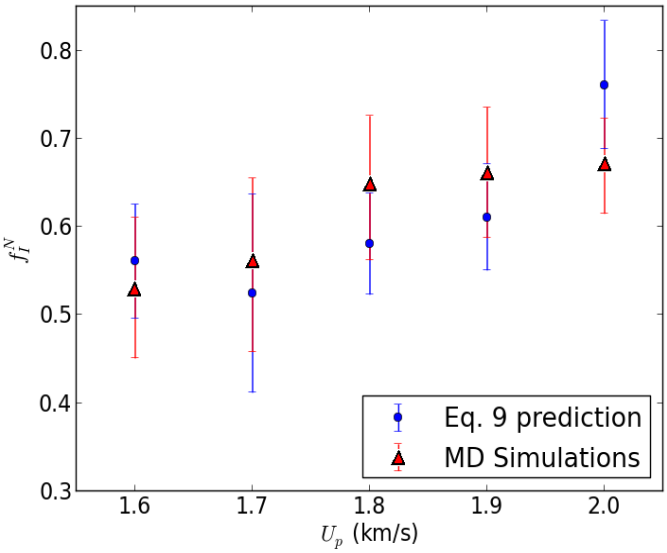


Figure 5.16: Comparison between the number fraction of the *Imma* phase f_I^N predicted by Eq. (5.29), with those derived from the Set I simulations. MD number fractions were calculated by separating the two phases according to their internal energy.

5.4 Thermodynamics of the mixed-phase region

Under the conditions of constant temperature and pressure such as those predicted to be found in shock-induced mixed-phase regions [52, 53], the condition of relative stability between phases is given by the minimisation of the Gibbs free energy G of the material as explained in the previous chapter -

$$G = E + PV - TS \tag{5.30}$$

where E is the internal energy, P the pressure, V the volume, T the temperature and finally S the entropy. This condition is such that along the phase boundary

of a phase transition where two phases coexist in equilibrium, the Gibbs free energies of the two phases are equivalent, while away from it the stable phase is the one with the lower G. The same considerations apply when comparing the mixed-phase region with the state of elastic compression, except that the definition of G under uniaxial compression is given by [52] -

$$G^{uniaxial} = E + P_z V - TS \tag{5.31}$$

In what follows, we shall neglect the entropic contributions to the Gibbs free energies embodied by the term TS, so that G reduces to another thermodynamic potential, that is the enthalpy -

$$H = E + PV \tag{5.32}$$

or equivalently -

$$H = E + P_z V \tag{5.33}$$

for the case of uniaxial compression. We find this assumption to be reasonable given the high stiffness of both the *cd* and *Imma* phases. Within the approximation that the thermal contribution to the entropy can be reasonably evaluated by assigning an Einstein frequency to each phase, we can use the Einstein model, which predicts the following expression for the TS term [72] -

$$TS = 3k_B T \left(-\ln\left(1 - e^{-\frac{h\upsilon_e}{k_B T}}\right) + \frac{\frac{h\upsilon_e}{k_B T} e^{-\frac{h\upsilon_e}{k_B T}}}{\left(1 - e^{-\frac{h\upsilon_e}{k_B T}}\right)} \right) \tag{5.34}$$

where ν_e is the Einstein's frequency, given simply by $\sqrt{k/m}$, where k is the elastic spring constant that defines the interatomic potential, and m is the mass of a silicon atom. The change in the TS term was found to be of order 25 meV for the *cd* phase and around 40 meV for *Imma*, and therefore small compared with the order 10^3 meV change in the enthalpy in both cases which will be demonstrated later.

The configurational entropy due to the banding is also clearly negligible. This is a direct consequence of the highly ordered nature of the mixed-phase region, in which just two phases coexist with well-structured lattices. This suggests that the combinatory term Ω in the conventional expression for the entropy S -

$$S = k_B \ln \Omega \tag{5.35}$$

is relatively small, which implies that the overall entropy is negligible due to the size of Boltzmann's constant k_B. The TS term in the Gibbs free energy is consequently also negligible despite the considerable magnitude of the shock-induced rise in temperature, which is of order 10^3 K as will be illustrated later. The effects of temperature are not however completely left out of the enthalpy calculation, since they still significantly contribute to both the internal energy E and pressure P terms.

A complete thermodynamical analysis of the shock-loading process as seen in the MD simulations also requires knowledge of the state variables of the system. These are given by the Rankine-Hugoniot equations embodying the principles of conservation of mass, energy and momentum across a shock discontinuity. The Rankine-Hugoniot equations can be expressed in their most general form as

follows -

$$\begin{aligned}
&\rho_o\left(U_s - U_o\right) = \rho\left(U_s - U_p\right) \text{ conservation of mass} \\
&\rho_o\left(U_s - U_o\right)\left(U_p - U_o\right) = P - P_o \text{ conservation of momentum} \\
&e - e_o = \tfrac{PU_p - P_oU_o}{\rho_o(U_s - U_o)} - \tfrac{1}{2}\left(U_p^2 - U_o^2\right) \text{ conservation of energy}
\end{aligned} \tag{5.36}$$

where P is the external pressure exerted on the material by the shock, ρ is the density, T is the temperature, U_p is the particle velocity, U_S the shock velocity, U_0 the upstream flow velocity, e is the specific internal energy, and subscript 0 denotes the initial value of each of these variables in the region ahead of the shock-front. In addition to the Rankine-Hugoniot equations, the material behaviour under shock-compression is described by its Equation of State (EoS). For most materials we can employ a linear EoS of the form -

$$U_S = C_o + C'U_p \tag{5.37}$$

The Rankine-Hugoniot equations lead to the following expression for the jump in specific enthalpy across the shock-wave from the equilibrium state, known as the Hugoniot Relation [12] -

$$\Delta h = \frac{1}{2}\left(U_p - U_0\right)\left(2U_s - U_p - U_0\right) \tag{5.38}$$

The Hugoniot relation can be conveniently rephrased exclusively in terms of the piston and shock velocities U_p and U_S by making use of the EoS of Eq. (5.37). In general a distinction must be drawn between the leading elastic wave and the ensuing phase-transition wave present in the system, since in general two distinct

Equations of States apply across each of these discontinuities. When U_o, P_o and C' are all zero such as is the case for the leading elastic wave, which is found to travel at velocity $U_S^e = 9.064$ km s^{-1} regardless of pressure, the specific enthalpy jump Δh^e is given by -

$$\Delta h^e = \frac{U_p^e}{2}\left(2U_0 - U_p^e\right) \tag{5.39}$$

where U_p^e is the particle velocity in the elastically compressed region. Note that this quantity is distinct from, and lower than, the applied piston velocity, U_p, which will dictate the particle velocity in the phase-changed region behind the second wave. It is found that in the Set II simulations these velocities obey the linearity of the EoS. For the more general phase transition wave in which U_o, P_o and C' are all in general different from zero due to the initial impulse given to the system by the preceding elastic wave, the specific enthalpy change Δh^p can be calculated by noting that the second wave now travels into the elastically compressed region where the flow velocity $U_0 = U_p^e$ -

$$\Delta h^p = \frac{1}{2}\left(U_p - U_p^e\right)\left(2U_s^p - U_p - U_p^e\right) \tag{5.40}$$

where we again have a linear relation between shock and piston velocity for the phase transformation wave. The total enthalpy change for the two wave shock is therefore $\Delta h = \Delta h^e + \Delta h^p$. The parameters in the two Equations of State across each of the elastic and phase transition waves were estimated by fitting the values of U_S and U_p extracted directly from the time evolution of the wave profiles of the Set II simulations. The results of this fit for the Elastic EoS and for the

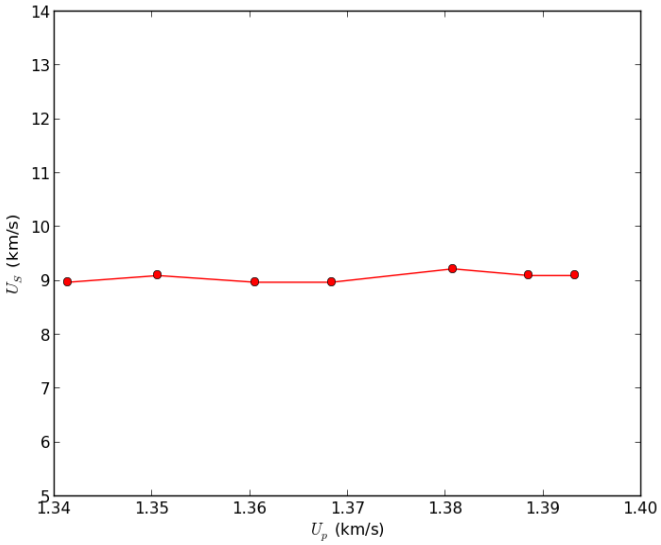


Figure 5.17: EoS of the elastic wave as measured directly from the wave profiles of the Set II simulations. As expected, it is roughly constant as a function of U_p.

Phase Transition EoS are shown in Fig. 5.17 and 5.18 respectively. Also shown in Fig. 5.19 is the dependence of the particle velocity across the elastic precursor U_o as a function of the corresponding piston velocity U_p, which is necessary in the computation of the enthalpy jump across the phase-transition wave according to Eq. (5.40). A summary of the parameters in the U_S-U_p relation of the two waves, the elastic and phase transition waves, is offered in Table 5.2.

In parallel with the dynamic MD simulations, we also computed the static ground state energy surface of the Tersoff potential at zero temperature for a variety of compressed lattice configurations encompassing the deformation path between the *cd* and the β-Sn phases (as a special case of the *Imma* phase for $a = b$ and $\Delta = 0.25$), in much the same way as the DFT calculations of Chapter 3 were performed. The resulting ground-state energy surface is shown in Fig. 5.20 in the form of a contour plot. Overall, the appearance of this ground state surface

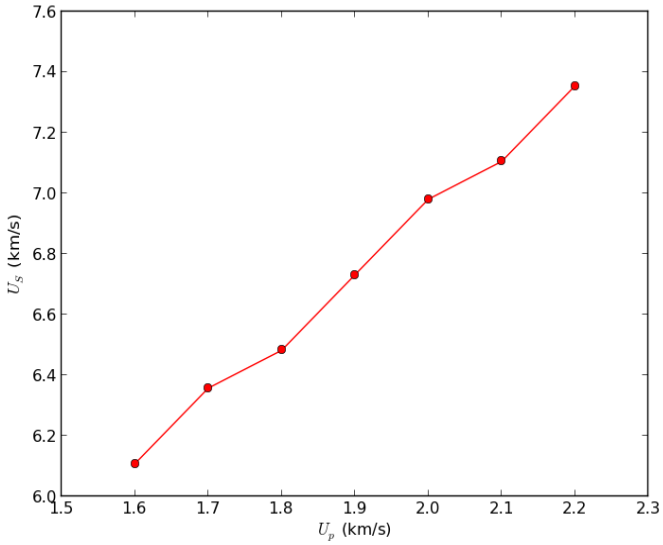


Figure 5.18: EoS of the phase-transition wave as measured directly from the wave profiles of the Set II simulations.

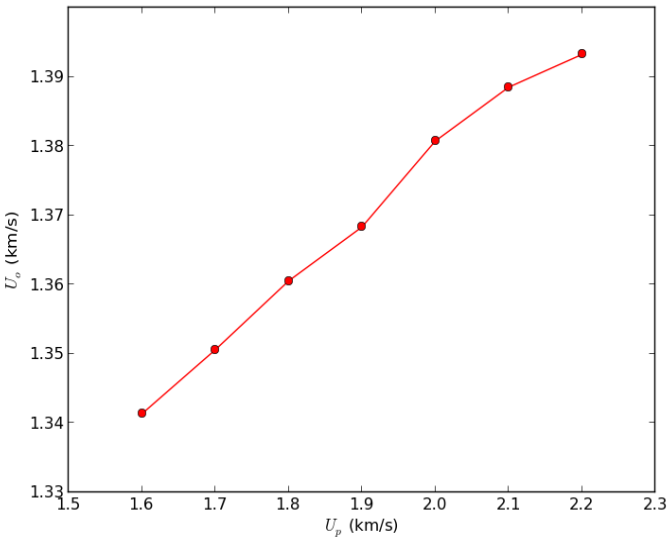


Figure 5.19: Particle velocity across the elastic front U_o as a function of piston velocity U_p according to the Set II wave profiles.

Table 5.2: Particle and shock velocities U_p and U_S across the elastic and phase transition waves according to the linear U_S-U_p relation $U_S = C_0 + C' U_p$. The top value in the column of C_0 parameters corresponds to the sound velocity in the material at zero pressure.

	C_0 (km s^{-1})	C'
U_p^e	9.064	0
U_S^e	1.1983	0.0899
U_p^p	0	1
U_S^p	2.8401	2.048

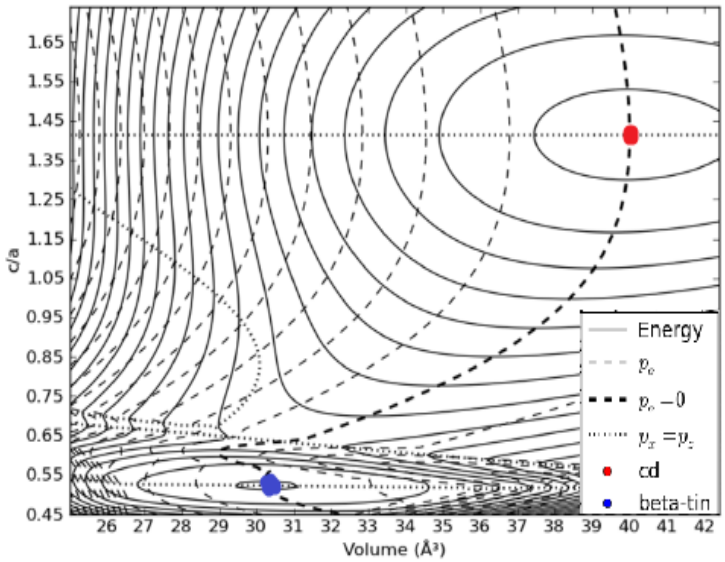


Figure 5.20: Combined pressure-energy contour plot from the Tersoff potential, highlighting in each case the precise location of the two phase equilibria (shown as a red dot for *cd* and blue dot for β-Sn). The energy and pressure contours at all points are shown as thin solid and thin dashed lines respectively. The spacing between the contours is 100 meV for the energy and 20 kbar for the pressure.

is very similar to that obtained with DFT techniques.

The enthalpies of the two phases were calculated from this energy surface under conditions as similar as possible to the environment as encountered in the shock simulations. In particular, we assumed that the pressure in each phase

was hydrostatic, so that the simple definition of enthalpy $H = U + PV$ could be used, and secondly that the total pressure was the same between the two phases. These two constraints applied together are enough to locate the positions of the *cd* and β-Sn phases on the energy surface as a function of varying total pressure. Finally, due to the significant magnitude of the shock-induced rise in temperature across the mixed-phase region observed in the simulations, we also decided to investigate the effects of finite temperature, in the form of the thermal contributions to the pressure and internal energy of the system (but not the entropic term TS in the Gibbs free energy, which is still being neglected), on the static calculation. Fig. 5.21 shows an example of temperature profile across the shocked sample predicted by the simulations. The temperature was computed using the conventional definition of two-dimensional cross-sectional temperature in terms of the transverse components of the particle velocities -

$$T_{2D} = \frac{m_{Si}\left(\overline{v_x^2 + v_y^2}\right)}{2k_B} \tag{5.41}$$

As observed in all simulations, the example of Fig. 5.21 shows how the shock-induced temperature rise across the elastic front is negligibly small compared to that accompanying the phase-transition wave. The evolution of the peak temperature attained in the mixed-phase region across the range of piston velocities is shown in Fig. 5.22. As expected, the stronger the shock intensity the higher the temperature rise. In order to probe its effects on the enthalpy of the mixed-phase region, we repeated the static calculation along the hydrostatic line of Fig. 5.20 at the temperature values predicted by the linear fit of the initial range of Fig. 5.22.

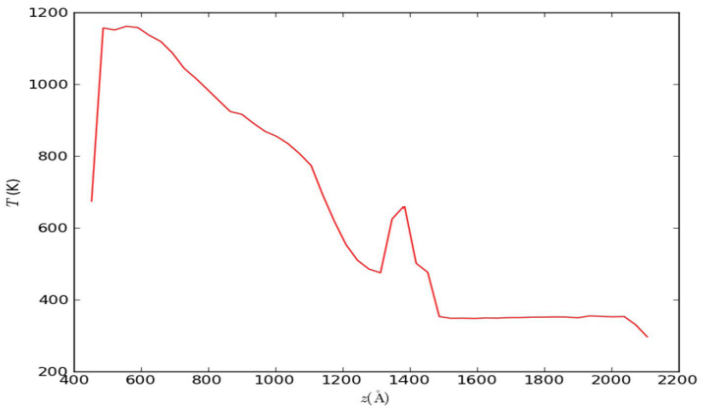


Figure 5.21: Two-dimensional temperature profile of the Set I simulation at $U_p = 1.9$ km/s. The peak in the temperature in the region between 1300 Å and 1500 Å is located across the phase transition wave. It does not correspond to a physical rise in temperature but is likely the result of the transverse displacement of atoms as the material undergoes the change in lattice parameters induced by the phase transition.

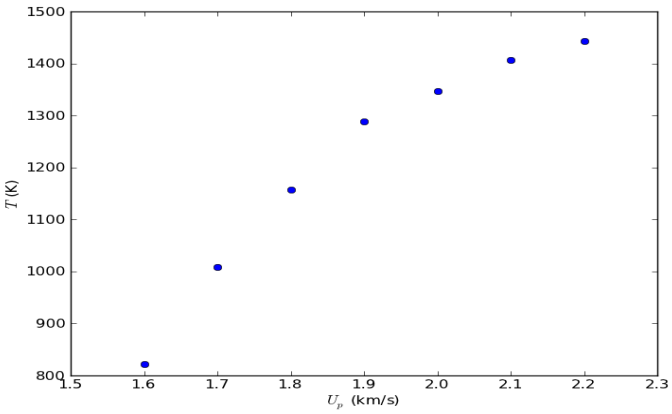


Figure 5.22: Maximum temperature recorded in the mixed-phase region of the Set I simulations. The linear fit as a function of pressure across the initial range of U_p values from 1.6 to 2.0 km/s is $6.5912p - 1017.8$.

The individual enthalpies of the *cd* and β-Sn phases as located on the energy surface were weighted by their number fraction predicted from the corresponding lattice parameters according to Eq. (5.27) for calculating f_I^V, together with Eq.

(5.29) for converting from f_I^V to f_I^N (with f_{cd-hp}^N given by $1 - f_I^N$). The total high-pressure mixed-phase enthalpy is consequently given by -

$$H_{Tot}^{HP} = f_{cd-hp}^N H_{cd-hp} + f_I^N H_I \tag{5.42}$$

where $H_i = E_i + P_i V_i$ for a general phase i. The enthalpy along the line of uniaxial compression along the c axis of the crystal, representative of the initial elastic response of the material for the case of shock-propagation along the z-direction, was also calculated using Eq. (5.33). However due to the negligible shock-induced heating that takes place across the elastic front according to the MD simulations, an investigation on the associated thermal effects such as the one performed for the mixed-phase region was not deemed necessary in this case.

Finally, a further estimate of the enthalpies for each of the two phases in the mixed-phase region was obtained by directly computing the total average energy and pressure from the MD simulations, and by estimating the atomic volume from the FT patterns. When calculating the enthalpies of the two phases, the pressure in each phase was assumed to be hydrostatic, such that the elementary definition of enthalpy $H = U + PV$ could be used. The two phases were separated from each other by thresholding the mixed-phase region relative to the intermediate value of the internal energy separating the two peaks in the internal energy distributions such as the one shown in Fig. 5.15. Similarly to the calculation of the total static enthalpy of Eq. (5.42), the individual enthalpies of the two phases were weighted relative to their first-principle volume fractions. The final outcome of all the different approaches for calculating the total enthalpy jump across the phase-transition from the initial equilibrium state, namely the EoS method based on

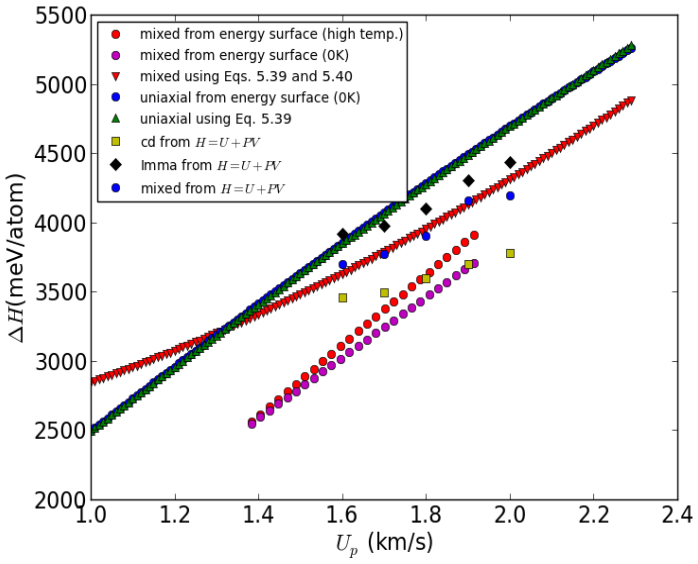


Figure 5.23: Enthalpy change from equilibrium per unit atom as a function of U_p predicted by the various enthalpy extraction methods. For the calculations based on the static energy surface, the corresponding value of U_p was calculated from the pressure through the Rankine-Hugoniot Equations. Data above $U_p = 2.0$ km/s is included for completeness but should be treated with precaution due to the onset of shock-induced melting in the sample.

Eq. (5.40) together with the results of the fits in Figures 5.17, 5.18 and 5.19, the static energy surface method of Eq. (5.42) and the method based on the direct extraction of data from the simulations which has just been outlined, is presented in Fig. 5.23.

The results from the EoS method suggest that the shock-induced phase transition to *Imma* should first occur in the range of U_p values between 1.3 and 1.4 km/s where the enthalpy of the mixed-phase region first becomes lower than that of the state of elastic uniaxial compression, thus marking the point at which the mixed-phase region becomes the most thermodynamically favourable state for the sample to be in according to the principle of minimisation of enthalpy. In both

the Set I and Set II of simulations however no phase-transition was observed at 1.4 km/s, with the first hints being detected only at 1.6 km/s in Set I and at 1.5 km/s in the larger Set II simulations, still in reasonable agreement with the enthalpy analysis. The slightly higher values of U_p found in practice could be linked to the enthalpy barrier between the two regions, which has not been explored here. Hence it appears that between 1.3 and 1.5 km/s the enthalpy advantage of the mixed-phase is still too small for the mixed-phase to begin to nucleate in the MD simulations.

Inspection of Fig. 5.23 also reveals a good agreement between the EoS predictions for the enthalpy jump and the results from using $H = U + PV$ with the data extracted directly from the simulations, thus confirming that our MD simulations of shock waves obey the Hugoniot relation. It is also worth noticing that this latter method predicts the enthalpy of the *cd* phase alone to be lower than that of *Imma*, which would explain why a mixed composition of *cd*/*Imma* material overall provides a more thermodynamically favourable state than a complete phase-transformation to *Imma*. Furthermore, when extrapolating the enthalpy to lower particle velocities, both methods suggest that the shock-induced phase transition to *Imma* should first occur in the range of U_p between 1.3 and 1.4 km s^{-1}, where the enthalpy of the mixed-phase region first becomes lower and therefore more thermodynamically favourable than that of the state of elastic uniaxial compression.

Although we find good agreement between the enthalpy determined by the Hugoniot relation and the wave velocities, and that found by directly determining U, P and V from the MD simulations, we caution that there remain aspects of the simulations that are still not understood. Most noticeably, we find that the

pressures within the two phases are not the same - with the pressure in the *cd* phase being considerably lower than that in the *Imma* phase. Indeed, it is for this reason that the enthalpy of the *cd* phase, shown in Fig. 5.23, is the lower of the two phases - if the pressures were the same, we would expect the new *Imma* phase to have the lower enthalpy.

We also note that the Hugoniot relation for the shock does provide some modest insight into a potential synergy between the inelastic behaviour - in terms of the stress relief being provided by the partial phase transformation - and the minimisation of the enthalpy. We see that the Hugoniot relation (Eq. 5.38) determines that if the two phases in the mixed-phase region are at the same hydrostatic pressure, then at the first point where the transformation can occur - where we expect the enthalpy per atom of each phase to be identical - we predict that the volume fraction of each phase should be proportional to the enthalpy increase in that phase.

Finally, the results of the static calculations agree with the observation made earlier about the shock-induced heating across the elastic wave being negligibly small compared to that across the phase-transition wave, which explains why the enthalpy along the line of uniaxial compression extracted from the cold energy surface nearly overlaps with that obtained through the shock EoS of Eq. (5.39). The application of the thermal effects on the pressure and energy components of the mixed-phase enthalpy on the other hand, despite tending to agree with the EoS data in the limit of high U_p, still leaves a significant discrepancy. We believe that this could be due to the large residual shear stresses left in the simulations for low U_p values between 1.5 and 1.8 km/s, as explained in Fig. 5.6, which makes the assumption of perfectly hydrostatic pressure conditions at the base of

the static enthalpy calculation less realistic.

5.5 Conclusions

We have conducted a comprehensive investigation into the mechanism underpinning the relief of shear stress in shock-compressed single crystal silicon. Multi-million atom simulations of shock-wave propagation in a single-crystal sample of silicon predict the onset of a high-pressure mixed-phase region following directly after the initial elastic response, consisting of nearly-hydrostatically compressed cubic diamond crystal structure and of phase-transformed material lying in the *Imma* high-pressure phase. This mixed-phase state manifests itself in a banding conformation made of interlocking parallelepipeds of *Imma* phase, and persists from piston velocities of around 1.5 km s^{-1} up to around 2.1 km s^{-1}, at which point the structure becomes very disordered indicating the shock-induced melting of the sample. By extracting the lattice parameters of the various phases from the Fourier Transform images of the real-space atomic positions, and interpreting the banding structure in terms of the relief of shear stress across the plane perpendicular to the shock propagation direction, we are able to quite accurately predict the volume fraction of the *Imma* phase. Furthermore, an analysis of the relative thermodynamic stability of the two phases by computing their enthalpies from the overall EoS deduced from the shock velocities, and from directly recording U, P and V within the simulations, are in good mutual agreement, predicting that the mixed-phase region first becomes thermodynamically advantageous in the range of U_p between 1.3 and 1.4 km s^{-1}, slightly less than the point of onset detected in the MD simulations. Overall, these results are supportive of our orig-

inal hypothesis that the relief of shear stress in shock-compressed single-crystal silicon is provided directly by the occurrence of a polymorphic phase-transition, without the need for an intermediate state of plasticity.

However, despite the insight that these simulations might afford, we note that it is still the case that our prediction for the value of U_p, and hence stress, for the onset of the inelastic behaviour, is still considerably higher than that found in experiments [80] (≈ 1.4 km s^{-1} as opposed to ≈ 0.8 km s^{-1} respectively), and the reasons for this discrepancy remain elusive. It is unlikely that experimental samples have an initial defect density that is sufficiently high to influence the material response, although clearly simulations including initial defects may provide further insight. Alternatively it is conceivable that the Erhart-Albe potential [56] is not fully capturing the material response under shock conditions, and some modifications to the potential may be required. We recall that it is not unknown for other types of potentials that faithfully encapsulate certain aspects of material behaviour under ambient conditions, to then fail to reproduce known shock response at higher pressures - a classic example being the potential by Ackland *et al.* for iron [2], that provides a good match to the phonon dispersion curves at ambient pressure and temperature, but cannot capture the $\alpha - \epsilon$ transition at 130 kbar, whereas the Voter-Chen potential [86, 235], whilst having a poorer match at ambient conditions, reproduces the phase transition.

Chapter 6

Conclusions and Future Work

6.1 Summary

In this section, the most significant results of the previous three chapters are summarised.

In Chapter 3, the computational technique of Density Functional Theory was employed to investigate from first principles the pressure-induced polymorphic phase transition from the equilibrium cubic diamond crystal structure of single-crystal silicon to the first stable high-pressure phase, which is known as the β-Sn phase. When applying the method of Ref. [65], we predicted a significant lowering of the transition pressure and enthalpy barrier of the phase transition under the non-hydrostatic effects of uniaxial compression representative of the initial stage of the dynamical response of silicon under shock-wave loading. By investigating the evolution of the transition parameters as a function of increasing uniaxial shear stress, the stress at which the phase transition occurs is observed to decrease to values which are below the HEL measurements reported by Gust and Royce [80]. However, we identified several problems with the analysis presented with the method of Ref. [65], most notably with the formulation of enthalpy employed in

the analysis of the transition parameters under non-hydrostatic stress conditions. The results of the corresponding numerical integration scheme have in fact been observed to yield path-dependent results, in contradiction with the fundamental definition of enthalpy as a path-independent function of state. This ill-definition of enthalpy, or equivalently of Gibbs free energy, under anisotropic stress appears to have remained a persistent problem in the literature to this day. Furthermore, Gaál-Nagy *et al.* [65] assumed that the transition occurred under constant shear stress, which is unlikely to be the boundary condition encountered under shock loading.

The lack of understanding within the high-pressure physics research community of how pressure-induced phase transitions should be analysed away from a perfectly hydrostatic stress configuration is what motivated the development of Chapter 4 of this thesis. In this chapter, following a general review of the issues which lead previous researchers to consider path-dependent formulations of the enthalpy, we introduce the principle of minimisation of Availability as a possible solution for establishing phase equilibrium when the applied stress driving the phase transition is non-hydrostatic in nature. To establish its validity, we then apply this concept to three cases for which an analytical solution is known with certainty, which consist in phase transitions occurring under hydrostatic pressure, under uniaxial elastic compression for the system, and finally under constant volume of the system. In the second case, we observe only a minor decrease of the transition pressure from the hydrostatic case, from roughly 121 kbar to 118 kbar, although once more this constraint is unlikely to represent shock conditions. Finally, we propose a general method for expressing the Availability of a solid under generic non-hydrostatic stress conditions, which relies on the assumption of

constant external force components acting on the system across the phase transition. Even though the final result obtained can be analytically shown to be a path-independent function of state, and appears to be the only such possible solution under the constraint of fixed external conditions required in the definition of Availability, the lack of comparative experimental data prevents us from benchmarking this theoretical model and from verifying its validity conclusively. Ideally, to obtain data directly comparable with the theoretical predictions developed in this chapter, future research should aim at establishing an experimental relation between the transition force of a given phase transition and the degree of shear force being exerted on the system. Such experiment could for example be implemented through the use of a DAC configured purposely to apply a non-hydrostatic load on the sample and to measure the corresponding force components acting on it. It is not clear however whether such experiments have been attempted in the past or are at all feasible in general.

No investigation of material response properties under the dynamical effects of shock-wave compression would be complete without the implementation of a fully dynamical simulation technique capable of reproducing the high-strain rate effects of real shock experiments, and for this reason the computational technique of classical MD was applied to our case study of single-crystal silicon in Chapter 5. Multi-million atom MD simulation of shock-wave propagation in a single-crystal sample of silicon predict the onset of a high-pressure mixed-phase region ensuing directly after the initial elastic response, consisting on one hand of nearly-hydrostatically compressed material in the equilibrium cubic-diamond crystal structure and on the other of phase-transformed material lying in the high-pressure stable phase known as *Imma*, which has a body-centred othorhom-

bic lattice. This mixed-phase region manifests itself as a banding conformation composed of interlocking parallelepipeds of *Imma* phase. By analysing the overall morphology of this banding structure, together with the relative thermodynamic stability of the various phases involved in the phase transition, we find that this pressure-induced phase transition is capable by itself of relieving shear stress in uniaxially-compressed silicon, without the need for an intermediate transient state of plastic deformation. Furthermore, by extracting the lattice parameters of the various phases from the Fourier Transform images of the real-space atomic positions, we were able to quite accurately predict the number fraction of the *Imma* phase compared to a direct counting of the atoms in the simulations. However, despite the insight gained by performing these simulations, there are aspects which are still not well understood. In particular, we note that our prediction for the value of U_p, and hence stress, for the onset of the inelastic behaviour, is still considerably higher than that found in experiments [80] (≈ 1.4 km s^{-1} as opposed to ≈ 0.8 km s^{-1} respectively), and the reasons for this discrepancy remain elusive. We suspect that the underlying physical cause might be in the choice of the inter-atomic potential employed in the simulations.

6.2 Future Work

In light of the main conclusions outlined in the previous section, it is worth mentioning that there remain many more variables in the simulations that could be adjusted in order to obtain a more realistic portrayal of the mechanical response properties of shock-compressed single-crystal silicon. This applies in particular to the case of the classical MD simulations performed in Chapter 5. One obvious pa-

rameter that could be modified in future investigations is the implementation of a non-perfect piston impactor oriented with a surface not precisely parallel to the crystal plane of the target sample, and capable therefore of inducing shock-waves which are not perfectly planar as encountered in real shock experiments. Furthermore, more realistic samples could be generated in simulations by inclusion of the correct isotopic composition of natural silicon, which consists essentially in three different stable isotopes with mass number of 28, 29 and 30 and with relative abundances in nature of 92.223%, 4.685% and 3.092% respectively. All the samples considered in this thesis were in fact isotopically pure, that is composed entirely of the most common isotope of silicon with mass number of 28. Finally, it is worth emphasising that the advent of fourth generation hard X-ray free-electron laser (FEL) light sources, marked by the opening of the Linac Coherent Light Source (LCLS) facility at Stanford in 2009, has opened unparalleled opportunities for gaining experimental understanding of the dynamic behaviour of solid matter under the effects of shock-wave compression at the microscopic lattice level [169]. These new generation X-ray sources are in fact characterised by vastly superior quality indicators compared to existing third-generation synchrotron-based light sources, or indeed laboratory laser-plasma X-ray sources. This superiority can be understood in terms of the shortness of the pulse duration, which in FELs such as LCLS can be of order 100 fs, that is faster than the typical period of a phonon vibration in solids and therefore capable of freezing atomic motion while taking X-ray diffraction snapshots of shock-induced transient phenomena. Furthermore, the peak brilliance of LCLS, characterised by a pulse photon count of 10^{12}, is as much as ten orders of magnitude higher than any existing synchrotron. Finally, another prodigious aspect of LCLS is the repetition rate of the X-ray

pulses, which has a theoretical limit of 120 Hz, although in practice the rate at which different target samples can be diffracted from is limited by the replacement time of the sample and other various practical aspects of experiments. The success of LCLS in revolutionising the field of laser-based *in situ* X-ray diffraction experiments has been deeply appreciated by a wide range of research communities, and several other similar hard X-ray FEL facilities have been opened since or are currently under construction around the world. In particular, we mention the SACLA FEL in Japan, which has been inaugurated very recently, and the European XFEL and the Swiss FEL, which are currently under construction in Germany and Switzerland respectively. An experimental X-ray diffraction investigation of the shock-response properties of single-crystal silicon in any of these facilities, to confirm that the phase transition to β-Sn or *Imma* represents indeed the mechanism providing the relief of shear stress in the shocked lattice, is currently being envisaged for the near future by our research group and other collaborators.

References

[1] Wikipedia, the free online encyclopedia. http://www.wikipedia.org. 4, 25, 30, 32, 75

[2] G. J. Ackland, D. J. Bacon, A. F. Calder, and T. Harry. Computer simulation of point defect properties in dilute Fe - Cu alloy using a many-body interatomic potential. *Phil. Mag. A*, **75**:713–732, 1997. 220

[3] G.J. Ackland. High-pressure phases of group IV and III-V semiconductors. *Rep. Prog. Phys.*, **64**:483–516, 2001. 80

[4] C.J. Adkins. *Equilibrium thermodynamics*. Cambridge University Press, third edition, 1983. 95, 122, 137, 138, 142, 143, 154

[5] D. Alfè. PHON: A program to calculate phonons using the small displacement method. *Comp. Phys. Comm.*, **180**:2622–2633, 2009. 166

[6] L.V. Al'tshuler. Use of shock-waves in high pressure physics. *Sov. Phys. Usp.*, **8**:52–91, 1965. 9

[7] N.W. Ashcroft and N.D. Mermin. *Solid state physics*. Saunders College Publishing, 1976. 19, 22, 63, 70

[8] H. Balamane, T. Halicioglu, and W. A. Tiller. Comparative study of silicon empirical interatomic potentials. *Phys. Rev. B*, **46**:2250–2279, 1992. 175

[9] A. Baldereschi. Mean-value point in the Brillouin zone. *Phys. Rev. B*, **7**:5212–5215, 1973. 77

[10] D. Bancroft, E.L. Peterson, and S. Minshall. Polymorphism of iron at high pressure. *J. Appl. Phys.*, **27**:291–298, 1956. 14

[11] L.M. Barker and R.E. Hollenbach. Laser interferometer for measuring high velocities of any reflecting surface. *J. Appl. Phys.*, **43**:4669–4675, 1972. 11

[12] A. F. M. Barton and A. P. W. Hodder. Explosive phase transitions. *Chem. Rev.*, **73**:127–139, 1973. 208

[13] M. Baublitz. X-ray diffraction from high pressure Ge using synchrotron radiation. *J. Appl. Phys.*, **53**:5669–5671, 1982. 81, 106

[14] A.B. Belonoshko. Atomistic simulation of shock wave - induced melting in argon. *Science*, **275**:955–957, 1997. 172

[15] G. Ben-Dor, O. Igra, and T. Elperin. *Handbook of shock waves, Vol. 1*. Academic Press, 2001. 6, 37

[16] E.I. Bichenkov, S.D. Gilev, and A.M. Trubachev. Shock-induced conduction waves in electrophysical experiments. *J. Appl. Mech. Tech. Phys.*, **30**:291–303, 1989. 80

[17] P.E. Blochl. Projector augmented-wave method. *Phys. Rev. B*, **50**:17953–17979, 1994. 73

[18] S.J. Blundell and K.M. Blundell. *Concepts in thermal physics*. Oxford University Press, second edition, 2010. 122, 137, 138, 142, 143

[19] P.W. Bridgman. *The physics of high pressure*. G. Bell, 1949. 1

[20] P.W. Bridgman. *Collected experimental papers*. Harvard University Press, 1964. 3, 14

[21] E. M. Bringa, K. Rosolankova, R. E. Rudd, B. A. Remington, J. S. Wark, M. Duchaineau, D. H. Kalantar, J. Hawreliak, and J. Belak. Shock deformation of face-centred-cubic metals on subnanosecond timescales. *Nature Materials*, **5**:805–809, 2006. 17, 18, 172, 186

[22] E.M. Bringa, A. Caro, Y. Wang, M. Victoria, J.M. McNaney, B.A. Remington, R.F. Smith, B.R. Torralva, and H. Van Swygenhoven. Ultrahigh strength in nanocrystalline materials under shock loading. *Science*, **309**:1838–1841, 2005. 17

[23] E.M. Bringa, J.U. Cazamias, P. Erhart, J. Stolken, N. Tanushev, B.D. Wirth, R.E. Rudd, and M.J. Caturla. Atomistic shock Hugoniot simulation of single-crystal copper. *J. Appl. Phys.*, **96**:3793–3799, 2004. 17, 172

[24] F.P. Bundy, , and J.S. Kasper. Electrical behaviour of sodium-silicon clathrates at very high pressures. *High Temp.–High Pressures*, **2**:429–436, 1970. 86

[25] F.P. Bundy. Phase diagrams of silicon and germanium to 200 kbar, 1000 °C. *J. Chem. Phys.*, **41**:3809–3814, 1964. 81

[26] A.V. Bushman, I.V. Lomonosov, and K.V. Khishchenko. Shock wave database. http://www.ficp.ac.ru/rusbank/. 8

[27] D.M. Ceperley and B.J. Alder. Ground state of the electron gas by a stochastic method. *Phys. Rev. Lett.*, **45**:566–569, 1980. 70

[28] D.J. Chadi and M.L. Cohen. Special points in the Brillouin zone. *Phys. Rev. B*, **8**:5747–5753, 1973. 77

[29] E.C.T. Chao, E.M. Shoemaker, and B.M. Madsen. Fist natural occurrence of Coesite. *Science*, **132**:220–222, 1960. 16

[30] C. Cheng. Uniaxial phase transition in Si: ab initio calculations. *Phys. Rev. B*, **67**:134109–1–134109–6, 2003. 90, 117, 119, 132, 142, 158, 160

[31] C. Cheng, W. Huang, and H. Li. Thermodynamics of uniaxial phase transition: ab initio study of the diamond-to-β-tin transition in Si and Ge. *Phys. Rev. B*, **63**:153202–1–153202–4, 2001. 90, 117, 119, 132, 142, 158, 160

[32] D.M. Clatterbuck, C.R. Krenn, M.L. Cohen, and J.W. Morris. Phonon instabilities and the ideal strength of aluminum. *Phys. Rev. Lett.*, **91**:135501–1–135501–4, 2003. 166

[33] M.L. Cohen. Pseudopotentials and total energy calculations. *Physica Scripta*, **T1**:5–10, 1982. 73

[34] M.L. Cohen. Electronic structure of solids. *Phys. Rep.*, **6**:293–309, 1984. 73

[35] N.L. Coleburn. Electrical measurements in silicon under shock-wave compression. *J. Appl. Phys.*, **43**:5007–5012, 1972. 85, 86

[36] J. Colvin and J. Larsen. *Extreme physics: properties and behavior of matter at extreme conditions*. Cambridge University Press, 2013. 1

[37] S. J. Cook and P. Clancy. Comparison of semi-empirical potential functions for silicon and germanium. *Phys. Rev. B*, **47**:7686–7699, 1993. 175

[38] A. Dal Corso, A. Pasquarello, A. Baldereschi, and R. Car. Generalized-gradient approximations to density-functional theory: a comparative study for atoms and solids. *Phys. Rev. B*, **53**:1180–1185, 1996. 100

[39] L. Davison. *Fundamentals of shock wave propagation in solids*. Springer, 2008. 36

[40] L. Davison and R.A. Graham. Shock compression of solids. *Phys. Rep.*, **55**:255–379, 1979. 9, 37

[41] M.S. Daw and M.I. Baskes. Embedded-atom method: derivation and application to impurities, surfaces, and other defects in metals. *Phys. Rev. B*, **29**:6443–6453, 1984. 17

[42] P.S. DeCarli and J.C. Jamieson. Formation of diamond by explosive shock. *Science*, **133**:1821–1822, 1961. 16

[43] A. Di Cicco, A.C. Frasini, M. Minicucci, E. Principi, J.P. Itiè, and P. Munsch. High-pressure and high-temperature study of phase transitions in solid germanium. *Phys. Status Solidi (B)*, **240**:19–28, 2003. 81, 106

[44] G. Dolling. *Inelastic scattering of neutrons in solids and liquids*. IAEA, 1963. 168

[45] M.T. Dove. *Structure and dynamics: an atomic view of materials*. Oxford University Press, 2002. 22

[46] R.P. Drake. *High-energy density physics*. Springer, 2006. 1

[47] H. G. Drickamer and S. Minomura. Pressure-induced phase transitions in silicon, germanium and some III-V compounds. *J. Phys. Chem. Solids*, **23**:451–456, 1962. 81

[48] L. Dubrovinsky, N. Dubrovinskaia, V.B. Prakapenka, and A.M. Abakumov. Implementation of micro-ball nanodiamond anvils for high-pressure studies above 6 Mbar. *Nat. Comm.*, **3**:1163–1170, 2012. 2, 4

[49] R.E. Duff and F.S. Minshall. Investigation of a shock-induced transition in bismuth. *Phys. Rev.*, **108**:1207–1212, 1957. 16

[50] M. Durandurdu. Structural phase transition of germanium under uniaxial stress: an ab initio study. *Phys. Rev. B*, **71**:054112–1–054112–5, 2005. 90, 91

[51] M. Durandurdu. Diamond to β-sn phase transition of silicon under hydrostatic and nonhydrostatic compressions. *J. Phys.: Condens. Matt.*, **20**:325232–325238, 2008. 90, 91

[52] G.E. Duvall. Shock-induced phase transitions in solids. In *Propagation of shock waves in solids*, pages 97–113, 1976. 126, 128, 205, 206

[53] G.E. Duvall and R.A. Graham. Phase transitions under shock wave loading. *Rev. Mod. Phys.*, **49**:523–579, 1977. 14, 79, 126, 205

[54] E. Engel and R.M. Dreizler. *Density functional theory: an advanced course*. Springer, 2011. 61

[55] M.I. Eremets. *High pressure experimental methods*. Oxford University Press, 1996. 3

[56] P. Erhart and K. Albe. Analytical potential for atomistic simulations of silicon, carbon, and silicon carbide. *Phys. Rev. B*, **71**:035211–1–035211–14, 2005. 60, 139, 175, 220

[57] R.A. Evarestov and V.P. Smirnov. Special points of the Brillouin zone and their use in the solid state theory. *Phys. Stat. Sol. (B)*, **119**:9–40, 1983. 77

[58] J.E. Field, S.M. Walley, W.G. Proud, H.T. Goldrein, and C.R. Siviour. Review of experimental techniques for high rate deformation and shock studies. *Int. J. Imp. Eng.*, **30**:725–775, 2004. 9

[59] J.W. Forbes. *Shock wave compression of condensed matter*. Springer, 2012. 36

[60] V.E. Fortov. *Extreme states of matter*. Springer, 2011. 1

[61] K. Gaál-Nagy. Ab initio study of the enthalpy barriers of the high-pressure phase transition from the cubic-diamond to the β-tin structure of silicon and germanium. *Comput. Mat. Sci.*, **30**:1–7, 2004. 94, 100, 106

[62] K. Gaál-Nagy, A. Bauer, M. Schmitt, K. Karch, P. Pavone, and D. Strauch. Temperature and dynamical effects on the high-pressure cubic-diamond $\rightarrow$ β-tin phase transition in Si and Ge. *Phys. Status Solidi (b)*, **211**:275–280, 1999. 95, 166

[63] K. Gaál-Nagy, P. Pavone, and D. Strauch. Ab initio study of the β-tin$\rightarrow$imma$\rightarrow$sh phase transitions in silicon and germanium. *Phys. Rev. B*, **69**:134112–1–134112–11, 2004. 90, 94, 104

[64] K. Gaál-Nagy, M. Schmitt, P. Pavone, and D. Strauch. Ab initio study of the high-pressure phase transition from the cubic-diamond to the β-tin structure of Si. *Comput. Mat. Sci.*, **22**:49–55, 2001. 166

[65] K. Gaál-Nagy and D. Strauch. Transition pressures and enthalpy barriers for the cubic diamond→ β-tin transition in Si and Ge under non-hydrostatic conditions. *Phys. Rev. B*, **73**:134101–1–134101–7, 2006. 20, 90, 92, 98, 99, 100, 104, 106, 108, 109, 110, 116, 117, 119, 120, 121, 130, 132, 221, 222

[66] T.C. Germann, B.L. Holian, P.S. Lomdahl, and R. Ravelo. Orientation dependence in molecular dynamics simulations of shocked single crystals. *Phys. Rev. Lett.*, **84**:5351–5354, 2000. 17, 172

[67] J.W. Gibbs. *The collected works of J.W. Gibbs*. Longmans, Green and Co., 1928. 129

[68] A.F. Gibson and M.H. Key. High-power lasers. *Rep. Prog. Phys.*, **43**:1–65, 1980. 11

[69] S.D. Gilev and A.M. Trubachev. Measurement of high electrical conductivity in silicon in shock waves. *J. Appl. Mech. Tech. Phys.*, pages 61–67, 1989. 85

[70] S.D. Gilev and A.M. Trubachev. Metallization of monocrystalline silicon under shock compression. *phys. stat. sol. (b)*, **211**:379–383, 1999. 85

[71] S.D. Gilev and A.M. Trubachev. Metallization of silicon in a shock wave: the metallization threshold and ultrahigh defect densities. *J. Phys.: Condens. Matt.*, **16**:8139–8153, 2004. 85, 86

[72] M. Glazer and J.S. Wark. *Statistical mechanics - A survival guide*. Oxford University Press, 2001. 206

[73] R.W. Goranson. Thermodynamic relations in multicomponent systems. *Carnegie Inst. Wash. Publ.*, **408**:329, 1930. 129, 130

[74] R.W. Goranson, D. Bancroft, B.L. Burton, T. Blechar, E.E. Houston, E.F. Gittings, and S.A. Landeen. Dynamic determination of the compressibility of metals. *J. Appl. Phys.*, **26**:1472–1479, 1955. 8

[75] T. Goto, T. Sato, and Y. Syono. Reduction of shear strength and phase-transition in shock-loaded silicon. *Jap. J. Appl. Phys.*, **21**:L369–L371, 1982. 83

[76] R. Graham, O. Jones, and J. Holland. Physical behavior of germanium under shock wave compression. *J. Phys. Chem. Solids*, **27**:1519–1529, 1966. 82

[77] R.A. Graham. *Solids under high-pressure shock compression*. Springer, 1993. 36

[78] H.W. Green. On the thermodynamics of non-hydrostatically stressed solids. *Phil. Mag. A*, **41**:637–647, 1980. 129

[79] M.C. Gupta and A.L. Ruoff. Static compression of silicon in the [100] and in the [111] directions. *J. Appl. Phys.*, **51**:1072–1075, 1980. 81, 106

[80] W.H. Gust and E.B. Royce. Axial yield strengths and two successive phase transition stresses for crystalline silicon. *J. Appl. Phys.*, **42**:1897–1905, 1971. 82, 84, 114, 115, 174, 220, 221, 224

[81] W.H. Gust and E.B. Royce. Axial yield strengths and phase-transition stresses for ⟨100⟩, ⟨110⟩, and ⟨111⟩ germanium. *J. Appl. Phys.*, **43**:4437–4442, 1972. 82, 84, 114, 115

[82] G. Hager and G. Wellein. *Introduction to high performance computing for scientists and engineers*. CRC Press, 2011. 17, 90

[83] D.R. Hamann, M. Schluter, and C. Chiang. Norm-conserving pseudopotentials. *Phys. Rev. Lett.*, **43**:1494–1497, 1979. 75

[84] C. Hammond. *The basics of crystallography and diffraction*. Oxford University Press, third edition, 2009. 22

[85] R.J. Hardy. Formulas for determining local properties in molecular-dynamics simulations: Shock waves. *J. Chem. Phys.*, **76**:622–628, 1982. 53

[86] R. Harrison, A. Voter, and S. Chen. *Atomistic simulation of materials: beyond pair potentials*. Plenum Press, 1989. 220

[87] J. Hawreliak and *et al.* Analysis of the X-ray diffraction signal for the α–ϵ transition in shock-compressed iron: simulation and experiment. *Phys. Rev. B*, **74**:184107–1–184107–16, 2006. 13

[88] R. Hennig, A. Wadehra, K. Driver, W. Parker, C. Umrigar, and J. Wilkins. Phase transformation in Si from semiconducting diamond to metallic β-Sn phase in QMC and DFT under hydrostatic and anisotropic stress. *Phys. Rev. B*, **82**:014101–1–014101–9, 2010. 90, 100, 118

[89] C. Herring. A new method for calculating wave functions in crystals. *Phys. Rev.*, **57**:1169–1177, 1940. 72

[90] Y. Hironaka, A. Yazaki, F. Saito, and K.G. Nakamura. Evolving shock-wave profiles measured in a silicon crystal by picosecond time-resolved X-ray diffraction. *Appl. Phys. Lett.*, **77**:1967–1969, 2000. 85

[91] P. Hohenberg and W. Kohn. Inhomogeneous electron gas. *Phys. Rev.*, **136**:B864–B871, 1964. 64

[92] B. L. Holian. Atomistic computer simulations of shock waves. *Shock Waves*, **5**:149–157, 1995. 16, 171

[93] B.L. Holian. Modeling shock-wave deformation via molecular dynamics. *Phys. Rev. A*, **37**:2562–2568, 1988. 16, 171

[94] B.L. Holian. Molecular dynamics comes of age for shock wave research. *Shock Waves*, **13**:489–495, 2004. 16, 171

[95] B.L. Holian and P.S. Lomdahl. Plasticity induced by shock waves in nonequilibrium molecular-dynamics simulations. *Science*, **280**:2085–2088, 1998. 172

[96] M. Holt, Z. Wu, H. Hong, P. Zschack, P. Jemian, J. Tischler, H. Chen, and T.C. Chiang. Determination of phonon dispersions from X-ray transmission scattering: the example of silicon. *Phys. Rev. Lett.*, **83**:3317–3319, 1999. 168

[97] W.B. Holzapfel. Physics of solids under strong compression. *Rep. Prog. Phys.*, **59**:29–90, 1996. 1

[98] W.B. Holzapfel and N.S. Isaacs. *High-pressure techniques in chemistry and physics*. Oxford University Press, 1997. 3

[99] M.A. Hopcroft, W.D. Nix, and T.W. Kenny. What is the Young's modulus of silicon? *J. Microelectromech. sys.*, **19**:229–238, 2010. 115

[100] J.Z. Hu, L.D. Merkle, C.S. Menoni, and I.L. Spain. Crystal data for high-pressure phases of silicon. *Phys. Rev. B*, **34**:4679–4684, 1986. 81

[101] J.Z. Hu and I.L. Spain. Phases of silicon at high pressure. *Solid State Comm.*, **51**:263–266, 1984. 81, 106

[102] H. Hugoniot. Memoire sur la propagation des mouvements dans les corps et specialement dans les gaz parfaits. *J. l'Ecole Polytech.*, **57**:397, 1887. 38

[103] R. Hull. *Properties of crystalline silicon*. INSPEC, 1999. 81

[104] Y. Ida. Thermodynamic theory of nonhydrostatically stressed solid involving finite strain. *J. Geophys. Res.*, **74**:3208–3218, 1969. 129, 130

[105] H. Injeyan and G.D. Goodno. *High-power laser handbook*. McGraw-Hill, 2011. 11

[106] S. Izumi and S. Sakai. Internal displacement and elastic properties of the silicon Tersoff model. *JSME Int. J. A*, **47**:54–61, 2004. 175

[107] J.C. Jamieson. Crystal structures at high pressures of metallic modifications of silicon and germanium. *Science*, **139**:762–764, 1963. 81

[108] J.C. Jamieson and A.W. Lawson. X-ray diffraction studies in the 100 kilobar pressure range. *J. Appl. Phys.*, **33**:776–780, 1962. 15

[109] A. Jayaraman. Diamond anvil cell and high-pressure physical investigations. *Rev. Mod. Phys.*, **55**:65–108, 1983. 3

[110] J.W. Jeong and K.J. Chang. Molecular-dynamics simulations for the shock Hugoniot meltings of Cu, Pd and Pt. *J. Phys.: Condens. Matter*, **11**:3799–3806, 1999. 17

[111] J.W. Jeong, I.H. Lee, and K.J. Chang. Molecular-dynamics study of melting on the shock Hugoniot of Al. *Phys. Rev. B*, **59**:329–333, 1999. 17

[112] S.M. Jeong and T. Kitamura. Atomistic simulation on the phase transformation of silicon under nonhydrostatic stress. *Jap. J. Appl. Phys.*, **46**:5924–5929, 2007. 90, 132, 175

[113] J.N. Johnson. The role of the Gibbs function in solid-solid phase transformations under nonhydrostatic stress conditions. In *AIP Conf. Proc.*, **1426**, pages 11–18, 2012. 133

[114] J.N. Johnson and R. Cheret. *Classic papers in shock compression science*. Springer, 1998. 6

[115] J.N. Johnson and R. Cheret. Shock waves in solids: an evolutionary perspective. *Shock Waves*, **9**:193–200, 1999. 6

[116] R.O. Jones and O. Gunnarsson. The density functional formalism, its applications and prospects. *Rev. Mod. Phys.*, **61**:689–746, 1989. 18, 61

[117] K. Kadau, T.C. Germann, P.S. Lomdahl, R.C. Albers, J.S. Wark, A. Higginbotham, and B.L. Holian. Shock waves in polycrystalline iron. *Phys. Rev. Lett.*, **98**:135701–1–135701–4, 2007. 15, 171

[118] K. Kadau, T.C. Germann, P.S. Lomdahl, and B.L. Holian. Microscopic view of structural phase transitions induced by shock waves. *Science*, **296**:1681–1684, 2002. 15, 18, 92, 171

[119] K. Kadau, T.C. Germann, P.S. Lomdahl, and B.L. Holian. Atomistic simulations of shock-induced transformations and their orientation dependence in bcc Fe single crystals. *Phys. Rev. B*, **72**:064120–1–064120–14, 2005. 15, 171

[120] A. Kailer, Y.G. Gogotsi, and K.G. Nickel. Phase transformations of silicon caused by contact loading. *J. Appl. Phys.*, **81**:3057–3063, 1997. 81, 106

[121] D. Kalantar, J. Belak, G. Collins, J. Colvin, H. Davies, J. Eggert, T. Germann, J. Hawreliak, B. Holian, K. Kadau, P. Lomdahl, H. Lorenzana, M. Meyers, K. Rosolankova, M. Schneider, J. Sheppard, J. Stölken, and J. Wark. Direct observation of the α–ϵ transition in shock-compressed iron via nanosecond X-ray diffraction. *Phys. Rev. Lett.*, **95**:075502–1–075502–4, 2005. 13, 15

[122] D Kalantar, G Collins, J Colvin, J Eggert, J Hawreliak, H Lorenzana, M Meyers, R Minich, K Rosolankova, and M Schneider. In situ diffraction measurements of lattice response due to shock loading, including direct observation of the α–ϵ phase transition in iron. *Int. J. Imp. Eng.*, **33**:343–352, 2006. 13

[123] D. H. Kalantar, E. A. Chandler, J. D. Colvin, R. Lee, B. A. Remington, S. V. Weber, L. G. Wiley, A. Hauer, J. S. Wark, A. Loveridge, B. H. Failor, M. A. Meyers, and G. Ravichandran. Transient X-ray diffraction used to diagnose shock compressed Si crystals on the Nova laser. *Rev. Sci. Instrum.*, **70**:629–632, 1999. 85

[124] D.H. Kalantar, J. Belak, E. Bringa, K. Budil, M. Caturla, J. Colvin, M. Kumar, K. T. Lorenz, R. E. Rudd, J. Stolken, A.M. Allen, K. Rosolankova, J.S. Wark, M.A. Meyers, and M. Schneider. High-pressure, high-strain-rate lattice response of shocked materials. *Phys. Plasmas*, **10**:1569–1576, 2003. 85, 87

[125] D.H. Kalantar, E. Bringa, M. Caturla, J. Colvin, K. T. Lorenz, M. Kumar, J. Stolken, A. M. Allen, K. Rosolankova, J. S.

Wark, M. A. Meyers, M. Schneider, and T. R. Boehly. Multiple film plane diagnostic for shocked lattice measurements (invited). *Rev. Sci. Instrum.*, **74**:1929–1934, 2003. 85, 87

[126] D.H. Kalantar, B.A. Remington, J.D. Colvin, K.O. Mikaelian, S.V. Weber, L.G. Wiley, J.S. Wark, A. Loveridge, A.M. Allen, A.A. Hauer, and M.A. Meyers. Solid-state experiments at high pressure and strain rate. *Phys. Plasmas*, **7**:1999–2006, 2000. 85

[127] W.B. Kamb. The thermodynamic theory of nonhydrostatically stressed solids. *J. Geophys. Res.*, **66**:259–271, 1961. 129

[128] G.I. Kanel, S.V. Razorenov, and V.E. Fortov. *Shock-wave phenomena and the properties of condensed matter*. Springer, 2004. 36

[129] M. Kato and H.R. Pak. Thermodynamics of stress-induced first-order phase transformations in solids. *Phys. Status Solidi (B)*, **123**:415–424, 1984. 122

[130] C. L. Kelchner, S. J. Plimpton, and J. C. Hamilton. Dislocation nucleation and defect structure during surface indentation. *Phys. Rev. B*, **58**:11085–11088, 1998. 177, 179, 182

[131] G. Kimminau and *et al.* Simulating picosecond X-ray diffraction from shocked crystals using post-processing molecular dynamics calculations. *J. Phys.: Condens. Matter*, **20**:505203–1–505203–8, 2008. 177

[132] G. Kimminau, P. Erhart, E.M. Bringa, B. Remington, and J.S. Wark. Phonon instabilities in uniaxially compressed fcc metals as seen in molecular dynamics simulations. *Phys. Rev. B*, **81**:092102–1–092102–4, 2010. 166

[133] H. Kishimura. Lattice deformation in laser-irradiated silicon crystal studied by picosecond X-ray diffraction. *Appl. Surf. Sci.*, **207**:314–317, 2003. 85

[134] H. Kishimura and H. Matsumoto. Effect of phase transition in shock-recovered silicon. *J. Appl. Phys.*, **103**:023505–1–023505–6, 2008. 88

[135] H. Kishimura, H. Matsumoto, and N.N. Thadhani. Effect of shock compression on single crystalline silicon. *J. Phys.: Conf. Ser.*, **215**:012145–1–012145–4, 2010. 88

[136] H. Kishimura, H. Morishita, Y. Okano, Y. Hironaka, K. Kondo, K. Nakamura, and T. Atou. Micromosaic formation in laser-irradiated Si probed by picosecond time-resolved X-ray diffraction. *Phys. Rev. B*, **74**:224301–1–224301–5, 2006. 85, 87

[137] J. Kohanoff. *Electronic structure calculations for solids and molecules*. Cambridge University Press, 2006. 61

[138] W. Kohn and L.J. Sham. Self-consistent equations including exchange and correlation effects. *Phys. Rev.*, **140**:A1133–A1138, 1965. 66, 69

[139] P.O.K. Krehl. *History of shock waves, explosions and impact*. Springer, 2009. 6

[140] P.O.K. Krehl. Shock wave physics and detonation physics - a stimulus for the emergence of numerous new branches in science and engineering. *Eur. Phys. J. H*, **36**:85–152, 2011. 7, 8

[141] G. Kresse and J. Furthmüller. Efficient iterative schemes for ab initio total-energy calculations using a plane-wave basis set. *Phys. Rev. B*, **54**:11169–11186, 1996. 72, 100, 166

[142] G. Kresse and J. Hafner. Norm-conserving and ultrasoft pseudopotentials for first-row and transition elements. *J. Phys.: Condens. Matter*, **6**:8245–8257, 1994. 100

[143] M. Kumazawa. A note on the thermodynamic theory of nonhydrostatically stressed solids. *J. Geophys. Res.*, **66**:3981–3984, 1961. 129, 130

[144] L.D. Landau and E.M. Lifshitz. *Theory of elasticity*. Butterworth-Heinemann, third edition, 1986. 98, 130, 131

[145] J.M.D. Lane and A.P. Thompson. Molecular dynamics simulation of shock-induced phase transition in germanium. In *AIP Conf. Proc.*, **1195**, pages 1157–1160, 2009. 21, 173, 182

[146] I. Lee, J. Jeong, and K.J. Chang. Invariant molecular dynamics study of the diamond-to-β-sn transition in Si under hydrostatic and uniaxial compressions. *Phys. Rev. B*, **55**:5689–5693, 1997. 90, 175

[147] H. Libotte and J.P. Gaspard. Pressure-induced distortion of the β-sn phase in silicon: effects of nonhydrostaticity. *Phys. Rev. B*, **62**:7110–7115, 2000. 90, 128

[148] H. Libotte and J.P. Gaspard. A comparative study of non-hydrostaticity theoretical descriptions : the diamond-to-β-Sn transition in silicon under pressure. *J. Phys. Soc. Jap.*, **81**:074606–1–074606–3, 2012. 90

[149] Y. Lin, R. Perriot, V. V. Zhakhovsky, X. Gu, C. T. White, and I. I. Oleynik. Shock induced phase transition in diamond. In *AIP Conf. Proc.*, **1426**, pages 1171–1174, 2011. 173

[150] H.E. Lorenzana, J.F. Belak, K.S. Bradley, E.M. Bringa, K.S. Budil, J.U. Cazamias, B. El-Dasher, and J.A. Hawreliak. Shocked materials at the intersection of experiment and simulation. *Sci. Model. Simul.*, **15**:159–186, 2008. 50, 79

[151] J. Loveday. *High-pressure physics*. CRC Press, 2012. 1

[152] A. Loveridge-Smith and *et al.* Anomalous elastic response of silicon to uniaxial shock compression on nanosecond time scales. *Phys. Rev. Lett.*, **86**:2349–2352, 2001. 85, 87

[153] G.J.F. MacDonald. Thermodynamics of solids under non-hydrostatic stress with geological applications. *Am. J. Sci.*, **255**:266–281, 1957. 129, 130

[154] M.P. Marder. *Condensed matter physics*. Wiley, second edition, 2010. 22

[155] S.P. Marsh. *LASL shock Hugoniot data*. University of California Press, 1980. 8

[156] R.M. Martin. *Electronic structure - basic theory and practical methods*. Cambridge University Press, 2004. 19, 61, 65, 70

[157] A.G. McLellan. A thermodynamical theory of systems under nonhydrostatic stresses. *J. Geophys. Res.*, **71**:4341–4347, 1966. 129, 130

[158] A.G. McLellan. The chemical potential in thermodynamic systems under non-hydrostatic stresses. *Proc. Roy. Soc. Lond. A*, **307**:1–13, 1968. 129, 130

[159] A.G. McLellan. Non-hydrostatic thermodynamics of chemical and phase changes. *Pure Appl. Chem.*, **22**:287–292, 1970. 129, 130

[160] A.G. McLellan. Non-hydrostatic thermodynamics of chemical systems. *Proc. Roy. Soc. Lond. A*, **314**:443–455, 1970. 129, 130

[161] M. I. McMahon, R. J. Nelmes, N. G. Wright, and D. R. Allan. Pressure dependence of the Imma phase of silicon. *Phys. Rev. B*, **50**:739–743, 1994. 176

[162] M.I. McMahon and R.J. Nelmes. New high-pressure phase of Si. *Phys. Rev. B*, **47**:8337–8340, 1993. 93, 107, 176

[163] C.S. Menoni, J.Z. Hu, and I.L. Spain. Germanium at high pressures. *Phys. Rev. B*, **34**:362–368, 1986. 81, 106

[164] M. Methfessel and A.T. Paxton. High-precision sampling for Brillouin-zone integration in metals. *Phys. Rev. B*, **40**:3616–3621, 1989. 101

[165] M.A. Meyers. *Dynamic behavior of materials*. Wiley, 1994. 19, 36

[166] M.A. Meyers and K. Chawka. *Mechanical behavior of materials*. Cambridge University Press, second edition, 2009. 97, 98

[167] M.A. Meyers, F. Gregori, B.K. Kad, M.S. Schneider, D.H. Kalantar, B.A. Remington, G. Ravichandran, T. Boehly, and J.S. Wark. Laser-induced shock compression of monocrystalline copper: characterization and analysis. *Acta Materialia*, **51**:1211–1228, 2003. 89

[168] M.A. Meyers and L.E. Murr. *Shock-waves and high-strain-rate phenomena in metals (pp 675-703)*. Plenum Publishing, 1981. 12

[169] D. Milathianaki, S. Boutet, G. J. Williams, A. Higginbotham, D. Ratner, A.E. Gleason, M. Messerschmidt, M. M. Seibert, D. C. Swift, P. Hering, J. Robinson, W. E. White, and J. S. Wark. Femtosecond visualization of lattice dynamics in shock-compressed matter. *Science*, **342**:220–223, 2013. 89, 225

[170] Y. Mishin, M.J. Mehl, D.A. Papaconstantopoulos, A.F. Voter, and J.D. Kress. Structural stability and lattice defects in copper: ab initio, tight-binding, and embedded-atom calculations. *Phys. Rev. B*, **63**:224106–1–224106–16, 2001. 17

[171] K. Mizushima, S. Yip, and E. Kaxiras. Ideal crystal stability and pressure-induced phase transition in silicon. *Phys. Rev. B*, **50**:14952–14959, 1994. 175

[172] G. Mogni, A. Higginbotham, K. Gaál-Nagy, N. Park, and J.S. Wark. Molecular dynamics simulations of shock-compressed single-crystal silicon. *Phys. Rev. B.*, **89**:064104–1–064104–10, 2014. 21, 174

[173] M. Moll, M. Bockstedte, M. Fuchs, E. Pehlke, and M. Scheffler. Application of generalized gradient approximations: the diamond-β-tin phase transition in Si and Ge. *Phys. Rev. B*, **52**:2550–2556, 1995. 100

[174] H.J. Monkhorst and J.D. Pack. Special points for Brillouin-zone integrations. *Phys. Rev. B*, **13**:5188–5192, 1976. 101

[175] A. Mujica, A. Rubio, A. Muñoz, and R. Needs. High-pressure phases of group-IV, III-V, and II-VI compounds. *Rev. Mod. Phys.*, **75**:863–912, 2003. 80, 90

[176] M.M. Murnane, H.C. Kapteyn, M.D. Rosen, and R.W. Falcone. Ultrafast X-ray pulses from laser-produced plasmas. *Science*, **251**:531–536, 1991. 86

[177] K.G. Nakamura, Y. Hironaka, H. Kawano, H. Kishimura, and K.I. Kondo. Picosecond time-resolved X-ray diffraction from laser-shocked semiconductors. *Laser Part. Beams*, **22**:285–288, 2004. 85, 88

[178] K.G. Nakamura, H. Kawano, H. Kishimura, Y. Okano, Y. Hironaka, and K. Kondo. Picosecond time-resolved X-ray diffraction from a laser-shocked germanium crystal above Hugoniot elastic limit. *Jap. J. Appl. Phys.*, **43**:5477–5479, 2004. 88

[179] R.J. Needs and A. Mujica. First-principles pseudopotential study of the structural phases of silicon. *Phys. Rev. B*, **51**:9652–9660, 1995. 100

[180] G. Nilsson and G. Nelin. Study of the homology between silicon and germanium by thermal-neutron spectrometry. *Phys. Rev. B*, **6**:3777–3786, 1972. 168

[181] I. I. Oleynik, S. V. Zybin, M. L. Elert, and C. T. White. Nanoscale molecular dynamics simulation of shock compression of silicon. In *AIP Conf. Proc.*, **845**, pages 413–416, 2005. 172

[182] W.C. O'Mara, R.B. Herring, and L.P. Hunt. *Handbook of semiconductor silicon technology*. Noyes Publications, 1990. 78

[183] D.C. Pack, W.M. Evans, and H.J. James. The propagation of shock waves in steel and lead. *The Proceedings of the Physical Society*, **60**:1–8, 1948. 8

[184] M.S. Paterson. Nonhydrostatic thermodynamics and its geologic applications. *Rev. Geophys. Space Phys.*, **11**:355–389, 1973. 129, 130

[185] M.N. Pavlovskii. *Sov. Phys. Solid State*, **9**:2514, 1968. 82

[186] M.C. Payne, M.P. Teter, D.C. Allan, T.A. Arias, and J.D. Joannopoulos. Iterative minimization techniques for ab initio total-energy calculations: molecular dynamics and conjugate gradients. *Rev. Mod. Phys.*, **64**:1045–1097, 1992. 61

[187] J.P. Perdew, K. Burke, and M. Ernzerhof. Generalized gradient approximation made simple. *Phys. Rev. Lett.*, **77**:3865–3868, 1996. 71

[188] J.P. Perdew, K. Burke, and Y. Wang. Generalized gradient approximation for the exchange-correlation hole of a many-electron system. *Phys. Rev. B*, **54**:533–539, 1996. 71

[189] J.P. Perdew, J.A. Chevary, S.H. Vosko, K.A. Jackson, M.R. Pederson, D.J. Singh, and C. Fiolhais. Atoms, molecules, solids and surfaces: applications of the generalized gradient approximation for exchange and correlation. *Phys. Rev. B*, **46**:6671–6687, 1992. 100

[190] J.P. Perdew and W. Yue. Accurate and simple density functional for the electronic exchange energy: generalized gradient approximation. *Phys. Rev. B*, **33**:8800–8802, 1986. 71

[191] J.P. Perdew and A. Zunger. Self-interaction correction to density-functional approximations for many electron systems. *Phys. Rev. B*, **23**:5048–5079, 1981. 70

[192] R. Perriot, Y. Lin, V. V. Zhakhovsky, N. Pineau, J. H. Los, J. B. Maillet, L. Soulard, C. T. White, and I. I. Oleynik. Shock compression of diamond: molecular dynamics simulations using different interatomic potentials. In *AIP Conf. Proc.*, **1426**, pages 1175–1178, 2011. 173

[193] K.E. Petersen. Silicon as a mechanical material. *Proc. IEEE*, **70**:420–457, 1982. 79

[194] S. Pfalzner. *An introduction to inertial confinement fusion*. Taylor and Francis, 2006. 13

[195] W.E. Pickett. Pseudopotential methods in condensed matter applications. *Comp. Phys. Rep.*, **9**:115, 1989. 73

[196] S. Plimpton. Fast parallel algorithms for short-range molecular dynamics. *J. Comp. Phys.*, **117**:1–19, 1995. 17, 139, 175

[197] P. Pulay. Ab initio calculation of force constants and equilibrium geometries. I. Theory. *Mol. Phys.*, **17**:197–204, 1969. 101

[198] S. B. Quadri, E. F. Skelton, and A. W. Webb. High pressure studies of Ge using synchrotron radiation. *J. Appl. Phys.*, **54**:3609–3611, 1983. 81, 106

[199] W.J.M. Rankine. On the thermodynamic theory of waves of finite longitudinal disturbance. *Phil. Trans. Roy. Soc. Lond.*, **160**:277–288, 1870. 6, 38

[200] D.C. Rapaport. *The art of molecular dynamics simulation*. Cambridge University Press, 2004. 51

[201] B.A. Remington, P. Allen, E.M. Bringa, J. Hawreliak, D. Ho, K.T. Lorenz, H. Lorenzana, J.M. McNaney, M.A. Meyers, S.W. Pollaine, K. Rosolankova, B. Sadik, M.S. Schneider, D. Swift, J. Wark, and B. Yaakobi. Material dynamics under extreme conditions of pressure and strain rate. *Mat. Sci. Tech.*, **22**:474–488, 2006. 79

[202] B.A. Remington, G. Bazan, J. Belak, E. Bringa, M. Caturla, J.D. Colvin, M.J. Edwards, S.G. Glendinning, D.S. Ivanov, B. Kad, and D.H. Kalantar. Materials science under extreme conditions of pressure and strain rate. *Metal. Mat. Trans. A*, **35A**:2587–2607, 2004. 79

[203] M.H. Rice, R.G. McQueen, and J.M. Walsh. Compression of solids by strong shock waves. *Sol. State. Phys.*, **6**:1–63, 1958. 8

[204] K.F. Riley, M.P. Hobson, and S.J. Bence. *Mathematical methods for physics and engineering*. Cambridge University Press, third edition, 2006. 158, 159

[205] S. Root, R.J. Hardy, and D.R. Swanson. Continuum predictions from molecular dynamics simulations: shock waves. *J. Chem. Phys.*, **118**:3161–3165, 2003. 53

[206] C. Rose-Petruck, R. Jimenez, T. Guo, A. Cavalleri, C.W. Siders, F. Raksi, J.A. Squier, B.C. Walker, K.R. Wilson, and C.P.J. Barty. Picosecond-milliangstrom lattice dynamics measured by ultrafast X-ray diffraction. *Nature*, **398**:310–312, 1999. 87

[207] G. Rosenberg. Resistivity measurements in silicon compressed by shock waves. *J. Phys. Chem. Solids*, **41**:561–567, 1979. 85, 86

[208] M. Ross. Matter under extreme conditions of temperature and pressure. *Rep. Prog. Phys.*, **48**:1–52, 1985. 1

[209] M.H. Sadd. *Elasticity - theory, applications and numerics*. Academic Press, second edition, 2009. 97, 98

[210] M.D. Salas. The curious events leading to the theory of shock waves. In *Invited Lecture at the 17th Shock Interaction Symposium, Rome, Italy*, 2006. 6

[211] M. Schaible. Empirical molecular dynamics modeling of silicon and silicon dioxide : a review. *Crit. Rev. Sol. Stat. Mat. Sci.*, **24**:265–323, 1999. 60, 175

[212] I. Shimizu. Nonhydrostatic and nonequilibrium thermodynamics of deformable materials. *J. Geophys. Res.*, **97**:4587–4597, 1992. 129

[213] P. Siffert and E.F. Krimmel. *Silicon - evolution and future of a technology*. Springer, 2004. 78

[214] D.J. Singh and L. Nordstrom. *Planewaves, pseudopotentials, and the LAPW method*. Springer, second edition, 2006. 61, 72

[215] S. A. Sous, B. O. Hildmann, and W. A. Kaysser. Characterization of dislocation densities in germanium and silicon single crystals by high resolution X-ray diffraction. *Phys. Stat. Sol. (a)*, **159**:343–353, 1997. 176

[216] M.O. Steinhauser and S. Hiermaier. A review of computational methods in materials science : examples from shock-wave and polymer physics. *Int. J. Mol. Sci.*, **10**:5135–5216, 2009. 16, 18

[217] M. E. Straumanis and E. Z. Aka. Lattice parameters, coefficients of thermal expansion, and atomic weights of purest silicon and germanium. *J. Appl. Phys.*, **23**:330–334, 1952. 93

[218] M.J. Suggit, A. Higginbotham, J.A. Hawreliak, G. Mogni, G. Kimminau, P. Dunne, A.J. Comley, N. Park, B.A. Remington, and J.S. Wark. Nanosecond white-light Laue diffraction measurements of dislocation microstructure in shock-compressed single-crystal copper. *Nat. Comm.*, **3**:1224–1230, 2012. 89

[219] M.J. Suggit, G. Kimminau, J. Hawreliak, B.A. Remington, N. Park, and J.S. Wark. Nanosecond X-ray Laue diffraction apparatus suitable for laser shock compression experiments. *Rev. Sci. Instrum.*, **81**:083902–1–083902–4, 2010. 85

[220] E.B. Tadmor and R.E. Miller. *Modeling materials - continuum, atomistic and multiscale techniques*. Cambridge University Press, 2011. 16, 51

[221] D. Tanguy, M. Mareschal, P.S. Lomdahl, T.C. Germann, B.L. Holian, and R. Ravelo. Dislocation nucleation induced by a shock wave in a perfect crystal: molecular dynamics simulations and elastic calculations. *Phys. Rev. B*, **68**:144111–1–144111–10, 2003. 172

[222] R. Teisseyre and E. Majewski. *Earthquake thermodynamics and phase transformations in the Earth's interior (pp 81-102)*. Academic Press, 2001. 129

[223] J. Tersoff. New empirical model for the structural properties of silicon. *Phys. Rev. Lett.*, **56**:632–635, 1986. 57, 175

[224] J. Tersoff. Empirical interatomic potential for silicon with improved elastic properties. *Phys. Rev. B*, **38**:9902–9905, 1988. 57, 175

[225] J. Tersoff. New empirical approach for the structure and energy of covalent systems. *Phys. Rev. B*, **37**:6991–7000, 1988. 19, 57, 175

[226] J. Tersoff. Modeling solid-state chemistry: interatomic potentials for multicomponent systems. *Phys. Rev. B*, **39**:5566–5568, 1989. 57, 175

[227] E.Y. Tonkov and E.G. Ponyatovsky. *Phase transformations of elements under high pressure (pp 96-115)*. CRC Press, 2005. 81

[228] S.J. Turneaure and Y. M. Gupta. Inelastic deformation and phase transformation of shock compressed silicon single crystals. *Appl. Phys. Lett.*, **91**:201913–1–201913–3, 2007. 84, 85

[229] S.J. Turneaure and Y.M. Gupta. X-ray diffraction and continuum measurements in silicon crystals shocked below the elastic limit. *Appl. Phys. Lett.*, **90**:051905–1–051905–3, 2007. 84

[230] D. Vanderbilt. Soft self-consistent pseudopotentials in a generalized eigenvalue formalism. *Phys. Rev. B*, **41**:7892–7895, 1990. 76, 100

[231] J. Veerhogen. The chemical potential of a stressed solid. *Trans. Am. Geophys. Union*, **32**:251–258, 1951. 129, 130

[232] L. Verlet. Computer "experiments" on classical fluids. I. Thermodynamical properties of Lennard-Jones molecules. *Phys. Rev.*, **159**:98–103, 1967. 54

[233] H. Veselka, A. Neuber, and J. Dickens. Shock induced conductivity for high power switching. *IEEE*, pages 734–737, 2005. 80

[234] G. Voronin, C. Pantea, T. Zerda, L. Wang, and Y. Zhao. In situ X-ray diffraction study of silicon at pressures up to 15.5 GPa and temperatures up to 1073 K. *Phys. Rev. B*, **68**:020102–1–020102–4, 2003. 81, 95, 106

[235] A. Voter. Embedded atom method potentials for seven FCC metals: Ni, Pd, Pt, Cu, Ag, Au and Al. In *Los Alamos Unclassified Technical Report*, **93**, page 3901, 1993. 220

[236] J.R. Waldram. *The theory of thermodynamics*. Cambridge University Press, 1985. 143

[237] J.M. Walsh and M.H. Rice. Dynamic compression of liquids from measurements on strong shock waves. *J. Chem. Phys.*, **26**:815–823, 1957. 15

[238] J. S. Wark, D. Riley, N. C. Woolsey, G. Keihn, and R. R. Whitlock. Direct measurements of compressive and tensile strain during shock breakout by use of subnanosecond X-ray diffraction. *J. Appl. Phys.*, **68**:4531–4534, 1990. 85

[239] J.S. Wark. Time-resolved X-ray diffraction. *Cont. Phys.*, **37**:205–218, 1996. 85

[240] J.S. Wark, R.R. Whitlock, A. Hauer, J.E. Swain, and P.J. Solone. Shock launching in silicon studied with use of pulsed X-ray diffraction. *Phys. Rev. B*, **35**:9391–9394, 1987. 85

[241] J.S. Wark, R.R. Whitlock, A.A. Hauer, J.E. Swain, and P.J. Solone. Subnanosecond X-ray diffraction from laser-shocked crystals. *Phys. Rev. B*, **40**:5705–5714, 1989. 85

[242] R.H. Wentorf and J.S. Kasper. Two new forms of silicon. *Science*, **139**:338–339, 1963. 81

[243] A. Werner, J.A. Sanjurjo, and M. Cardona. X-ray investigation of the α–β phase transition in the Ge_xSi_{1-x} solid solutions at high pressure. *Solid State Comm.*, **44**:155–158, 1982. 106, 107

[244] B.R. Wu. Vibrational properties of Si and Ge under high pressures. *Chin. J. Phys.*, **44**:454–466, 2006. 166

[245] S. Yip. *Handbook of materials modeling, Vol. 1 (pp 565-588).* Springer, 2005. 19, 51, 54

[246] Y.B. Zel'dovich and Y.P. Raizer. *Physics of shock waves and high-temperature hydrodynamic phenomena.* Academic Press, 1966. 36

[247] H. Zhao, Z. Tang, G. Li, and N. R. Aluru. Quasiharmonic models for the calculation of thermodynamic properties of crystalline silicon under strain. *J. Appl. Phys.*, **99**:064314–1–064314–12, 2006. 175

[248] M.V. Zhernokletov and B.L. Glushak. *Material properties under intensive dynamic loading.* Springer, 2006. 36